RÉPUBLIQUE FRANÇAISE
Liberté
Égalité
Fraternité

cnes
CENTRE NATIONAL D'ÉTUDES SPATIALES

Recueil des posters scientifiques

JOURNÉES CNES
JEUNES CHERCHEURS
Du 16 au 18 octobre 2024
Cité de l'Espace de Toulouse

JC2

Recueil des posters

Session 1

S01-01 | Doc | **AIT TALEB Hind** | ONERA, Toulouse | Encadrant CNES : Steven MERCIER | POSTER |
Traitement multi-antennes et formes d'ondes optimisées pour radar compact embarqué

S01-02 | Doc | **AYKROYD Christopher** | OBSPM – SYRTE, Paris | Encadrant CNES : Martin BOUTELIER | POSTER |
Galactic Binaries avec LISA

S01-03 | Post-doc | **BAJIC Slaven** | CNES, Toulouse | Encadrant CNES : Guillaume BOUDIER | POSTER |
Pulsating Heat Pipe Simulation Enhancement

S01-04 | Post-doc | **BENDINGER Arne** | LOPS, Plouzané | Encadrant CNES : Yannice FAUGERE | POSTER |
Dynamical interpretation of SWOT SSH south of New Caledonia

S01-05 | Doc | **CONAN Lucile** | LATMOS, Guyancourt | Encadrant CNES : Francis ROCARD | POSTER |
De Venus Express à EnVision : contribution au développement du spectromètre VeSUV

S01-06 | Doc | **GELAGAY Habtamu Sewnet** | CIRAD, Montpellier | Encadrant CNES : Philippe MAISONGRANDE | Poster à venir |
Large – scale yield gap estimation and characterization with multi – source remote sensing date – case study of rainfed wheat in Ethiopia

S01-07 | Doc | **LAHLIMI ALAMI Hiba** | XLIM, Limoges | Encadrant CNES : Pedro RYNKIEWICZ | POSTER |
Impression 3D métallique de composants innovants pour applications millimétriques

S01-08 | Doc | **MÉTAYER Clément** | CNRS – LP2N, Talence | Encadrant CNES : Thomas LEVEQUE | POSTER |
Gaz bi-espèce de Rubidium et Potassium ultra-froid en microgravité

S01-09 | Doc | **PINNEPALLI Chandrika** | CESBIO, Toulouse | Encadrant CNES : Philippe GAMET | POSTER |
Characterization of directional effects in thermal domain for the preparation of TRISHNA mission

S01-10 | Doc | **SAUNIÈRE Lucas** | CPPM, Marseille | Encadrant CNES : Philippe LAUDET | POSTER |
Modélisation de la réponse instrumentale du NISP

S01-11 | Post-doc | **SCHMIDT Winfried** | LIPhy, Saint Martin d'Hères | Encadrant CNES : Thierry BRET-DIBAT | POSTER |
Effects of microgravity on cell motility

Traitement multi-antennes et formes d'ondes optimisées pour radar compact embarqué

Hind AIT TALEB [1,3] Valentine WASIK [1] Abigael TAYLOR [2] Yassin EL HILLALI [3]
[1]ONERA/DEMR, Université de Toulouse, F-31055 Toulouse
[2]DEMR, ONERA, Université Paris-Saclay, F-91123 Palaiseau
[3]IEMN, UMR CNRS 8520, UPHF, 59300 Valenciennes

Contexte

Dans le domaine spatial, les nano-satellites (satellites artificiels mesurant quelques dizaines de centimètres de côté) interviennent dans une multitude d'applications, parmi elles la détection de débris spatiaux. Ces nano-satellites intègrent des capteurs embarqués pour détecter des cibles et déterminer certaines de leurs caractéristiques (distance, vitesse, angle). Afin d'améliorer les performances de détection, et plus précisément la résolution angulaire, le radar MIMO (Multiple-Input Multiple-Output) peut être utilisé. Ce radar doit être optimisé en termes de formes d'ondes et d'architectures. Plusieurs critères interviennent dans le choix des formes d'ondes (portée, résolution, taille des lobes secondaires). Les traitements radar doivent également être adaptés au contexte spatial (caractéristique des débris, temps d'intégration . . .).

Choix de la forme d'onde

- Le signal reçu est une copie atténuée, retardée et soumise à l'effet Doppler du signal émis.
- Pour estimer les paramètres (distance, vitesse, angle) de la cible, un filtre adapté est appliqué au signal reçu.

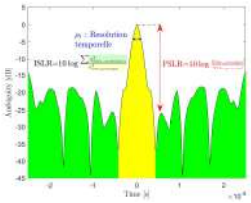

Figure 1: Coupe de la fonction d'ambiguïté (sortie du filtre adapté) dans le domaine temporel

- Pour faire le choix entre différentes formes d'ondes, il faut comparer leurs fonctions d'ambiguïté en utilisant les critères : résolution, PSLR (peak side-lobe ratio) ou ISLR (integral side-lobe ratio).

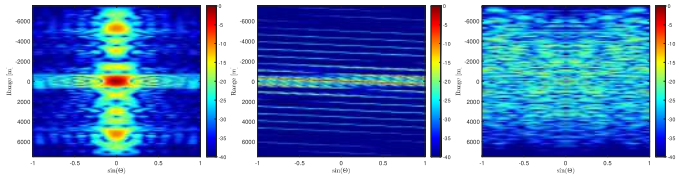

(a) TDMA (b) FDMA (c) CDMA

Figure 2: Coupe distance-angle de la fonction d'ambiguïté pour différentes formes d'ondes [1]

Méthode de génération de formes d'ondes CDMA

Principe du CDMA (Code Division Multiple Access)

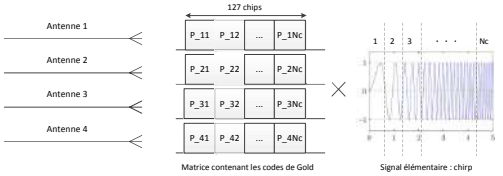

Figure 3: Principe du CDMA.

Comparaison du CDMA avec codes de Gold ou polynômes d'Hermite

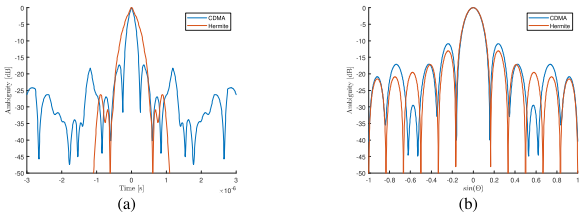

(a) (b)

Figure 4: Coupes de la fonction d'ambiguïté dans (a) le domaine temporel et (b) le domaine angulaire.

Modulations	Avantages	Inconvénients
CDMA (codes de Gold)	Bonne résolution temporelle.	Forts lobes secondaires en distance et angle liés au choix du code.
CDMA (Polynômes [2])	Polynômes parfaitement orthogonaux selon le diagramme d'énergie. Lobes secondaires bas en distance et en angle.	Dégradation de la résolution. Bande passante différente pour chaque polynôme.

Table 1: Tableau comparatif des modulations pour le CDMA.

Modèlisation de la trajectoire du débris et du satellite

But : déterminer la trajectoire de la cible par rapport au nano-satellite à partir de ses coordonnées initiales dans le repère terrestre (modèle de Clohessy-Wiltshire [3]).

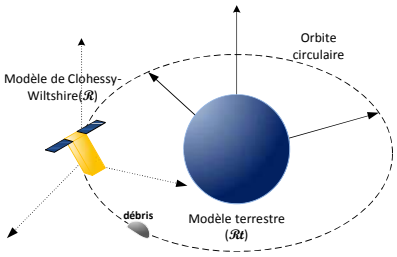

Correction de la migration distance sur une longue durée d'observation

- Méthode utilisée pour compenser la migration distance de la cible durant le temps d'intégration [4].
- Transformation sur l'axe temporel pour éliminer le terme qui induit la migration distance.

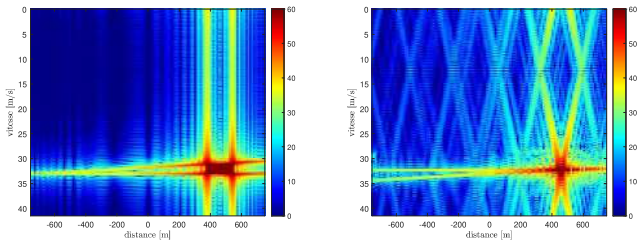

(a) (b)

Figure 5: Coupe distance-vitesse de la fonction d'ambiguïté (a) avant application de la transformée de Keystone et (b) après application de la transformée de Keystone

Problématiques	Pistes proposées
Apparition de lobes secondaires sur la dimension vitesse durant le temps d'intégration.	Appliquer un filtre passe-bas.
Modification de la distribution du bruit.	Déterminer le modèle du bruit après chaque étape de la transformation de Keystone.
Temps de calcul important pour les paramètres utilisés.	Adapter la méthode de Keystone au calcul matriciel.

Table 2: Tableau regroupant les différentes problématiques liées au traitement Keystone et les pistes proposées pour les traiter

Références

[1] Olivier Rabaste et al. Signal waveforms and range/angle coupling in coherent colocated mimo radar. In *2013 International Conference on Radar*, pages 157–162. IEEE, 2013.

[2] Hind Ait Taleb, Valentine Wasik, Abigael Taylor, and Yassin El Hillali. Comparaison de formes d'ondes pour radar mimo. In *GRETSI 2023*, 2023.

[3] WH Clohessy and RS Wiltshire. Terminal guidance system for satellite rendezvous. *Journal of the aerospace sciences*, 27(9):653–658, 1960.

[4] Mark A Richards. The keystone transformation for correcting range migration in range-doppler processing. *pulse*, 1000(1), 2014.

Galactic binaries with LISA

C. Aykroyd[1,*] A. Bourgoin[1] C. Le Poncin-Lafitte[1]

Laser Interferometer Space Antenna (LISA)

LISA is an upcoming *space-based gravitational wave observatory*. As ESA's third large-class mission, LISA is planned to launch in 2035 with a mission duration of 4–5 years. The detector setup will consist of three separate spacecraft in triangular formation 2.5 million km apart, trailing the Earth in heliocentric orbit. The spacecraft will be interconnected by lasers which can detect passing gravitational waves via time-delay interferometry.

Current ground-based instruments can detect the final moments of the merger (i.e. the plunge) of stellar-sized objects like black-hole and neutron-star pairs. Space-based instruments have the potential to peer into a range of much lower frequencies, accessing a rich variety of sources, from supermassive black-holes in galactic centres to primordial events (see Fig.). Among other sources, LISA will continuously observe the gravitational waves emitted by inspiraling white-dwarf and neutron-star binaries within the Milky Way (i.e. galactic binaries). The data acquisition can cover years for each system, with tens of thousands of binaries monitored simultaneously.

These observations will enable the characterisation of the source systems and our understanding of their internal physics and state of matter. Detection is based on matched-filtering, and shall require templates which remain accurate over thousands of orbits. This suggests further refinement of dynamical models considering a variety of physical effects, including spin and magnetic field interaction, tidal forces, and radiation-reaction effects.

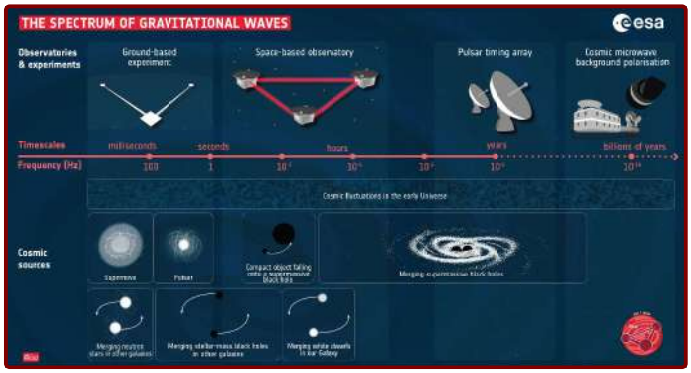

Gravitational waves

Gravitational waves (GWs) are minuscule ripples in spacetime produced from the acceleration of massive bodies. Predicted back in the early days of General Relativity, they were finally observed directly in 2015 by the LIGO-VIRGO observatories.

As they travel, GWs deform spacetime by alternately stretching and compressing it. They can be polarised into two independent 'modes' $h_+(t)$ and $h_\times(t)$.

The GWs emitted by a binary can be computed from the quadrupole formula:

$$h_{ij}(t,\boldsymbol{x}) = \frac{2G}{c^4}\frac{\mathrm{d}^2}{x\,\mathrm{d}t^2}Q_{ij}(t) \qquad (1)$$

where $Q_{ij}(t)$ is the mass quadrupole moment, which is a function of the orbital trajectory.

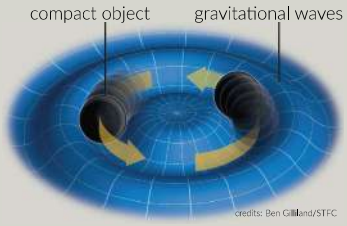

Thus, an analytical description of the trajectory of the source is required for modelling the gravitational waveform. This waveform may conceivably depend on many parameters of each body, such as masses, spins, magnetic and tidal properties, etc.

Post-Newtonian expansions

The Einstein field equations describe how matter and energy influence the curvature of spacetime, which in turn dictates the motion of bodies. Despite an elegant formulation, scarcely any exact solutions are known. Most practical scenarios, such as merging black holes or other compact systems, require the use of numerical or approximation methods.

Among analytical methods, post-Newtonian (PN) expansion schemes excel at describing 'weak-field' binary orbits, such as inspiraling compact binaries. The approach involves expanding the field equations perturbatively in powers of $\varepsilon \sim v/c$ and solving for the curvature (or rather the 'spacetime metric'). By doing so, one is left with **equations of motion** for the bodies [3], occasionally in the form of a Lagrangian or a Hamiltonian [8], resembling those of Newtonian gravity with additional relativistic corrections.

While post-Newtonian expansions have been

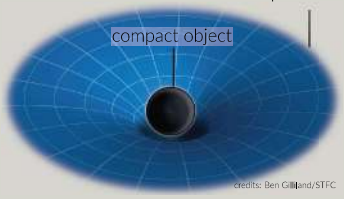

progressively reaching higher orders, the development of tools to analytically **solve** the resulting equations remains behind, with ad-hoc methods frequently restricted to secular or quasi-circular approximations. The quasi-Keplerian parametrisation (see [3]) has been sucessfully determined up to 4PN order to describe the orbits of non-spinning binaries. However, a systematic extension of this approach to broader perturbative situations including spinning or dissipative systems remains a challenge.

Orbital motion

The orbital dynamics of a purely gravitational binary system can be described by the post-Newtonian Arnowitt–Deser–Misner (ADM) formalism. For a non-spinning point-mass binary, the conservative Hamiltonian is:

$$\mathcal{H}(\boldsymbol{r},\boldsymbol{p}) = \mathcal{H}_0(\boldsymbol{r},\boldsymbol{p}) + \varepsilon^2\mathcal{H}_1(\boldsymbol{r},\boldsymbol{p}) + \varepsilon^4\mathcal{H}_2(\boldsymbol{r},\boldsymbol{p}) + \ldots, \qquad (2)$$

where $(\boldsymbol{r},\boldsymbol{p})$ are the binary separation and conjugate momentum seen from the centre-of-mass frame, and the leading term $\mathcal{H}_0$ is the Hamiltonian for Newtonian gravity. Any further dissipative or non-gravitational interactions will show up as additional perturbations.

In general, the above Hamiltonian is not directly integrable, due to the presence of the non-linear perturbation terms $\varepsilon^2\mathcal{H}_1$, $\varepsilon^4\mathcal{H}_2$, etc. In [1], we propose incorporating the Lie series approach into the post-Newtonian context. This technique, described below, provides a systematic framework for computing the orbital trajectories, capturing both long-term (secular) and short-term dynamics, arbitrary eccentricities, and can be applied to systems with a diverse range of perturbations.

The Lie series method

The approach involves finding a near-identity canonical coordinate transformation $\mathcal{T}_g$, which maps the original Hamiltonian $\mathcal{H}$ into a new Hamiltonian $\mathcal{H}^* = \mathcal{T}_g(\mathcal{H})$. The mapping is carefully chosen such that the non-integrable terms in $\mathcal{H}$ are deferred to high PN orders in $\mathcal{H}^*$, where they can be formally neglected. At this point, the dynamics of $\mathcal{H}^*$ can be easily extracted, giving the secular orbital motion $(\boldsymbol{r}^*,\boldsymbol{p}^*)$. Finally, the process is reversed by applying $\mathcal{T}_g$ to the secular coordinates, recovering the complete dynamics of the system.

$$\begin{array}{ccc} \mathcal{H} = \sum_{\ell=0}^{K}\varepsilon^{2\ell}\mathcal{H}_\ell & \xrightarrow{\quad\mathcal{T}_g\quad} & \mathcal{H}^* = \mathcal{T}_g(\mathcal{H}) \\ \downarrow & & \downarrow \\ \boldsymbol{r}(t),\,\boldsymbol{p}(t) & \xleftarrow{\quad\mathcal{T}_g\quad} & \boldsymbol{r}^*(t),\,\boldsymbol{p}^*(t) \end{array}$$

The core challenge of the approach lies in determining the generator of the transformation, which parametrically encodes $\mathcal{T}_g$ as:

$$\mathcal{T}_g(x) = x + \varepsilon^2\{x,g\} + \frac{\varepsilon^4}{2}\{\{x,g\},g\} + \ldots,$$

where $\{\cdot,\cdot\}$ is the Poisson bracket. To find the generator, we progressively solve equations of the form:

$$\{g_\ell,\mathcal{H}_0\} = F_\ell(\boldsymbol{r},\boldsymbol{p}) - \mathcal{H}^*_\ell, \quad \ell = 1,2,\ldots, \qquad (3)$$

where $F_\ell(\boldsymbol{r},\boldsymbol{p})$ are expressions derived from the original Hamiltonian (2). The two unknowns g_ℓ and $\mathcal{H}^*_\ell$ correspond to expansion terms of g and $\mathcal{H}^*$ in powers of ε^2. In [1], we derive generator solutions for (3) for typical Hamiltonian terms in (2), which include the *local conservative* ADM sector but also other rotation-invariant perturbations. The framework can be naturally extended to include non-conservative contributions such as radiation-reaction terms (Aykroyd et al., in prep.), by using the variable-doubling formalism [5].

Magnetic interactions

Isolated white dwarfs and neutron stars can exhibit external magnetic fields as strong as 10^9 and 10^{15} Gauss, respectively. However, whether such strongly magnetic degenerate stars are commonly found in binary systems remains unclear. Clarifying this subtlety could provide crucial information on the stability and formation mechanisms of magnetic fields in these binaries.

Recent studies show that magnetic interactions in galactic binaries create distinct signatures in GWs that should be detectable by LISA [4, 6]. Analyzing these signals can reveal the magnetic properties of the systems, providing valuable data for population models and insights into the magnetic fields of degenerate stars.

Magnetic model

At leading order, the perturbing magnetic interaction can be encoded by a non-relativistic term:

$$\mathcal{H}_B = \frac{\mu_0}{4\pi r^3}\big(\boldsymbol{\mu}_1\cdot\boldsymbol{\mu}_2 - 3(\boldsymbol{\mu}_1\cdot\boldsymbol{r})(\boldsymbol{\mu}_2\cdot\boldsymbol{r})\big). \qquad (4)$$

where the dipole moments $\boldsymbol{\mu}_{1,2}$ are assumed to be aligned with the spins of the stars. We show [2] that given enough time, the magnetic interaction will drive the dipoles into a configuration where they are anti-aligned and perpendicular to the plane of the orbit.

Magnetic signature in GWs

In this configuration, we can compute the orbital motion and demonstrate [7] that magnetism will manifest as a frequency shift in the GW mode harmonics proportional to the magnetic interaction energy (4).

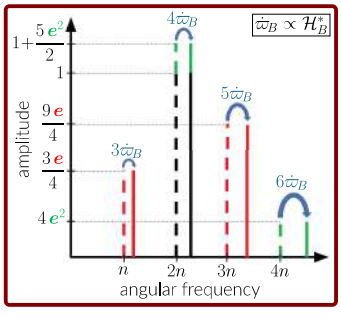

References

[1] Aykroyd, C., Bourgoin, A., & Poncin-Lafitte, C. L. 2024 [[arXiv]2409.12204]
[2] Aykroyd, C., Bourgoin, A., Poncin-Lafitte, C. L., Mathis, S., & Angonin, M.-C. 2023, A&A, 675, A32
[3] Blanchet, L. 2024, Living Reviews in Relativity, 27, 4
[4] Bourgoin, A., Le Poncin-Lafitte, C., Mathis, S., & Angonin, M.-C. 2022, Phys. Rev. D, 105, 124042
[5] Galley, C. R. 2013, Physical Review Letters, 110
[6] Lira, M., Degollado, J. C., Moreno, C., & Núñez, D. 2022, Gen. Rel. Grav., 54, 146
[7] Savalle, E. and Bourgoin, A. and Le Poncin-Lafitte, C. and Mathis, S. and Angonin, M.-C. and Aykroyd, C. 2024, Phys. Rev. D, 109, 083003
[8] Schäfer, G. & Jaranowski, P. 2024, Living Reviews in Relativity, 27

(*) christopher.aykroyd@obspm.fr
(1) SYRTE, Observatoire de Paris, Université PSL, CNRS, Sorbonne Université, LNE, 61 avenue de l'Observatoire, 75014 Paris, France

RÉPUBLIQUE FRANÇAISE
Liberté Égalité Fraternité

PULSATING HEAT PIPE (PHP)

AS A VERSATILE THERMAL MANAGEMENT TOOL

Slaven BAJIĆ
Post-Doc
Centre National d'Études Spatiales (CNES), Toulouse, France
Supervisor: Guillaume Boudier

CNES CENTRE NATIONAL D'ÉTUDES SPATIALES

STUDY OBJECTIVE

To gain a deeper understanding of the physical phenomena governing Pulsating Heat Pipes (PHPs) and to optimize their design and development process.

WHAT IS A PHP?

Passive heat transfer device consisting of a meandering capillary structure partially filled with a working fluid[1]. Heat generated in the evaporator section is transferred to the condenser through both conduction in the channel walls and latent and sensible heat transfer with the working fluid.

HOW DOES IT WORK?

CONDENSER

The working fluid releases heat to the condenser, which is usually maintained at a constant temperature. Condensation of vapor bubbles.

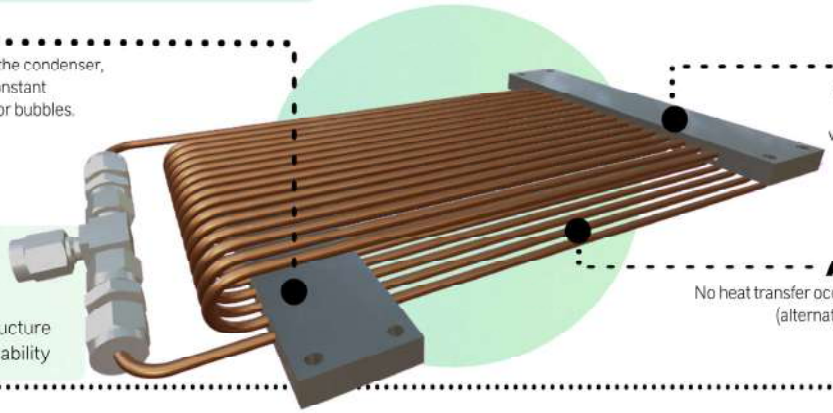

EVAPORATOR

Heat input leads to latent and sensible heat transfer between the evaporator and the working fluid, resulting in bubble nucleation and growth.

ADIABATIC ZONE

No heat transfer occurs. Intermittent slug-plug flow (alternating liquid slugs and vapor plugs) transports heat along the pipe..

ADVANTAGES

- Passive operation
- Design simplicity
- No internal capillary wick structure
- Ease of integration and adaptability

MAIN CHALLENGE

Incomplete understanding of the relationship between internal physical mechanisms (*two-phase flow, heat transfer*) and design parameters (*geometry, fluid properties, boundary conditions*).

NUMERICAL

CASCO v4.0 1D transient simulation software[2] (developed by CEA) is used to predict PHP performance and behavior under various input parameters, such as structural geometry, working fluid, thermal boundary conditions.

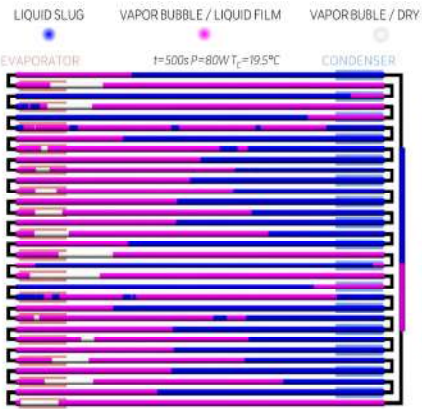

Schematic representation of fluid distribution inside the PHP channels within CASCO.

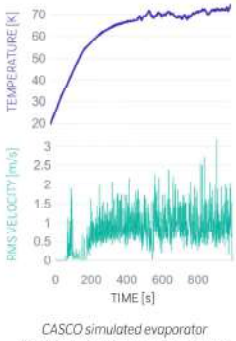

CASCO simulated evaporator temperature and root-mean-square fluid velocity temporal variation.

EXPERIMENTAL

A 16-turn tubular PHP was manufactured using a copper tube with a 1 mm internal diameter and a 0.6 m adiabatic zone length. PHP was tested at varying heating powers and inclination angles.

Experimental parameters

Heating power	Inclination angle	Cooling Temp.	Working fluid
2 – 40 W	**-5 to +6 °C**	**20 °C**	**Acetone**

Key observations

Fluid movement initiated at low heat inputs.

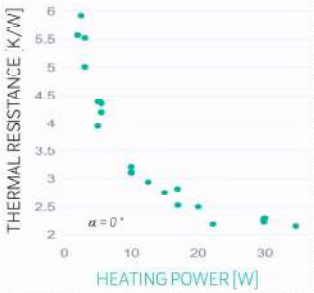

Strong dependenance of the PHP performance on the inclination angle, due to gravity effects.

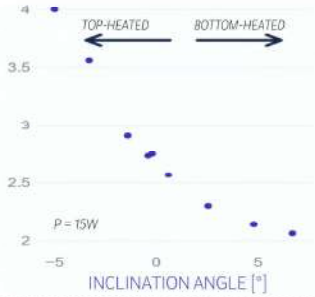

APPLICATION DOMAINS

EMBEDDED SYSTEMS

Enhancement of heat dissipation for small-scale electronic components (CPUs, GPUs, ...).

HYPERSONIC VEHICLES

Cooling of high-temperature leading edges on hypersonic vehicles and spacecraft during atmospheric re-entry.

BATTERY COOLING

Improvement of temperature regulation and cooling efficiency in battery packs for electric vehicles and other high-performance applications.

HEAT HARVESTING

PHPs can be used to recover thermal energy from waste heat sources, such as solar power, contributing to energy efficiency improvements.

References
[1] Akachi, H. (1993). *U.S. Patent No. 5,219,020*. Washington, DC: U.S. Patent and Trademark Office.
[2] Nikolayev, V. S. *Physical principles and state-of-the-art of modeling of the pulsating heat pipe: A review*. Applied Thermal Engineering, 195, 117111 (2021).

Partners cea AIRBUS

Arne Bendinger, Clément Vic, Sophie Cravatte, Lionel Gourdeau

Dynamical interpretation of SWOT SSH south of New Caledonia

SWOT | Unraveling the ocean's fine-scale circulation

SSH Sea Surface Height along two 60-km wide swaths

10x higher spatial resolution than conventional altimetry

AdAC Adopt-A-Crossover consortium to assist in-situ experiments

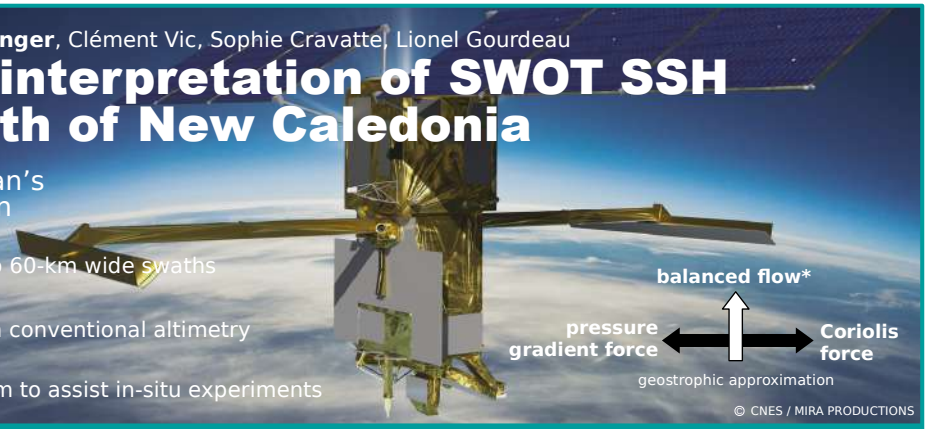

Objective Infer ocean dynamics beneath SWOT swaths

SWOT SSH requires accurate disentanglement since it resolves wavelengths at which ocean dynamics are not purely associated with balanced motions, i.e. large-scale, slowly evolving dynamics, as it the case for conventional altimetry.

balanced*		unbalanced
mesoscale	submesoscale	internal gravity waves (IGWs)
O(10-100 km) O(1 week - 1 month)	O(1-10 km) O(1 day – 1 week)	O(10-100 km) O(1 hour – 1 day)

! Geostrophic approximation partially not valid as the submesoscale can be strongly ageostrophic

! Balanced motions and IGWs with overlapping spatial scales and equal contribution to SSH variance

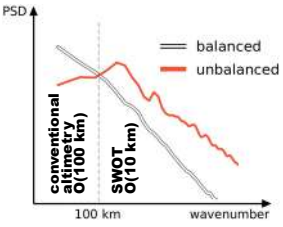

NEMO CALEDO60 - regional numerical model output with tides (1/60°)

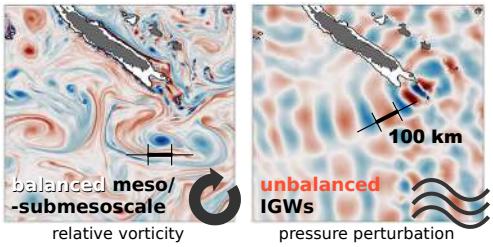

New Caledonia Unique study site to address SWOT SSH observability

Elevated mesoscale and submesoscale activity (i.e. eddies and fronts)

Internal-tide generation hot spot due to complex bathymetry (i.e. ridges and seamounts)

Located beneath the swaths of SWOT's fast-sampling phase (1-day repeat orbit)

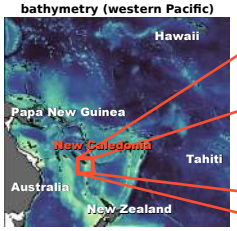

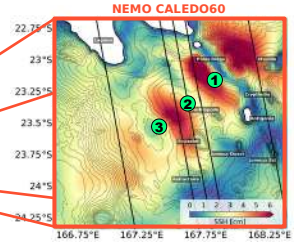

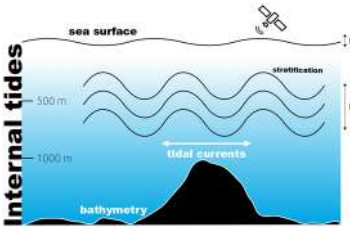

Internal tides IGWs at tidal frequency which form when barotropic tide interacts with bathymetry causing the vertical displacement of density surfaces

Methodology Full-depth moorings

SWOTALIS (involvement in SWOT-AdAC)

An extensive in-situ experiment was carried out in March 2023 subject to the deployment of three oceanographic moorings providing at fixed locations ① ② ③ for 9 months high-frequency measurements of temperature, salinity, pressure, and ocean currents.

Time-filtering technique

Knowing at what time scales and frequency bands the dynamics of interest dominate, we can decompose the time series into the different dynamical flow regimes.

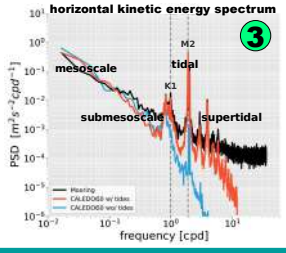

Allowing for…

the derivation of steric SSH (***sSSH***), i.e. SSH induced by density (***ρ***) changes in the water column such as the downward and upward displacement of density surfaces, for both balanced and unbalanced motions: $sSSH(t) = \int g\rho(t,z)dz$

$$\rho_{full} = \underbrace{\rho_{mesoscale}}_{>5\ days} + \overbrace{\rho_{submesoscale} + \rho_{inertial} + \rho_{diurnal}}^{1\text{-}5\ days} + \underbrace{\rho_{semidiurnal}}_{\sim 12\ hours} + \ldots$$

Preliminary results & outlook

2024
Mooring data processing and quality control

Derivation of SSH signature based on steric height depth integral **2025**

Comparison of mooring-derived and SWOT SSH

2026

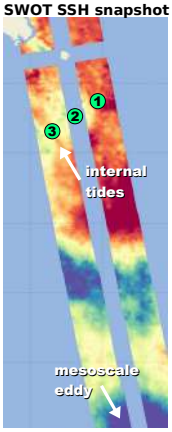

Decomposing the time series

Full-depth velocity time series reveals balanced **mesoscale** component alongside high-frequency variability dominated by the **unbalanced semidiurnal tide**.

Coherent semidiurnal tide

The fraction of tidal variability which is in phase with astronomical tidal forcing, i.e. spring-neap tide cycle (M2, S2, N2), estimated by harmonic analysis.

$$u_{full,D2} = u_{coherent,D2} + u_{residual,D2}$$

The residual (also referred to as incoherent tide) is the time-varying component which is out of phase with tidal forcing, highly unpredictable and challenging for SWOT.

Full-depth moorings will help allocate…

SWOT SSH to the different dynamics in a region where balanced and unbalanced motions are equally important.

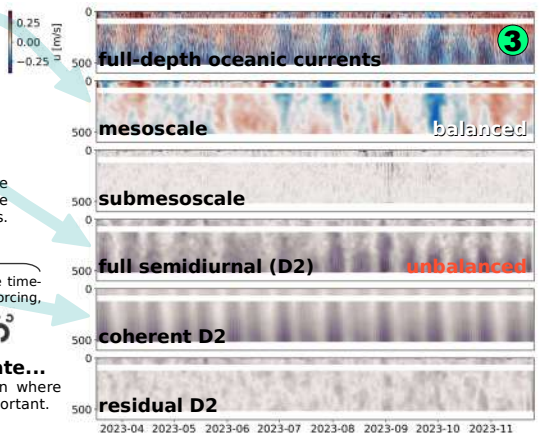

Take home

Unique dataset of **full-depth mooring observations** in the internal-tide generation hot spot south of **New Caledonia** beneath the SWOT swaths during its fast-sampling phase with valuable insight into the governing dynamics at play. The associated surface signature will help **interpret and understand SWOT SSH** in a region of complex circulation.

Accuracy assesments for the VenSpec-U/VeSUV instrument onboard ESA's EnVision mission

L. Conan[1], E. Marcq[1], B. Lustrement[1], N. Rouanet[1], L. Parc[1], S. Bertran[2], S. Robert[3], J. Helbert[4], G. Alemanno[4]

[1]LATMOS/IPSL (France), [2]Hensoldt Space Consulting (France), [3]Royal Belgian Institute for Space Aeronomy (Belgium), [4]DLR Institute of Planetary Research (Germany)

► Submitted to SPIE "Infrared Remote Sensing and Instrumentation XXXII" (2024)

VenSpec-U / VeSUV:

The next ESA mission to Venus, EnVision, aims to study the planet as a whole, including its various constituting parts, their interactions and coupling processes. The payload includes a suite of three spectrometers, the VenSpec suite [1], among which the UV channel called VenSpec-U or VeSUV ("Venus Spectroscopy in UV") [2] will focus on the upper layer of the atmosphere. It aims to monitor sulphured species such as SO_2 and SO, as well as the unidentified UV absorber, and will also observe small scale dynamical patterns such as convection cells or atmospheric waves.

Constituted of two channels called "LR" and "HR", referring respectively to the low and high spectral resolution, the instrument will perform dayside observations of the UV sunlight backscattered by Venus' clouds. Radiance factor spectra using the spectral solar irradiance will then be derived.

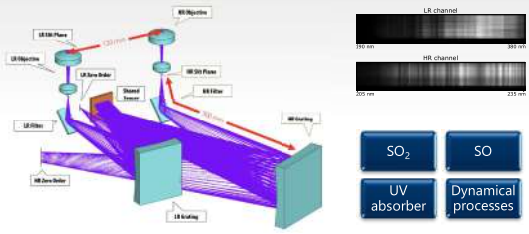

Scientific objectives	SNR (normalised at 220 nm)	Random precision	Effective Spectral Radiometric Accuracy	Absolute Radiometric Accuracy
Measure the SO_2 columns density above the clouds	≥ 200	< 20%	< 50%	-
Measure the SO/SO_2 columns density ratio	≥ 100	< 25%	< 100%	-
Perform long-term monitoring of the UV absorber and clouds	≥ 100	-	-	< 10%

Radiative Transfer Model:

These studies are performed with the Radiative Transfer Model (RTM) updated from the one used for the data analysis of the SPICAV-UV instrument onboard the previous ESA mission Venus Express [3]. The model computes radiance factor spectra from a set of parameters describing the atmospheric characteristics, including VenSpec-U's science objectives:

- **qSO2**: SO_2 mixing ratio at 70 km of altitude
- **img**: imaginary part of the refractive index representing the UV absorber
- **Z2**: cloud-top altitude control point
- **rSO**: SO/SO_2 abundance ratio

Three scenarios are defined in order to estimate variations of the studied performances indicators within an envelope of expected radiometric conditions.

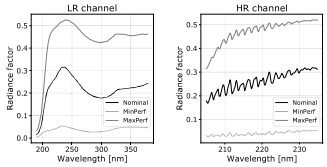

Requirements:

The main science objectives of the instrument have driven the elaboration of a preliminary design based on the requirements (such as spectral ranges, spectral and spatial resolutions) that were formulated with respect to these goals. The compliance of the current design with these requirements, regarding in particular the accuracy of the retrieved science data, should therefore be assessed.

Random errors characterisation

Influence of the Signal-to-Noise Ratio:

The Signal-to-Noise Ratio (SNR) is used as an optimisation parameter in the Levenberg-Marquardt fitting algorithm involved in the inverse RTM, which leads to an increased reliance on portions of the spectra with higher SNR to find the best estimation of the atmospheric features.

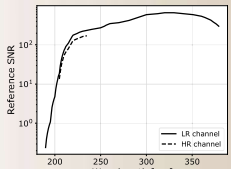

In order to estimate how the uncertainties associated to the retrieved parameters are impacted, variations in the SNR curve are introduced. Two types of SNR alterations are considered:

- Multiplicative factor: global attenuation similar for all wavelengths
- Gamma correction: modification of the contrast between short and longer wavelengths without changing the maximal SNR level

$$SNR(\lambda) = SNR_{ref}(\lambda) \cdot f \qquad SNR = \max_{\lambda}(SNR_{ref}) \cdot \left(\frac{SNR_{ref}(\lambda)}{\max_{\lambda}(SNR_{ref})}\right)^{\gamma}$$

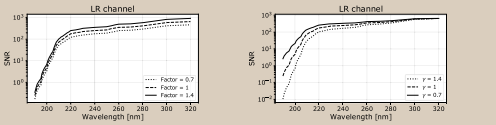

SNR forbidden domains:

The resulting uncertainties are then retrieved using the inverse RTM for each of these modified SNR spectra and compared to the requirements in order to determine limits until where the SNR can be degraded while still reaching the required precision.

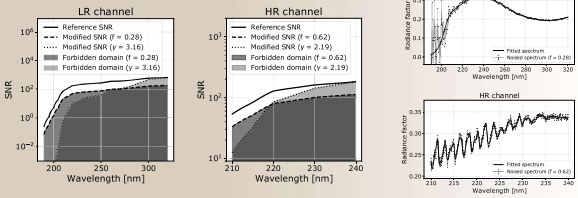

Systematic errors characterisation

ESRA requirement and gain matrices formalism:

The implemented method is based on the "Effective Spectral Radiometric Accuracy" (ESRA) requirement, previously defined within the framework of the ESA Sentinel missions [4], which evaluate the effects of the similarities between the spectral characteristics of biases and those of the atmospheric components aiming to be detected.

The "Gain matrices" (**G**) involved in this method are representing the linearised inverse RTM, by translating a deviation in radiance factor into a deviation in the estimated atmospheric parameters, and are defined for each parameter of interest. They are computed using the Moore-Penrose pseudo-inverse of the Jacobian matrix associated to the linearised forward RTM (**A**) with a consideration of the SNR influence in the fitting algorithm through a diagonal covariance matrix (**S**). The spectral index is here noted **j** and **k** refers to the index of the retrieved RTM parameter **p**.

$$G = \frac{1}{\Delta\lambda} \cdot \left(A^T \cdot S^{-1} \cdot A\right)^{-1} \cdot \left(A^T \cdot S^{-1}\right)$$

$$\text{with } A_{jk} = \frac{\delta\beta_j}{\delta p_k / p_k} \text{ and } S_{jj} = \left(\frac{\beta_j}{SNR_j}\right)^2$$

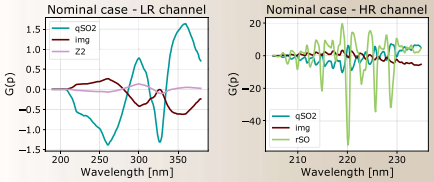

Identified biases:

Sources of biases expected to be encountered by VenSpec-U and their impact on the radiance factor spectra have been identified:

- Straylight mainly due to scattering by optical components
- Loss of transmission caused by the progressive deposition of contaminants on the optics
- Sensitivity to the slight polarisation of the observed Venus scene
- Uncertainties on the solar spectral irradiance variability used to derive the radiance factor

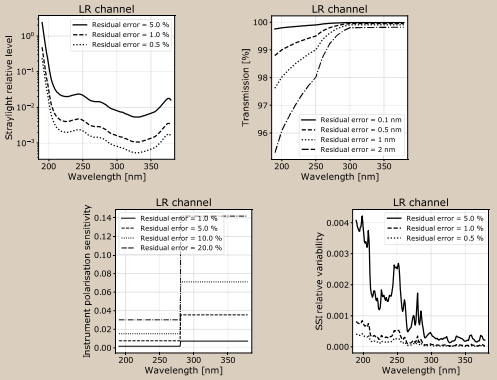

Generic types of biases are also considered to account for non-specific source of biases, described with simple mathematical expressions such as constant additive offset or multiplicative factor. As these biases aims to be corrected, this study is focused on the effects of remaining errors due to the uncertainties of the corrections, and referred to as "residual errors".

ESRA budget allocations :

The ESRA contribution of each individual biases can then be computed. A sensitivity factor is defined for each bias using the residual error level necessary to fill the total required ESRA budget, and is used to compare the severities of the various biases. In order to compute the resulting global ESRA, the biases are combined quadratically, as they are considered to be independent.

$$\text{ESRA}(p_k) = \Delta\lambda \cdot \sum_j G_{kj} \cdot (\beta_{j,\text{measured}} - \beta_{j,\text{true}})$$

The allocation of a maximal residual error for each bias can be made as a first approach by considering their contribution to the total ESRA budget as equivalents.

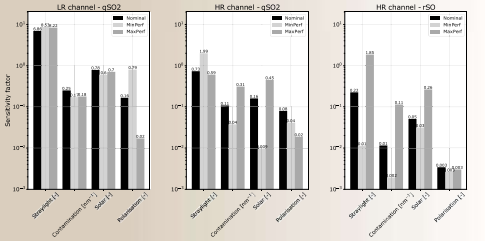

In order to make these allocations more representative of the instrument, Monte-Carlo simulations can be implemented with realistic estimations of the statistical distribution of residual errors levels for each bias, depending on the calibrations and corrections' expected efficiencies.

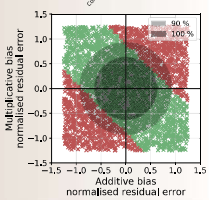

References

[1] J. Helbert, et al. The VenSpec suite on the ESA EnVision mission to Venus. Infrared Remote Sensing and Instrumentation XXVII, SPIE, San Diego, United States. p. 6.907. 2019. doi:10.1117/12.2529248

[2] E. Marcq, et al. Instrumental requirements for the study of Venus' cloud top using the UV imaging spectrometer VeSUV. Advances in Space Research, 68(1) :275–291. 2021. ISSN 02731177. doi : 10.1016/j.asr.2021.03.012

[3] E. Marcq, et al. Climatology of SO2 and UV absorber at Venus' cloud top from SPICAV-UV nadir dataset. Icarus, 335 :113368. 2020. ISSN 00191035. doi : 10.1016/j.icarus.2019.07.002

[4] ESA Mission Science Division, COPERNICUS SENTINELS 4 AND 5 MRTD, 2017. URL https://sentinel.esa.int/documents/247904/2506504/Copernicus-Sentinels-4-and-5-Mission-Requirements-Traceability-Document.pdf

S01-06 | Doc | **GELAGAY Habtamu Sewnet** | CIRAD, Montpellier | Encadrant CNES : Philippe MAISONGRANDE

Large – scale yield gap estimation and characterization with multi – source remote sensing date – case study of rainfed wheat in Ethiopia

NON FOURNI

Impression 3D métallique de composants innovants pour applications millimétriques

Hiba LAHLIMI ALAMI[1] , Cyril GUINES[1], Aurélien PERIGAUD[1], Nicolas DELHOTE[1] , Stéphane BILA [1], Pedro RYNKIEWICZ[2]

1 XLIM UMR 7252, Université de Limoges/CNRS, 123 Avenue Albert Thomas, 87060 Limoges, France
2 CNES - Centre Spatial de Toulouse, 31401 Toulouse, France
Hiba.lahlimi-alami@xlim.fr

Contexte et objectif:

Les systèmes RF évoluent vers des fréquences > 100 GHz, essentielles pour les technologies avancées. Ces fréquences permettent des transferts de données volumineux et améliorent la précision dans divers domaines comme la radiométrie et l'étude de l'atmosphère. Cependant, concevoir des composants adaptés à ces hautes fréquences reste un défi en raison des limitations des technologies actuelles. Ce travail explore l'utilisation de l'impression 3D métallique, via la machine CERES, pour créer des lignes de transmission innovantes capables de fonctionner jusqu'à 600 GHz.

Système d'impression 3D CERES

Principe de fonctionnement :

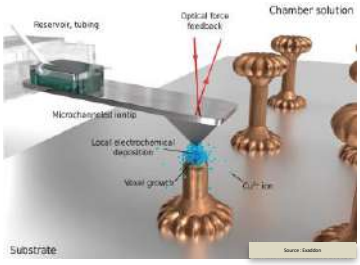

[1] [2]

- Formation de **voxels** (blocs élémentaires métalliques) par **dépôt électrochimique.**
- Différence de **potentiel** nécessaire entre le substrat et la pointe d'impression.
- Fin d'impression du voxel détecté par la **mesure de déflexion** de la pointe **.**

Spécifications et retour d'expérience :

✓Résolution et précision micronique :

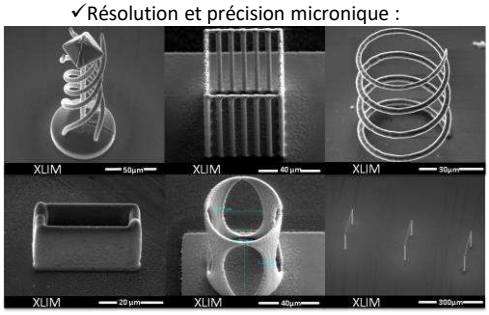

✓Cartographie de surface :

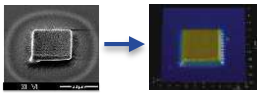

✓ Identification de l'état des voxels :

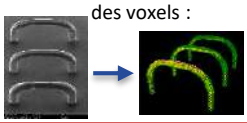

× Effet « Spray »:

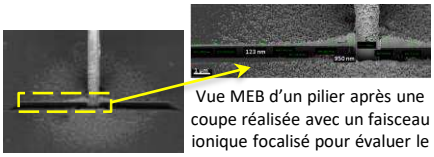

Vue MEB d'un pilier après une coupe réalisée avec un faisceau ionique focalisé pour évaluer le spray.

- ✓ Micro-impression métallique (Cu, Au..)
- ✓ Impression directe sur substrat pré-métallisé, sans support.
- × Zone d'impression limitée (8 -16 mm)
- × Volume imprimable limité (10^6 µm³)

Dimensions des voxels imprimables:
Diamètre de 1 µm -10 µm
Hauteur de 250 nm - 4 µm

Conception de la stripline suspendue:

***Objectifs**: faibles pertes, large bande, fonctionnement à partir de **100 GHz** - Fréquence maximum ?*

- **Contrainte :** Mesure sous pointe.
- **Sortie attendue :** positionnement par rapport : waveguide , structure planaire multicouche.

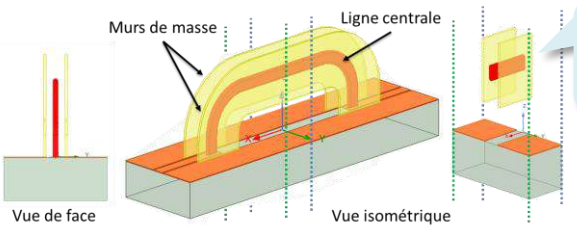

Ligne suspendue → Pertes liées aux caractéristiques du matériau : Conductivité / Rugosité / paramètres de fabrication

Conductivité (MS/m)	Atténuation à 300 GHz (dB/mm)
5	0,75
13	0,54
26	0,38

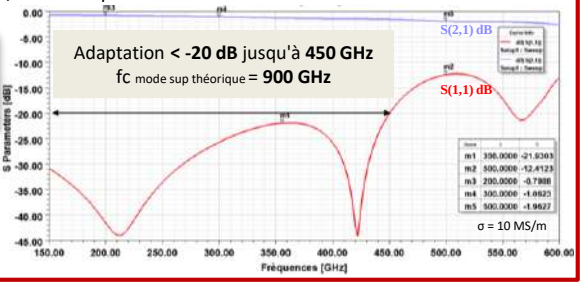

Fabrication de la stripline suspendue:

Procédure de fabrication :

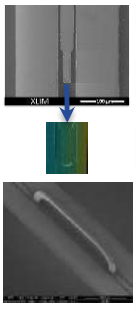

1. Préparation du substrat.
2. Alignement par rapport au motif
3. Impression 3D
4. Gravure de la métallisation
5. Mesure sous pointe

Challenges:

- Qualité de l'état de surface:

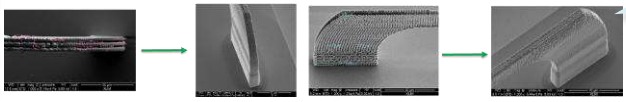

- Elimination des défauts géométriques:

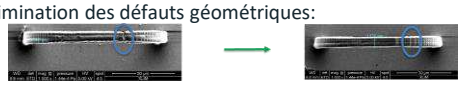

- Amélioration générale et meilleur alignement:

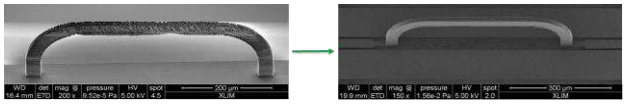

Surface plus lisse MAIS plus de consommation de l'encre ionique

→ Fabrication de la ligne complète (en cours)

Conclusions:

- Confirmation de la précision de fabrication et de positionnement à ±1µm.
- Application de la technologie à THF.
- Composant passifs : structures 3D suspendue compliquée à faire avec d'autres technologies à cette échelle.
- Phase d'optimisation : rugosité/temps d'impression.

Perspectives :

- Obtention d'un prototype fonctionnel
- Positionnement par rapport à d'autres structures guidantes (atténuation, adaptation, fréquence max)
- Amélioration des performances de cet objet.
- Conception et fabrication d'autres composants HF (filtres, autres guides…) en utilisant cette technologie.

Références :

[1] : https://www.exaddon.com/
[2] : WHITE PAPER: EXADDON CERES – "Mapping of Surface Topography Using µAM". EXADDON AG, SÄGEREISTRASSE 25, 8152 GLATTBRUGG, SWITZERLAND

Atom interferometry with ultra-cold atoms onboard a Zero G plane for space applications

Clement Metayer[1], Julien Le Mener, Celia Pelluet[1], Romain Arguel[1,2], Vincent Jarlaud[1,3], Baptiste Battelier[1]

[1]Laboratoire Photonique, Numérique et Nanosciences (LP2N), Université de Bordeaux – CNRS – IOGS, 33400 Talence, France
[2]CNES, 18 avenue Edouard Belin, 31400 Toulouse, France
[3] eXail – Rue François Mitterrand, 33400 Talence, France

1. Abstract

The **ICE** project (Interférométrie à source Cohérente pour l'Espace) aims to be a proof of concept for a space mission using **quantum particles**, i.e., atomic clouds of potassium and rubidium in a matter-wave interferometer to **test the Weak Equivalence Principle** in microgravity [1]. The whole experiment is adapted to the **Novespace Zero G aircraft** that provides 22 s of microgravity per parabolic trajectory. In parallel with the onboard experiments, a **microgravity simulator** installed in the laboratory allows the sensor head (200 kg) to be in weightlessness for 500 ms, with a high repetition rate. To increase the interrogation time and the sensitivity of the measurement, the production of **ultra-cold sources** in microgravity with all-optical methods is studied both on the simulator [2] and onboard the Zero G plane. In microgravity with ultra-cold sources, a particular regime of atomic interferometry called **double diffraction** takes place, which we study theoretically and experimentally on the simulator. We report on the production of **Bose-Einstein Condensates** (BEC) in microgravity both on the simulator and onboard the aircraft, and on our first results of interferometry in the double diffraction regime.

2. The ICE experiment

Universality of Free Fall (UFF)

- "The trajectory of a body in free fall with a gravitationnal field is independent of its mass or its internal composition"

$$\vec{F} = m_{inert}\vec{a} \qquad \vec{F} = \frac{G m_{grav}^{Earth}}{R^2}\vec{u}$$

^{87}Rb ^{39}K

- Eotvös parameter : $\eta = 2\frac{a_{Rb} - a_K}{a_{Rb} + a_K}$
- Ultimate goal on ICE : UFF test at **10^{-11}** level

Experimental setup

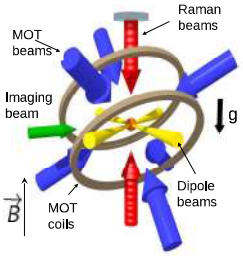

- A transportable experiment, adapted to the 0g-plane
- Telecom fiber-based laser systems at 780 nm (^{87}Rb) and 767/770 nm (^{39}K)
- Compact, 1 titanium chamber vacuum system (+ 2D MOT), 19 optical axes
- Fringe Reconstruction by Accelerometer Correlation (FRAC): Hybridization with classical sensors
- Dipole trap for evaporative cooling

Experiment on the 0g plane

A dual-species atom interferometer

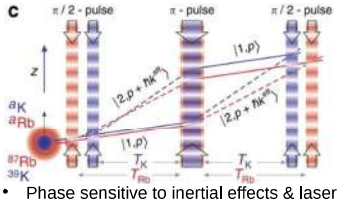

- Phase sensitive to inertial effects & laser : $\Delta\phi = (\mathbf{k_{eff}}.\mathbf{a})T^2 + \Delta\varphi_{laser}$
- On ground η = **$1.6.10^{-6}$**
- Systematic effects : $\delta\eta$ = **5.10^{-8}**

3. Ultra cold atoms on the zero-g simulator

Performances

- Up to 500 ms of microgravity
- Repetition rate : 1 parabola every 12 s
- Thousands of parabolas per day
- Maximum vibration amplitude : **100 mg**
- Repeatability : **< 5 mg**

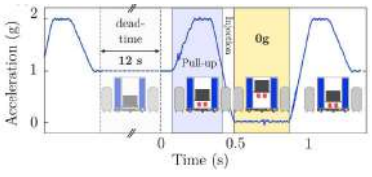

Ultra cold atoms in µ-gravity

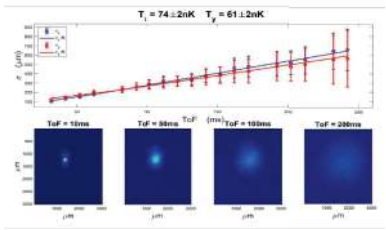

- Work in progress
- Evaporation ramps adapted to the
- The absence of sag in microgravity allows us to reach cooler température compare to standard gravity

4. Ultra-cold sources onboard the Zero-G plane

Motivation

- Increase the contrast (more atoms addressed)
- Increase the interrogation time (atoms must stay in Raman beams effective area)

Setup

- Far-off resonance dipole trap : 1550 nm
- Time averaged potential with spatially modulated beams → add a degree of freedom to optimize the evaporation [5]

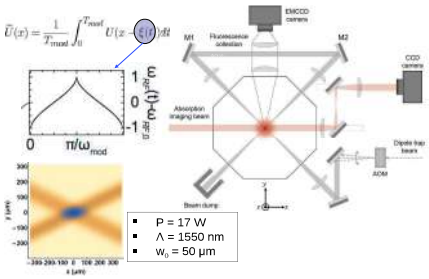

Experiment onboard the plane

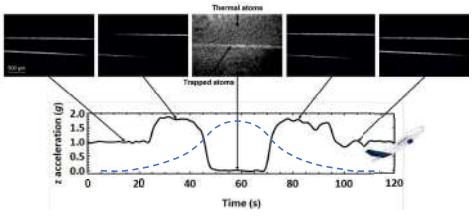

- Compensation of misalignment with an active beam stabilization system

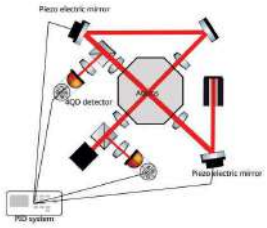

Novespace Zero G plane

- Flight campaign : 3 days, 31 parabolas per day, **22 s** of microgravity

Fluorescence imaging of the cloud in 0g

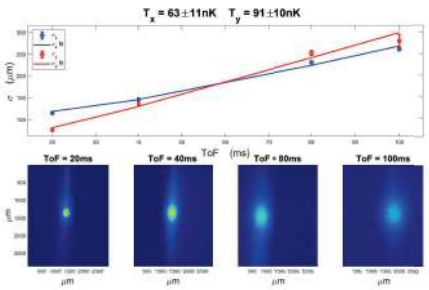

- Work in progress !
- Evaporation ramps adapted to microgravity : no gravity sag
- Estimated temperature (using time of flight method): 80 **nK**
- Estimated PSD : 2.3

Efficiency of evaporation in 1g and 0g

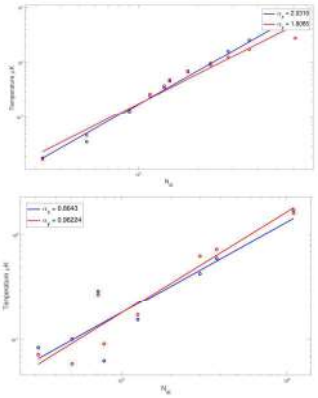

Future work & applications

- Pathfinder mission for the development of an engineering model (CARIOQA)
- Earth observation and gradiometry (GRICE)
- Weak Equivalence Principle test from space (STE-QUEST)

References

[1] B. Barrett et al, *Dual matter-wave inertial sensors in weightlessness,* Nature Comm. **7**, 13786 (2016)
[2] G.Condon et al, *All-Optical Bose-Einstein Condensates in Microgravity,* Phys. Rev. Lett. **123**, 240402 (2019)
[3] B. Barrett et al, *Correlative methods for dual-species quantum tests of the weak equivalence principle,* New J. Phys. **17**, 085010 (2015).
[4] B. Barrett et al, *Testing the Universality of Free Fall using correlated 39K 87Rb atom interferometer,*
[5] R. Roy et al, *Rapid cooling to quantum degeneracy in dynamically shaped atom traps*, Phys. Rev. A **93**, 043403 (2016)

www.coldatomsbordeaux.org

RÉPUBLIQUE FRANÇAISE
Liberté Égalité Fraternité

cnes CENTRE NATIONAL D'ÉTUDES SPATIALES

Thesis Title

"Characterization of Directional Effects in Thermal InfraRed :Preparation to the TRISHNA mission"

Objectives

- ***Understanding of the physics behind directional effects and factors that primarily drive them***
- ***Different combinations of BRDF kernels (hot spot, emissivity) will be tested with the proper data sets***
- ***Field campaigns implemented - Aim is to build a database of TIR BRDF for different vegetation types, also depicted by SCOPE 1D and DART 3D (mock-up in construction)***
- ***Calibration of the BRDF coefficients of parametric model with SCOPE 1D and DART 3D models***
- ***Several inversion BRDF model procedures to be tested in accounting for TRISHNA orbital pass***

Context

Pressure on water supply for irrigation !

Global scale Regional scale Plot scale → Optimized management And consumption of water → Evaporation of water from soils, Transpiration of plants, Local climate → Land Surface Temperature (LST) and its dynamics → Precision required on LST is ~1 K to detect water stress

The TRISHNA mission
(ISRO-CNES, launch in 2026 for 5 years)

Targeted objectives

- Detect and monitor water stress (design driver): optimize irrigation, manage consumption, water saving, drought, etc
- Other main topics: urban, cryosphere, coastal areas and inland waters

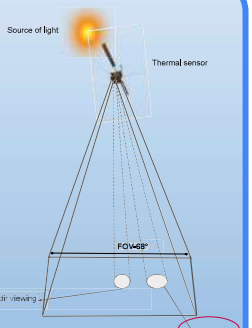

Characteristics:

Spectral bands: 5 VNIR + 2 SWIR + 4 TIR

Temporal: revisit time (3 times / 8 days at equator and more towards the poles)

Spatial: 60 meters

Directional : wide FOV (+/-34°), 12:30 PM => **anisotropic effects expected !**

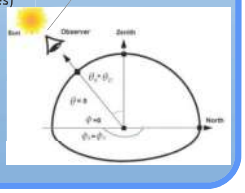

Two strategies: Correction or discard the data in the presence of directional effects?

This depends if we know how to correct it and also its impact.

Methodology

- Meteosat - 3 km Spatial resolution, 15 minutes temporal resolution datasets provide scope for a detail study of Diurnal Temperature cycle (DTC) in directional effects.
- To cross-calibrate DART using TIRAMISU (in-situ) experiment BRDF datasets (time series of optical and thermal vegetation images) acquired over the crop growing season.
- Simulated datasets from DART-EB could a generate large BRDF continuum to do model inversions of the parametric models in consideration (KDM -Kernel Driven Models and DTC - Diurnal Temperature cycle models)
- A semi-empirical kernel-driven (KDM) model KDMs impose constraints on physical coefficients to best fit the empirical values and also computationally efficient.

In-Situ Measurements

Overview of the Nawagam site

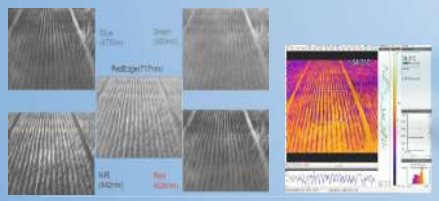

Optical and Thermal Images of rice crop

DART mock-up

Rice crop mock-up top view

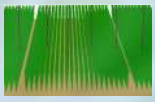

Rice crop mock-up front view

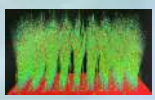

DART-EB simulation - vertical temperature profile over rice crop

MeteoSat Satellite Datasets:

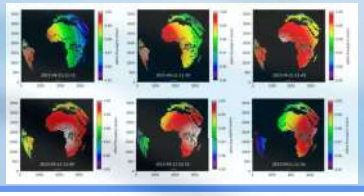

Parametric modelling

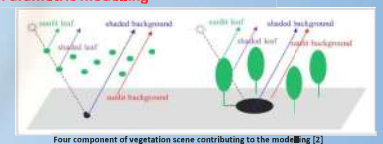

Four component of vegetation scene contributing to the modelling [2]

$$T(\theta_s, \theta_v, \Delta\varphi) = f_{iso} + f_{BaseShape} K_{BaseShape}(\theta_v) + f_{Hotspot} K_{Hotspot}(\theta_s, \theta_v, \Delta\varphi, \text{width})$$

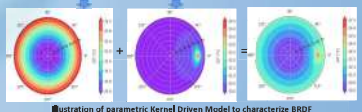

Illustration of parametric Kernel Driven Model to characterize BRDF

Results

- Hotspot conditions are tracked using scattering angle equation $\cos\xi = \cos(\theta_s).\cos(\theta_v) + \sin(\theta_s).\sin(\theta_v).\cos(\varphi_s - \varphi_v)$
- Solar peak , directional conditions, and thermal inertia are considered to completely understand thermal anisotropy.
- DTC + TRD (Thermal Radial Directionality) model's performance is better. However, **DTC +TRD has six retrieval parameters, thus, need more observations**

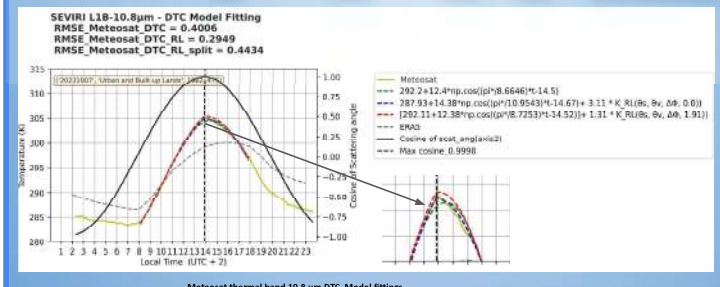

Meteosat thermal band 10.8 µm DTC Model fittings

Future Scope

- **Identify the existing datasets to extract a priori information needed for the model inversions to correct TRISHNA directional effects**
- **To understand directional effects at different spatial resolutions.**
- **Angular normalization techniques in Thermal Domain at TRISHNA resolution.**

References

1. Duan, S.-B., Li, Z.-L., Tang, B.-H., Wu, H., Tang, R., Bi, Y., & Zhou, G. (2014b), *https://doi.org/10.3390/rs6043247*
2. Biao Cao, Jean-Louis Roujean, Jean-Philippe Gastellu-Etchegorry, Qinhuo Liu, Yongming Du, Jean-Pierre Lagouarde, Huaguo Huang, Hua Li, Zunjian Bian, Tian Hu, Boxiong Qin, Xueting Ran, Qing Xiao (2021),*https://doi.org/10.1016/j.rse.2020.112157*
3. Roselyne Lacaze, Jean-Louis Roujean (2001), *https://doi.org/10.1016/S0034-4257(00)00193-0*

Contact : chandrika.pinnepalli@univ-tlse3.fr , jean-louis.roujean@univ-tlse3.fr , mark.irvine@inrae.fr

CESBIO ACRI-ST ISRO INRAE TRISHNA

Decoding Optical Aberrations of Low-Resolution Instruments from PSFs: Machine Learning and Zernike Polynomials Perspectives

Lucas SAUNIERE[1], William GILLARD[1], Julien ZOUBIAN[1]
[1] : Aix Marseille Université, CNRS/IN2P3, CPPM, Marseille, France

INTRODUCTION

The accurate modeling of the Point Spread Function (PSF) is essential to understand the instrumental impact on images taken by optical systems. As a key indicator of an instrument's optical quality, it reveals the nature of its optical aberrations which are fundamental in evaluating image quality and systematics. Knowledge of this instrumental response plays a crucial role in applications such as image deconvolution, where it enables the extraction of ideal images from observed data. While deconvolving images using the PSF, we improve the image clarity and allow the extraction of finer details, and such an improvement on images global quality can advance our comprehension of physical phenomena.

In this study, our objective is to develop a machine learning model that can establish a connection between Zernike coefficients, which define the Wavefront Error (WFE) of optically deformed systems, and the related PSF images. Resulting from the combination of neural networks and Zernike Polynomials, a brand-new model was created : ZerNet.

METHODS

Zernike Polynomials and WFE

When describing the Wavefront Error, Zernike Polynomials stand as a powerful tool for representing a wide range of optical aberrations, the lowest orders commonly acknowledged by scientists are represented below.

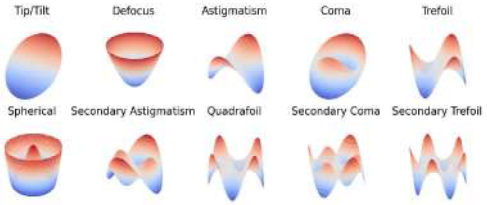

Fig. 1 Visualization of Zernike Polynomials and optical aberrations

We may describe WFE, as a linear combination of infinite order [1] : $\Phi(\rho,\theta) = \sum_{j=1}^{\infty} \alpha_j Z_j(\rho,\theta)$

However, in real-world situations, optical systems are tuned to reduce higher-order aberrations, thereby limiting Noll's index j to N_{orders}. This allows us to express the maximum values of each radial order (in nanometers of optical path difference) as a finite WFE budget for the Zernike coefficients α_j in our simulations :

$$B = [0{,}100{,}50{,}36{,}18{,}9]$$

PSF simulation

The Python module `poppy` [2] allowed to model a telescope with a Newtonian shape, consisting of two mirrors, a primary and a secondary supported by three struts.

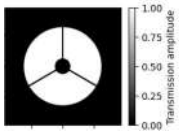

Fig. 2 Designated pupil

Such a configuration is commonly used, particularly in astronomy, while remaining basic allowing to be customized and adapted.

Unfortunately, one main issue stands out while using machine learning algorithms : it requires extensive samples of data.

`poppy` stood out as the perfect tool for our study because it includes a ZernikeWFE class implementation and parallelized PSF calculations, which significantly reduces the typically large amount of time needed to generate PSFs.

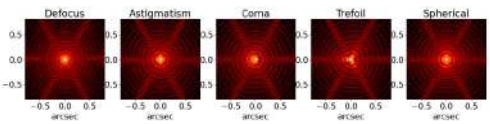

Fig. 3 Aberrated PSFs simulated at 0.2 µm

As a result, it allows the computation of PSFs shown in the previous plot, where optical aberrations mainly play a role in the center part of the PSF.

Fraunhofer approximation

While `poppy` allows to compute PSFs from Fresnel and Fraunhofer regions, choice has been made to take advantage of Fraunhofer diffraction region which implies both far field and paraxial hypothesis, very common in astronomy.

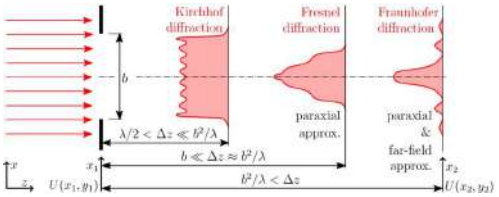

Fig. 4 Diffraction regions after aperture / Credit : Figure from Störkle [3]

After selecting a wavelengths range λ between 0.2 µm and 1 µm, we made use of encircled energy (EE) as estimator of our PSF loss while cropping it to the region of interest we need.

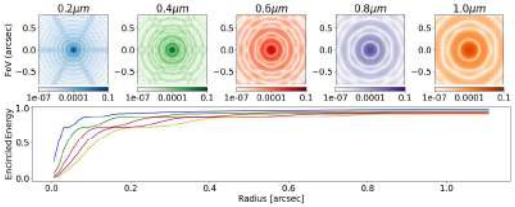

Fig. 5 PSFs and EEs for λ between 0.2 µm and 1 µm

Fortunately, for any value of λ, our chosen region of interest (ROI) was big enough to contain more than 98% of the PSF.

ZerNet model

To link the images and their corresponding coefficients, we made use of Zernet. This study's model is built on the Inception model's premise and converts a $2D$ tensor as the input and a $1D$ tensor of N_{orders} values as the output.

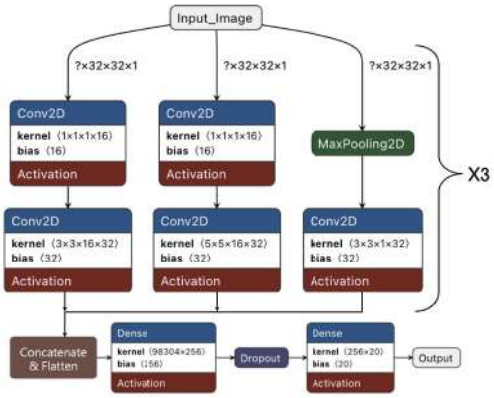

Fig. 6 ZerNet model architecture

RESULTS

ZerNet Performance with 1µm PSFs

The following figure features an upper plot comparing the Zernike coefficient of the model with the reconstructed ZerNet predictions, colors corresponding to different orders. The lower plot shows the error over a range of real coefficients values.

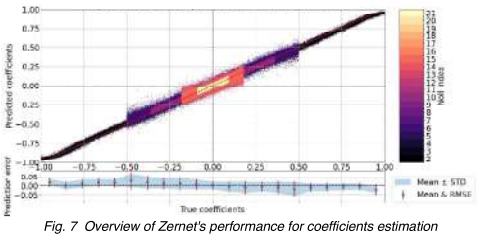

Fig. 7 Overview of Zernet's performance for coefficients estimation

The PSF reconstruction error is crucial to the propagation of uncertainty in scientific applications, and it must be minimized to limit systematics. In this instance, the error ϵ resulting from coefficients' estimation until order j_{max} was measured using the Frobenius norm [4]:

$$\epsilon_{j_{max}} = \left\| (PSF_{True} - PSF(\alpha_{:j_{max}})) \right\|_F$$

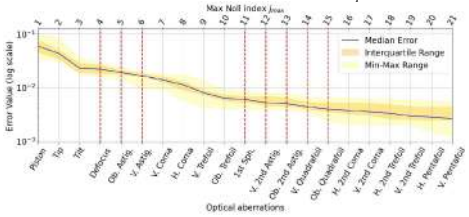

Fig. 8 Error Analysis Between True and Reconstructed PSFs

The previous plot showcases, through $\epsilon_{j_{max}}$ computation, the ability of ZerNet to precisely assess optical system aberrations. Even though min-max range appears wide and variable, the continuous decrease of median error confirms that using the predictions of several orders is constructive.

DISCUSSIONS

Our novel approach demonstrated that machine algorithms can establish a relationship between PSF images and corresponding optical aberrations without prior knowledge of the WFE.

Key assumptions and Constraints :

- Approximation in Fraunhofer region
- Specific WFE budget
- Low system's resolving power

Findings :

Models failed to converge on even radial orders in radially symmetrical optical system, highlighting the advantages of radially asymmetric systems.

Future Improvements:

- Add noise to match real-case scenarios : Autoencoders & Diffusion Denoising Probabilistic Models
- Train on polychromatic PSFs
- Perform element-wise analysis : WFE description per optical element
- Integrate physics into loss functions : Physics Integrated Neural Networks

In the future, it might be applied to plenty of fields such as astronomy, microscopy, or medical imaging where the understanding of WFE might pose a substantial challenge.

REFERENCES

1. Niu, Kuo, and Chao Tian. "Zernike Polynomials and Their Applications." Journal of Optics, vol. 24, no. 12, Dec. 2022, p. 123001. DOI.org (Crossref), https://doi.org/10.1088/2040-8986/ac9e08.
2. Perrin, Marshall, et al. "POPPY: Physical Optics Propagation in PYthon." Astrophysics Source Code Library, Feb. 2016, p. ascl:1602.018. NASA ADS, https://ui.adsabs.harvard.edu/abs/2016ascl.soft02018P.
3. Störkle, Johannes. Dynamic Simulation and Control of Optical Systems. Shaker Verlag, 2018.
4. G. H. Golub and C. F. Van Loan, Matrix Computations, Baltimore, MD, Johns Hopkins University Press, 1985, pg. 15

ACKNOWLEDGEMENTS

This research effort is part of a project funded by the Agence Nationale de la Recherche (ANR) under the ANR-22-CE46-0009 grant, hosted by the Centre de Physique des Particules de Marseille. We take this opportunity to express our gratitude to the French space agency (CNES) for co-funding Lucas Sauniere's PhD.

Effects of microgravity on cell motility

Winfried Schmidt, Alexander Farutin, and Chaouqi Misbah

Univ. Grenoble Alpes, CNRS, LIPhy, 38000 Grenoble, France
winfried.schmidt@univ-grenoble-alpes.fr

Introduction

- the immune system of astronauts is severely impaired after return from space flight [1]
- *in vitro* experiments during space flight show disruptions of the actin cytoskeleton of immune cells [2]
- such severe microgravity-induced cytoskeletal alternations have been shown to impact cell shape and motility [3]
- microgravity leads to changes of, e.g., cortical thickness and distribution of focal adhesion proteins [3,4]

Question: What are the effects of such microgravity-induced changes on the ability of the cell to migrate, polarize, and deform?

	1g cell	**μ-g cell**
in vitro experiments [3]:	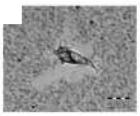 wide migration tracks, typical elongated shape of a migrating cell	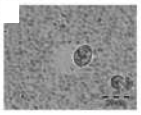 short migration tracks, contracted morphology
presumed cytoskeletal changes [5]:	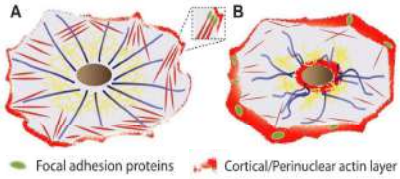	

Key terms

- The **cell cortex** is a thin layer of actin filaments on the inner face of the cell membrane. It is an important part of the cell's cytoskeleton.
- **Actin** is a filamenteous protein which dynamically polymerizes and depolymerizes. Actin **polymerization** creates membrane protrusions which are essential for cell migration.
- **Focal adhesion proteins** link the cortex to the extracellular environment, transmitting forces which allow for migration.

Two-dimensional model for the cell

- cortex is described as a closed, one-dimensional contour of compressible viscous fluid which forms the cell surface
- cortex force includes membrane tension and cell area conservation

$$\boldsymbol{f} = -\left[\gamma \frac{p_{\max} - p_0}{p_{\max} - p} H + \frac{2\kappa}{A_0}(A - A_0)\right]\hat{\boldsymbol{n}}$$

surface tension γ, maximum perimeter $p_{\max}$, reference perimeter $p_0 = 2\pi R_0$, radius of circular reference cell shape R_0, curvature of contour $H(\varphi, t)$, area modulus κ, cell area $A(t)$, reference area A_0, unit normal vector $\hat{\boldsymbol{n}}(\varphi, t)$

- cortex velocity (cortex deformation rate) $\boldsymbol{v}_c = \frac{f}{\zeta}$

drag coefficient ζ

- polymerization velocity (filament growth) depends on actin concentration $c(\varphi, t)$ [6]

$$\boldsymbol{v}_p = V e^{\frac{-c}{c_r}} \hat{\boldsymbol{n}}$$

polymerization speed V, reference concentration c_r

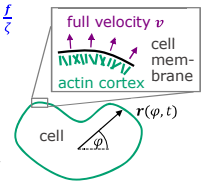

- full velocity $\boldsymbol{v} = \boldsymbol{v}_c + \boldsymbol{v}_p$ describes motion of filament end points and cell shape evolution
- time-evolution of actin concentration due to filament advection, diffusion, and restoration (due to, e.g., depolymerization) [7,8]

$$\dot{c} = -\boldsymbol{\nabla}^l \cdot (\boldsymbol{v}c) + D\Delta^l c + \beta(c_0 - c)$$

contour Laplace operator $\Delta^l = \boldsymbol{\nabla}^l \cdot \boldsymbol{\nabla}^l$, homeostatic actin concentration c_0, diffusion coefficient D, restoration rate β

Spontaneous onset of motility

Non-motile base state: circular cell (radius R_0) with homogeneous actin concentration c_0 along the cortex

Linear stability analysis:

- first circular harmonic: No cell shape changes
- stationary instability for polymerization speeds above

$$V_1^{crit} = \frac{c_r}{c_0} e^{\frac{c_0}{c_r}} \left[\frac{D}{R_0} - R_0\beta\right]$$

- spontaneous onset of cell polarity and motility: Retrograde flow of cortex from cell front to rear
- see also three-dimensional case [9]

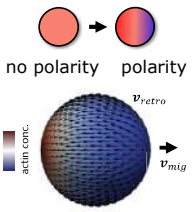

Shape dynamics

Linear stability analysis:

- higher-order harmonics: Shape changes
- consider small perturbations $\delta R(t)$, $\delta c(t)$ of circular cell shape and homeostatic concentration
- coupled dynamics of shape and concentration
- complex growth rate λ_l of perturbation
- oscillatory instability (Hopf bifurcation) for polymerization speeds above

$$V_l^{crit} = \frac{c_r}{c_0} e^{\frac{c_0}{c_r}} \left[(l^2 - 1)\frac{\gamma}{R_0\zeta} + l^2 \frac{D}{R_0} - R_0\beta\right]$$

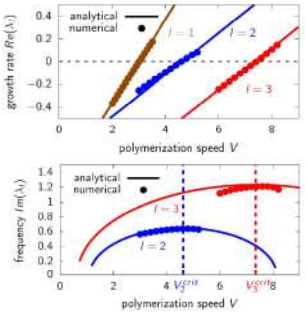

Numerical simulations:

- Second harmonic ($l = 2$)
- Third harmonic ($l = 3$)
- Circular trajectories (see also experiments on fish keratocytes [10])

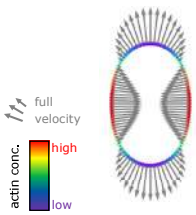

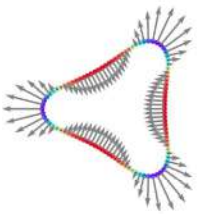

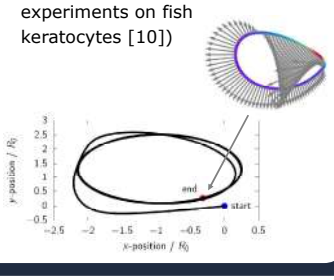

Conclusion

Summary:

- the developed physical model for a cell allows to study the effects of microgravity on cell migration
- linear stability analysis reveals spontaneous symmetry breaking, leading to cell polarization, motility, and dynamic shape changes
- numerical simulations allow investigation of large cell deformations

Outlook:

- include anisotropic diffusion of cortical filaments to account for microgravity-induced disruptions of cortex
- study effects of external forces on cell migration
- include coupling of the cortex to extracellular environment using a focal adhesion model

References

[1] M. ElGindi *et al.*, Cells **10**, 1941 (2021).
[2] K. Paulsen *et al.*, Acta Astronaut. **94**, 277 (2014).
[3] M. A. Meloni *et al.*, Cytoskeleton **68**, 125 (2011).
[4] N. Nabavi, A. Khandani, A. Camirand, and R. E. Harrison, Bone **49**, 965 (2011).
[5] D. Vorselen *et al.*, FASEB J. **28**, 536 (2014).
[6] A. Farutin, J. Étienne, C. Misbah, and P. Recho, Phys. Rev. Lett. **123**, 118101 (2019).
[7] A. Colin *et al.*, EMBO J. **42**, 9 (2023).
[8] A. Mietke, F. Jülicher, and I. F. Sbalzarini, Proc. Natl. Acad. Sci. **116**, 29 (2019).
[9] W. Schmidt, W. Zimmermann, C. Misbah, and A. Farutin, under review (2024).
[10] G. M. Allen *et al.*, Cell Syst. **11**, 286 (2020).

Recueil des posters

Session 2

S02-01 | Post-doc | **ALALAM Perla** | LISA, Créteil | Encadrant CNES : Adrien DESCHAMPS | POSTER |
Global Scale Mapping of Mineral Dust in situ Optical Properties in the MIR+FIR spectral domain (2–100 µm, 100 to 5000 cm−1): Spectroscopic studies towards the exploitation of IASI−NG and FORUM forthcoming missions

S02-02 | Doc | **BOISSENIN Adrien** | CEA / CNES, Gif sur Yvette | Encadrant CNES : Kévin MATHIS | POSTER |
Development and study of laminated composite material integrating carbon nanotubes for launcher cryogenic tank application

S02-03 | Doc | **BONASSIES Quentin** | CERFACS-CNES-CLS, Toulouse | Encadrant CNES : Santiago PENALUQUE
Assimilation of SWOT data and flood extent extraction for flood forecasting

S02-04 | Doc | **DE CALBIAC Joséphine** | ICA, Toulouse | Encadrant CNES : Marion BROUTELLE | POSTER |
Vitrimer matrix composites for space applications

S02-05 | Doc | **DENG Senwen** | APC, Paris | Encadrant CNES : Martin BOUTELIER | POSTER |
Disentangling and characterizing astrophysical GW signals with LISA

S02-06 | Doc | **GUENDOUZ Nadir** | LATMOS/IPSL, Paris |Encadrant CNES : Carole DENIEL | POSTER |
Pollution: role of ammonia and surface temperature using IASI and IRS

S02-07 | Doc | **LEMETTAIS Louise** | ULILLE, Villeneuve d'Ascq | Encadrant CNES : Philippe MAISONGRANDE
Caractérisation des états de surface sous influence des variations climatiques dans le subantarctique

S02-08 | Post-doc | **PROVOST Floriane** | ITES/EOST, Strasbourg | Encadrant CNES : Félix PEROSANZ | Poster à venir |
SAFE-SLOPE – Identification of landSlide meteorologicAl Forcing factors at rEgional ScaLe frOm multi-Platform/-sEnsor monitoring

S02-09 | Doc | **REOT François** | LAPLACE, Toulouse | Encadrant CNES : Ulysse WELLER | POSTER |
Étude des instabilités micro-ondes dans les propulseurs à courant de Hall

S02-10 | Post-doc | **SEPETAUSKAS Vinicius** | Supersonic flow, Marseille | Encadrant CNES : Simon BLANCHARD | POSTER |
Free separation with harmonic downstream excitation

S02-11 | Doc | **TARRASSE Maxime** | CEA, Villebon Sur Yvette | Encadrant CNES : Philippe MAISONGRANDE | POSTER |
Dévoiler la naissance des premières galaxies massives avec le télescope spatial James Webb

S02-12 | Doc | **THOREAU Romain** | CNES, Toulouse | Encadrant CNES : Pierre LASSALLE | POSTER |
Jumeaux numériques pour la modélisation de la propagation des feux de forêts

Global Scale Mapping of Mineral Dust in situ Optical Properties in the MIR+FIR spectral domain (100 to 2000 cm^{-1}): Spectroscopic studies towards the exploitation of IASI–NG and FORUM forthcoming missions

P. Alalam[1,2], C. Di Biagio[3], P. Sellitto[1,4], H. Herbin[5], D. Petitprez[6], E. Bru[3], A. Orta[3], J. Cuesta[1], P. Formenti[3], P. Roy[7], J.–B. Brubach[7], L. C.-Labonnote[5], Q. Libois[8]

[1] Université Paris Est Creteil and Université Paris Cité, CNRS, LISA, F-94010 Créteil, France
[2] CNES (Centre National d'Études Spatiales), 75001, Paris, France
[3] Université Paris Cité and Université Paris Est Creteil, CNRS, LISA, F-75013 Paris, France
[4] Istituto Nazionale di Geofisica e Vulcanologia, Osservatorio Etneo, Catania, Italy
[5] Université de Lille, CNRS, UMR 8518, LOA, F-59000 Lille, France
[6] Université de Lille, CNRS, UMR 8522, PC2A, F-59000 Lille, France
[7] SOLEIL Synchrotron, L'Orme des Merisiers, 91190 Saint-Aubin, France
[8] CNRM, Université de Toulouse, Météo-France, CNRS, CNRM, F-31057 Toulouse, France

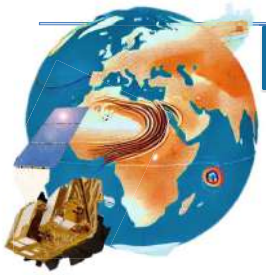

Mineral dust

Carried by winds from deserts, mineral dust is one of the most abundant aerosols in the atmosphere. It affects the Earth's climate by interacting with solar and terrestrial radiation. Satellites observations can detect dust in the infrared spectrum allowing to quantify its size, concentration, and composition—important data for climate models. Over the past 20 years, research has focused on satellite observations in the mid-infrared range, leaving a gap in understanding the dust interactions in the far-infrared spectrum, especially at night and in colder regions.

This study aims to measure the optical properties of dust in the far-infrared for the first time, helping improve climate models and satellite observations for more accurate climate predictions.

Methodology and Results

1- SOIL COLLECTION AND SELECTION

Six samples were selected to represent different geographic regions and cover the diversity of mineral dust composition on a global scale

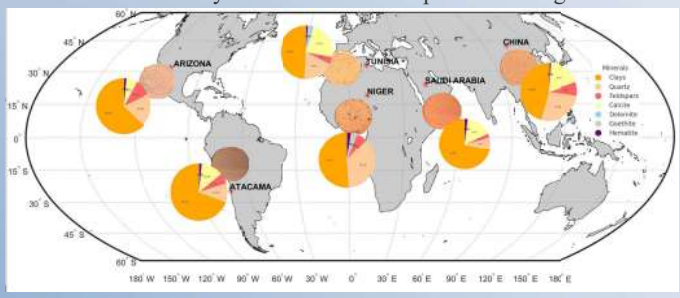

Samples and minerology from *Di Biagio et al., 2017*

2- EXPERIMENTAL MEASUREMENTS

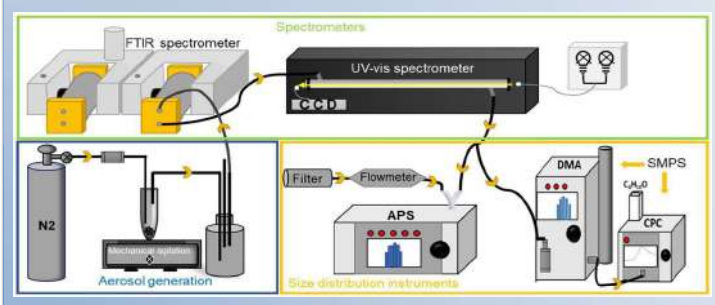

Chehab et al., 2024

EXTINCTION MEASUREMENTS : The spectral features reveal diverse mineral compositions, including the first-time detection of iron oxides peaks.

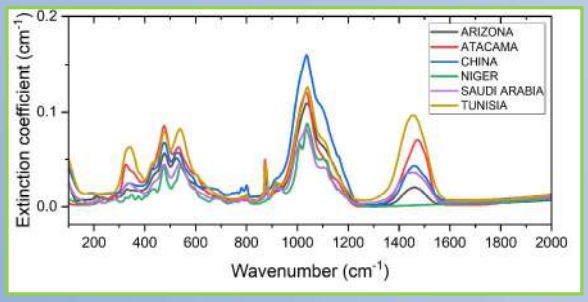

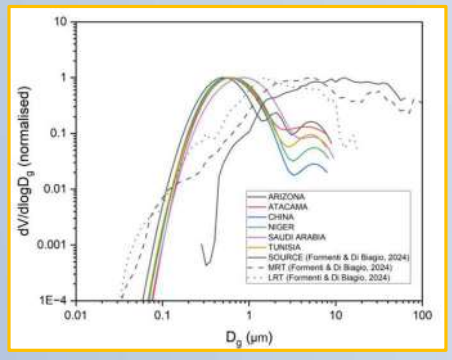

SIZE DISTRIBUTION MEASUREMENTS:

Results compared to mean size distributions representing:
SOURCE: Emissions;
MRT: Mid-range transport (1 to 4 days);
LRT: Long-range transport (> 4 days).
Best coherence with LRT size distribution.

3- OPTICAL PROPERTIES RETRIEVALS

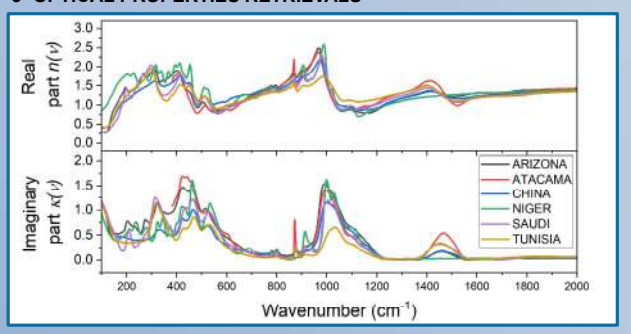

Complex refractive indices of dust were obtained in the infrared range filling the gap for the first time in the far-infrared spectrum.

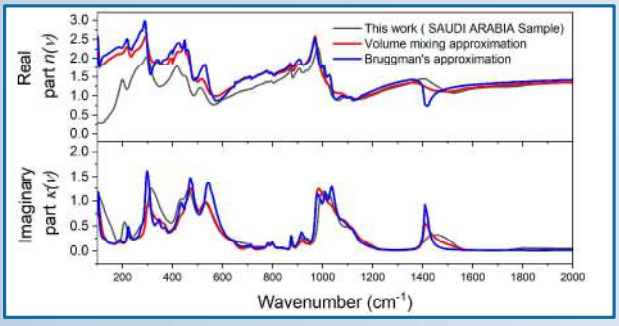

With knowledge of the mineral composition percentages, the results were compared to pure mineral mixtures from literature, revealing similarities

Conclusions and Perspectives

First-time measurements of mineral dust's optical properties filled a crucial gap in the far-infrared spectrum. Future spectral measurements at SOLEIL synchrotron will provide high signal-to-noise data, which can be implemented in radiative transfer models to improve dust characterization and support IASI-NG and FORUM satellite missions.

References

Chehab et al., 2024. *Aerosol Sci. Technol.* https://doi.org/10.1080/02786826.2024.2318371
Di Biagio et al., 2017. *Atmos. Chem. Phys.* https://doi.org/10.5194/acp-17-1901-2017
Formenti & Di Biagio., 2024. *Preprint.* https://doi.org/10.5194/essd-2023-481

DEVELOPMENT AND STUDY OF LAMINATED COMPOSITE MATERIAL INTEGRATING CARBON NANOTUBES FOR LAUNCHER CRYOGENIC TANK APPLICATION

Adrien Boissenin[1], Kevin Mathis[2], Emeline Charon[1], Antoine Lavaud[3], Aldo Cocchi[3], Martine Mayne-l'Hermite[1], Mathieu Pinault[1]

[1]Université Paris-Saclay, CEA, CNRS, NIMBE, 91191, Gif-sur-Yvette, France ;[2]CNES, Direction du Transport Spatial, 52 rue Jacques Hillairet, 75 612 Paris Cedex, France; [3]CMP Composites, 17 rue Jean-Baptiste Perrin 33320 Eysines, France

adrien.boissenin@cea.fr

Context of this study:

Cryogenic fuel tanks count for **more than 80%** of the **dry weight** of a launcher. **A more performant alternative** to their current design would be **carbon fiber reinforced polymer (CFRP)**.

From density 2,7 to 1,5, replacing aluminum with CFRP is an economic necessity.

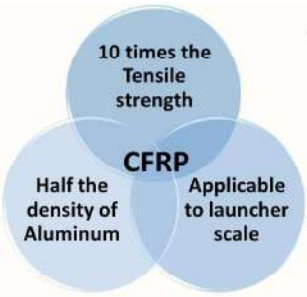

It is necessary for these CFRP composites to:

Prevent microcracking at **cryogenic temperatures** (-200°C) → **Resist** the **oxidizing** effects of the **Liquid Oxygen** environment → **Maintained Overall structural integrity & Absence of leaks**

As it stands, CF/Epoxy composites aren't resilient enough for cryofuel tanks.

A new optimized composite material is needed for the application

This work:

The stratified association of Carbon nanotubes (CNT), Carbon fiber (CF), and Cyanate ester resin (CE) holds a high potential for cryogenic applications.

This study aims to **determine the best of three** different **processing ways** to **integrate CNT** into a stratified **carbon fiber/cyanate ester composite.**

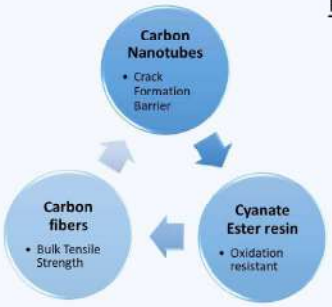

Previous works: CNT/Cyanate ester composites

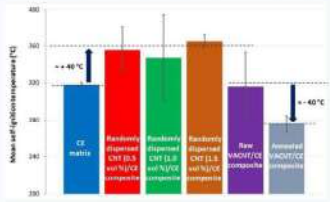

Mean self-ignition temperature of CE/CNT composites under oxygen atmosphere*

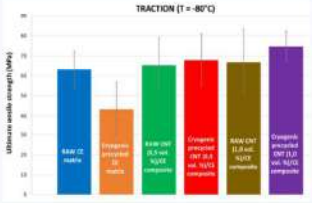

Tensile strength of CNT/CE composites before and after cryogenic cycling

CNT/CE synergize in regards to oxidation and cryogenic cracks resistance

Bouillonnec, Champonnois et al, EUCASS Proceedings (2022)

Direct growth of vertically aligned CNT forests on carbon fiber textile

Synthesis (LEDNA)
- On a 30cm SiO_2 covered carbon fiber cloth, in a 800°C furnace.
- Of up to 300 µm thick VACNT carpets

*30cm*5cm carbon fiber sample after VACNT growth*

Stacking, infusion, and polymerization
- To make samples fit for mechanical testing. (CMP)

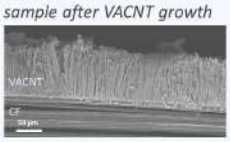

SEM of VACNT on Carbon fibers

Stratified composite rough sample

Mechanical testing (I2M)
- Cyclic traction trials
- Observing crack formation via optical microscopy
- At cryogenic temperatures

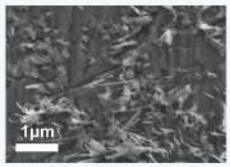

Zoomed in SEM of VACNT in a CF/CE stratified composite

+ Covalent binding between **CF** and **CNT**
+ Growth of VACNT through CF textile
+ Control over CNT length
- **CF** slightly **damaged** by the **high temperature** of the **VACNT synthesis**

Final sample architecture

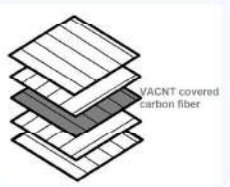

Hot pressing transfer of VACNT on preimpregnated carbon fiber textile

Synthesis (LEDNA)
- On a 25 cm, flexible aluminium foil in a 615°C furnace.
- Of up to 100 µm thick VACNT carpets by CCVD

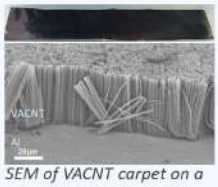

SEM of VACNT carpet on a flexible aluminum foil

Hot pressing transfer (LEDNA)
- On a 25*5cm VACNT carpet
- On a prepreg composite
- Hot CE Resin permeates the VACNT carpet

Bouillonnec, Champonnois et al, EUCASS Proceedings (2022)

Stacking & polymerisation
- To obtain a sample fit for mechanical testing (CMP)

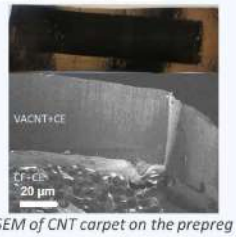

SEM of CNT carpet on the prepreg composite after Transfer

Mechanical testing (I2M)
- Cyclic traction trials
- Observing crack formation via optical microscopy
- At cryogenic temperatures

Final sample architecture

+ Undamaged carbon fibers
+ Maintained CNT alignment
+ Control over CNT length
- Presence of **CNTs only at the interlayer**
- **No covalent binding** of **CNT** on **CF**

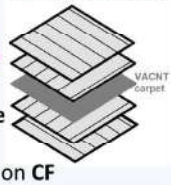

Dispersion of CNT within the cyanate ester matrix

Synthesis (LEDNA)
- In a 800°C quartz reactor
- Of 400 to 600 µm thick VACNT carpets by CCVD

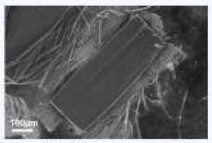

SEM of VACNT out of synthesis.

Dispersion (LEDNA)
- In water with 1%m Brij® S20
- Via a sonic probe

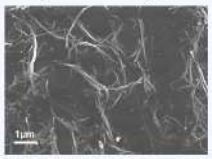

SEM of dried dispersed CNT after sonication.

Mixing, stacking & infusion
- Mixing hot cyanate ester resin with CNT dispersion under vacuum to dehydrate (CMP)

Mechanical testing (I2M)
- Cyclic traction trials
- Observing crack formation via optical microscopy
- At cryogenic temperatures

SEM of Dispersed CNT in CE resin.

+ Undamaged carbon fibers
+ Homogeneous presence of **CNT** through the **matrix**
- **CNT length** reduced to roughly **1µm**
- **No covalent binding** of **CNT** on CF

Final sample architecture

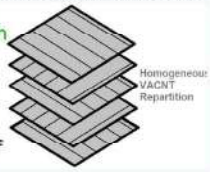

Conclusion:

- Several **sample sets of composite** architectures integrating **carbon nanotubes, carbon fibers and cyanate ester** have been produced.
- **Mechanical characterizations** will reveal the **influence of CNT length and concentration on mechanical properties.**
- **The mechanical behavior** of samples for each investigated processing ways will be **characterized at room temperature** and under a **cryogenic environment**
- Investigation of the **influence of CNTs** on **crack propagation** in CF composites at **room temperature and in Liquid N_2.**

S02-03 | Doc | **BONASSIES Quentin** | CERFACS-CNES-CLS, Toulouse | Encadrant CNES : Santiago PENALUQUE

Assimilation of SWOT data and flood extent extraction for flood forecasting

Absent

Vitrimer matrix composites for space applications

Authors : Joséphine de Calbiac,[a,b,c] Helie Reiniger,[a] Marion Broutelle,[a] Mathias Destarac,[d] Rima Sfar Zbed,[d] Marc Guerre,[c] Philippe Olivier,[b]

[a]CNES, Centre National d'Etudes Spatiales, 18 avenue Edouard Belin, 31400 Toulouse, France

[b]Laboratoire Softmat, Université de Toulouse, CNRS UMR 5623, Université Paul Sabatier, 118 route de Narbonne, 31062 Toulouse Cedex 9, France.

[c] Institut Clément Ader, Université de Toulouse, UT3, UMR CNRS 5312, 3 Rue C. Aigle, 31400 Toulouse, France

[d] IRT Saint Exupéry, Bâtiment B612, 3 rue Tarfaya, CS 34436, 31405 Toulouse cedex 4, France

Abstract : Vitrimers present an alternative to traditional thermosets, offering a dynamic structure that exhibits thermoset properties at application temperatures while it displays enough flow at higher temperatures. In this study, a space-grade epoxy thermoset matrix has been transformed into a high Tg vitrimer matrix with a glass transition temperature (Tg) of 175° C. By exploring a non-stoichiometric ratio, the effect of excess amine on the material's Tg is investigated, revealing a decrease in Tg. To separate the influence of stoichiometry and lower Tg on the exchange reactions, a third formulation is examined, maintaining a stoichiometric ratio while achieving a comparable Tg to the non-stoichiometric. Reactivity and rheological properties are evaluated to assess the compatibility of the cross-linking kinetics with classical kinetic models employed in composite manufacturing processes. The filament winding process is used to produce CFRV and reparation of composite parts is investigated.

Matrix characterisation

Table 1 : Ratios and Tg of the 3 formulations

	Formulation 1	Formulation 2	Formulation 3
Epoxy	1	1	1
Amine	1	1,2	1
Tg	199 ° C	175 ° C	170 ° C

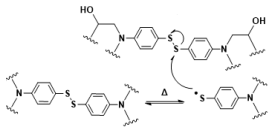

The 4-AFD hardener forms a polymer network with disulfide bonds, allowing exchanges when T > Tg. An amine excess (1/1.2 ratio) adds more disulfide bonds.

Kamal- Sourour model

$$\frac{d\alpha}{dt} = (k_1 + k_2\alpha^m)(1-\alpha)^n$$

$$k_i(T) = A_i e^{\frac{-E_i}{RT}} \quad i = 1;2$$

dα/dt the reaction rate, k_1 and k_2 the reaction rate constants
Ai is the pre-exponential factor, Ei the activation energy according to Arrhenius' law, R the universal gas constant, and T the curing temperature.

Di Benedetto model

$$Tg = Tg_0 + (Tg_\infty - Tg_0)\frac{\lambda\alpha}{1-(1-\lambda)\alpha}$$

Tg is the transition temperature at a given α, with Tg∞ at α=1 and Tg0 at α=0.
λ, a structure-dependent parameter, is approximated by $(\Delta\mathbf{Cp}\infty)/\Delta\mathbf{Cp0}$, where ΔCp is the heat capacity difference between the non-polymerized and fully cured polymer.

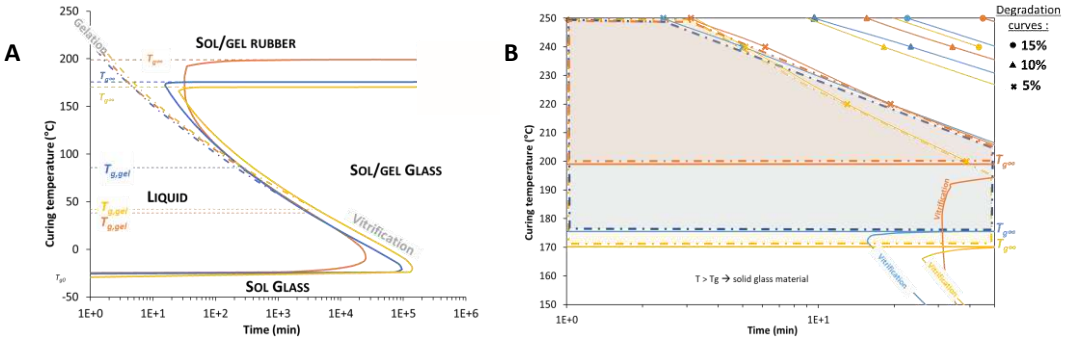

The cure kinetics model fits all formulations, regardless of the ratio. TTT diagrams, extrapolated from experimental results, show non-stoichiometric ratios cure 15% faster than stoichiometric ones at high temperatures (>120° C) but slower at lower temperatures, easing resin processing. A vitrimer processing window can be defined by the cured resin's properties, with a lower Tg offering a larger reprocessing window before degradation.

Figure 2 : TTT diagrams; (A) time temperature transformation diagram for curing stage of the resin; (B) reprocessing diagram with reprocessing area of stoichiometric (Formulation 1 -orange), non-stoichiometric (Formulation 2- blue) and stoichiometric modified (formulation 3 -yellow) formulations

Composite manufacturing and reprocessing

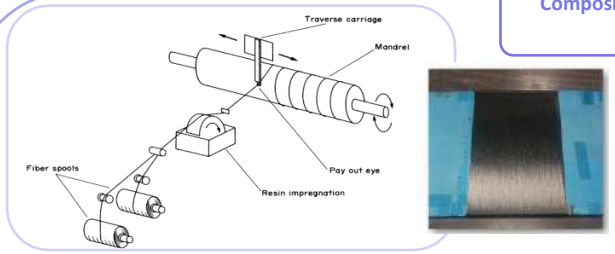

Figure 3 : filament winding process and an obtained plate CFRV with formulation 2 as vitrimer matrix and M55J carbon fibres

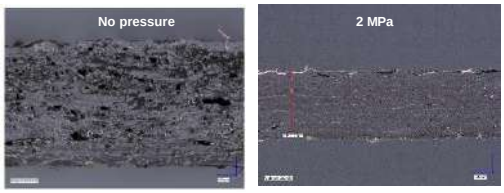

Figure 4 : microscopic sections of CFRV

CFRV was initially consolidated without pressure, resulting in voids due to the 20% overlap of fiber strands needed for mechanical strength. Applying a compaction force during consolidation helps minimize these voids.

Table 3 : neat matrix reprocessing via hot press for the 3 formulations

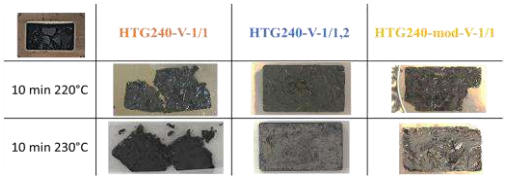

The vitrimer matrix allows composite repair (Table 3) and enables a second consolidation phase with controlled pressure and temperature to reduce voids, ensuring high-quality composite parts. As shown in the image, the repaired composite can be reused like a standard composite.

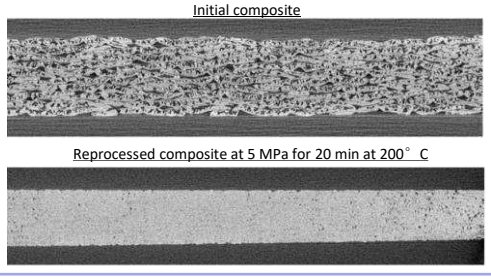

Figure 5 : X-Ray tomography of initial composite sample and repaired sample

Conclusions : Using a non-stoichiometric ratio, while reducing Tg, results in a more reactive system. Classic cure kinetics model can be applied to control the system's evolution at any temperature and time. The excess amine and the increase in disulfide bonds accelerate the resin's reprocessing, regardless of the reduction in Tg. Composite parts can be manufactured through filament winding using this matrix, Defective parts can be reprocessed and repaired due to the matrix properties, even when carbon fibers are incorporated.

Perspectives : Optimization of the process parameters to improve the final quality of composite parts. Comparison of mechanical properties between a well manufactured original part and a reprocessed defective composite part. Durability testing in space environments to ensure that the dynamic bonds within these matrices remain intact, meeting space qualification standards

(1) V.Shenk, K Labastie, M. Destarac, P.Olivier, M.Guerre, *Mater. Adv.* **2022** (2) A. Riuz de Luzuriaga, N. Markaide, A.M. Salaberria, I. Azcune, A. Rekondo, H.J. Grande, *Polymers*, **2022**, 14 (15), 3180 (3) M.R Kamal, S. Sourour, *Thermomecanica Acta*, **1976**, 14, 41-59

Disentangling and characterizing astrophysical GW signals with LISA

Modular global-fit pipeline for LISA data analysis

Senwen Deng, Stanislav Babak, Maude Le Jeune, Sylvain Marsat, Éric Plagnol and Andrea Sartirana*
*deng@apc.in2p3.fr

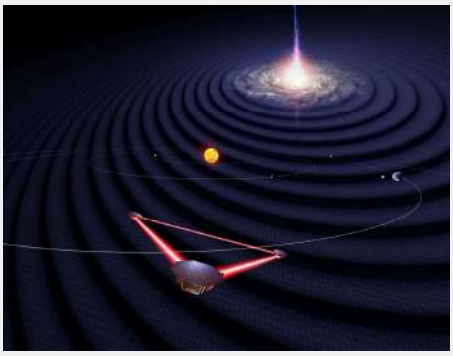

LISA constellation in the solar system
(Credit: University of Florida / Simon Barke / CC BY-SA 4.0)

What is LISA?

LISA is the acronym for Laser Interferometer Space Antenna, a space-based gravitational wave observatory.

- Collaboration between ESA, its member states and NASA.
- Constellation of three spacecrafts, exchanging laser beams, forming an equilateral triangle with 2.5 million km sides.
- Detect gravitational waves in the millihertz frequency band.

Astrophysical sources

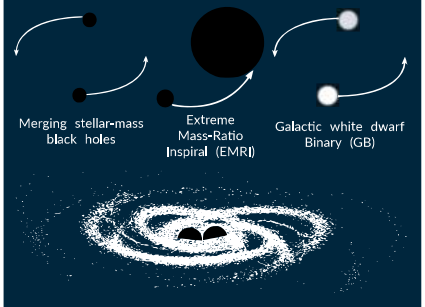

Massive Black Hole Binary (MBHB)
(Reproduction / Credit: ESA)

Why is LISA data analysis challenging?

- LISA data is dominated by signal, making the noise level estimation difficult.
- Signals are long-lasting, and they overlap in time and frequency domains.
- All the Galactic binary signals cannot be resolved individually, and the unresolved ones form a confusion foreground.
- High dimensionality due to the large number of sources.

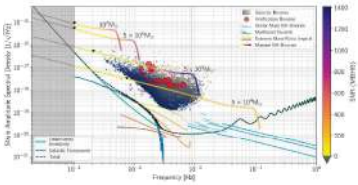

Primary LISA sources in the frequency-amplitude plane
(Credit: ESA / LISA Definition Study Report - ESA-SCI-DIR-RP-002)

"Sangria" dataset

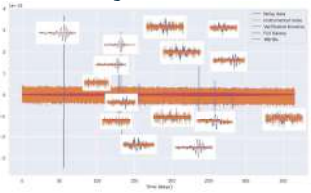

LISA Data Challenge 2 (aka "Sangria") training dataset (simulation of 15 MBHBs + 30 million GBs + stationary instrumental noise)

How to tackle the challenge?

We designed a modular framework applied to analyse the "Sangria" dataset. The framework relies on:

- The transitional nature of broadband loud MBHB signals
- Parallel tempering MCMC algorithm
- Block parallel Gibbs sampling technique
- Refinement through iterations
- Product space model selection
- Accelerated likelihood computation with heterodyning

Schema of the pipeline

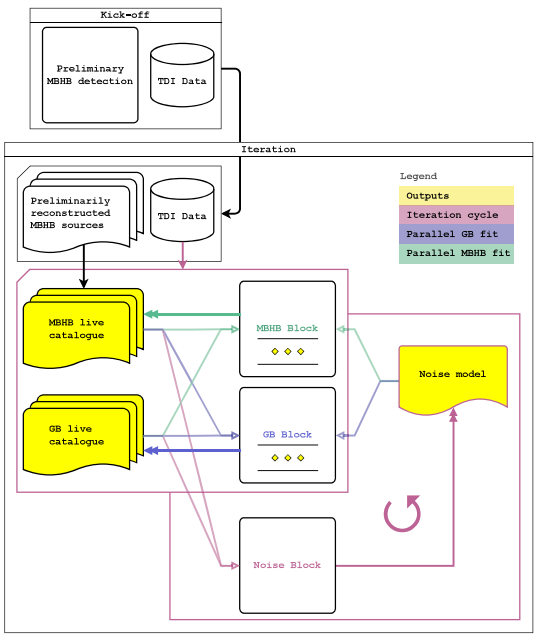

Our results

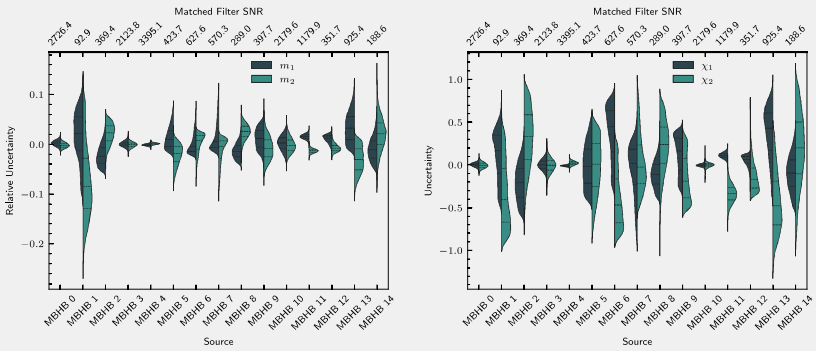

Posterior distribution for MBHB masses m_1, m_2 and spins χ_1, χ_2

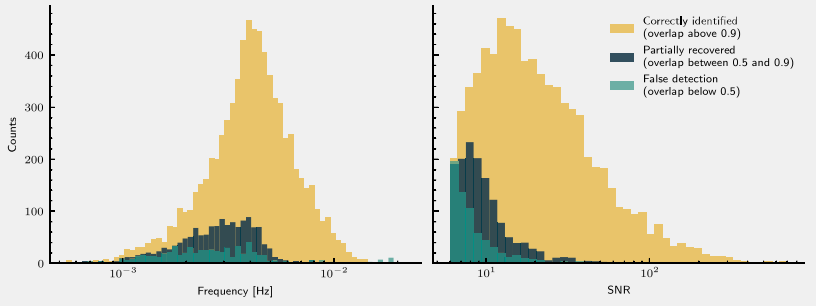

Detected GB counts as a function of frequency and SNR

Conclusion

- We developed a global-fit pipeline for LISA data analysis.
- We applied it to the "Sangria" training dataset and obtained promising results.
- Our pipeline is modular and can be adapted to future datasets.

Assessing the future IRS-MTG NH_3 observations

Nadir Guendouz[1], Camille Viatte[1], Anne Boynard[1,2], Sarah Safieddine[1], Carsten Standfuss[2], Solène Turquety[1], Martin Van Damme[3,4], Lieven Clarisse[3], Pierre Coheur[3], Pascal Prunet[2], and Cathy Clerbaux[1,3]

[1] LATMOS/IPSL, Sorbonne Université, UVSQ, CNRS, Paris, France
[2] SPASCIA, Ramonville-Saint-Agne, France
[3] Université libre de Bruxelles (ULB), Spectroscopy, Quantum Chemistry and Atmospheric Remote Sensing (SQUARES),Brussels, Belgium
[4] Royal Belgian Institute for Space Aeronomy, Brussels, Belgium

Introduction

Ammonia (NH_3), primarily emitted by agriculture[1], is a key atmospheric pollutant linked to public health[2] and climate change[3]. While satellite data have assessed **NH_3 variability** globally[4], regionally[5], and locally[6], understanding its diurnal changes and relationship with temperature remains limited, impacting accurate modeling of NH_3 emissions and associated pollution events.

IASI[7] (Infrared Atmospheric Sounding Interferometer) instruments (**Fig 1**) aboard Metop-A,B and C satellites, launched in 2006, 2012 and 2018 respectively, retrieve NH_3 total columns within the 800-1200 cm^{-1} spectral range. The upcoming **IRS**[8] (InfraRed Sounder) on the MTG (Meteosat Third Generation) satellite[9], scheduled for late 2025, will offer high-resolution observations in space and time, promising insights into the role of NH_3 and temperature during pollution episodes. In this study we assess the future satellite **measurement uncertainties** and explore its contribution to the observation of atmospheric NH_3.

	IASI	IRS
Spatial resolution (nadir)	Circle of 12 km diameter	4 km X 4 km
Temporal resolution	Twice a day 9:30 AM - 9:30 PM	Every 30 minutes (Europe)
Spectral resolution	0.5 cm^{-1}	0.754 cm^{-1}
Spectral bands	645cm^{-1} – 2760cm^{-1}	700cm^{-1} - 1210cm^{-1} and 1600cm^{-1} -2175cm^{-1}

Figure 1: Technical comparison between IASI and IRS

Method

This study explores the potential of the IRS-MTG mission in capturing NH_3 variability over the Brittany region in France. To assess IRS NH_3 measurement capabilities, synthetic IRS spectra are computed using the **4A/OP**[10] radiative transfer model and a realistic atmosphere simulated by the **CHIMERE** model[11] (**Fig 2**) with a temporal resolution of 1 hour and a spatial resolution of 4 km x 4 km for July 2016.

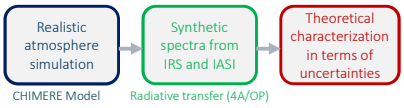

Figure 2: Methodology applied to assess the potential of IASI/IRS to measure NH_3

Fig 3 illustrating the **absolute Thermal Contrast** (TC) on the 19th of July 2016 at 1 AM shows lower TC near urban areas, such as Paris (TC 2 times lower). In this study, TC is defined as the difference between the surface temperature (T_{surf}) and the temperature at 600 meters above ground level (**Equation 1**).

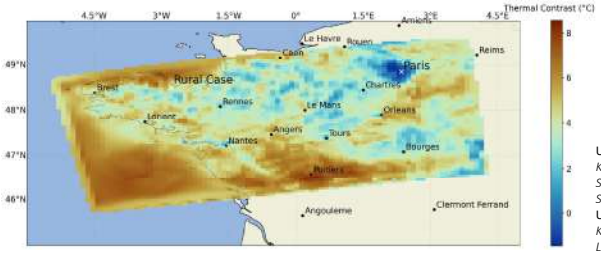

Figure 3: Monthly average of absolute thermal contrast (°C) simulated by CHIMERE for the 19/07/2016 at 1AM

Measurement uncertainties are determined using **Equation 2**[12], utilizing the NH_3 Jacobian (**Equation 3**) and the Instrumental Noise Covariance Matrices for IASI and IRS (given by Eumetsat).

$$TC = Tsurf - T_{600m} \quad (1)$$

$$\sigma^2_{instrument} = S = (K^T S_\varepsilon^{-1} K)^{-1} \quad (2)$$

$$K = (L(X + dX) - L(X))/dX \quad (3)$$

Units Equation 2 :
K :NH_3 Jacobian ($W/(m^2.sr.cm^{-1})/(molecules/cm^2)$)
Sε :Full Instrumental Noise Covariance Matrix($W/(m^2.sr.cm^{-1})$)²
S :Measurement Uncertainty Matrix ($molecules/cm^2$)²
Units Equation 3 :
K :NH_3 Jacobian ($W/(m^2.sr.cm^{-1})/(molecules/cm^2)$)
L(X) :Radiance spectra ($W/(m^2.sr.cm^{-1})$)
X :NH_3 total column ($molecules/cm^2$)
dX :0.01% increment of the total column (~10^{12} $molecules/cm^2$)

Results

1. Computing IRS and IASI measurements uncertainties

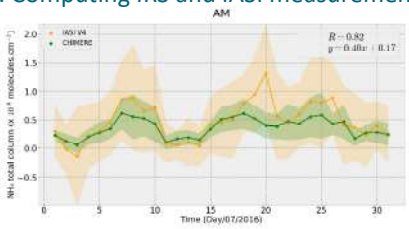

Figure 4: Timeseries of daily NH_3 total column derived from IASI and CHIMERE simulation in July 2016

1.1 Can CHIMERE simulate a real atmosphere ?

The monthly NH_3 total column measured by IASI and simulated by CHIMERE coincident with the morning overpasses in July 2016 are 0.46 ± 0.06 10^{16} and 0.37 ± 0.03 10^{16} $molec/cm^2$, respectively (**Fig 4**). The main difference between both datasets is the NH_3 enhancement observed by IASI on the 20th of July 2016, which is almost 4 times higher than the CHIMERE simulation.

The **strong correlation** (R=0.82) between IASI observations and the CHIMERE model suggests that CHIMERE represents a realistic atmosphere.

1.2 Distribution of measurement uncertainties

Fig 5 displays measurement uncertainty over the CHIMERE domain for the 19th of July 2016 at 1 AM. The measurement uncertainty variability is very high (9.4 10^{15} $molec/cm^2$ corresponding to 1.17 times the mean total column of NH_3) with the minimum at 3.2 10^{14} $molec/cm^2$ and the maximum at 4.6 10^{17} $molec/cm^2$. These high measurement uncertainties are correlated to areas with a thermal contrast close to 0 (**Fig 3**).

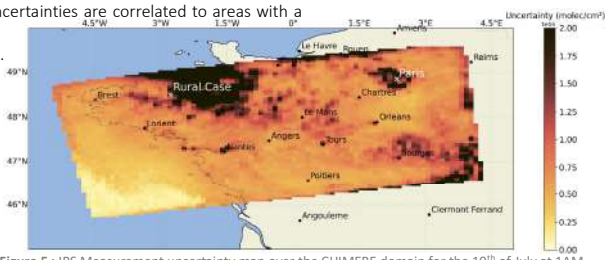

Figure 5 : IRS Measurement uncertainty map over the CHIMERE domain for the 19th of July at 1AM

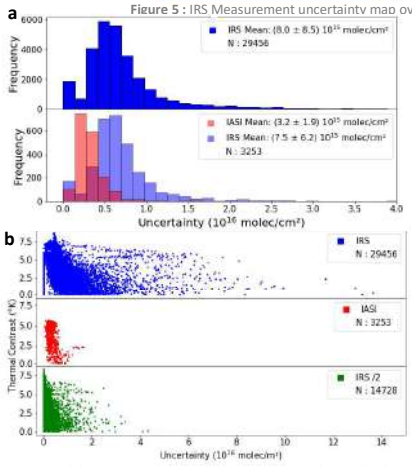

Figure 6: (**a**) Measurement uncertainty distribution for IRS (top), IASI and IRS at the overpass time of IASI (bottom). (**b**) Thermal Contrast as a function of measurement uncertainties of IRS (blue), IRS averaged by pairs of observations (green), and IASI (red).

The average of the IRS measurement uncertainties (**Fig 6.a**; 7.5 10^{16} $molec/cm^2$) is **twice higher** than IASI one (3.2 10^{16} $molec/cm^2$) but with a variability **3 times higher** than IASI. This larger variability of IRS measurement uncertainty might be due to the higher number of observations (factor of 10) with respect to IASI.

Measurement uncertainties depend on thermal contrast with higher measurement uncertainties associated with lower thermal contrast (**Fig 6.b**). Considering the entire IRS dataset (top panel), the averaged IRS measurement uncertainty is 2.5 times larger than the IASI one (middle panel). However, considering IRS data averaged every 2 hours (bottom panel), the IRS measurement uncertainty decreases by a factor of 2.3 and is similar than IASI measurement uncertainty (3.5 10^{16} $molec/cm^2$ for IRS against 3.2 10^{16} $molec/cm^2$ for IASI). This means that **analyzing IRS data every 2 hours is sufficient to achieve a similar measurement uncertainty than IASI.**

2. Difference between urban and rural sites

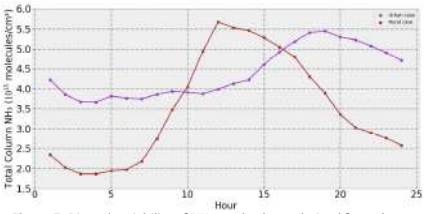

Figure 7: Diurnal variability of NH_3 total column derived from the CHIMERE simulation in July 2016 for urban (purple) and rural (red) case studies

2.1 NH_3 diurnal variability

The mean NH_3 total column simulated by CHIMERE in July 2016 is higher at the rural than at the urban sites with 4.39 ± 2.61 10^{15} $molec/cm^2$ compared to 3.50 ± 3.21 10^{15} $molec/cm^2$.

The **diurnal variability** for the rural case is **4.73 times higher** than for the urban case (**Fig 7**), suggesting the local influence of NH_3 source at the rural site.

2.2 Diurnal variability of measurements uncertainty

Daily, the **thermal contrast** begins to increase at 6 AM at the urban site, whereas it starts to increase at 8 AM at the rural site (**Fig 8**). The NH_3 total column of the first day of July 2016 (Fig 8 purple big dots) is the **lowest of the month** (2.70 ± 0.88 10^{15} $molec/cm^2$) and the NH_3 Jacobian is one the highest for the month. When the **NH_3 total column is low, the measurement uncertainty is highly linked to the thermal contrast**.

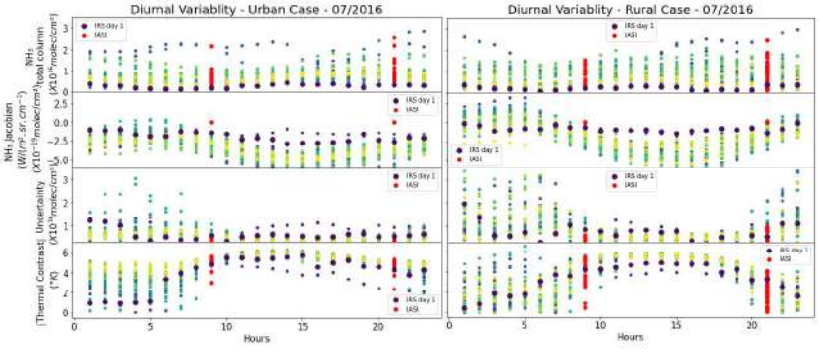

Figure 8: Diurnal Variability calculated at the urban (**a**) and rural (**b**) cases. From top to bottom panels: NH_3 total column, NH_3 Jacobian, measurements uncertainty, and the absolute thermal contrast. Colors indicate days of the month for hourly IRS observations, and red dots correspond to IASI observations.

Conclusion

A realistic atmosphere simulation from the CHIMERE model was used to simulate atmospheric conditions at the pixel size of IRS, generating synthetic spectra for 40 case studies using the 4A/OP radiative transfer algorithm. Comparing NH_3 uncertainties over Brittany in July 2016, IASI showed lower uncertainties than IRS, but IRS exhibited higher variability. Averaging IRS observations every 2 hours reduced uncertainties below those of IASI, suggesting this interval provides better NH_3 concentration estimates. Analysis of rural and urban cases revealed significant variability in TC and uncertainties, especially when NH_3 total column are low. This study demonstrates the ability of the future IRS satellite to study NH_3 variability and how this variability changes as a function of the area. By averaging IRS data by pairs to minimize its uncertainty, it will be possible to use IRS data to improve our understanding of NH_3's relationship with temperature.

References

1. Fowler et al. 2013. « The Global Nitrogen Cycle in the Twenty-First Century ». Philosophical Transactions of the Royal Society B: Biological Sciences 368 (1621): 20130164. https://doi.org/10.1098/rstb.2013.0164.
2. Lelieveld et al. 2015. « The Contribution of Outdoor Air Pollution Sources to Premature Mortality on a Global Scale ». Nature 525 (7569): 367-71. https://doi.org/10.1038/nature15371.
3. Myhre et al. 2013. « Radiative Forcing of the Direct Aerosol Effect from AeroCom Phase II Simulations ». Atmospheric Chemistry and Physics 13 (4): 1853-77. https://doi.org/10.5194/acp-13-1853-2013.
4. Clarisse et al. 2009. « Global ammonia distribution derived from infrared satellite observations ». Nature Geoscience, 2(7), 479–483. https://doi.org/10.1038/ngeo551.
5. Van Damme et al. 2020. « Global, regional and national trends of atmospheric ammonia derived from a decadal (2008-2018) satellite record ». Environmental Research Letters. http://iopscience.iop.org/article/10.1088/1748-9326/abd5e0.
6. Viatte et al. 2022. « NH3 spatiotemporal variability over Paris, Mexico City, and Toronto, and its link to PM2.5 during pollution events ». Atmospheric Chemistry and Physics 20 (1): 577-96. https://doi.org/10.5194/acp-20-577-2020. Clarisse et al. 2023. « The IASI NH 3 version 4 product: averaging kernels and improved consistency ». Atmospheric Measurement Techniques 16 (21): 5008-5028. https://doi.org/10.5194/amt-2023-48
7. Clerbaux et al. 2009. « Monitoring of atmospheric composition using the thermal infrared IASI/MetOp sounder ». Atmos. Chem. Phys., 9, 6041–6054. https://doi.org/10.5194/acp-9-6041-2009.
8. Coopmann et al. 2022. « Analysis of MTG-IRS observations and general channel selection for Numerical Weather Prediction models ». Quarterly Journal of the Royal Meteorological Society., 148. https://doi.org/10.1002/qj.4282.
9. Stuhlmann et al. 2005. « Plans for EUMETSAT's Third Generation Meteosat (MTG) Geostationary Satellite Program ». Advances in Space Research., 36, 975–981. https://doi.org/10.1016/j.asr.2005.03.091.
10. Scott and Chedin. 1981 « A Fast Line-by-Line Method for Atmospheric Absorption Computations: The Automated Atmospheric Absorption Atlas ». J. Appl. Meteor. Climatol., 20, 802–812. https://doi.org/10.1175/1520-0450(1981)020<0802:AFLBLM>2.0.CO;2
11. Menut et al. 2021. « The CHIMERE v2020r1 online chemistry-transport model ». Geoscientific Model Development 14(11) : 6781–6811. https://doi.org/10.5194/gmd-14-6781-2021.
12. Rodgers, C.D. 1990 « Characterization and error analysis of profiles retrieved from remote sounding measurements », Journal of Geophysical Research: Atmospheres, 95(D5) : 5587–5595. https://doi.org/10.1029/JD095iD05p05587

S02-07 | Doc | **LEMETTAIS Louise** | ULILLE, Villeneuve d'Ascq | Encadrant CNES : Philippe MAISONGRANDE

Caractérisation des états de surface sous influence des variations climatiques dans le subantarctique

Absente

S02-08 | Post-doc | **PROVOST Floriane** | ITES/EOST, Strasbourg | Encadrant CNES : Félix PEROSANZ

SAFE-SLOPE – Identification of landSlide meteorologicAl Forcing factors at rEgional ScaLe frOm multi-Platform/-sEnsor monitoring

NON FOURNI

RÉPUBLIQUE FRANÇAISE
Liberté Égalité Fraternité

Laplace
cnes
AGENCE INNOVATION DÉFENSE

Spectral dependencies of GHz electromagnetic emission from Hall thrusters

F. Réot[*], **L. Liard**[*], **F. Gaboriau**[*], **V. Mazières**[†] and **O. Pascal**[*]
[*]Laboratoire Plasma et Conversion d'Energie, Toulouse, France
[†]ISAE-SUPAERO, Toulouse, France
francois.reot@laplace.univ-tlse.fr

CONTEXT

- **Pulsed electromagnetic emission** from Hall thrusters in the **GHz range**
- Unclear **physical origin**
- Source of electromagnetic **noise**

- Where does this emission **come from?** Is it **independant** from the **discharge dynamics**?

→ Investigations of a **connection** with **low-frequency oscillations** of the discharge

Hall thruster

- **Most proven technology** for **electric propulsion** of satellites
- **Thrust** generated by **acceleration of ions**

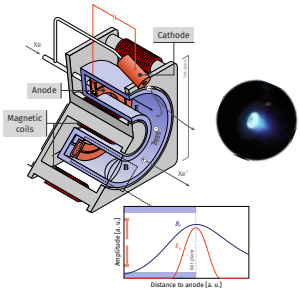

- Combination of $\mathbf{E} \perp \mathbf{B}$: **closed electron drift** with velocity :

$$V_d = \frac{\|\mathbf{E}\times\mathbf{B}\|}{B^2} \simeq \frac{E_x}{B_r}$$

Experimental setup

- **ID-HALL II** [1] double-stage Hall thruster, used in **single stage** operation

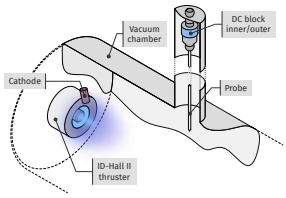

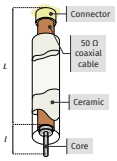

- Detector is an **open-ended coaxial cable** [2], positioned **inside the metallic vacuum chamber**
- Acts as an **electrically small antenna** on a]0,4] GHz range
- Simultaneous recording of : **probe signal** and **discharge current** I_d

Data processing

- Time-frequency analysis based on **Continuous Wavelet Transform** (CWT)
- Adapted to **2 different objectives**

Pulse detection

- Detection based on the **HF envelope** of the probe signal
- **Threshold** for detection following a fixed value of **Signal to Noise Ratio** (SNR)

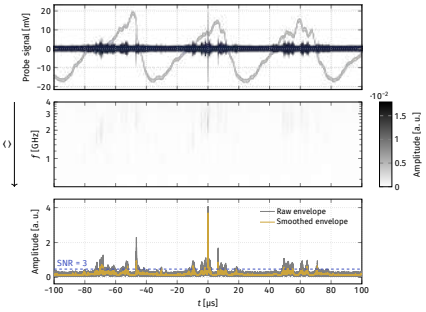

Phase retrieval of *Breathing Mode*

- **Amplitude** of CWT gives the value of the **BM frequency** when a pulse occurs
- The **phase of the BM** ϕ_{BM} is retrieved from the **argument of CWT** at the same time and BM frequency

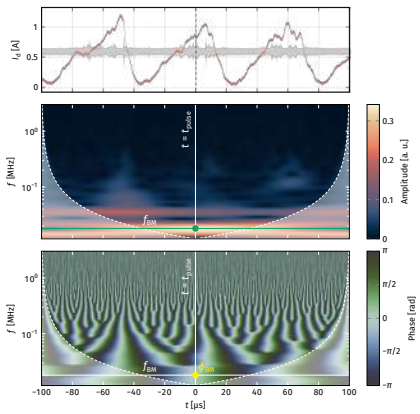

Main findings

- Recorded 99 samples of 200 µs each
- **1089 pulses** detected for SNR = 3

Mean frequency of occurence : **55 000 pulses.s^{-1}**

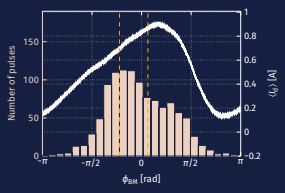

- Pulse **appearance** dependent on the **phase** of the **Breathing Mode** : few pulses for low I_d values

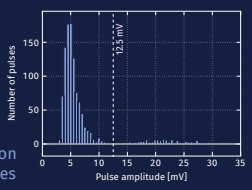

- **Amplitude** distribution of the pulses

Spectral dependence

- Search for a spectral dependency : pulse **spectra stacked** by **increasing values of ϕ_{BM}**

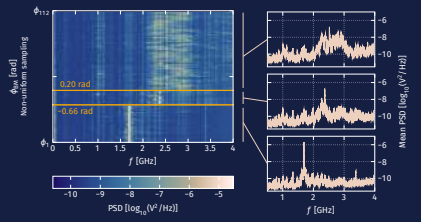

Pulses of **highest amplitude**

- **Explicit classification** of the pulse spectra following **3 phase ranges** of BM oscillations
- In particular, **quasi-monochromatic** character for ϕ_{BM} < −0.66 rad at **1.7 GHz**

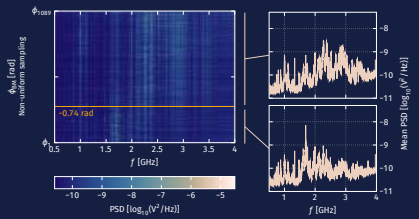

Total set of pulses

- Classification less obvious, but still discernible
- 2 phase ranges for ϕ_{BM} rather than 3
- Similar behavior and value of phase boundary

Discussion

- Recorded pulses are the result of a **convolution** by the **impulse response** of the **measuring system**
- Inf uence of **resonance frequencies** of the metallic **vacuum chamber**
- **Does not contradict** the spectral dependency revealed

CONCLUSION

- First evidence for a **dependency** of the pulsed GHz emission on **Breathing Mode oscillations** regarding :
  - Pulse **appearance**
  - Pulse **spectra**
- Valuable **insight** into the **physical origin** of this emission

[1] Dubois L. et al., *Physics of Plasmas* **2018**, 25, 093503.
[2] Mazières V. et al., *Physics of Plasmas* **2022**, 29, 072107.

Other relevant references :
[3] Beiting E. J. et al., *46th AIAA/ASME/SAE/ASEE Joint Propulsion Conference & Exhibit*, **2010**.
[4] Beiting E. J. et al., *ISPC-2008-070*, **2008**.
[5] Beiting E. J. et al., *IEPC-2009-072*, **2009**.

Download this poster

cnrs INP N7 UNIVERSITÉ TOULOUSE III PAUL SABATIER

Free Shock Separation with Downstream Excitation

Vinicius Sepetauskas, CNES/IUSTI, Marseille

1. CONTEXT

The Vulcain Engine is designed to operate at high altitude where the pressure is low. During the liftoff, Vulcain is not adapted to operate at 1 atm, leading to flow separation inside the nozzle.

Free Shock Separation (FSS) - without flow reattachment:

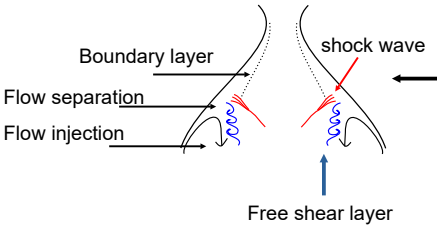

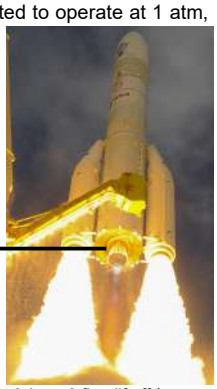

Ariane 6 first liftoff [1]

2. OBJECTIVES

- The nozzle is axisymmetric, however, a new 2D experimental setup developed by Demni (PhD 2022, CNES)[2] enables the study of FSS. The main goal is to extend Demni's setup to also allow **controlled acoustic excitation** downstream of the FSS region.
- Does the shock's response to a downstream acoustic wave depend on the flow state (whether it is attached or detached) and on the frequency (transfer function)?

3. SKETCH OF THE 2D MODEL

The nozzle accelerates the flow, reducing its pressure through expansion waves. At the shock position, there is a pressure jump. The 2D model aims to mimic this pressure distribution.

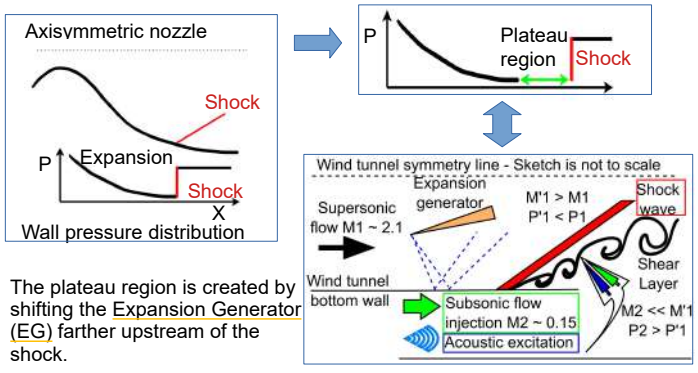

The plateau region is created by shifting the Expansion Generator (EG) farther upstream of the shock.

4. THE EXPERIMENTAL SETUP

The experiments were conducted in the supersonic wind tunnel at IUSTI lab., Marseille. The incoming flow conditions are M = 2.1, U_∞ = 522 m/s, δ^* = 1.67 mm, θ = 0.55 mm, Re_θ = 4850.

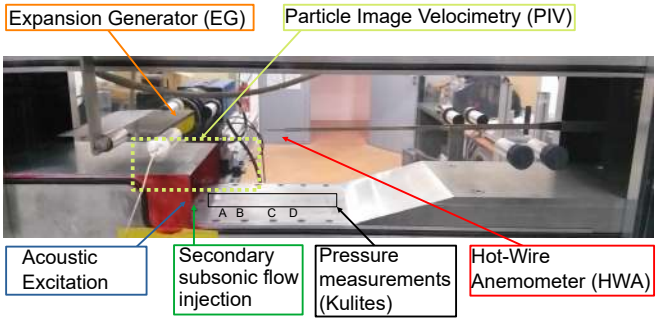

5. PREVIOUS WORK

Demni (PhD 2022, CNES)[2]: For the same small variation in pressure, the separation length (L_{sep}) varies significantly more for the detached flow case.

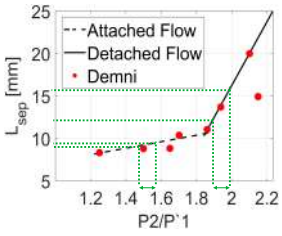

Where:
- P'1 is the static pressure upstream of the shock.
- P2 is the static pressure downstream of the shock.

The PIV result for the EG6.5 case shows the separated free shear layer induced by the shock.

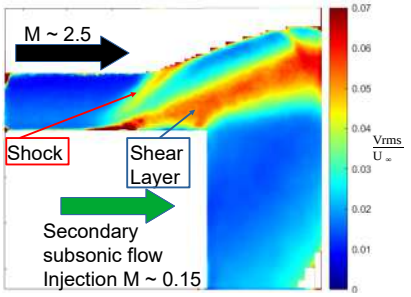

6. RESULTS: Acoustic excitation at 5 kHz

The Power Spectra Density (PSD) is presented for three different Expansion Generator (EG) angles: 4° (attached - EG4), 5° (incipient - EG5) and 6.5° (detached – EG6.5). All three cases are subjected to the same acoustic excitation at 5 kHz.

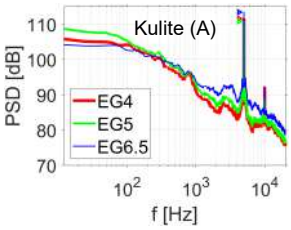

The kulite placed at the exit of the secondary flow injection (sensor A, see Fig. In Experimental Setup) measures the pressure fluctuation, and its PSD (left Fig.) gives approximately the same max. peak ~110dB at 5 Khz for all three cases.

The HWA placed at the mean shock position, used to measure the shock's response, shows a decrease in the PSD peak (right Fig.) as the flow separation increases.

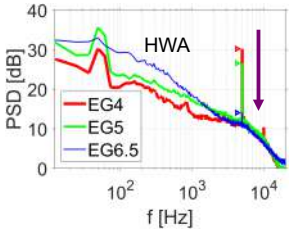

7. CONCLUSION + FUTURE WORK

The downstream acoustic excitation generates **the same air displacement and acoustic pressure perturbation** for all three cases. As the shock displacement is greater for detached flow compared to attached flow, the acoustic excitation becomes relatively weaker as flow separation increases, resulting in a reduced shock response.

The next step is to study how the shock behaves at different excitation frequencies and to identify a transfer function between the controlled downstream acoustic excitation and the shock displacement.

8. REFERENCES

1) https://www.esa.int/ESA_Multimedia/Missions/Ariane_6

2) Demni, N. (2022). Etude expérimentale d'un décollement supersonique ouvert (Doctoral dissertation, CNES).

Supervisors: Pierre Dupont and Sébastien Piponniau, IUSTI
Reference: Simon Blanchard, CNES
Collaborators: Daniel Mazzoni and Muriel Amielh, IRPHE
Funding/Sponsorship: CNES

Dust-obscured star-forming phase at the origin of the galaxy bimodality

M.Tarrasse, D.Elbaz, B. Magnelli, C.Gómez-Guijarro

CNES, CEA, IRFU, DAp, AIM, Université Paris-Saclay, Université Paris Cité, CNRS

maxime.tarrasse@cea.fr

Abstract :

The combined capabilities of the *James Webb* Space Telescope/NIRCam and the *Hubble* Space Telescope/ACS instruments provide enhanced spatial resolution imaging from the UV-to-NIR wavelengths that offer unprecedented insights into the internal structure of star-forming galaxies (SFGs) even when they are shrouded in dust.
In particular, a population of highly attenuated and massive SFGs, faint in the optical, named optically-faint galaxies (OFGs) can now be spatially resolved and studied in the rest-frame optical/near infrared. These OFGs represent a crucial population for unraveling the mechanisms driving the transition from vigorous star formation to quiescence, as they probably are the progenitors of the massive and passive galaxies already in place at cosmic noon.
We used the outstanding spatial resolution of the JWST images from the CEERS survey in the Extended Groth Strip (EGS) field combined with HST data to investigate the spatial distribution of $\Sigma_{\star}$, Σ_{SFR} , A_V^{ISM}, sSFR and mass-weighted age within a mass-complete sample of massive galaxies at z=3–4 while also emphasizing the peculiarity of OFGs relative to SFGs and quiescent galaxies (QGs) at these early redshifts.

This work reveals a primeval bimodality between extended blue SFGs and red, compact and strongly attenuated SFGs that have undergone a phase of major gas compaction. We show evidence that this primeval bimodality leads to the bimodality observed between blue SFGs and red QGs in the local Universe.

Aim

Study and compare the morphology of blue and red SFGs to the one of QGs in a mass-complete sample at 3<z<4.

A mass-complete sample in the CEERS field

We performed injection-recovery of 1000 Sérsic profiles in the CEERs field to derive the limiting magnitude of the survey. We then translated this into a mass-limit empirically using the the evolution of the mass-to-light ratio and its dispersion. Our sample is 90% complete for $\log(M_\star/M_\odot)$>9.6 and contains 190 galaxies.

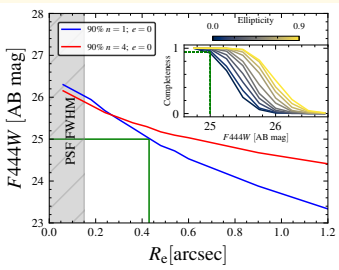

(a) Limiting magnitude determination

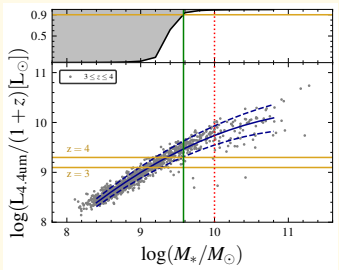

(b) Mass completeness determination

Fig 1. **(a)** Evolution of the limiting magnitude for extended objects with various Sérsic profiles. **(b)** Illustration of the method used to obtain the 90% mass-limit. The sample of low mass-to-light galaxies at high mass are the OFGs and is complete for $\log(M_\star/M_\odot)$>10.

Optically-Faint Galaxy population

To identify this massive and highly obscured population, we used the [1] color selection criteria. These galaxies were missed by the Lyman break selection and only the most massive of them were detected as H-dropout by the [2] criteria. This population is located in the Star-Forming Main Sequence.

There is a correlation between the dust attenuation and the stellar mass for both the obscured and unobscured SFGs. At a given mass, red SFGs (OFGs) are systematically more attenuated than blue SFGs while dust attenuation of QGs does not evolve with mass as it is the case for SFGs and OFGs. They contain similar dust attenuation as SFGs with $\log(M_\star/M_\odot) \sim 10.2$. This low A_V^{ISM} demonstrates that despite being compact and cuspy these galaxies have little gas and dust.

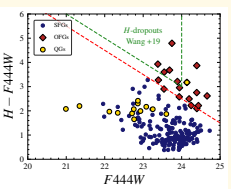

(a) Color selection

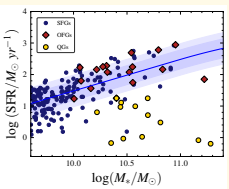

(b) Main Sequence relation

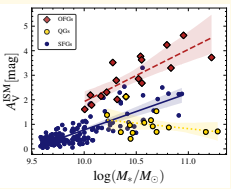

(c) Dust attenuation

Fig 2. **(a)** OFGs color selection criteria (red dotted line) from [1]. OFGs are shown as red squares. Blue and yellow circles are the UVJ selected blue SFGs and QGs. **(b)** Location of these three populations in the SFR- $M_\star$ plane. The [3] main sequence is displayed as a solid blue line with its 1σ scatter. **(c)** Dust attenuation as a function of stellar mass. The regression lines for each population are displayed as solid and dotted lines.

Resolved SED-fitting

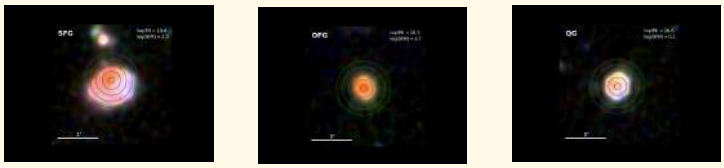

We binned each galaxy in five concentric annuli with a width = F444W FWHM and ran the SED code CIGALE on their respective UV-to-NIR photometry.

Bulge formation and compaction event

We renormalized the median radial profiles to the median stellar mass of the SFGs. For the radius, we used the mass-size relation from [4]. For Σ_{SFR} we rescaled to the main sequence from [3]. For A_V^{ISM} we used the relation traced by the SFGs in **Fig 2. (c)**.

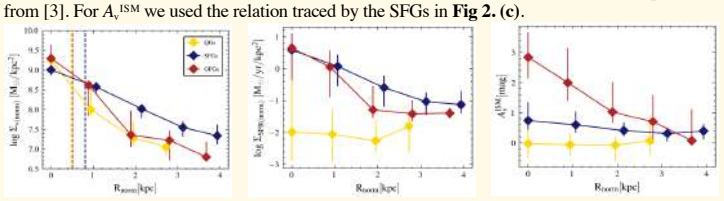

Fig 3. OFGs and QGs show similar stellar profiles and in terms of Σ_{SFR} OFGs are more concentrated than SFGs. The dust attenuation is particularly concentrated in OFGs, explaining their high attenuation compared to SFGs. These observations suggest a compaction event occurring *in-situ* within OFGs that is building the bulge of massive quiescent galaxies.

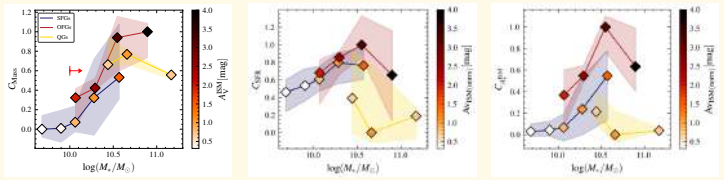

Fig 4. OFGs mass profiles are more concentrated than SFGs at all mass and become analog to the one of QGs for $\log(M_\star/M_\odot)$~10.5. The SFR concentration of OFGs and SFGs are alike up to this mass. The dust concentration in OFGs being significantly higher at a given mass than the one of SFGs, suggests a real bimodality between SFGs and OFGs that takes its seed in the compaction event that OFGs undergo.

Origin of the galaxy bimodality

For $\log(M_\star/M_\odot)$>10.5 the concentration of SFR and dust decays significantly. This suggests that above this mass, the bulge formation is over thanks to a major gas compaction event and that star formation happens majoritarily in the outer part of these OFGs. Therefore OFGs might start inside-out quenching in their future. We connect our finding with the galaxy evolution of (e.g [5], and [6]) which predict such a major compaction phase near this « critical mass ». Observations in the local Universe such as [7] have highlighted this mass as being the mass defining the bimodality between SFGs and QGs.

To conclude, we unveiled in this work the nature of the OFG population as the link between the morphological transition of SFGs into QGs.

References

◊ [1] Xiao et al. 2023b, Astronomy & Astrophysics, 672, A18 ◊ [2] Wang, T et al. 2019, Nature, 572, 211
◊ [3] Schreiber, C et al. 2015, Astronomy & Astrophysics, 575, A74 ◊ [4] Ward, E et al. 2024, The Astrophysical Journal, 962, 176
◊ [5] Behroozi, P. S., Wechsler, R. H., & Conroy, C. 2013, The Astrophysical Journal, 770, 57
◊ [6] Dekel, A., Lapiner, S., & Dubois, Y. 2019, Origin of the Golden Mass of Galaxies and Black Holes
◊ [7] Baldry, I. K., Glazebrook, K., Brinkmann, J., et al. 2004, The Astrophysical Journal, 600, 681

S02-12 | Doc | **THOREAU Romain** | CNES, Toulouse |
Encadrant CNES : Pierre LASSALLE

Jumeaux numériques pour la modélisation de la propagation des feux de forêts

Ce poster n'est pas dans le recueil pour des raisons de Copyright

Recueil des posters

Session 3

S03-01 | Doc | **BARBOSA FERREIRA Vitória** | CIRAD, Montpellier | Encadrant CNES : Mireille PAULIN | POSTER |
Biophysical and contextual modelling for forest plantations disturbances

S03-02 | Post-doc | **BOILEAU Guillaume** |UMR Lagrange, OCA, Nice | Encadrant CNES : Thierry BRET-DIBAT | POSTER |
Pipeline de construction des catalogues LISA

S03-03 | Doc | **BOULFANI Hani Raouf** | CEA/IRFU, Saclay | Encadrant CNES : Cédric VIRMONTOIS | POSTER |
Design d'un nouveau circuit de lecture pour un détecteur hybride à forte densité

S03-04 | Post-doc | **CUSICANQUI Diego** | CNES/ISTerre, Gieres | Encadrant CNES : Philippe MAISONGRANDE
Combinaison d'imagerie satellitaire SAR et optique pour la détection, la caractérisation et la surveillance des instabilités de versants en haute montagne

S03-05 | Doc | **EL HAOUARI Jihanne** | Laboratoire TéSA, Toulouse |Encadrant CNES : Christelle PITTET | POSTER |
Machine learning pour l'estimation de paramètres instrument basée sur des problèmes inverses

S03-06 | Doc | **FOISSEAU Antoine** | APC, Paris | Encadrant CNES : Philippe LAUDET | POSTER |
Study of accretion and ejection processes in variable black hole systems

S03-07 | Doc | **FRIESS Thibaud** | CEA / Airbus DS / ISAE, Grenoble | Encadrant CNES : Anne ROUVIE | POSTER |
Etude du comportement aux irradiations de détecteurs infra-rouges faible gap

S03-08 | Doc | **LOVERY Bertrand** | ISTerre, Gieres | Encadrant CNES : Félix PEROSANZ | POSTER |
Déformation Crustale Associée au Cycle Sismique dans les Andes Centrales à partir de Séries Temporelles Géodésiques InSAR et GNSS

S03-09 | Doc | **RICHARD Chloé** | INRAE – UNH, Saint-Gènes-Champanelle | Encadrant CNES : Guillemette GAUQUELINKOCH | POSTER |
Manipulation de la signalisation TGFβ/BMP pour lutter contre l'atrophie musculaire

S03-10 | Post-doc | **STCHERBININE Aurélien** | IRAP, Toulouse | Encadrant CNES : Francis ROCARD | POSTER |
Couplage Surface–Orbite en spectroscopie infrarouge pour la caractérisation des aérosols martiens et de l'hydratation de la surface

BIOPHYSICAL AND CONTEXTUAL MODELLING FOR FOREST PLANTATIONS DISTURBANCES

Vitória Barbosa Ferreira[1, 2], Guerric le Maire[1], Jean-Baptiste Féret[3]

[1]CIRAD, UMR Eco&Sols, Montpellier, France; [2]Université de Montpellier; [3]INRAE, UMR TETIS, Montpellier, France

Introduction

Forest ecosystems are increasingly vulnerable to climate-related disturbances. Optical remote sensing has long been used to detect anomalies like fire and pest outbreaks, often relying on spectral vegetation indices (SVI) (Gao et al., 2020). While these studies successfully identify anomalies through SVI thresholds, they often lack insight into changes in vegetation structure and biochemical components. Monitoring biophysical properties such as leaf area index (LAI), chlorophyll content (Cab), leaf mass per area (LMA) and leaf water content (EWT) is crucial for understanding plant-environment interactions. **This study aims to detect forest plantation disturbances by monitoring biophysical properties in Eucalyptus plantations using Sentinel-2 images.** The focus is on radiative transfer models (RTM) and inversion strategies to estimate biophysical properties (LAI, Cab, LMA and EWT) to assess anomalies such as fire risk. **This poster highlights the data processing and testing efforts related to using the PROSAIL model as a radiative transfer model (RTM).**

Keywords: Radiative transfer models, PROSAIL, Biophysical Variables retrieval, Forestry

Materials and Methods

Study area

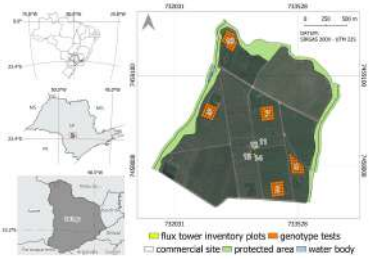

In-situ data

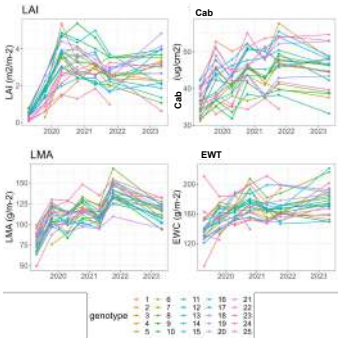

Model

PROSAIL

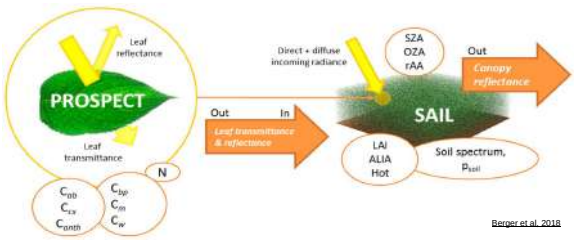

Berger et al. 2018

Cab : chlorophyll a + b
Ccx: Total carotenoid content
Canth: Total anthocyanin content
Cbp: Brown pigments
Cm: Dry matter content
Cw: Equivalent water thickness
N: Leaf structural parameter
LAI: Leaf area Index
ALIA: Average leaf inclination angle
Hot: Hot spot parameter
psoil: Soil spectrum
SZA: Sun zenith Angle
OZA: Viewing (observer) zenith angle
rAA: Relative zenith angle

Workflow

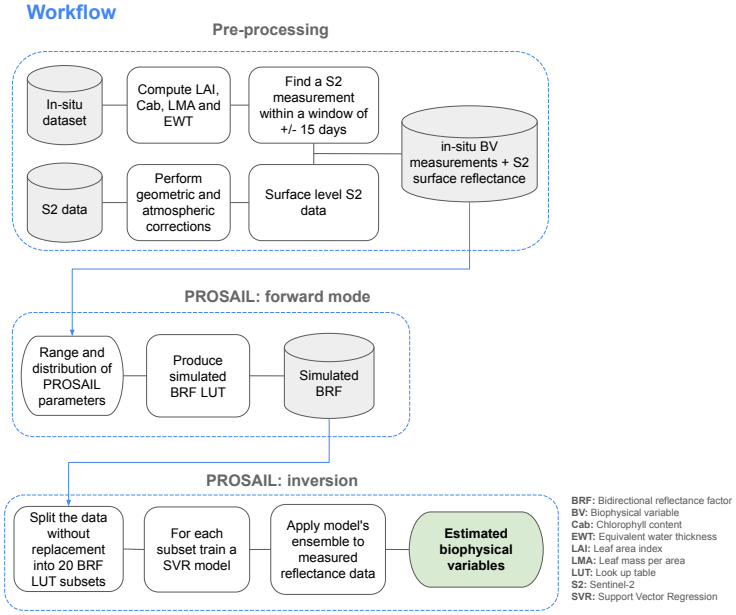

BRF: Bidirectional reflectance factor
BV: Biophysical variable
Cab: Chlorophyll content
EWT: Equivalent water thickness
LAI: Leaf area index
LMA: Leaf mass per area
LUT: Look up table
S2: Sentinel-2
SVR: Support Vector Regression

Results

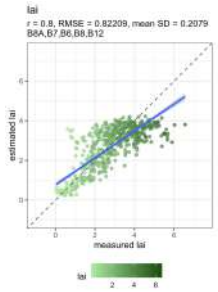

- LAI is the ratio between the total leaf area and the ground area.
- This variable is involved in various functions, such as canopy radiation balances (e.g. photosynthesis net primary production, etc.)
- **It is very well estimated by inverting PROSAIL with a RMSE of 0.82 m^2/m^2**

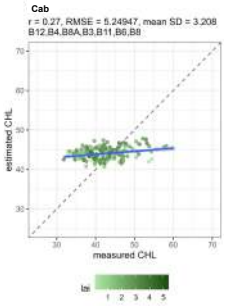

- Cab is the main leaf pigment responsible for light absorption in plants and is an indicator of plant photosynthetic capability.
- **It is very poorly estimated by inverting PROSAIL**
- The unsatisfactory results may be due to several reasons, such as model parametrization, correlation with other variables, high Cab variability within the canopy, among others.

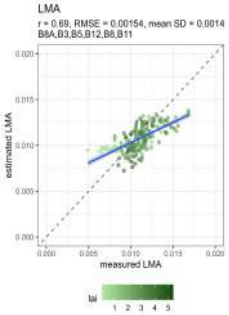

- LMA corresponds to the leaf dry mass per unit area. The LMA is key in many plant adaptation strategies.
- For instance, low LMA species typically have rapid metabolisms (high rates of photosynthesis and respiration per unit leaf dry mass)
- **It is well estimated by inverting PROSAIL with a RMSE of 0.0154 g/m^2**

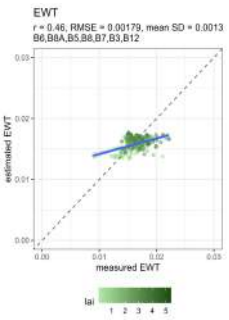

- EWT refers to a hypothetical water layer thickness spread across the leaf surface
- It is yet another crucial attribute for assessing plant physiology, ecosystem processes, hydraulic status, and leaf-level tolerance to dehydration.
- **It is modestly well estimated by inverting PROSAIL with a RMSE of 0.00179 g/m^2**

Take home messages

This study focused on estimating biophysical variables (BVs) such as LAI, chlorophyll content (Cab), LMA, and EWT by simulating spectral measurements using PROSAIL in forward mode. A machine learning algorithm was then applied to estimate these BVs from the simulated data. **Key findings highlight the critical importance of model parameterization, noise levels, background spectra selection, and spectral subdomain choice when using radiative transfer models (RTMs). Accurately estimating Cab, however, remains a challenging task that continues to be a subject of investigation.**

Acknowledgements

We acknodwledge CNES and CIRAD for funding Vitória Barbosa Ferreira. We are grateful for the long-term colaboration with IPEF, the IN-SYLVA network and the staff at the Itatinga Experimental Station.

References

Berger, K., Atzberger, C., Danner, M., D'Urso, G., Mauser, W., Vuolo, F., Hank, T., 2018. Evaluation of the PROSAIL Model Capabilities for Future Hyperspectral Model Environments: A Review Study. Remote Sens. 10, 85. https://doi.org/10.3390/rs10010085

Gao, Y., Skutsch, M., Paneque-Gálvez, J. and Ghilardi, A. "Remote sensing of forest degradation: a review," Environ. Res. Lett., vol. 15, no. 10, p. 103001, Sep. 2020, doi: 10.1088/1748-9326/abaad7.

Challenges in Producing Final Products and L3 Data for Galactic Binaries in the LISA Mission.

Guillaume Boileau, Astrid Lamberts, Martin Vannier, Christophe Ordenovic, Mathias Schultheis, Philippe Berio

guillaume.boileau@oca.eu Université Côte d'Azur, Observatoire de la Côte d'Azur, CNRS, Laboratoire Lagrange, 06304 Nice, France

1. Introduction

For the LISA mission, the creation of final products is a crucial step in the data processing process. Multiple global fit (L2) pipelines will identify and fit the same sources in different ways, and the goal is to merge these into a single comprehensive catalog. This involves comparing data from global fits, consolidating the data, and statistically validating it. Several global fit algorithms have distinct properties, resulting in varied submissions results to the LISA Data Challenge. The challenge lies in producing final products that encompass all observed sources while establishing connections between Global fits and providing all necessary informatin for scientific interpretation in an easily accessible way. Furthermore, algorithms capable of assessing the quality of adjustments and ensuring convergence have been developed as part of this study. To achieve this, we propose a preliminary protocol that outlines the essential steps needed to produce the final products. We have analyzed Sangria [1] data challenge for only Galactic binaries. Additionally, we propose an algorithm to merge L2 Global Fits [2, 3, 4, 5] and validate them against injected data.

2. Injection and Submissions

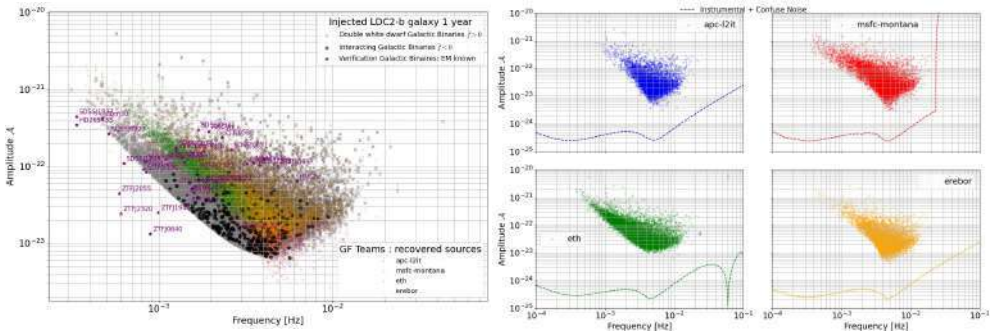

The inputs are from the LISA Data Challenge Sangria V2 [1], which includes both fully specified and blind datasets with simulated waveforms and Gaussian noise from millions of Galactic white dwarf binaries and merging massive black-hole binaries. The data also incorporates LISA noise produced using LISACode to generate "TDI-1.5" observables X, Y, Z. The submissions are the products of the global fit L2 [2, 3, 4, 5], estimating individual signals from the dataset and submitting a table with the parameters of each observed source and the posteriors for each of the sources.

3. Convergence check| L3 preprocessing

Mismatch between Global Fits and Posteriors

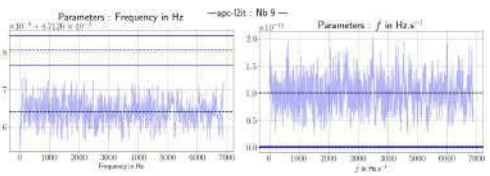

Distribution of Mismatches

Mismatches

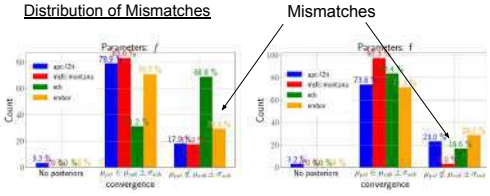

Before proceeding to the L3 pipeline, it is crucial to ensure the proper convergence of the global fits. To achieve this, we examine the consistency between the submitted L2 catalog and the posteriors. On the left, mismatches and overlap issues between Global Fits and posteriors are observed. The black and blue dotted lines shows respectively the trace mean and the quoted value of the parameter, and solid lines 5σ interval, which do not correspond to the trace of the GF. On the right, the distribution of the various Global Fits under study is depicted. A significant portion of L2 entries exhibit mismatches for at least one parameter.

4. Gaussianity Test

The Gaussian Mixture Model (GMM) is used to determine the number of Gaussian components for each chain from global fits to assess the convergence of each Global Fit. This test is crucial because we do not expect the data to be Gaussian. If many Gaussian components are found, it indicates a more uniform distribution, suggesting that the fit is poor and the model may not be suitable. GMM is a probabilistic model that represents data as a mixture of K Gaussian distributions, each with a mean vector $\boldsymbol{\mu}_k$, a covariance matrix $\boldsymbol{\Sigma}_k$, and a mixing coefficient π_k. The Probability Density Function (PDF) of a GMM is given by $p(\mathbf{x}) = \sum_{k=1}^{K} \pi_k \mathcal{N}(\mathbf{x}|\boldsymbol{\mu}_k, \boldsymbol{\Sigma}_k)$

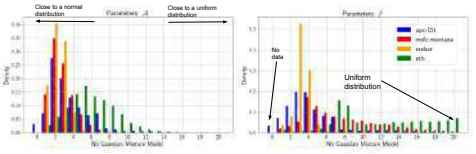

5. Proposal of fusion L3 Algorithm

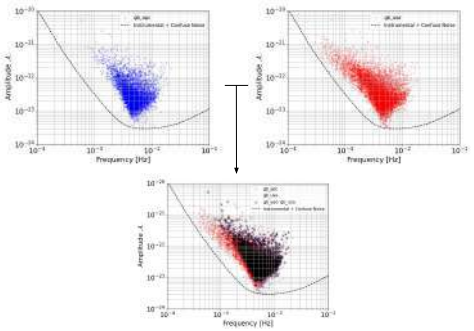

The Global Fits merging method integrates parameter information from two Global Fits, assessing overlap based on specified standard deviation levels. It aims to merge these Global Fits into a unified catalog, ensuring each candidate from one catalog overlaps optimally with candidates from the other. This overlap, which represents the correlation between waveforms, also serves to prioritize candidates when multiple entries coincide. This facilitates a streamlined selection process within overlapping regions.

6. Results : A first comparison for GB

Result of recovery between APC and USA / recovery between Injection:

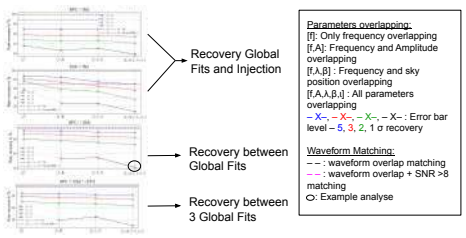

Example:

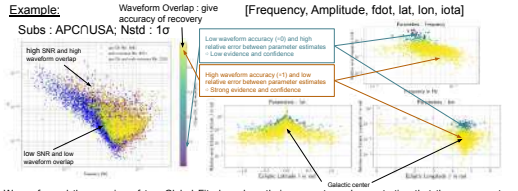

We performed the merging of two Global Fits based on their parameters, demonstrating that these parameters significantly impact the merging outcome. Additionally, the quality level (– X– Error bar level) also provides different levels of recovery, which have a significant impact. This level allows the construction of catalogs with an emphasis on either purity or completeness. This illustrates the current recovery capability enabled by this tool, allowing direct interaction with L2 to accurately assess the performance of various Global Fits.

Verification Galactic Binaries

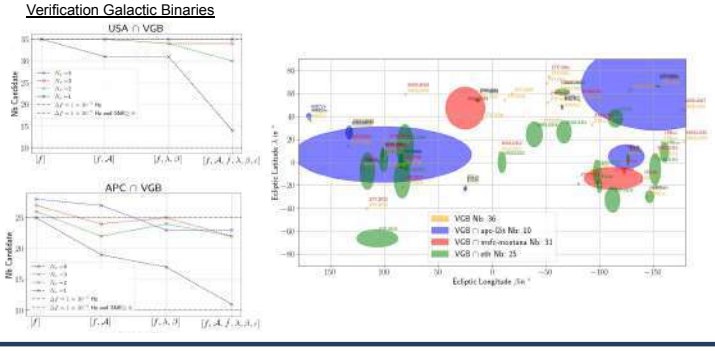

Steps for an Frist transition L2 /L3:

- Convergence criteria :
  - Check Mismatch posterior/Global Fits
  - Check Priors
- Statistical test of Gaussianity
  - Global Quality check of the convergence
  - Comparison of normality distributions.
- Overlap and relative error between Global Fits
  - Comprehensive view of the recovery.
  - Quality assessment criteria.

7. Conclusions/Next step

1. Continuous integration with new Global Fits
2. Fusion catalogue with quality user variation
   - Purity vs completeness.
   - Adaptability to different LISA sources.
3. Developp Visualization tools in collaboration
4. Implement other sources

8. References

[1] Stas Babak et al.. Lisa data challenge 2a: Sangria. Technical report, 2020.

[2] Stefan H. Strub et al.. *arXiv e-prints*, page arXiv:2403.15318, March 2024.

[3] Tyson B. Littenberg and Neil J. Cornish. *PRD*, 107(6):063004, March 2023.

[4] Michael L. Katz et al.. *arXiv e-prints*, page arXiv:2405.04690, May 2024.

[5] APC. In preparation. 2024.

GB thanks the Centre national d'études spatiales (CNES) for support for this research and the LISA Data Challenge (LDC) for providing input data and continuous feedback on this work.

Design of a new readout circuit for a highly dense hybrid detector

H. Boulfani[1], D. Baudin[1], O. Gevin[1], O. Limousin[2] , A. Meuris[2] ,M. Prieur[2], S.Beaumont [3], C.Virmontois[3] ,

[1]DEDIP, IRFU, CEA, Université Paris-Saclay, CEA Saclay, 91191 Gif-sur-Yvette, France; [2] DAP-AIM, IRFU, CEA, Université Paris-Saclay, CEA Saclay; [3]CNES, OptoElectronic Detection department.

CONTEXT

What do we want to understand ?

Fig 1: Sun in EUV view (solar flare focus)

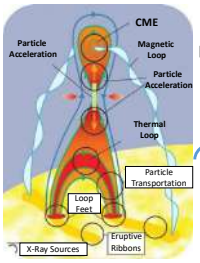

Fig 2: Schematic representation Of a solar eruptive event

What do we need:

- Localizing and measuring Energy of X-ray photons **0.5-100 keV** With:

High spectral resolution to study thermal and non-thermal emission mechanisms.

High spatial resolution to discriminate different X-ray generating events.

Sun and its Magnetic Field

How to measure ?

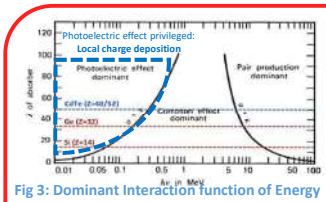

Fig 3: Dominant Interaction function of Energy and Atomic Number Z

Aimed spectral resolution: **500 eV @ 60 keV (FWHM)**

Low noise (< 20 el.rms)

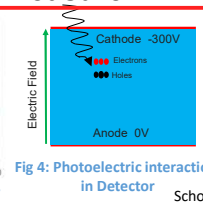

Fig 4: Photoelectric interaction in Detector

Low noise (< 20 el.rms)

Low leakage current (~1pA)

Low capacitance (~300 fF)

Schottky contact

Operating at – 20 °C

CdTe based Semiconductor Detector (1000 µm thick)

Detection Principle : Photoelectric Effect

Our Solution

CdTe pixel detector (64x64 pixels 250 µm pitch)

4 Full-Custom front-end Pixelated Readout ASIC

3D Packaging (full-custom ADC "OWB-1")

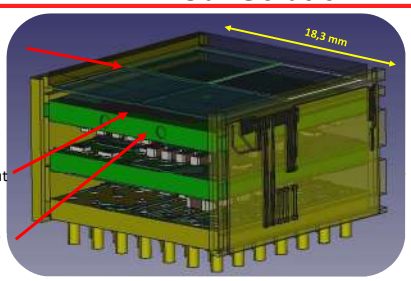

- **Maximum pixel size** : 250 μm x 250 μm
- **Energy Range** = 1 – 220 keV
- **1st fully digital single photon counting module**
- 32 channels full-custom ADC

Fig 5: Mini CdTe On-Chip (MC2 Module)

4 Sides Abutable, Compact, and fully digital Imaging Spectroscopy Module

My work

Fig 6: Simplified View of In-Pixel Analog Chain

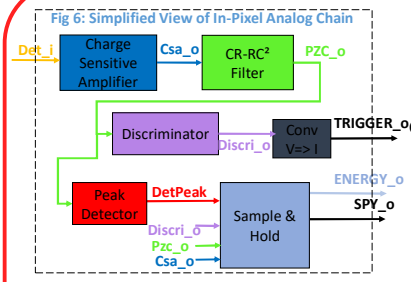

High Spectral Resolution Readout ASIC

High Spectral Resolution needs Low noise Analog Channel

Charge Sensitive Amplifier has the most important impact on the noise

Design a Proto-Chip to test and study different optimizations and architectures for CSA

Design prototype ASIC (Application Specific Integrated Circuit)

DESIGN

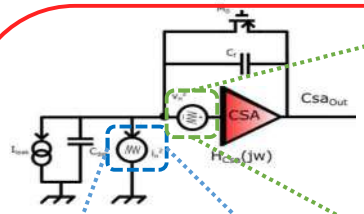

Fig 7:Charge Sensitive Amplifier Noise Model

contribution of input noise considered as a voltage noise

Mainly Determined by the **Voltage Amplifier's Input Transistor**

Thermal Noise (agitation of charge carriers)

Flicker Noise (MOS fabrication process)

contribution of input noise considered as a current

Mainly Determined by the **Detector** and the **Reset Transistor**

Shot Noise (discrete nature of electric current)

Parallel Thermal Noise (agitation of Reset MOS charge carriers)

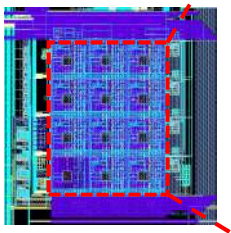

Fig 8: Close-up look on the ChipTest

$$ENC = \sqrt{ENC_{/}^2 + ENC_{/\!/}^2 + ENC_{1/f}^2}$$

Charge Sensitive Amplifier Noise Model

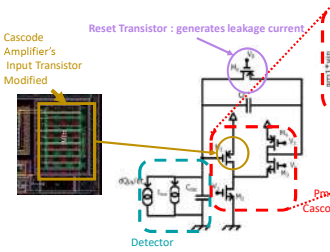

Fig 9: Pmos based Charge Sensitive Amplifier Circuit

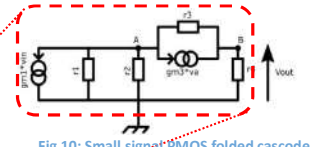

Fig 10: Small signal PMOS folded cascode

We need A_0 to be high: $A_0 * C_f >> C_{det}$

$$A_0 = \frac{gm_1 r_4}{1 + \frac{(r_3+r_4)}{r_3 r_2 (1+gm_3 r_3)}}$$

$$A_0 \simeq gm_1 r_4$$

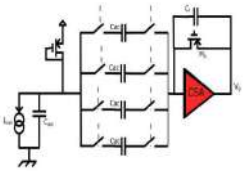

Fig 11: Classical AC-Coupled CSA (Cac ={0.1; 1 ;10; 30 pF}

Require High Value Capacitance to maintain Gain

Cac min =30 pF (inconceivable)

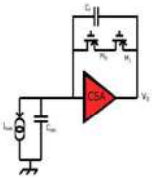

Fig 12: Multi-Transistor Reset DC-Coupled CSA

Dynamic Range Collapse with Two Reset Transistors

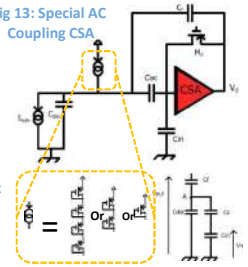

Fig 13: Special AC Coupling CSA

Mini Matrix of Pixels with Different Charge Sensitive Amplifier Architectures

RESULTS

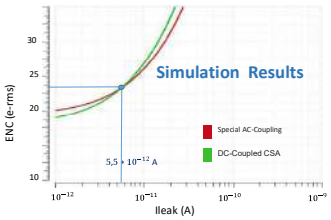

Fig 14: Equivalent Noise Charge Function Leakage Current

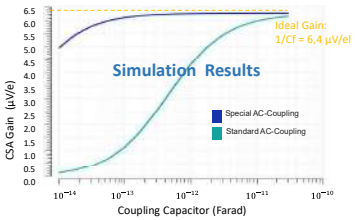

Fig 15: AC Classic VS AC Special Function Coupling Capacitor

PERSPECTIVES

Total Ionizing Dose (TID) on X-FAB Technology

- Gamma Rays : 100 Krad / 1Mrad
- "Cocase" component irradiation bench ^{60}Co. (CEA)

Fig 16: Dose effect on MOSFET (side view)

P-MOSFETs
1. Trapped holes: + Vth ↓
2. Interface traps: + Vth ↓ Leakage Current ↑

N-MOSFETs
1. Trapped holes: + Vth ↓
2. Interface traps: + Vth ↑ Leakage Current ↑

PhD Perspective:

- **Reception of ASIC**
- **Wire Bonding**
- **Characterization Of Pixels: Validation of Noise Calculation Models for the New architectures (<20 el.rms Expected).**
- **Choosing the most performing pixel for MC2**

MC2 Project:

- **Design of a full scale Readout ASIC (32x32 or 48x48 pixels) with the pixel architecture chosen from my work.**

S03-04 | Post-doc | **CUSICANQUI Diego** | CNES/ISTerre, Gieres | Encadrant CNES : Philippe MAISONGRANDE

Combinaison d'imagerie satellitaire SAR et optique pour la détection, la caractérisation et la surveillance des instabilités de versants en haute montagne

Absent

MACHINE LEARNING FOR INVERSE PROBLEM-BASED INSTRUMENT PARAMETER ESTIMATION

Jihanne El Haouari[1,2], Jean-Yves Tourneret[1,2], Herwig Wendt[2], Christelle Pittet[3], Jean-Michel Gaucel[4]

[1] Laboratoire TéSA, Toulouse France
[2] IRIT-ENSEEIHT, CNRS, Univ. Toulouse, France
[3] Centre National d'Etudes Spatiales, Centre spatial de Toulouse, France
[4] Thales Alenia Spaces Cannes, France

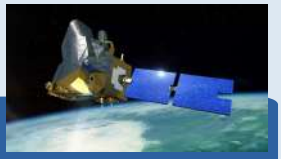

Introduction

Contexte

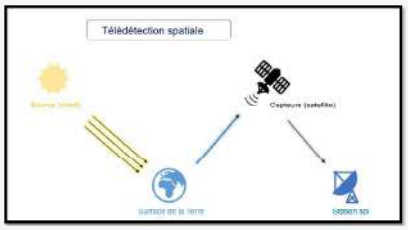

- Détermination de la concentration de différents gaz dans l'atmosphère
- Utilisation de spectromètres à haute résolution
- Besoin d'estimer le plus précisément possible les fonctions de réponses spectrales (ISRFs) du spectromètre et de corriger les mesures spectrales

1. Estimation des ISRFs en présence d'erreurs

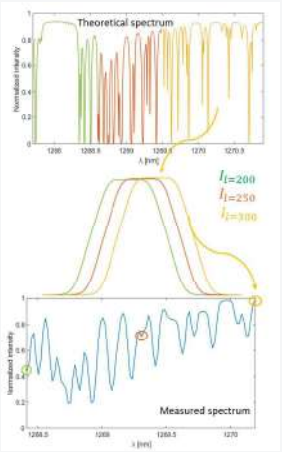

Modèle d'observation

Pour chaque longueur d'onde λ_l , l =1,…,N_λ

- 1 observation $x_{l,q} \in \mathbb{R}^+$, q=1,…, Q
- 1 ISRF $\boldsymbol{I}_l \in \mathbb{R}^{N+1}$
- 1 fonction non-linéaire décrivant les défauts radiométriques f_l (1)
- 1 fonction non-linéaire décrivant les décalages spectraux g_l (2)
- Modèle d'observation

(1) $x_{l,q}=f_l(s_{l,q})=\sum_{p=0}^{P} d_p{}^l\ [\boldsymbol{s}_{\text{th},l}{}^{(q)}\boldsymbol{I}_l]^p$, $\forall q$=1,…, Q

(2) $x_l=g_l(\boldsymbol{s}_{\text{th}})\boldsymbol{I}_l=\text{interp}(\boldsymbol{s}_{\text{th}}, \lambda_l+\sum_{p=0}^{P} d_p (l/l_{\max})^p)\ \boldsymbol{I}_l$

Hypothèses

- Les ISRFs varient peu sur une fenêtre W_l
- Nombre Q suffisamment élevé

2. Méthode d'estimation des ISRFs et des erreurs de mesure

Représentation parcimonieuse des ISRFs

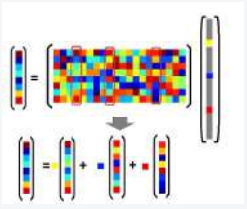

Représentation parcimonieuse des ISRFs

- Dictionnaire $\boldsymbol{\Phi} \in \mathbb{R}^{(N+1)\times N_D}$ (SVD)
- ISRF $\boldsymbol{I}_l \approx \boldsymbol{I}_l{}^K = \boldsymbol{\Phi}\,\boldsymbol{\alpha}_l$, avec K coefficients non nuls
- $\boldsymbol{s}_l{}^{(q)} \approx \boldsymbol{s}_{\text{th},l}{}^{(q)}\,\boldsymbol{I}_l = \boldsymbol{\Psi}_l{}^{(q)}\,\boldsymbol{\alpha}_l$

Résolution du problème inverse linéaire (SPIRIT)

$\arg\min_{\boldsymbol{\alpha}_l} L(\boldsymbol{\alpha}_l, \mu) = \arg\min_{\boldsymbol{\alpha}_l} ||\boldsymbol{s}_l - \boldsymbol{\Psi}_l\,\boldsymbol{\alpha}_l||_2^2 + \mu\,||\boldsymbol{\alpha}_l||_0$

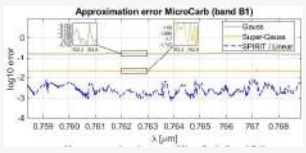

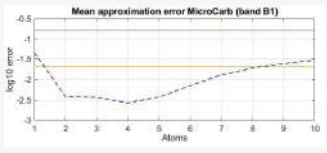

Estimation conjointe des ISRFs et des erreurs de mesure (SPIRITUAL)

3. Résultats obtenus

Données utilisées et protocole expérimental

Données simulées par le CNES pour la mission MicroCarb

- Spectres théoriques obtenus en utilisant le logiciel de transfert radiatif 4A/OP
- Spectres mesurés générés par convolution
- Modèle polynomial de degré P=3 pour les erreurs

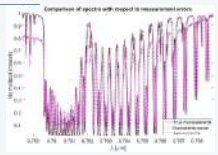

Critère de performance

- Erreur de reconstruction du spectre mesuré
- Erreur absolue normalisée pour l'approximation des ISRFs $E_l = \frac{\sum_{n=1}^{N+1} |\boldsymbol{I}_l[n] - \boldsymbol{I}_l[n]|}{\sum_{n=1}^{N+1} \boldsymbol{I}_l[n]}$

Résultats en présence d'erreurs radiométriques

Reconstruction du spectre mesuré pour différents degrés polynomiaux (haut), résidus associés (milieu) et erreurs d'approximation des ISRFs (N_D=25, K=4 atomes)

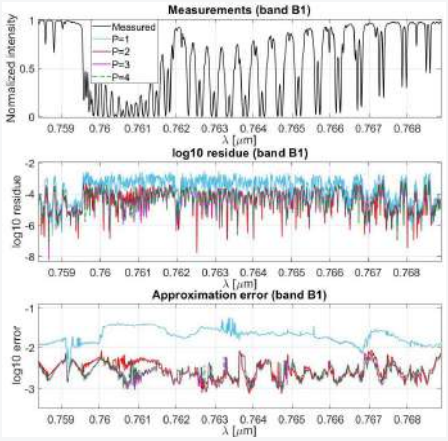

Erreurs d'approximation des ISRFs avec un degré fixé à P=3 (N_D=25)

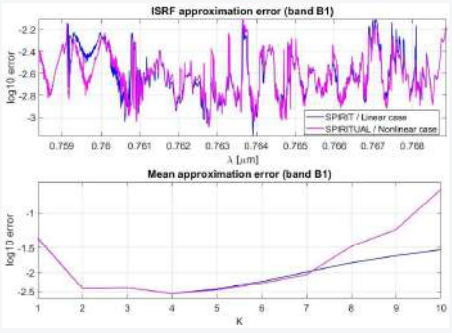

Résultats en présence de décalages spectraux

Erreurs d'approximation des ISRFs avec un degré fixé à P=3 et estimation du décalage spectral

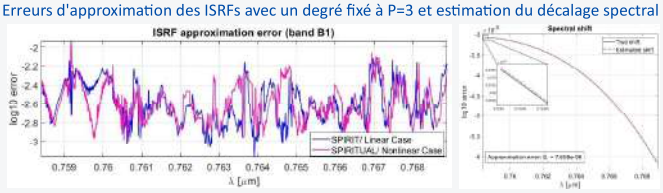

Conclusion & Perspectives

Conclusion

- Représentation parcimonieuse des ISRFs dans un dictionnaire
- Estimation conjointe des ISRFs et des erreurs de mesure (radiométriques ou de décalages spectraux)
- Bonne performance des méthodes proposées

Perspectives

- Estimation des ISRFs en présence d' erreurs radiométriques et spectrales
- Utilisation du machine learning pour estimer les ISRFs

Contact : Jihanne El Haouari - *jihanne.elhaouari@tesa.prd.fr*

Unveiling the hard X-ray emission of NGC 1068, a possible high energy neutrino source

A. Foisseau[1], A. Coleiro[1], F. Cangemi[1], A. Goldwurm[2], C. Lachaud[1]

[1] : Université Paris Cité, CNRS, Astroparticule et Cosmologie, F-75013 Paris, France

[2] : Université Paris Cité, CNRS, CEA, Astroparticule et Cosmologie, F-75013 Paris, France

I – INTRODUCTION / CONTEXT :

What is an AGN ?

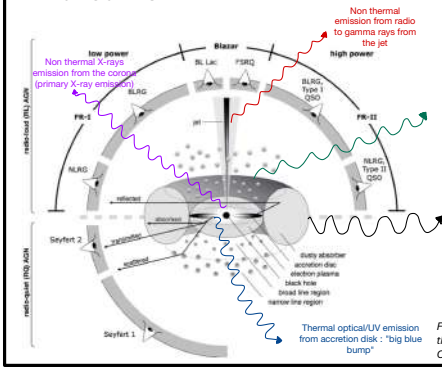

Figure 1 : Schematic view of the unified model of AGNs. Crédit : Beckmann et al. 2012

AGNs as probable emitters of high energy neutrinos?

The study of Active Galactic Nucleus (AGNs) allows us to better understand the accretion and ejection processes and address the question of the origin of high-energy cosmic rays (HECRs). While **HECRs**, being charged particles, **are deflected by magnetic fields, high-energy neutrinos produced by hadronic interactions near black holes, travel unaffected by such fields.** Unlike gamma-ray photons, these **neutrinos** are also **not absorbed by $\gamma\gamma$ interactions**, making them unique probes for investigating HECR sources. In this context, the IceCube neutrino observatory has identified **the Seyfert 2 galaxy NGC 1068 as one of the most promising candidates** with a significant neutrino excess of **4.2σ** over 10 years of observations [1]. Located at 14.4 Mpc, NGC 1068 is currently the strongest known neutrino source in the northern hemisphere.

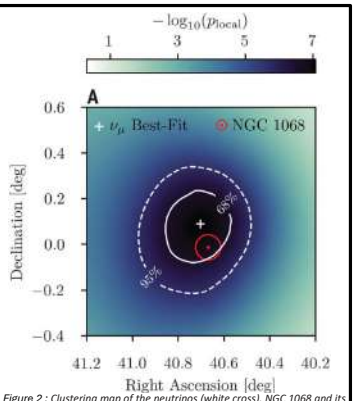

Figure 2 : Clustering map of the neutrinos (white cross). NGC 1068 and its angular size are highlighted with red dot and circle (optical wavelength). Crédit : [1]

X-rays as a key to understand the emission of AGNs

Astrophysical neutrinos are mainly produced through hadronuclear and photohadronic interactions, which also generate same amount of γ-rays. However, observations of NGC 1068 show that its GeV-TeV γ-ray flux is over ten times weaker than its neutrino flux, suggesting the neutrino production region is highly opaque to GeV-TeV photons. This points to a compact emission region, possibly involving the AGN's disk and corona. Emissions in the X-ray to soft gamma-ray range (~50 keV to ~100 MeV) are key to probing hadronic contributions in NGC 1068. Several studies (e.g. [7, 8]) have proposed that AGNs may appear faint in γ-rays due to gamma-ray interactions, producing secondary particle cascades that re-emit in the keV-MeV range. This signal is expected to be significantly stronger than the usual leptonic coronal emission, which cuts off between 100 and 400 keV. Therefore, detailed X-ray observations are crucial to refining AGN emission models and exploring leptonic and hadronic components. **In this study, we analyze the most up-to-date datasets of NGC 1068 from XMM-Newton, NuSTAR, Swift-BAT, INTEGRAL-IBIS, and INTEGRAL-SPI to search for the hard X-ray signature of a hadronic component.**

MODEL AND RESULTS :

Model :

The hard X-ray flux includes Compton reflection, which can dominate in heavily obscured sources like NGC 1068. This leads to uncertainty in estimating the primary intrinsic luminosity from the black hole environment, potentially linked to hadronic emission. To accurately model the various emission components, we use the approach outlined in [2, 3, and 4]. It consists of a **double reflection emission scenario combined with an additional primary emission originating from the corona**. The **primary X-ray radiation from the corona passes through the dusty torus, resulting in significant absorption in the soft X-ray range (see figure 3)**. We also account for the reflection on the far-side of the dusty torus and for the emission of the host galaxy.

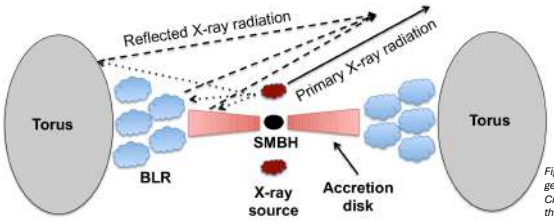

Figure 3: Scheme of the geometry of the model. Crédit : Ricci 2011, PhD thesis

Results :

We fit the model described above to our data following the methodology outlined in [4]. The intrinsic emission of the corona is described by an absorbed cutoff power law leading to : $\Gamma = 2.08^{+0.02}_{-0.03}$, $N_H = 3.67^{+0.36}_{-0.34}\times10^{24}\mathrm{cm}^{-2}$, $E_c = 118.6^{+19.9}_{-15.8}$ keV, and $K = 5.77^{+3.03}_{-1.93}\times10^{-2}$ ph/cm²/s/keV at 1 keV with a $\chi^2_{reduced} = 1.55$. All the parameters are consistent with previous works of [2] and [4] except the normalization which is found weaker than in the previous studies. Computing the intrinsic X-ray luminosity in the range 15-55 keV, we find $L_{X,prim} = 2.25^{+1.75}_{-0.9}\times10^{42}$erg/s which is smaller than the values found in [2] and [3]. While the exact value of $L_{X,prim}$ depends on the complex structure of the reflection components, this result is still **fully compatible with a leptonic scenario** as origin of the observed X-ray emission. Finally, we find that the **primary X-ray emission starts to dominate above a few hundred keV, showing the importance of having data in the range [100 keV - 1 MeV] to constrain further the presence of a hadronic component.**

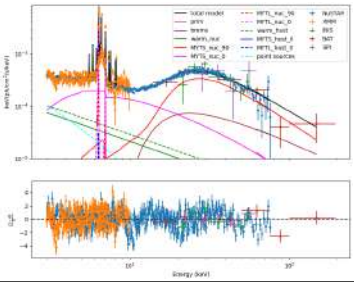

Figure 4 : Spectral energy distribution (SED). Here "MYTS-L" components stands for the reflections at different angles. The term "host" refers to the emission of the host galaxy whereas "nuc" is for the emission of the nucleus. The primary X-ray emission of the corona is represented by "prim" in the legend.

CONCLUSIONS AND DISCUSSIONS :

We present the **most recent spectral fit of NGC 1068 from 3 to 195 keV.** Our results remain **consistent with a leptonic scenario**, indicating a cutoff energy of the primary emission at $E_c = 118.6^{+19.9}_{-15.8}$ keV, compatible with inverse Compton scattering of soft photons. Still, our analysis also confirms that the [15-55] keV luminosity $\boldsymbol{L_{X,prim} = 2.25^{+1.75}_{-0.9}\times10^{42}}$**erg/s is compatible with the neutrino luminosity** $\boldsymbol{L_\nu = (2.9 \pm 1.1)\times10^{42}}$ **erg/s [1].** This result may also be consistent with neutrino production in γ-obscure regions as suggested e.g., by [5, 6] who predict a **correlation between hard X-ray and neutrino luminosities.** The lack of a definitive conclusion highlights the need for MeV-range data, where the primary X-ray emission from the vicinity of the black hole becomes dominant, to conclusively distinguish between hadronic and leptonic processes in the future.

REFERENCES:

[1]: IceCube Collaboration, Abbasi, R., Ackermann, M., et al. 2022, Science, 378, 538. doi:10.1126/science.abg3395

[2]: Bauer, F. E., Arévalo, P., Walton, D. J., et al. 2015, ApJ, 812, 116. doi:10.1088/0004-637X/812/2/116

[3]: Marinucci, A., Bianchi, S., Matt, G., et al. 2016, MNRAS, 456, L94. doi:10.1093/mnrasl/slv178

[4]: Zaino, A., Bianchi, S., Marinucci, A., et al. 2020, MNRAS, 492, 3872. doi:10.1093/mnras/staa107

[5]: Kun, E., Bartos, I., Becker Tjus, J., et al. 2024, arXiv:2404.06867. doi:10.48550/arXiv.2404.06867

[6]: Neronov, A., Savchenko, D., & Semikoz, D. V. 2023, arXiv:2306.09018. doi:10.48550/arXiv.2306.09018

[7]: Kohta Murase, Shigeo S. Kimura, et al. jun 2020, Physical Review Letters, 125, 011101

[8]: Björn Eichmann, Foteini Oikonomou, et al. nov 2022, The Astrophysical Journal, 939, 43

[9]: Yoshiyuki Inoue *et al* 2020 *ApJL* **891** L33

Étude du comportement aux irradiations de détecteurs infra-rouges faible gap

T. FRIESS[1,2,3,4], V. GOIFFON[3], O. GRAVRAND[2], A. ROUVIE[1], S. RIZZOLO[4], A. LE ROCH[3], E. DE BORNIOL[2]

[1]Centre National d'Etudes Spatiales (CNES), Toulouse, France. [2]CEA Leti, Grenoble, France.
[3]ISAE-SUPAERO, Toulouse, France. [4]AIRBUS Defence and Space, Toulouse, France.

Contexte

Les capteurs d'images sont de plus en plus présents dans nos vies (appareils photos, cameras, etc.) et représentent un enjeu **scientifique** et **stratégique** majeur. Les capteurs d'images numériques transforment **l'information lumineuse (photon) en signal électrique** en utilisant l'effet photo-électrique. Un photon interagit avec un semi-conducteur, générant une paire électron-trou collectée sous forme de courant. Cependant, des charges peuvent parfois être générées sans photon, créant du faux signal encore appelé "**courant d'obscurité**". Comprendre et limiter ce courant, qui varie selon les capteurs, est un défi central et constitue l'objectif de ce travail de thèse.

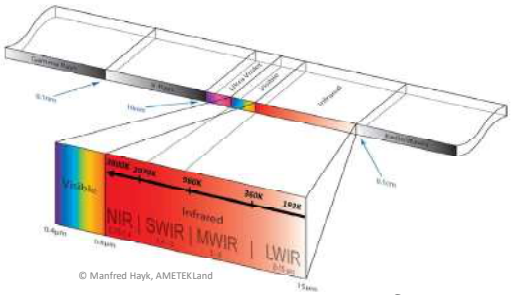

© Manfred Hayk, AMETEKLand

Pourquoi observer dans les infra-rouges?

- Permet d'observer les **émissions de chaleur**
- Essentiel pour les missions de météorologie, thermographie et astronomie

Le matériau privilégié aujourd'hui pour l'observation des IRs est le **tellure de mercure cadmium (HgCdTe)** car en faisant varier la proportion de mercure de l'alliage, il est possible d'adapter son gap pour observer l'ensemble du spectre IR.

Les effets de l'environnement spatial

- Dégradations des performances des capteurs d'images induite par les rayonnements spatiaux (**solaire ou cosmique**) [1]
- Les particules (**protons, gamma, rayon X**, etc.) provoquent 2 phénomènes principaux:

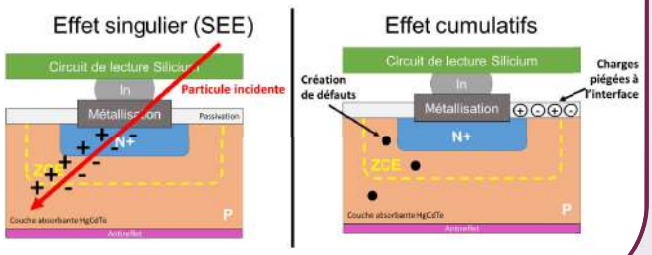

Exemple d'expérimentation d'irradiations

Objectifs: caractériser les dégradations de performances provoquées par des **irradiations de protons** sur un capteur infra-rouge bas flux à vocation astronomique (opérant dans le **SWIR**).

Etapes d'une campagne d'irradiation

1. Mesures préliminaires du capteur non dégradé
2. Déplacement et mise en place du banc au lieu d'irradiation
3. Irradiations et mesures du capteur dégradé
4. Analyse des résultats et interprétation physique

Périodes durant lesquelles le capteur est maintenu à température cryogénique (-193°C) pour limiter le courant d'obscurité thermique

Résultats

- **Augmentation** du courant d'obscurité après irradiations

→ **dommages de déplacement** causés par l'impact des protons.

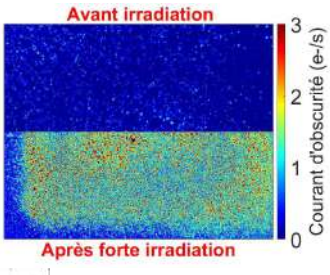

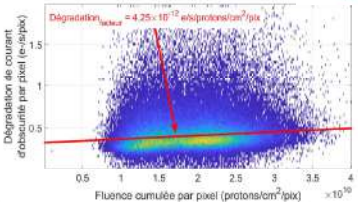

Estimation d'un facteur de **dégradation du courant d'obscurité** suite aux irradiations de protons dans la technologie.

Perspectives

- Reproduire les expérimentations dans d'autres technologies HgCdTe et à d'autres longueurs d'ondes
- Comparer les résultats pour étudier et comparer la physique de dégradation
- Déterminer un facteur de dégradation universel dans l'infrarouge à la manière du Silicium [2].

Références

[1] G. Hopkinson. "Radiation effects on solid state imaging devices". In : Radiation Physics and Chemistry 43.1-2 (1994), p. 79-91 (cf. p. 30, 39, 123).
[2] J. R. Srour and D. H. Lo, "Universal damage factor for radiation-induced dark current in silicon devices," *IEEE Transactions on Nuclear Science*, vol. 47, no. 6, pp. 2451–2459, Dec. 2000, doi: 10.1109/23.903792.

Crustal Deformation Associated with the Seismic Cycle in the Central Andes from InSAR and GNSS Geodetic Time Series

Bertrand Lovery[1], Anne Socquet[1], Mohamed Chlieh[1], Marie-Pierre Doin[1], Mathilde Radiguet[1], Juan Carlos Villegas-Lanza[2], Juliette Cresseaux[1], Edmundo Norabuena[2], Philippe Durand[3]

[1]ISTerre, Université Grenoble Alpes, CNRS, IRD, Grenoble, France
[2]Instituto Geofísico del Perú (IGP), Lima, Peru
[3]CNES, Toulouse, France

corresponding author: bertrand.lovery@univ-grenoble-alpes.fr

Interseismic Coupling and Megathrust Earthquake Potential on the South Peru subduction

The Central Andes subduction has been the theatre of **several large earthquakes** since the beginning of the 21th century:
→ 2001 Mw8.4 Arequipa, 2007 Mw8.0 Pisco, 2014 Mw8.1 Iquique earthquakes

In Lovery et al. (2024) we analyzed **73 GNSS points covering the last decade** to extract the interseismic velocity field. This field has been inverted to model the interseismic coupling distribution at the scale of South Peru in an elastic half-space. Then, by performing a moment budget analysis (Avouac, 2015), we are able to estimate the **potential maximum magnitude earthquake** in the area, with the associated recurrence time.

The **interseismic coupling** (or locking) quantifies how locked the plate interface is. **Interseismic coupling** is defined between **0** (plates are **slipping** without any friction) and **1** (plates are fully **locked**)

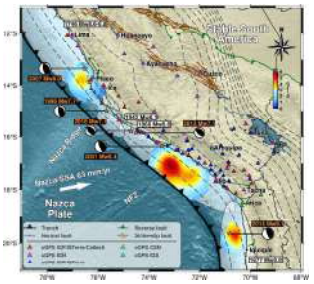

Seismotectonic background of the Central Andes subduction zone. The slip models for the M_w8.0 2007 Pisco (Chlieh et al., 2011), M_w8.4 2001 Arequipa (Lovery et al., 2024), and M_w8.1 2014 Iquique (Lovery et al., 2024) earthquakes are displayed in colors along the subduction interface. Triangles show the location of GNSS stations.

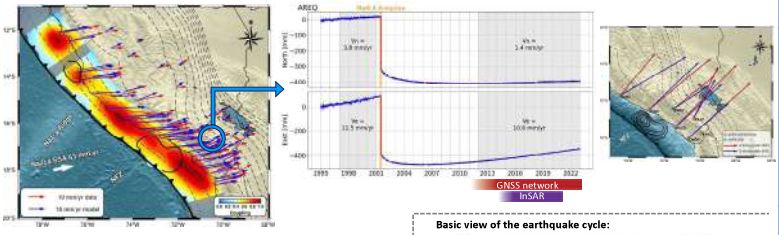

→ During the observation period in this study (2012-2023 for most stations), the observed interseismic velocity at AREQ is reduced by about 15% relative to its value before 2001

→ **What is the impact of postseismic relaxation on interseismic loading?**

→ **Can we extend the spatial coverage of measurements with InSAR?**

Basic view of the earthquake cycle:

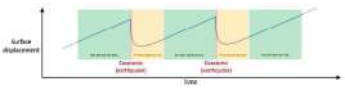

→ **Postseismic** can be caused by:
- aseismic slip on the fault (afterslip) → medium-term
- viscoelastic relaxation in the asthenosphere → long-term
- poroelastic rebound → short-term

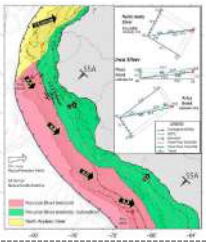

Figure from Villegas et al. (2016) defining the so-called Peruvian Sliver. The rigid block motion has been defined from the residuals of the inversion in the Stable South America frame.

Evidence for a Peruvian Sliver?

We inverted the interseismic velocities corrected from the rigid block motion defined by Villegas et al. (2016), the so-called **Peruvian Sliver (PS)**. The results tend to accredit the Peruvian Sliver hypothesis, with a lowered misfit and a more sensible locking depth.

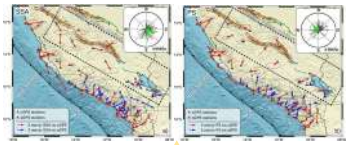

Residuals from our inversions using GNSS data in the SSA frame (a) and in the PS frame (b). Residuals at inland stations, within the black dashed rectangle, are highlighted in green on the roses.

Moment budget analysis and earthquake potential:

We performed a **moment budget** at the scale of the **South Peru segment**, from the Nazca Ridge to the Arica bend. This methodology, described in Avouac (2015), balance the seismicity rate with the moment deficit rate on the megathrust interface to estimate the earthquake potential in the area. 864 combinations of these parameters have been computed, following the logic tree on the right. The b-value of instrumental catalogues as well as the amount of aseismic slip in the transient slips (alpha) are the two parameters that show the largest variability in the determination of the Mmax.

→ **Overall, we found a median value of Mw=8.55, a 15th percentile at Mw=8.15, and a 85th percentile at Mw=9.0**. Considering the largest earthquake recorded on the South Peru segment was the 2001 Mw=8.4 Arequipa earthquake, we can state that the earthquake potential on this segment is at least Mw=8.4. The recurrence time for a Mw=8.4 would be ~100 years, while it would be ~1,000 years for a Mw=9.0.

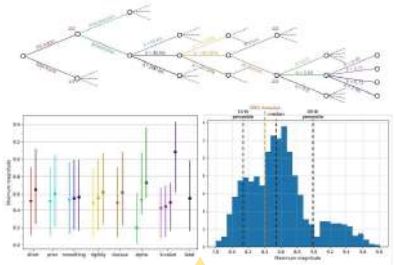

Top: Logic tree used for exploration of uncertainties.
Bottom left: Earthquake potential in function of the parameters. The dots represent the median Mw value, while the vertical bars represent the variability between the 15th and 85th percentiles on the 864 models considered.
Bottom right: Distribution of the earthquake potential, accounting for all the discussed factors of uncertainty. Median, 15th and 85th percentiles are depicted by dashed lines.

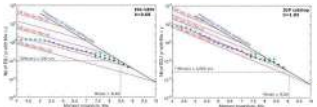

Estimation of maximum expected magnitude with α = 0.7 and μ = 40 GPa, in the PS frame and with a smoothing λ = 30 km, for the ISC-GEM catalog (left) and the IGP catalog (right). Instrumental earthquakes from the catalogs are depicted by cyan dots, historical earthquakes from Villegas et al. (2016) by green dots.

Conclusions

→ 2001 M_w8.4 Arequipa earthquake postseismic relaxation is still ongoing

→ Accounting for the viscoelastic relaxation following the 2001 Arequipa earthquake increases the moment deficit by 6%, but remains within uncertainties with M_{max} ranging from M_w=8.4 to M_w=9.0 (Lovery et al., 2024)

→ The Nazca Ridge can be assumed as a strong barrier, however the Nazca Fracture Zone can only be seen as a weak barrier

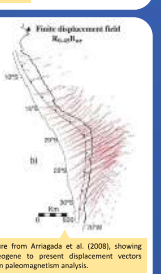

Figure from Arriagada et al. (2008), showing Paleogene to present displacement vectors from paleomagnetism analysis.

Next challenges

→ Inversion of interseismic velocities with viscoelastic Green functions
  → We expect a viscoelastic model to produce a broader displacement, with horizontal displacements extending further inland. Uplift and subsidence amplitudes are also expected to increase with a viscoelastic rheology.
  → Viscoelastic models should also predict higher magnitudes of deformation in the late stage of the interseismic period, especially in the near-field and in the far-field.
  → Finally, a shallower optimal locking depth for visco-elastic models is expected.

→ Combine GNSS and InSAR in a joint inversion of interseismic at the scale of the central Andes

→ Discriminate slip on the slab interface from internal deformation, benchmarking the solid sliver motion hypothesis

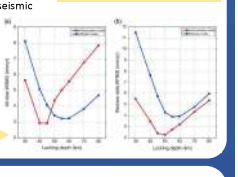

Figure from Li et al. (2015) . Comparison between elastic and viscoelastic models, for horizontal displacement (a) and vertical displacement (b).

References:

Arriagada, C., Roperch, P., Mpodozis, C., & Cobbold, P. R. (2008). Paleogene building of the Bolivian Orocline: Tectonic restoration of the central Andes in 2-D map view. *Tectonics, 27*(6). https://doi.org/10.1029/2008TC002269

Avouac, J.-P. (2015). From Geodetic Imaging of Seismic and Aseismic Fault Slip to Dynamic Modeling of the Seismic Cycle. *Annual Review of Earth and Planetary Sciences, 43*(1), 233–271. https://doi.org/10.1146/annurev-earth-060614-105302

Doin, M.-P., Guillaso, S., Jolivet, R., Lasserre, C., Lodge, F., Ducret, G., & Grandin, R. (2011). Presentation of the small baseline NSBAS processing chain on a case example: The Etna deformation monitoring from 2003 to 2010 using Envisat data. In *Proceedings of the Fringe symposium* (pp. 3430–3437). ESA SP-697, Frascati, Italy.

Lovery, B., Chlieh, M., Norabuena, E., Villegas-Lanza, J. C., Radiguet, M., Cotte, N., et al. (2024). Heterogeneous locking and earthquake potential on the South Peru megathrust from dense GNSS network. *Journal of Geophysical Research: Solid Earth, 129*, e2023JB027114. https://doi.org/10.1029/2023JB027114

Luo, H., & Wang, K. (2021). Postseismic geodetic signature of cold forearc mantle in subduction zones. *Nature Geoscience, 14*(2), 104–109. https://doi.org/10.1038/s41561-020-00679-5

Marill, L., Marsan, D., Socquet, A., Radiguet, M., Cotte, N., & Rousset, B. (2021). Fourteen-Year Acceleration Along the Japan Trench. *Journal of Geophysical Research: Solid Earth, 126*(11), e2020JB021226. https://doi.org/10.1029/2020JB021226

Radiguet, M., Cotton, F., Vergnolle, M., Campillo, M., Valette, B., Kostoglodov, V., & Cotte, N. (2011). Spatial and temporal evolution of a long term slow slip event: the 2006 Guerrero Slow Slip Event. *Geophysical Journal International, 184*(2), 816–828. https://doi.org/10.1111/j.1365-246X.2010.04866.x

Thollard, F., Clesse, D., Doin, M.-P., Donadieu, J., Durand, P., Grandin, R., et al. (2021). FLATSIM: The ForM@Ter Large-Scale Multi-Temporal Sentinel-1 InterferoMetry Service. *Remote Sensing, 13*(18), 3774. https://doi.org/10.3390/rs13183774

Villegas-Lanza, J. C., Chlieh, M., Cavalié, O., Tavera, H., Baby, P., Chire-Chira, J., & Nocquet, J.-M. (2016). Active tectonics of Peru: Heterogeneous interseismic coupling along the Nazca megathrust, rigid motion of the Peruvian Sliver, and Subandean shortening accommodation. *Journal of Geophysical Research: Solid Earth, 121*(10), 7371–7394. https://doi.org/10.1002/2016JB013080

Wang, K., Hu, Y., & He, J. (2012). Deformation cycles of subduction earthquakes in a viscoelastic Earth. *Nature, 484*(7394), 327–332. https://doi.org/10.1038/nature11032

Acknowledgements:

Bertrand Lovery's PhD is funded by the French national space agency CNES and the DEEPtrigger ERC project (PI: Anne Socquet).

Postseismic viscoelastic FEM model

In order to assess the local rheology, we carried out a case study on the **2001 Mw8.4 Arequipa earthquake** using a **postseismic viscoelastic FEM model** of the subduction. Our model is constrained by the timeseries of the AREQ continuous GNSS station, operating since 1993 in Arequipa.

→ 3-D FEM model solved using PyLith, meshing performed with Coreform CUBIT
→ Slab contours from Slab2 (Hayes, 2018), Bathymetry & topography from SRTM15+

→ "Cold-nose" up to 85-km depth
→ Bi-viscous **Burger** rheology in the asthenosphere

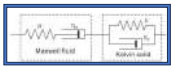

Burger body

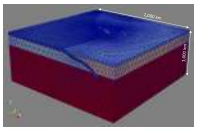

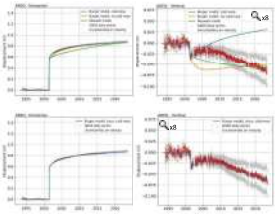

→ The blue model fits the horizontal but not the long-term vertical

→ Fitting the vertical requires a low-viscosity zone in the cold-nose

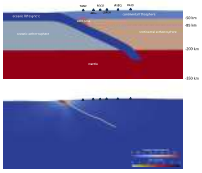

→ We compute the velocities associated with the viscoelastic relaxation during the observation period of the GNSS network used for interseismic coupling modelling (~2012-2024), at each GNSS sites

Body	Rheology	Depth (km)	Shear modulus (GPa)	Maxwell viscosity (Pa.s)	Kelvin viscosity (Pa.s)
Lithosphere	Elastic	0 - 40	59	-	-
Cold nose	Maxwell	40 - 85	70	1.10^{20}	-
Upper asthenosphere	Burger	40 - 200	70	1.10^{19}	5.10^{18}
Lower asthenosphere	Maxwell	200 – 1,000	105 - 294	5.10^{20}	-

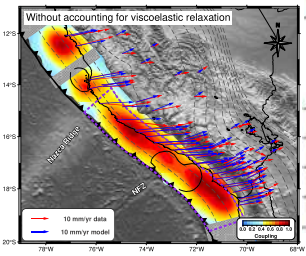

Viscoelastic correction

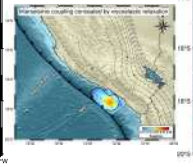

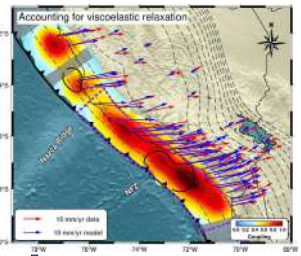

Higher coupling in the Southern segment, no more creeping where the NFZ is subducting

Moment deficit on the Nazca-Arica segment:

$\frac{dM_0}{dt} = 2.24 \times 10^{20}$ Nm/yr, without accounting for relaxation
→ M_{max} ~ **8.70**

$\frac{dM_0}{dt} = 2.37 \times 10^{20}$ Nm/yr, accounting for relaxation (+6%)
→ M_{max} ~ **8.73**

Large-scale InSAR coverage - FLATSIM Andes project

Mean velocity map in LOS

→ Sentinel-1 C-band **InSAR timeseries**: 2015-2021
→ Processed on the CNES HPC using the NSBAS processing chain (Doin et al., 2011; Thollard et al., 2021)
→ 12 orbits in 16-look resolution

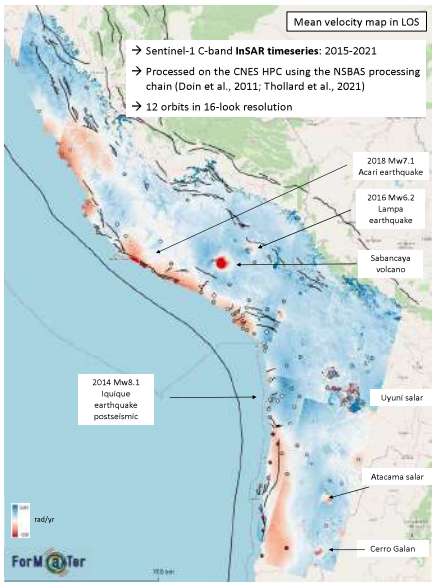

Modelling ocean tide loading (OTL), solid Earth tides (SET), and total electronic content (TEC):

→ SET show strong correlation in range

→ TEC shows good correlation on ascending tracks (acquisition time in the evening)

→ OTL shows moderate correlation. This correlation is improved by removing SET and TEC from the FLATSIM ramps, the OTL signal being significantly smaller

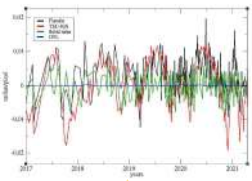

Ramps in range removed during the FLATSIM time series inversion (black) for the A076N track, with modelled IGS TEC ramps (red), SET ramps (green), and OTL ramps (blue)

Ramps in range removed during the FLATSIM time series inversion (black) for the A076N track, with modelled IGS TEC ramps (red), SET ramps (green), and OTL ramps (blue)

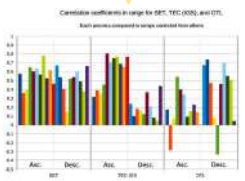

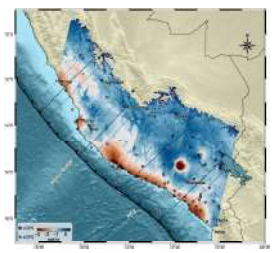

Viscoelastic correction

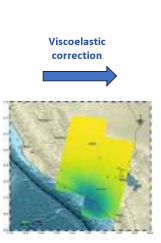

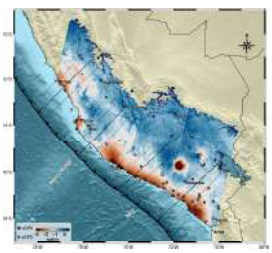

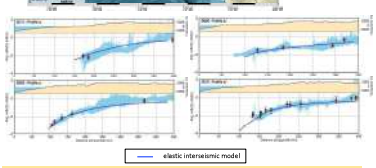

Mean velocity map (2015-2021) in LOS on descending tracks. Corrected from the 2018 Mw7.1 Acari (model from J. C. Villegas-Lanza) and 2014 Mw8.1 Iquique earthquakes (Lovery et al., 2024)

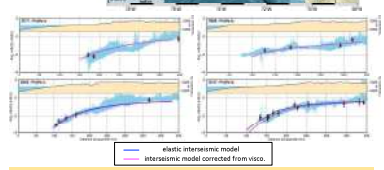

Mean velocity map (2015-2021) in LOS on descending tracks. Corrected from the 2018 Mw7.1 Acari (model from J. C. Villegas-Lanza) and 2014 Mw8.1 Iquique earthquakes (Lovery et al., 2024) + viscoelastic

Insights into the Transforming Growth Factor superfamily specific modulation: unravelling the impact of winter-hibernating bear serum in primary human muscle cells

Chloé Richard[1], Guillaume Fourneaux[1], Charlène Pourpe[1], Alexandre Geffroy[2], Gwendal Cueff[1], Christophe Tatout[3], Alina L. Evans[4], Jonas Kindberg[5], Guillemette Gauquelin-Koch[6], Fabrice Bertile[2], Etienne Lefai[1], Lydie Combaret[1]

[1]Université Clermont Auvergne, INRAE, Unité de Nutrition Humaine, UMR 1019, Clermont-Ferrand, France, [2]Université de Strasbourg, CNRS, IPHC UMR 7178, Strasbourg, France UCA, [3]Université Clermont Auvergne, CNRS, Inserm, GReD, Clermont-Ferrand, France, [4]Department of Forestry and Wildlife Management, Inland Norway University of Applied Sciences, Campus Evenstad, NO-2480 Koppang, Norway, [5]Norwegian Institute for Nature Research (NINA), Trondheim, Norway, [6]Centre National d'Etudes Spatiales, CNES, 75001 Paris, France

Introduction

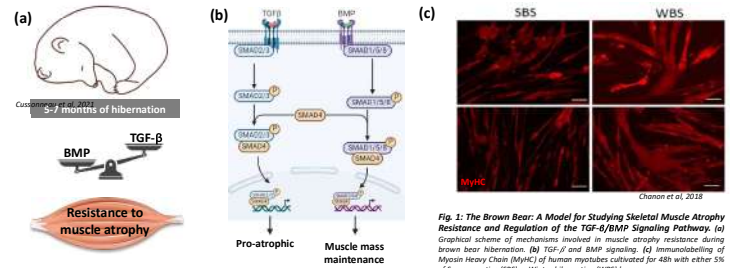

Fig. 1: The Brown Bear: A Model for Studying Skeletal Muscle Atrophy Resistance and Regulation of the TGF-β/BMP Signaling Pathway. *(a) Graphical scheme of mechanisms involved in muscle atrophy resistance during brown bear hibernation. (b) TGF-β and BMP signaling. (c) Immunolabelling of Myosin Heavy Chain (MyHC) of human myotubes cultivated for 48h with either 5% of Summer-active (SBS) or Winter-hibernating (WBS) bear serum.*

Context **Investigating the effects of Winter Bear Serum on human myotubes, focusing on *TGF-β* and BMP signaling**

Muscle atrophy poses significant challenges in patient care, with **no proven effective treatment available**, despite the huge knowledge acquired using rodent and human models of induced atrophy. We seized opportunity to study a **natural model of resistance to muscle atrophy:** the brown bear. **Despite prolonged fasting and physical inactivity during hibernation**, brown bears do not experience **muscle loss**. This resistance is associated with a shift in the balance between **pro-atrophic TGF-β signaling and hypertrophic BMP signaling, favoring the latter in muscle from hibernating brown bears** (Fig. 1a,b)**.** Additionnally, bear serum demonstrates **translational effects on human myotubes,** resulting in higher myosin heavy chain protein content in WBS conditions (Fig 1c).

Methodology

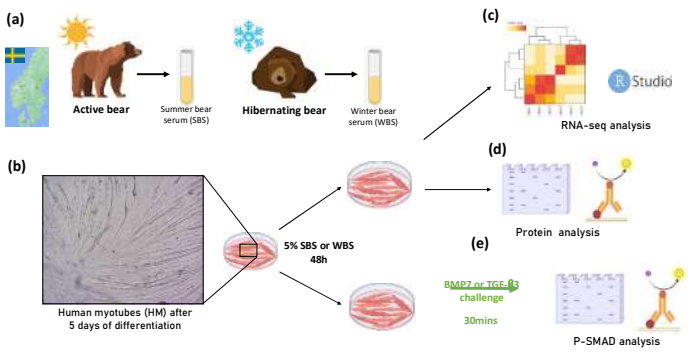

Fig. 2: Experimental procedures. ***(a) Sampling:*** *Serum samples were collected from paired free-ranging bears during active and hibernation periods (Sweden, Tackåsen).* ***(b) Cell culture:*** *Human myotubes, cultivated in a differentiation medium, were treated for 48h with 5% SBS or WBS.* ***(c) Transcriptomic analysis:*** *Total RNA samples were subjected to DNBSEQ Sequencing (BGI, China). DESeq2 analysis was used to identify differentially expressed genes (DEGs, Padj<0.05), and functional analysis of the DEGs was conducted using Rstudio software.* ***(d) Protein content*** *for some identified DEGs from (c) was assessed using Western blotting.* ***(e) TGF-β/BMP challenge:*** *Human myotubes cultivated with 5% SBS or WBS for 48h were then treated for 30 min with increasing concentrations of BMP7 (0 to 2000 ng/mL) or TGF-β3 (0 to 100 ng/mL). SMAD1/5 and SMAD3 phosphorylation (P-SMAD) were analyzed by Western blotting on whole protein content.*

Results

Fonctional analysis reveals enrichment of muscle development processes and BMP signaling among DEGs identified in human myotubes in WBS conditions

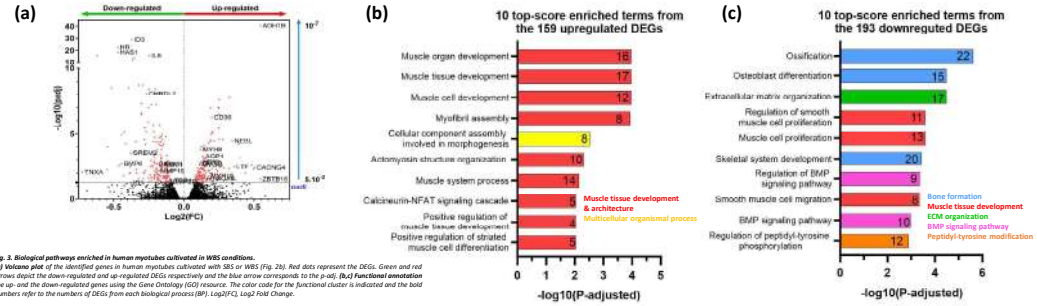

Fig. 3. Biological pathways enriched in human myotubes cultivated in WBS conditions. ***(a) Volcano plot*** *of the identified genes in human myotubes cultivated with SBS or WBS (Fig. 2b). Red dots represent the DEGs. Green and red arrows depict the down-regulated and up-regulated DEGs respectively and the blue arrow corresponds to the p-adj.* ***(b,c) Functional annotation*** *the up- and the down-regulated genes using the Gene Ontology (GO) resource. The color code for the functional cluster is indicated and the bold numbers refer to the numbers of DEGs from each biological process (BP). Log2FC1, Log2 Fold Change.*

Key informations

- Transcriptomic analysis identified **352 DEGs** between human myotubes cultivated with WBS vs. SBS (Fig. 3a). Functional annotation revealed a significant enrichment of multiple biological processes within up and down-regulated genes.
- The **159 upregulated DEGs** are mainly involved in muscle tissue development and sarcomere architecture (Fig. 3b) and the **193 downregulated DEGs** are involved in extracellular matrix organization and BMP signaling pathway regulation (Fig. 3c).

WBS induced an up-regulation of several genes associated with the structural organization of human myotubes

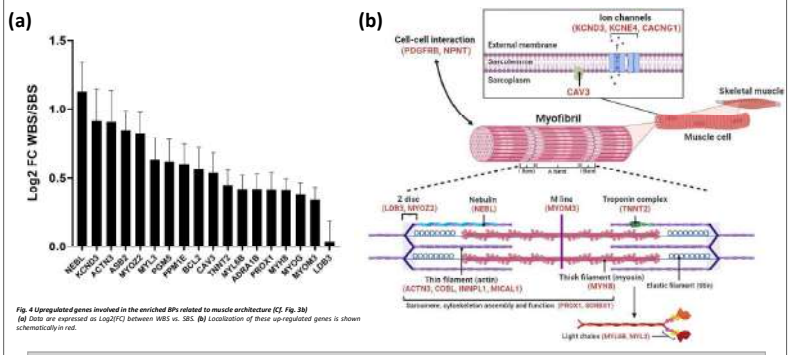

Fig. 4 Upregulated genes involved in the enriched BPs related to muscle architecture (Cf. Fig. 3b) *(a) Data are expressed as Log2(FC) between WBS vs. SBS.* ***(b)*** *Localization of these up-regulated genes is shown schematically in red.*

These specific genes are involved in the organisation of the sarcolemma and ion exchanges (CAV3, KCND3, KCNE4, CACNG1), sarcomere, cytoskeleton assembly and function (NEBL, MYOM3, TNNT2…), and also in cell-cell interaction (PDGFRB, NPNT).

WBS mainly down-regulates the expression of extracellular and intracellular BMP modulators

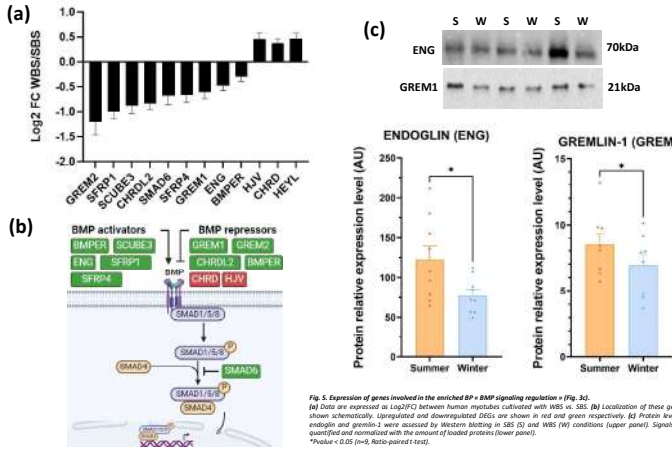

Fig. 5. Expression of genes involved in the enriched BP « BMP signaling regulation » (Fig. 3c). *(a) Data are expressed as Log2FC between human myotubes cultivated with WBS vs. SBS.* ***(b)*** *Localization of these genes is shown schematically. Upregulated and downregulated DEGs are shown in red and green respectively.* ***(c)*** *Protein levels for endoglin and gremlin-1 were assessed by Western blotting in SBS (S) and WBS (W) conditions (upper panel). Signals were quantified and normalized with the amount of loaded proteins (lower panel). *Pvalue < 0.05 (n=9, Ratio-paired t-test).*

Most BMP signaling inhibitors (e.g. GREM1/2, CHRDL2, SMAD6) or activators (ENG) were downregulated at the mRNA level. Several BMP repressors such as HJV and CHRD were however upregulated (Fig. 5a). Among these regulators, ENG and GREM1 were also downregulated at the protein level.

WBS changes the TGF-β and BMP response to their respective ligand

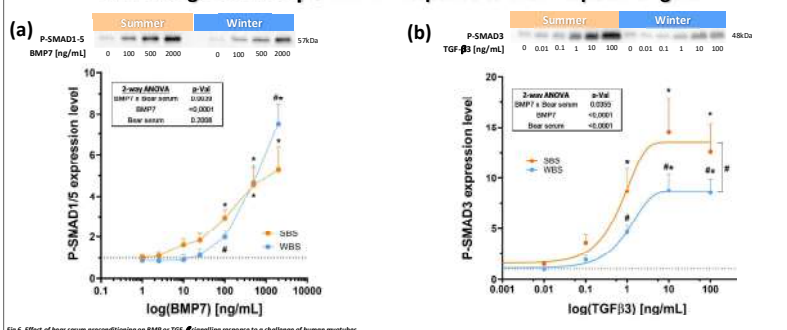

Fig 6. Effect of bear serum preconditioning on BMP or TGF-β signalling response to a challenge of human myotubes. *TGF-β/BMP challenge of human myotubes cultured with SBS or WBS were challenged with increasing BMP7 (a) or TGF-β3 (b) ligands (Fig. 2e). SMAD1/5 (a) and SMAD3 (b) phosphorylation were assessed by Western blotting (upper panels). Signals were quantified and normalized with the amount of loaded proteins (lower panels). *Pval<0.05 vs. untreated myotubes from SBS or WBS conditions; #Pval<0.05 vs. same dose of ligands in SBS condition (n=10-12, 2-way ANOVA, Tukey's post-hoc test). Dot lines are arbitrary set at 1.*

BMP7 and TGF-β3 treatment induces dose-dependent SMAD1/5 and SMAD3 phosphorylation, respectively. BMP7 triggers SMAD1/5 phosphorylation at 100 ng/ml in SBS, but at 500 ng/ml in WBS. However, at high concentration, SMAD1/5 phosphorylation was much higher in the WBS. TGF-β3-induced SMAD3 phosphorylation is consistently lower in WBS compared to SBS.

Conclusion

Overall, our findings indicate a **transcriptomic reprogramming** with an enrichment of biological processes associated to muscle tissue development and **regulation of BMP signaling,** with **down-regulation of several BMP regulators in WBS conditions.**

Challenging the BMP and TGF-β pathways shows a **higher responsiveness of the BMP pathway in myotubes under WBS conditions**, contrarily to the TGF-β signaling which remained consistently weaker.
This suggests that WBS shifts the TGF-β/BMP balance towards the BMP pathway.

Altogether, our results are in agreement with the hypertrophic phenotype observed in human myotubes cultured with WBS *(Chanon et al. 2018)* and the specific TGF-β/BMP balance depicted in atrophy-resistant muscles from the hibernating brown bear *(Cussonneau et al. 2021).*

Further studies will investigate how bear serum induced this reprogramming and how this might influence BMP signaling and/or muscle mass maintenance during catabolic conditions.

Couplage Surface-Orbite en spectroscopie infrarouge pour la caractérisation des aérosols martiens et le l'hydratation de la surface

Aurélien Stcherbinine, *IRAP, CNES, Université Toulouse III Paul Sabatier, CNRS, Toulouse, France*

LA RICHESSE ACTUELLE DES OBSERVATIONS MARTIENNES

La compréhension et caractérisation des **aérosols** est un **enjeu crucial** pour mieux **comprendre et modéliser le climat martien** ainsi que les **échanges entre la surface et l'atmosphère** de la planète.

Aujourd'hui de **nombreuses sondes en orbite et à la surface** de Mars permettent d'**étudier les aérosols** (poussière & nuages) ainsi que l'**hydratation de la surface** et les **glaces**, incluant plusieurs instruments à contribution française portés par le CNES.

Complémentarité des différentes géométries d'observation pour l'étude des aérosols :

- **Nadir :** profondeur optique colonne intégrée, large couverture spatiale
- **Occultation Solaire :** extinction, taille, structure verticale détaillée, haute sensibilité
- **Passive sky :** fonction de phase, albédo de simple diffusion, basses couches atmosphériques

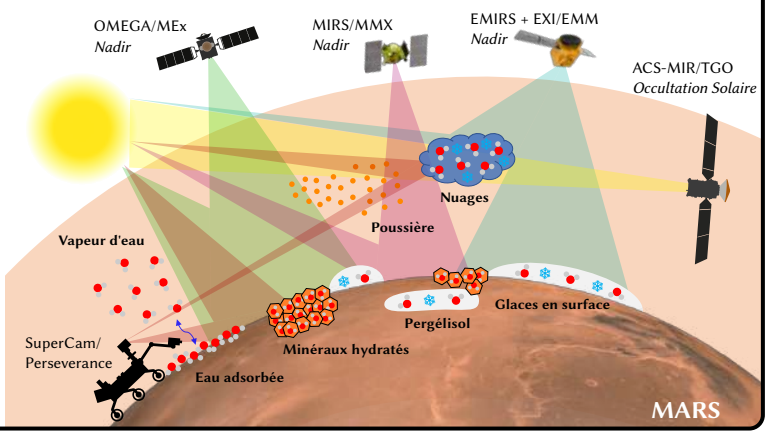

COUPLER LES JEUX DE DONNÉES POUR MIEUX CARACTÉRISER LES AÉROSOLS MARTIENS

Des **observations simultanées multi-instruments** peuvent permettre de mieux contraindre les propriétés des aérosols en **combinant différentes géométries.**

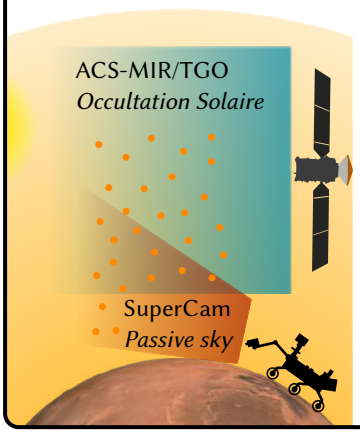

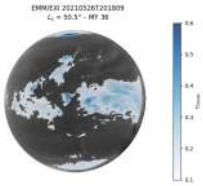

Profondeur optique des nuages de glace d'eau avec EMM/EXI (UV nadir – Wolff et al., 2022).

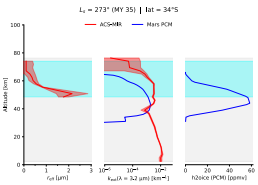

Profils verticaux taille et extinction des nuages avec TGO/ACS-MIR comparés aux prédictions de modèles climatiques (Stcherbinine et al., 2022).

Adapted from Stcherbinine et al. (2022)

Les mesures en occultation solaire fournissent désormais une **climatologie précise de la distribution verticale des aérosols dans l'atmosphère.**

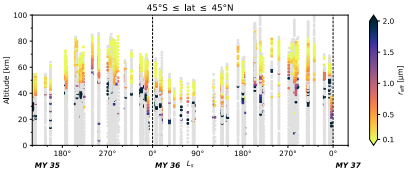

Or, les profils verticaux des aérosols sont nécessaires pour dériver les propriétés atmosphériques en géométrie nadir, le choix d'une hypothèse empirique peut avoir des conséquences notables sur les résultats (Stcherbinine et al., 2025).

Workshop international à Toulouse les 23 & 24 Septembre 2024 sur les propriétés radiatives de la poussière martienne.

Lors d'un **workshop international** en septembre, des spécialistes des observations de la **poussière martienne** et des représentants des principaux modèles climatiques ont pu échanger sur les **moyens d'améliorer nos connaissances en travaillant ensemble**.
Parmi les principales actions mises en avant : l'intérêt de **réaliser des observations conjointes dans différentes géométries**, et le besoin d'observations spécifiques supplémentaires (mission MMX avec MIRS).

ÉCHANGES ATMOSPHÈRE-SURFACE & HYDRATATION DES SOLS

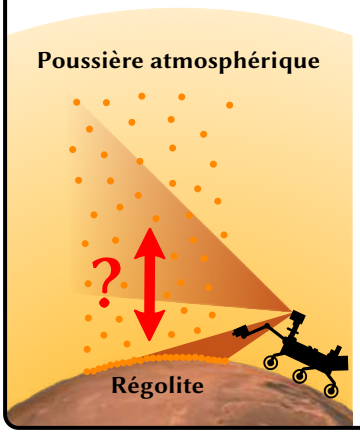

La **poussière martienne** est à l'**interface entre l'atmosphère et la surface** de Mars, issue de l'érosion du matériau de surface et élevée jusqu'à plusieurs dizaines de kilomètres dans l'atmosphère.

La question de l'**hydratation de la surface martienne**, de la **quantité d'eau** présente en surface et de sa **nature** (minéraux, adsorbée...) est **complexe** mais **d'une grande importance**. La poussière, élément mobile en partie hydraté pourrait jouer un rôle.

Récemment, les mesures infrarouges de l'instrument Supercam on révélé des **niveaux d'hydratation bien supérieurs à ceux obtenus depuis l'orbite** dans la **même gamme spectrale**. Cela soulève de nombreuses interrogations, mais **l'écart d'échelle rend la comparaison directe ardue**.
De **nouvelles mesures** en **spectroscopie infrarouge** par un potentiel futur instrument orbital à plus **haute résolution spatiale** que OMEGA ou CRISM pourraient permettre de combler l'écart entre les mesures orbitales actuelles et les observations réalisées depuis la surface à Jezero.

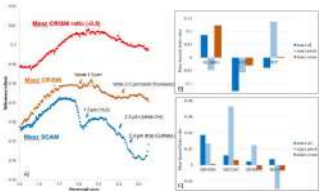

Quantin-Nataf et al. (2024)

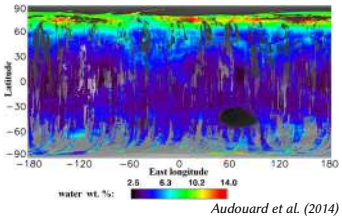

Audouard et al. (2014)

RÉFÉRENCES

Audouard et al. (2014). Water in the Martian regolith from OMEGA/Mars Express. *JGR: Planets*, 119, 1969-1989

Quantin-Nataf et al. (2024). Orbital infrared spectroscopy: lessons learned from in situ SCAM VISIR in Jezero. *10th Mars Conference*, abstract 3390

Stcherbinine et al. (2022). A Two Martian Years Survey of Water Ice Couds on Mars with ACS Onboard TGO. *JGR: Planets*, 127, e2022JE007502

Stcherbinine et al. (2025). On the impact of the vertical structure of Martian water ice clouds on nadir atmospheric retrievals from simultaneous EMM/EXI and TGO/ACS-MIR observations. *Icarus, in press*

Wolff et al. (2022). Diurnal Variations in the Aphelion Cloud Belt as Observed by the Emirates Exploration Imager (EXI). *GRL*, 49, e2022GL100477

CONTACT

Aurelien.Stcherbinine@irap.omp.eu

https://aurelien.stcherbinine.net

Recueil des posters

Session 4

S04-01 | Doc | **BEDOSSA Emma** | Météo-France (CNRM), Toulouse | Encadrant CNES : Annick SYLVESTRE-BARON | POSTER |
Apport des observations directionnelles CFOSAT pour le couplage vagues/océan

S04-02 | Doc | **DUFOURG Corentin** | IRISA / Univ Bretagne Sud, Vannes | Encadrant CNES : Stéphane MAY | POSTER |
Apprentissage et analyse d'objets spatio-temporels à partir de séries temporelles d'images satellitaires à hautes résolutions

S04-03 | Doc | **FRANEL Nathan** | IJCLab, Bures-sur-Yvette | Encadrant CNES : Philippe LAUDET | POSTER |
Polarimétrie de sursauts gamma avec une mission CubeSat

S04-04 | Doc | **GAUGNE Charlotte** | IPGP, Paris | Encadrant CNES : Mioara MANDEA | POSTER |
Étude des redistributions de masse à la frontière noyau manteau par gravimétrie spatiale

S04-05 | Doc | **HERVAS PETERS Fabian** | CosmoStat, CEA, Gif sur Yvette | Encadrant CNES : Philippe LAUDET | POSTER |
Mesurer la connexion entre matière noire et baryons dans la toile cosmique à l'aide de l'effet de lentille gravitationnelle faible et des corrélations croisées entre Euclid et DESI

S04-06 | Doc | **LESIGNE Thomas** | LATMOS/IPSL, Paris | Encadrant CNES : Adrien DESCHAMPS | POSTER |
Étude du cycle de vie des cirrus dans la tropopause tropicale à partir des mesures lidar de la campagne d'observation Stratéole2

S04-07 | Post-doc | **LIZARAZO Sindy Carolina** | Lab. Magmas et Volcans, Aubiere | Encadrant CNES : Félix PEROSANZ | POSTER |
Magmatic source modeling at the Colombian Andes stratovolcanoes revealed by ground-based and satellite geodetic data

S04-08 | Doc | **RIBEIRO Uelison** | UMR 6554 – LETG, Rennes | Encadrant CNES : Philippe MAISONGRANDE | POSTER |
Automatisation d'une méthode de suivi des écosystèmes humides en contexte tropical à partir d'images satellitaires Sentinel 1 et 2

S04-09 | Doc | **SOUDARIN Célia** | ISAE-ENSMA/PPRIME, Chasseneuil du Poitou | Encadrant CNES : Pierre LEROUX | POSTER |
Hypergolic ignition of liquid storable propellants

Long term assimilation of directional wave data from CFOSAT in the wave prediction model MFWAM

E. Bedossa[(1)(2)(3)], supervised by L. Aouf [(2)], H. Giordani [(3)], S. Law Chune[(4)]

[(1)] CNES, Toulouse [(2)] Météo-France, DirOP , Département Marine et Océanographie, Toulouse, [(3)] Météo-France - CNRM, [(4)] Mercator Ocean International, Toulouse

Abstract

- In recent years, satellite wave observations have stepped forward with the innovative measurements from the wave scatterometer SWIM of the CFOSAT mission which provides both the significant wave height along the nadir-track and the directional wave spectra on each side of the nadir track.
- In climate or ocean circulation models, wave-dependent ocean-atmosphere flows have often been parameterized by surface winds, or have been ignored altogether : too simplistic and far removed from reality.Or in the context of global warming and climate changes, ocean waves forecasting is crucial for predicting and analyzing the exchange of momentum and heat fluxes at the atmosphere/ocean interface and for the protection against natural hazards in coastal regions during severe storms.

The CFOSAT space mission

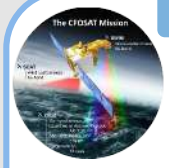

- Developed jointly by the Chinese (CNSA) and French (CNES) space agencies
- Launched in October 2018 ⇒ data available since January 2019

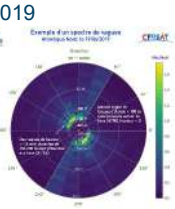

Géométrie des observations de SWIM

2 on-board instruments :

- SCAT : wind scatterometer
- **SWIM : wave scatterometer : measures wave energy density and wave numbers and wave heights[(1)]**

Models and simulations

1st step : assimilation of SWIM data in MFWAM

- Wave forecast model of Météo-France
- Spectral resolution of 24 directions and 30 frequencies
- Assimilation scheme : optimal interpolation

	Grid resolution	Wind forcing	Assimilation of SWH from nadir	Assimilation of wavenumbers components	Period
Run C	0.25°	IFS (CEP)	x	x	2021
Run A	0.25°	IFS (CEP)	✓	✓	2021

2nd step : NEMO simulations with improved or not, wave forcing from MFWAM

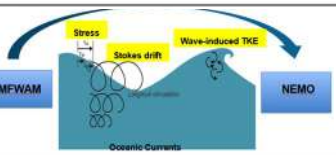

Wave forcing for NEMO computed by MFWAM

NEMO

Config iORCA025

	Wave forcing from MFWAM	SWIM DA in MFWAM forcing	Wind forcing	Grid resolution
ALL	Stokes drift Stress Wave-induced TKE	SWH (nadir) Wavenumbers components	IFS (CEP)	0.25°
FREE	Stokes drift Stress Wave-induced TKE	No	IFS (CEP)	0.25°

Validation of MFWAM simulations with buoys and altimeters

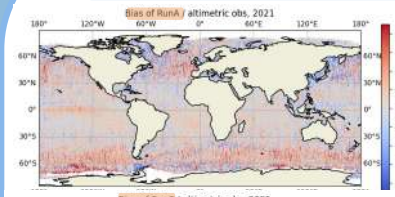

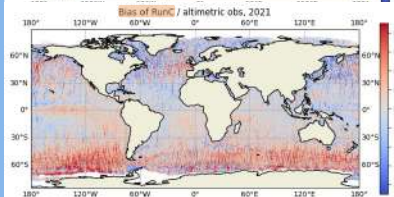

Area	Exp	Bias (m)	RMSE (%)	SI
Global	RUN C	0.02	12.3	12.3
	RUN A	0.05	10.7	10.5
Tropics	RUN C	-0.03	10.1	10
	RUN A	0.03	8. 9	8.8
Southern Ocean	RUN C	0.22	13.1	11.8
	RUN A	0.15	10.7	10
Arctic	RUN C	-0.1	14.6	14.1
	RUN A	-0.02	13.2	13.2
Middle Latitudes	RUN C	0.02	11.5	11.5
	RUN A	0.05	10.2	10.1

Fig. 1 and Table 1 :Validation of Significant Wave Heights (SWH) in MFWAM simulations in 2021 with Jason3, SARAL, Sentinel-3A and B CryoSat-2, HII-B

- SWH bias globally reduced, and particularly in depressions track in NH, a part of Southern Ocean, North and South Pacific ocean
- Still a large SWH bias in the Southern Ocean relative to uncertainties in the wind forcing

SI reduced for every type of waves, especially for long waves (Tp > 13s) : up to 34 %

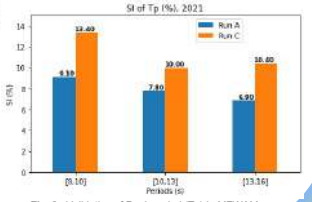

Fig. 2 : Validation of Peak period (Tp) in MFWAM simulations in 2021 with SOFAR (SPOTTER) buoys

Impacts on integrated wave parameters In the Southern Ocean

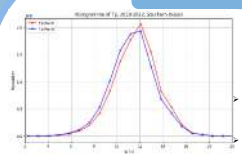

Fig. 3 : Histogramme of T_p for Run A and Run C in the Southern Ocean, 2019-2022.

Wave age is an indicator of wave dependence on wind : $wave_{age} = \frac{c_p}{U_{10} \cdot \cos\theta}$ With $c_p = \frac{gT_p}{2\pi}$ The peak velocity phase and T_p the peak period

- Waveage = 1.2, the equilibrium between wave and wind fields is reached
- Waveage < 1.2 : the dominant wave regime is the wind sea
- Waveage > 1.2 : the dominant wave regime is swell[(2)]

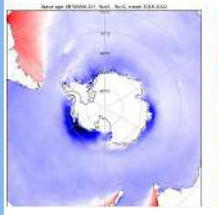

Fig. 4 : Impact of the SWIM DA on the wave age (RunA- RunC) 2019-2022.

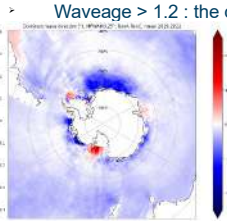

Fig. 5 : Impact of the SWIM DA on the domin direction (RunA- RunC) in the Southern Ocean, 2019-2022.

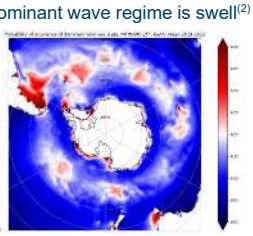

Fig. 6 : Probability of occurrence of swell in RunA in Southern Ocean, 2019-2022

- T_p smaller in RunA compare to RunC ⇒ so is waveage ⇒ wave growth and spread are impacted by SWIM data assimilation
- Southern Ocean is an area with infinite fetch with nonlinearities driving the transition from wind to swell waves : SWIM data assimilation helps reduce these model uncertainties[(3)]

Impacts on ocean key parameters

Integrated wave parameters significantly impacted by SWIM data assimilation ⇒ so are wave-ocean coupling processes

- **Correction of model bias ? → validation of surface currents with AIS data[(4)]**
- **What are the impacts of better representated waves on ocean key parameters? → case of an subtropical storm near Aghulas current**

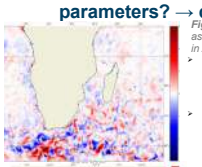

Fig. 7 : Impact of the SWIM data assimilation on the SST (ALL - FREE) in Aghulas current

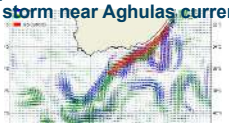

Fig. 8 : ALL, FREE and AIS surface current s

- Strong SST gradient in the current in ALL simulation
- Waves create an ondulation in this gradient : creation of dipolar structures

How can we explain that only the ALL simulation is in agreement with the AIS observations?

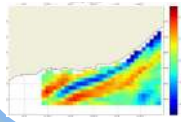

Fig. 9 : Bias of surface current module of FREE simulation (above) and ALL simulation (below) compare to AIS observations, in Aghulas current (JF 2020)

⇒ Uncertainties related to IFS wind forcing at 10m in this area

⇒ Modification of wind stress received by waves

⇒ Mean wave direction impacted

⇒ **A more accurate and faithful description of the directionality of the various wave trains through the assimilation of SWIM data 'compensates' for the wind forcing missfit**

Conclusions – Next steps

- Data assimilation reduces model bias on wave height and peak period and reduces the scatter at high latitudes, in the Tropics and in strong currents areas.
- The best corrected wave systems are long waves with peak periods greater than 13s.
- Data assimilation has a impact on the waveage and compensates for uncertainties due to non-linearities in the transition from wind waves to swell in the Souther Ocean.
- Wave forcing for NEMO improved with SWIM DA leads to a significant improvment of the representation of the module and direction of the current of Agulhas
- Ocean key parameters like SST are sensitive to wave forcing improved with SWIM data during a subtropical storm

References

[(1)] Hauser et al. (2017) SWIM: The First Spaceborne Wave Scatterometer
[(2)] Pierson and Moskowitz (1964), Alves et al. (2003)
[(3)] Aouf, L., Hauser, D., Chapron, B., Toffoli, A., Tourain, C., & Peureux, C. (2021). New directional wave satellite observations: Towards improved wave forecasts and climate description in Southern Ocean. Geophysical Research Letters, 48, e2020GL091187
[(4)] Le Goff, C., Boussidi, B., Mironov, A.,Guichoux, Y., Zhen, Y., Tandeo, P., et al. (2021). Monitoring the greater Agulhas Current with AIS data information. Journal of Geophysical Research: Oceans, 126, e2021JC017228. https://doi.org/10.1029/2021JC017228

emma.bedossa@meteo.fr
Météo-France - 42 avenue Gaspard Coriolis, 31100 Toulouse

JC² CNES
16, 17, 18 octobre 2024 - Toulous

RÉPUBLIQUE FRANÇAISE
Liberté Égalité Fraternité

cnes CENTRE NATIONAL D'ÉTUDES SPATIALES

GraphCast for SITS

Forecasting water resources from satellite image time series using a graph-based learning strategy

Corentin DUFOURG[1,*] *Charlotte PELLETIER*[1] *Stéphane MAY*[2] *Sébastien LEFÈVRE*[1]

[*] corentin.dufourg@univ-ubs.fr [1] Université Bretagne Sud, IRISA, UMR CNRS 6074, Vannes, France [2] Centre National d'Etudes Spatiales (CNES), Toulouse, France

CONTEXT

- Constellations of satellites with high spatial and temporal resolution enable precise and dynamic resource monitoring
- **Graph-based learning** can be used to exploit spatio-temporal dependencies in **Satellite Image Time Series** (SITS) [1]
- **GraphCast** is a state-of-the-art model for global meteorological forecasting based on graph neural networks [2]

How to adapt a model for global meteorological forecasting like GraphCast to a monitoring task of local water resources from satellite image time series?

METHODOLOGY

- **Objective:** forecast the next image of a sequence of N satellite images

- Use of a **single region-specific mesh**
  - SLIC segmentation applied to the stack of input images
  - input node's features = pixel time series, spatial (latitude-longitude) and temporal (day-of-year) embedding
- **Encoder-processor-decoder** architecture
  - encoder projects the pixel's features into the mesh nodes
  - processor learns representations of the mesh nodes via message passing
  - decoder maps the learned features to each pixel using only the three nearest mesh nodes

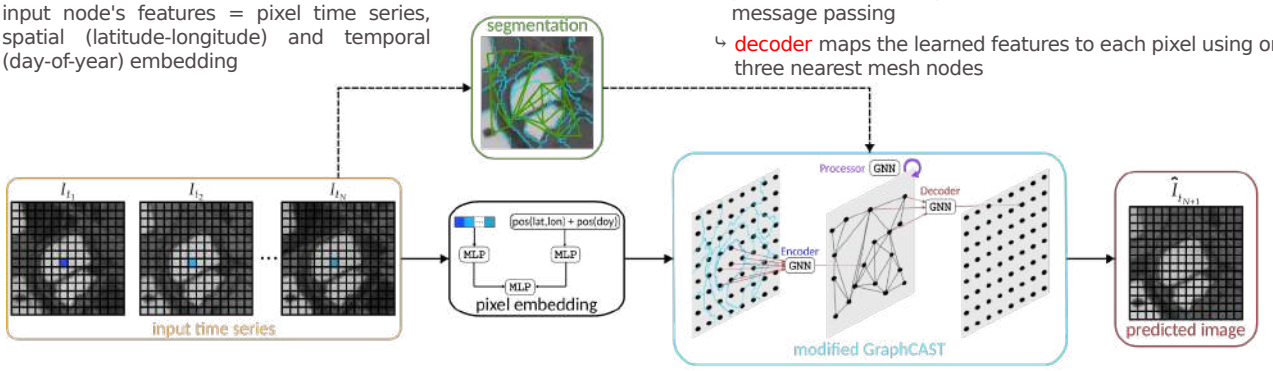

DATA & RESULTS

SEN2DWATER dataset [3]

- consisted of Sentinel-2 time series
- gathered from July 2020 to Dec. 2022
- over 17 basins in Spain and Italy
- at a 10 m spatial resolution
- about one cloud-free image every 2 months
- 3 682 NDWI patches of size 64 × 64 pix

	# Params	RMSE ↓	PSNR ↑	SSIM ↑	Runtime/epoch (s)
Input average	-	0.1550	23.32	0.7465	-
Persistence	-	0.1332	25.03	0.7897	-
LSTM	17,345	$0.1162_{\pm 0.0005}$	$25.53_{\pm 0.05}$	$\mathbf{0.8282}_{\pm 0.0005}$	26
ConvLSTM	150,721	$0.1197_{\pm 0.0029}$	$25.28_{\pm 0.19}$	$0.8113_{\pm 0.0030}$	31
TDCNN-ConvLSTM	407,681	$0.1111_{\pm 0.0008}$	$25.68_{\pm 0.08}$	$0.8083_{\pm 0.0008}$	55
Ours	228,673	$\mathbf{0.1097}_{\pm 0.0035}$	$\mathbf{26.42}_{\pm 0.27}$	$0.8170_{\pm 0.0070}$	49

Influence of the number of superpixels

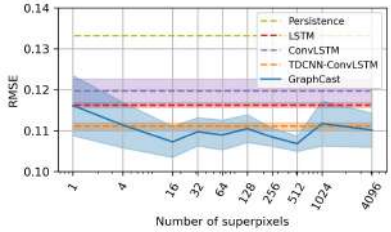

Influence of the input time-series length

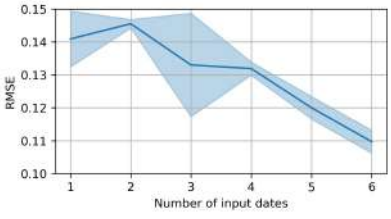

PROSPECTS

- Explore the capability of GraphCast roll-out
- Analyze more complex (multi-)mesh, especially for large patch predictions

Acknowledgments

The authors thank the French spatial agency (CNES) and the Brittany region (GIS BreTel) for their financial support. This work was granted access to the HPC resources of IDRIS under the allocation 2024-AD011014108R1 made by GENCI. Charlotte Pelletier is partially funded through project DECOL ANR-23-CE56-0003.

References

1. Dufourg, C., Pelletier, C., May, S., & Lefèvre, S. (2023). Graph Dynamic Earth Net: Spatio-Temporal Graph Benchmark for Satellite Image Time Series. IEEE International Geoscience and Remote Sensing Symposium (IGARSS). (pp. 7164-7167).
2. Lam, R., Sanchez-Gonzalez, A., Willson, M., Wirnsberger, P., Fortunato, M., Alet, F., ... & Battaglia, P. (2023). Learning skillful medium-range global weather forecasting. Science, 382(6677), 1416-1421.
3. Mauro, F., Rich, B., Muriga, V. W., Janku, F., Sebastianelli, A., & Ullo, S. L. (2023). SEN2DWATER: A Novel Multispectral and Multitemporal Dataset and Deep Learning Benchmark for Water Resources Analysis. In IEEE International Geoscience and Remote Sensing Symposium (IGARSS) (pp. 297-300).

ubs: UMR IRISA

Polarimétrie des sursauts gamma avec une mission CubeSat

Nathan Franel – IJCLab – nathan.franel@ijclab.in2p3.fr
Collaborateurs – V. Tatischeff[1], C. Hamadache[1], D. Murphy[2], A. Ulyanov[2], C. Mc Kenna[2], L. Hanlon[2] et al.
1 – IJCLab (Orsay, France) 2 – UCD (Dublin, Irlande)

Les sursauts gamma (GRBs)

Ce sont les évènements les plus lumineux de l'Univers, émettant principalement dans le domaine gamma. Ils se distribuent en deux populations :

Sursauts courts
Fusion d'objets compacts

Sursauts longs
Effondrement d'étoile massive

Du fait de leur distance ils pourraient être utilisés en cosmologie comme chandelles standards en comprenant mieux la physique de leurs jets ultra-relativistes.
De nombreux télescopes spatiaux fournissent des données spectroscopiques (Fermi, Swift, SVOM). Pour compléter ces informations une autre approche peu développée est d'étudier la polarisation de l'émission en gamma.

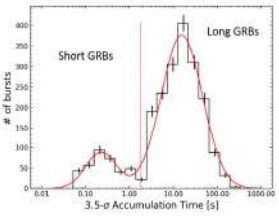

Durées d'émission des GRBs [5]

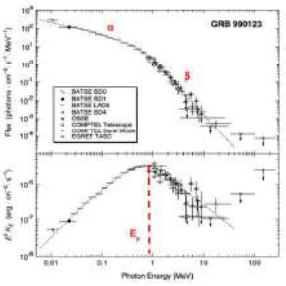

Spectre de GRB990123 [4]

La polarimétrie gamma repose sur la diffusion Compton.
La détermination de l'angle azimutal de diffusion η grâce aux énergies déposées et aux positions d'interaction des photons sert alors à estimer la fraction et l'angle de polarisation.

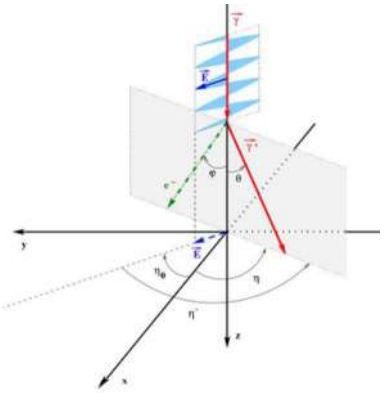

Mission COMCUBE-S pour la mesure de la polarisation des sursauts gamma

Sélectionnée par l'ESA pour une phase d'étude de faisabilité (Phase A), cette collaboration européenne (IJCLab (Orsay), UCD (Dublin), Clyde Space (Glasgow) + CEA (Saclay)) propose d'utiliser une constellation de CubeSat « Compton ».

La configuration optimale retenue : 27 CubeSats également espacés en orbite basse équatoriale à 500 km d'altitude. Ses performances ont été obtenues par simulation de la détection de sursauts par les satellites.

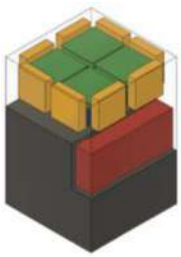

Polarimètre composé de 3 types de détecteurs :
- 2 détecteurs silicium double face à pistes (D1 en vert)
- Scintillateurs au GAGG (D2A en bleu)
- Scintillateurs au $CeBr_3$ (D2B en jaune)

Simulation des performances

L'estimation des performances de polarimétrie s'obtient par l'outil de simulation MEGALib basée sur GEANT4. Les sursauts sont simulés à une position dans le ciel et un moment aléatoires, en prenant en compte le bruit de fond et les zones de non-observation dues aux ceintures de radiation de Van Allen.

Les paramètres nécessaires aux simulations (spectres, courbes de lumière) sont tirés d'observations réelles (catalogue GBM) [5] ou estimés par des distributions ajustées sur les observations [1-3] et [6]. Un modèle de masse du satellite est ensuite nécessaire pour simuler la détection.

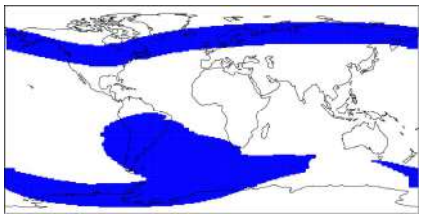

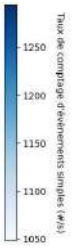

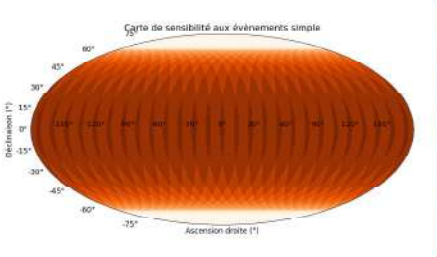

Surface efficace moyenne de 1500 cm². Taux de détection de 520 GRBs/an, plus que toute autre mission existante ou prévue.

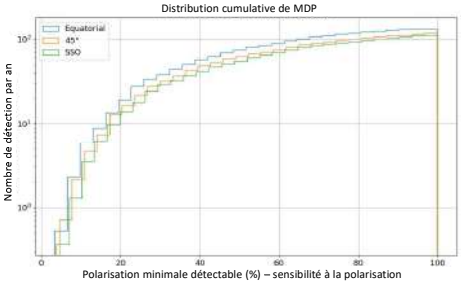

35 sursauts de faible fraction de polarisation (MDP ≤ 30%) détectables par an.

Test du prototype

Un prototype est développé au sein de la collaboration et a été testé en juin 2024 lors d'un vol ballon stratosphérique transatlantique organisé par le CNES.

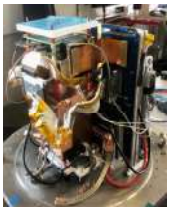

Le test a été un succès et les données sont en cours d'analyse.

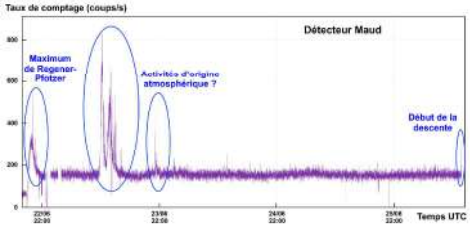

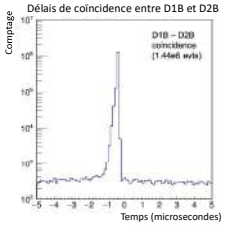

Références

[1] Ghirlanda et al. 2016, A&A, vol 594
[2] Lan et al. 2019, MNRAS, vol 488, Issue 4
[3] Lien et al. 2014, ApJ, vol 783, Issue 1
[4] Piron, C. R. Physique, 2015, vol 17, Issue 6
[5] Poolakkil et al., 2021, ApJ, vol 913, Issue 1
[6] Yonetoku et al. 2010, PASJ, vol 62, Issue 6

Mass redistributions at the core mantle boundary from satellite gravity

Charlotte Gaugne[1], Isabelle Panet[1,2], Marianne Greff[1], Mioara Mandea[3], Séverine Rosat[4]

[1] Université Paris Cité, Institut de physique du globe de Paris, CNRS, IGN, F-75005 Paris, France,
[2] ENSG - Géomatique, IGN, F-77455 Marne-la-Vallée, France,
[3] Centre National d'Etudes Spatiales, Paris, France,
[4] Université de Strasbourg, CNRS, EOST, ITES UMR7063, Strasbourg France

Motivations

Measurements of the space-time variations of the gravity field from the GRACE & GRACE-FO missions (since 2002) → **new constraints on deep mass redistributions ?**

Mass redistributions due to variations of the CMB **topography**: coupling with sudden changes in core flows ?

This could help to better understand sudden changes in the secular variation of the geomagnetic field, the **geomagnetic jerks**.

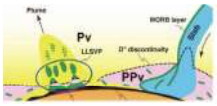

(Hirose et al. 2008)

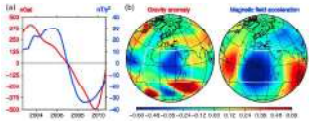

(Mandea et al. 2015)

Objective: Search for **gravity signals** of mass redistributions at the CMB at timescales of **months up to a few years**

Gravity signal related to the **2007** magnetic jerk in the **Atlantic ocean** ?

Detection of signal

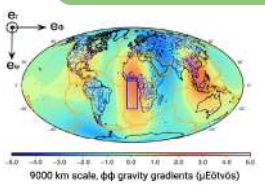

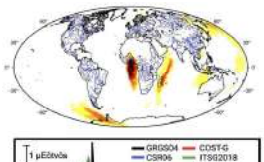

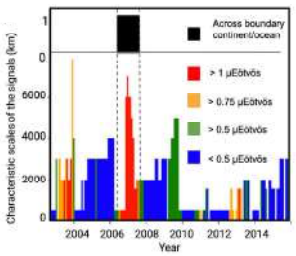

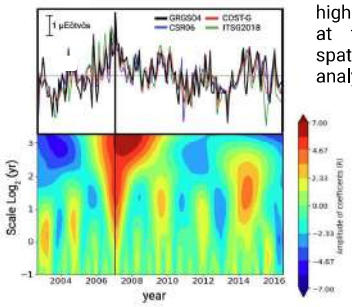

Anomalous North-South oriented signal **across** the boundary between the **Atlantic ocean** and the **African continent**, with a high intensity (≥1μEötvös) at the largest 9000-km spatial scales of the analysis in **January 2007**.

Detection of bump +/- 4 months around January 2007
→ **same spatial signature** over different timescales

Methods

- **GRACE/SLR** and pure SLR geoid models: GRGS04 compared with CSR06, ITSG2018, COST-G, SLR-AIUB
- We subtract a **mean**, **trend**, **annual** and **semi-annual** signals (2003-2015)

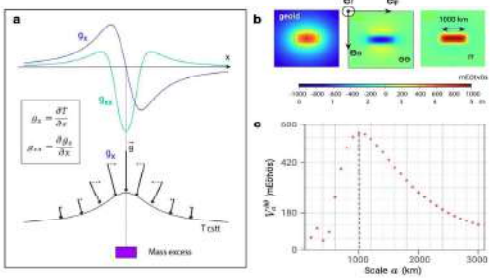

Figure 1 - Multi-scale gravity gradients (Panet et al. 2022)

- **Gravity gradients** in the local spherical frame, at different spatial scales (no terms of degree 0 nor 1)
- **Rotations of the spherical frame** to align with the orientation of the signals → **separate** signals with different **characteristic scales** and **orientations** (Panet et al. 2018 ; Panet 2019)
- Wavelet transform of the gravity gradients time series at scales **28-32 months** : search for peaks in the period **September 2006 - April 2007**
- **Bump** in the time series ↔ **peak** in the wavelet-transformed coefficients

Water cycle

To investigate a potential origin of the 2007 Atlantic signal within the **fluid envelopes of the Earth**, we now compare its spatio-temporal fingerprint with those of **hydrological**, **oceanic** and **atmospheric** sources based on global circulation models, GRACE-based reconstructions (V1) and the geographic distribution of land and ocean (V2).

Hypothesis: observed gravity variations are solely **due to water**.

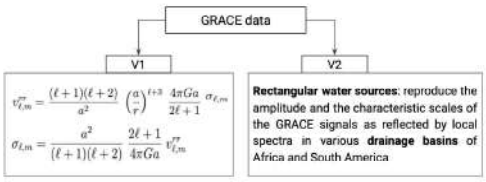

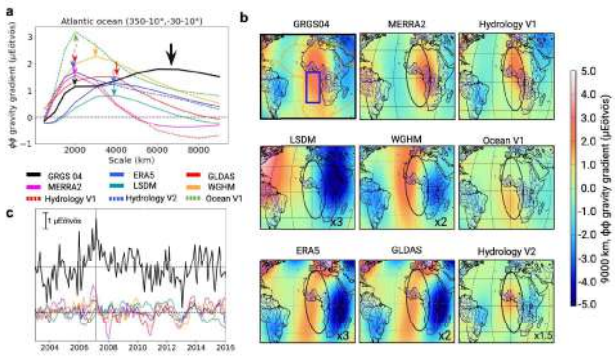

For continental hydrology and oceanic sources (modelled or reconstructed from GRACE), their combinations, and tests of coalescence of continental sources, the **characteristic scale** and **location** differ from those of the 2007 GRACE anomaly.

The 2007 Atlantic signal is not well explained by surface water sources.

These conclusions support the possibility of a **deeper origin within the solid Earth**.

Mass redistributions at the CMB / in the D" layer

Source from the core is expected to be to small to generate dynamic CMB topography, we focus on a **mantle side source**. Source at the top of the CMB can not explain both geomagnetic jerk and gravimetric magnitude anomaly.

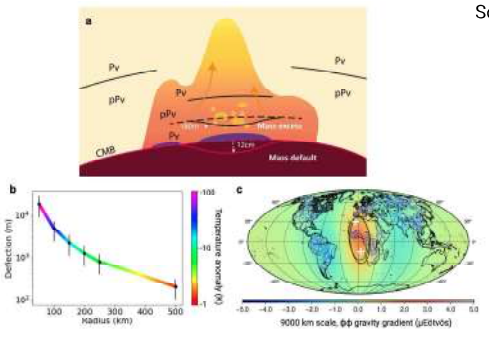

Source in the mantle above CMB:

- Characteristics of Pv-pPv : **fast** (Langrand et al 2019), density contrast (**100 kg/m^3**), occur in the D" region
- African LLSVP : **Pv-pPv phase transition** deeper (7-14 K/m)
- **Scenario proposed:** Pv **cold** anomaly (T') passing through the phase transition and transform to pPv before other material at temperature T creating a **mass anomaly**.
- **Model parameters:** elastic D" layer of 350 km, phase transition at 50 km above CMB, 2 calottes (4°W,29°N and 5°E,15°S) modelling the transformed pPv of different size (radius from 50 km to 500 km)

Reproduce characteristic of the 2007 anomalous signal (spatial fingerprints)
Generate a dynamic CMB topography of at least **12 cm**.

Conclusion

The 2007 Atlantic signal is **not well explained by surface water sources**. This leads us to propose that part of this gravity signal could **reflect deep mass redistributions** from the **Pv-pPv** phase transition and generate a **dynamic CMB topography** notable. We next propose to do the same study on the magnetic field.

References

- I, Panet JGR, 123 (12):11–062, 2018
- M. Mandea, et al., JGR, 120:5983–6000, 2015
- J. Wahr, et al, JGR, 103(B12):30205–30229, 1998
- Langrand et al, Nature communications,10(1), 5680, 2019

Acknowledgment

Authors have received funding from the European Research Council (ERC) GRACE-FUL Synergy Grant No. 855677 and from CNES.

Measuring Intrinsic Alignment in the UNIONS and BOSS/eBOSS surveys

Fabian Hervas Peters[1], Martin Kilbinger[1], Romain Paviot[1], Lucie Baumont[1]

Jean-Charles Cuillandre, Thomas Erben, Sébastien Fabbro, Axel Guinot, Stephen Gwyn, Valeria Pettorino, Hendrik Hildebrandt, Mike Hudson, Alan McConnachie, Lance Miller, Ludovic van Waerbeke

1. Université Paris-Saclay, Université Paris Cité, CEA, CNRS, AIM, 91191, Gif-sur-Yvette, France

Introduction

We use accurate shape measurements from 3500 deg^2 of the *Ultraviolet Near- Infrared Optical Northern Survey* (**UNIONS**) [1] with redshift information from BOSS/eBOSS to measure intrinsic alignement

Our goals are:

1. Measure the strength of intrinsic alignment with specific samples combining precise shape and redshift measurements
2. Identify galaxy properties allowing for a finer model of intrinsic alignment, either analytic or in simulations
3. Distinguish amongst the developed models the one which most accurately captures the intrinsic alignment signal

Weak-lensing, Intrinsic Alignment

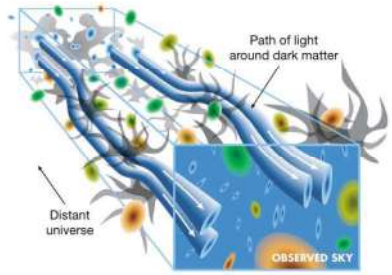

Weak lensing is the study of coherent distortions of galaxies to infer the foreground distribution of dark matter and to constrain cosmological scenarios from the amplitude of the lensing.

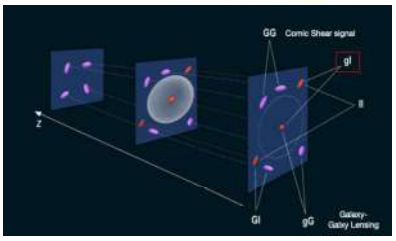

Intrinsic Alignment is a systematic for this effect as it produces a similarly coherent deformations in galaxies. During their formation galaxies get stretched by the tidal field which makes them align with the surrounding large scale structure.

Image credit: Fortuna and Chisari 2022

Survey sky-coverage

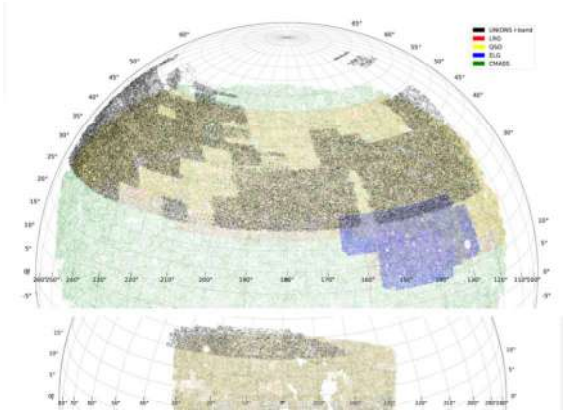

Sky coverage of the different surveys (NGC,SGC)

Catalogue Information

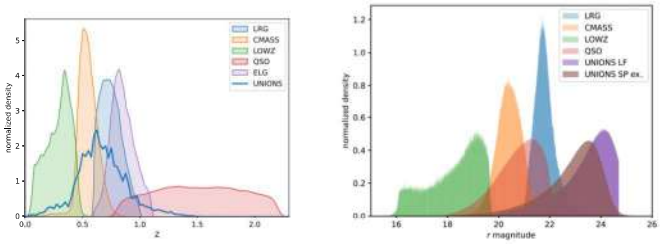

$n(z)$ distribution and r-magnitude distribution of the different samples

NLA or TATT?

The two most commonly used models to quantify the contribution of intinsic alignment are the non-linear alignment (NLA) [2] and Tidal Alignment and Tidal Torque (TATT) [3] model. TATT is a higher-order expansion of NLA.

The tidal tensor is defined as:

$$s_{ij}(k) = (\hat{k}_i\hat{k}_j - \frac{1}{3}\delta_{ij})\delta(k)$$

The intrinsic part of the shear of a galaxy is:

$$\gamma^I_{ij}(x) = C_1 s_{ij} + C_2(s_{ik}s_{kj} - \frac{1}{3}\delta_{ij}s^2) + C_{1\delta}(\delta s_{ij})...$$

Measuring the integrated correlation function

Estimator: $$\xi_{g+}(r_p, \Pi) = \frac{\text{Shape}_+(\text{Density} - \text{Rand}_D)}{\text{Rand}_D\text{Rand}_S}$$

L.O.S. Integration: $$w_{g+}(r_p) = \int_{-\Pi_{max}}^{\Pi_{max}} \xi_{g+}(r_p, \Pi)\mathrm{d}\Pi \; ; \; \Pi_{max} = 150\,\text{Mpc}$$

Signal – w_{g+} of different samples

CMASS $\approx$ 200 000 galaxies
NLA: $A_1 = 4.86 \pm 0.51$

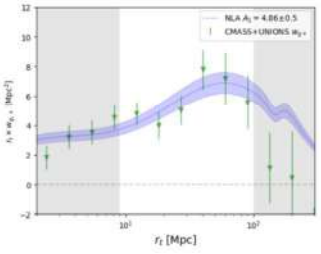

LRG $\approx$ 80 000 galaxies
NLA: $A_1 = 3.6 \pm 1.0$

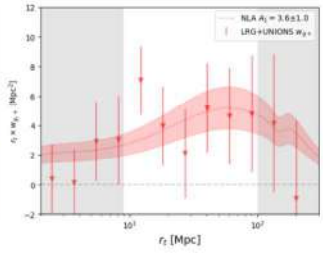

Results – NLA or TATT?

Best NLA fit:
χ^2/d.o.f. =3.40/(6-1)=0.68

Best TATT fit:
χ^2/d.o.f. = 3.58/(8-3)=0.72

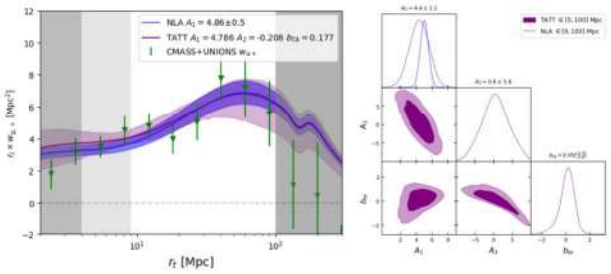

Conclusions

Our work is in broad agreement with previous measurements showing:

- Strong intrinsic alignment in Luminous Red Galaxies (LRG and CMASS)
- No preference for TATT on large linear scales
- Systematics in the UNIONS ShapePipe catalog are under control

We want to use these precise measurements to identify properties correlating with intrinsic alignment (luminosity, density...)

References

[1] A. Guinot, M. Kilbinger, S. Farrens, *et al.*, "ShapePipe: A new shape measurement pipeline and weak-lensing application to UNIONS/CFIS data", en, *Astronomy & Astrophysics*, vol. 666, A162, Oct. 2022, ISSN: 0004-6361, 1432-0746.

[2] C. M. Hirata and U. Seljak, "Intrinsic alignment-lensing interference as a contaminant of cosmic shear", en, *Physical Review D*, vol. 70, no. 6, p. 063526, Sep. 2004, ISSN: 1550-7998, 1550-2368.

[3] J. A. Blazek, N. MacCrann, M. A. Troxel, and X. Fang, "Beyond linear galaxy alignments", en, *Physical Review D*, vol. 100, no. 10, p. 103506, Nov. 2019, ISSN: 2470-0010, 2470-0029.

fabian.hervaspeters@cea.fr

Balloon-borne lidar observations of tropical cirrus clouds

Thomas Lesigne[1], François Ravetta[1], Aurélien Podglajen[2], Vincent Mariage[1], Jacques Pelon[1]

[1] Laboratoire Atmosphères, Observations Spatiales (LATMOS/IPSL), CNRS, Sorbonne Université, UVSQ, Paris, France
[2] Laboratoire de Météorologie Dynamique (LMD/IPSL), CNRS, Sorbonne Université, ENS, École Polytechnique, Paris, France

Tropical cirrus clouds have a significant impact on the climate, modulating both the Earth's radiative budget and the amount of water vapor transported to the stratosphere. Observing those clouds remains a challenge as their optical depth covers several orders of magnitude. In the framework of Strateole-2 project, three microlidars have been flown in the lower tropical stratosphere onboard super-pressure balloons, providing high-resolution observations of tropical clouds with an unprecedented sensitivity to very thin cirrus.

Strateole-2 project

- in situ and remote sensing balloon-borne observations of the Tropical Tropopause Layer (TTL)
- long duration super-pressure balloons flying at targeted levels (~20 km) for several weeks
- balloons released from Seychelles Islands, drifting with the wind along the equator
- first scientific campaign : October 2021 – January 2022, 17 balloons, 3 with BeCOOL on board

BeCOOL : Balloon-borne Cirrus and convective overshOOt Lidar

- light-weight, low-power lidar operating in the extreme conditions of the lower stratosphere
- elastic backscatter, single wavelength of 802 nm, no polarization channel
- nighttime observations only, temporal resolution of 1 min, vertical sampling of 15 m
- clouds' optical depth retrieved from 10-minutes averaged profiles
- Strateole-2 first scientific campaign: 137 nights of observation, ~40 000 lidar profiles

Balloon tracks of the 3 BeCOOL flights during Strateole-2 first scientific campaign

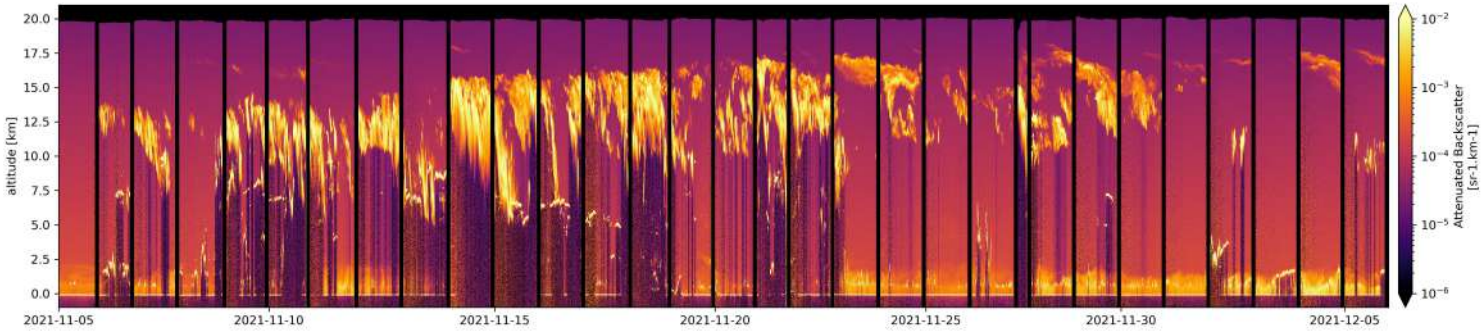

Example of lidar curtain (time vs altitude) of attenuated backscatter, 30 nights of the second BeCOOL flight

Extensive coverage of ultrathin TTL cirrus clouds

Comparisons with space-borne lidar CALIOP highlight the unique sensitivity of BeCOOL to ultrathin cirrus, both from case studies of collocated observations and from a statistical point of view. 23% of BeCOOL profiles exhibit TTL clouds (above 14 km) that are below the detection capabilities of CALIOP.

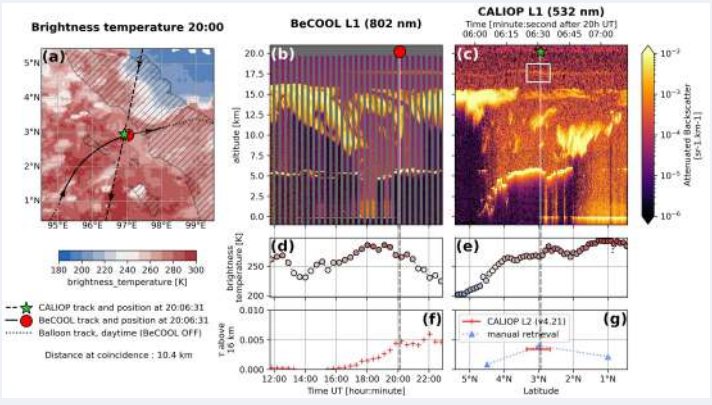

*A case study of collocated observations over a thin cirrus cloud. **a**: 11 µm brightness temperature map at coincidence; **b**: BeCOOL L1 curtain (along the solid line on the map); **c**: CALIOP L1 curtain (along the dashed line on the map); **d**, **e**: time series of brightness temperature under the balloon and the satellite; **f**, **g**: time series of optical depth τ above 16.5 km*

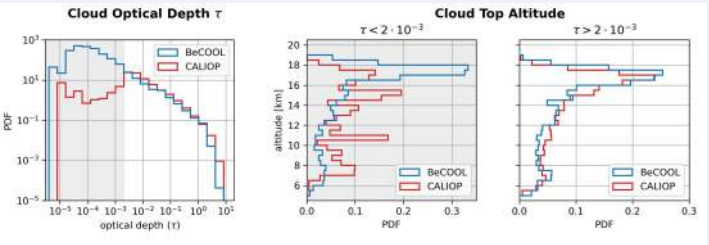

Distributions of cloud optical depth and cloud top altitude seen from BeCOOL and CALIOP during Strateole2 campaign. Clear cut-off at 2.10^{-3} in CALIOP's cloud optical depth distribution, with a perfect agreement between the two lidars above this threshold. 27% of BeCOOL's clouds have an optical depth lower than this threshold while it is below 1% for CALIOP. Those ultrathin clouds mainly exist in the TTL.

TTL cirrus and wave-induced temperature anomalies

Dynamical perturbations such as gravity waves trigger the in situ formation of TTL cirrus clouds by lowering temperatures enough for ice crystals to form and grow. BeCOOL's observations confirm results from recent studies about the distribution of clouds with respect to temperature anomalies : half of the TTL clouds are found in the cold and cooling phase of waves.

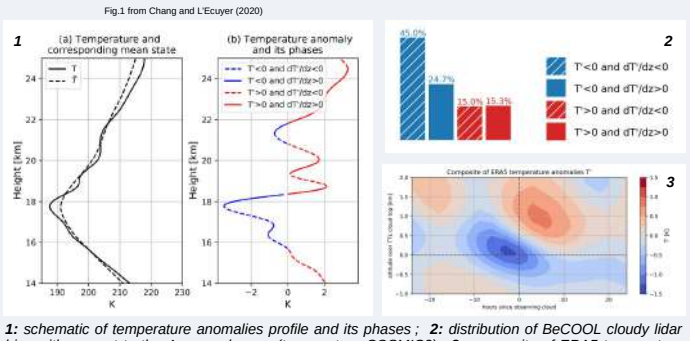

***1:** schematic of temperature anomalies profile and its phases ; **2:** distribution of BeCOOL cloudy lidar bins with respect to the 4 wave phases, (temperature COSMIC2) ; **3:** composite of ERA5 temperature anomalies (8-days rolling mean background removed) with respect to cloud top and cloud observation time.*

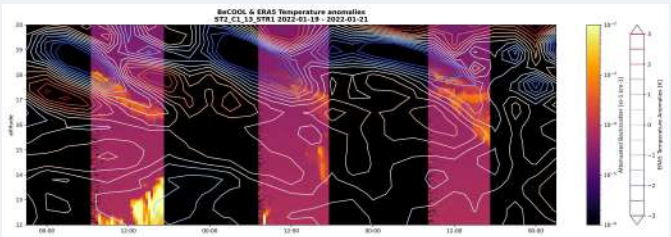

Three nights of BeCOOL cirrus observations with ERA5 temperature anomalies (8-days rolling mean background removed).

On-going work

- Characterizing the lifetime of TTL cirrus
- Microphysics simulations along backward/forward trajectories of air parcels initialized within and around observed clouds

MAGMATIC SOURCE MODELING AT THE COLOMBIAN ANDES STRATOVOLCANOES REVEALED BY GROUND-BASED AND SATELLITE GEODETIC DATA

Sindy Carolina Lizarazo[1], Valérie Cayol[1], Fabien Albino[2]
[1]*Laboratoire Magmas et Volcans – LMV, Université Clermont-Auvergne*
[2]*Institut des Sciences de la Terre – ISTerre, Université Genoble-Alpes*

1. INTRODUCTION

1.1. Study region and volcano features

Volcanism in Colombia is driven primarily by the subduction of the Nazca plate (NZ) beneath the North Andean Block (NAB).

- High conical edifices (>4000 m asl)
- Steep topography
- Snow-capped summits
- Dense vegetation
- Strong climatic disturbances

Nevado del Ruiz, Puracé and Galeras are among the most active volcanoes with a long record of eruptions. The eruptions of Puracé in 1949, Nevado del Ruiz in 1985 (~25,000 casualties), and Galeras in 1993, remain among the deadliest disasters in the country.

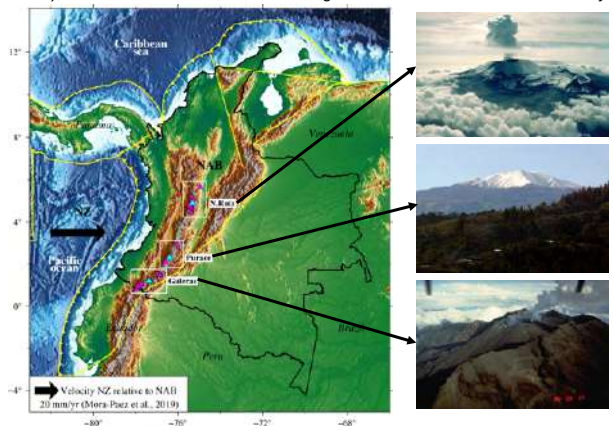

Fig 1. Colombia's tectonic and volcanic setting. Magenta triangles represent the volcanic arc. Studied volcanoes are shown in cyan: Nevado del Ruiz (north), Puracé (center) and Galeras (south). Volcanoes' photos taken from the Global Volcanism Program website.

1.2. Deformation monitoring and challenges

Volcano deformation relates to the storage or movement of fluids inside magmatic or hydrothermal reservoirs that might be linked to potential eruptions.

→ GPS and tiltmeters* and C-band SAR images (Sentinel).

(*installed and maintained by the volcanological observatories of the Servicio Geológico Colombiano)

CHALLENGES	POTENTIAL SOLUTIONS
• Limited resolution of displacement maps due to sparse instrumental networks.	• Continuous displacement maps by using satellite imagery SAR.
• C-band data is affected by vegetation (Sentinel mission).	• L-band data is **less** affected by vegetation **(ALOS mission)**.
• Large tropospheric noise due to strong weather fluctuations.	• Implementation of weather corrections with external datasets **(GACOS and GPS).**

1.3. Objectives

- To estimate accurate maps of displacement from satellite geodetic data.
- To perform precise models of each volcano's internal deformation source responsible of surface displacements (magmatic or hydrothermal).

2. DATA & METHODS

2.1. Data: 100 ALOS-2 images period 2014-2023 in ascending and descending orbits.

2.2. Methods

2.2.1. InSAR technique

Interferogram: Interference pattern between 2 images of the same region at different times → Time series.

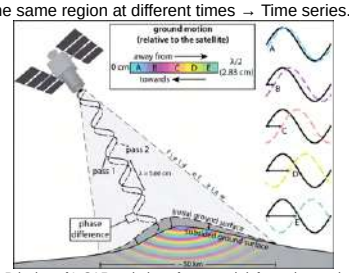

Fig 3. Principe of InSAR technique for ground deformation analysis. Taken from: http://insar.space/insar-technology/

2.2.2.Tropospheric noise corrections

- Based on elevation and phase linear correlation.
- Based on ZTD* GACOS products (weather models).
- Based on GPS-derived ZTD maps.

*ZTD: Zenith Total Delay.

2.2.3.Time series of displacements

Analysis of temporal evolution of surface displacements related to the volcano dynamics.

2.2.4. Modeling

Inversion of InSAR data to define the internal source responsible of the observed surface displacements.

DefVolc (https://doi.org/10.18145/defvolc)

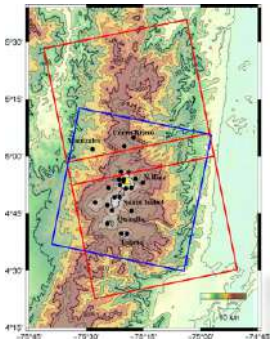

Fig 2. Nevado del Ruiz ALOS-2 footprints in ascending (red) and descending (blue) orbits. GPS stations are denoted by black dots.

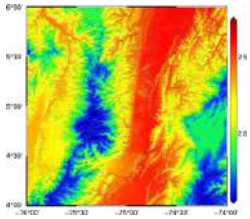

Fig 4. GACOS ZTD map on October 3rd, 2015 at Nevado del Ruiz volcano.

3. PRELIMINARY RESULTS

3.1. Cumulative displacement maps and time series

Nevado del Ruiz volcano

20 sequential interferograms (11 in ascending orbit and 9 in descending orbit).
20 cumulative maps of deformation.

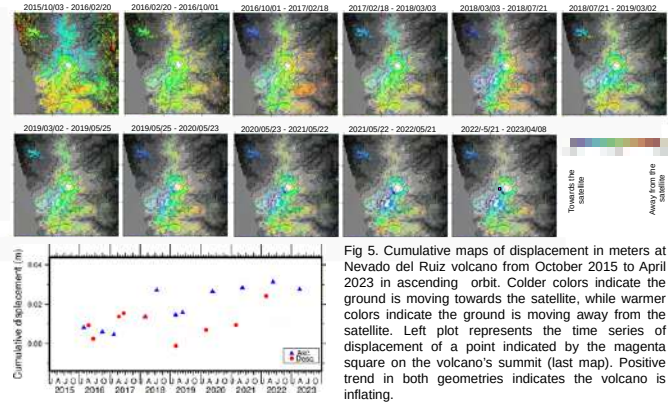

Fig 5. Cumulative maps of displacement in meters at Nevado del Ruiz volcano from October 2015 to April 2023 in ascending orbit. Colder colors indicate the ground is moving towards the satellite, while warmer colors indicate the ground is moving away from the satellite. Left plot represents the time series of displacement of a point indicated by the magenta square on the volcano's summit (last map). Positive trend in both geometries indicates the volcano is inflating.

Puracé volcano

21 sequential interferograms (12 in ascending orbit and 9 in descending orbit).
21 cumulative maps of deformation.

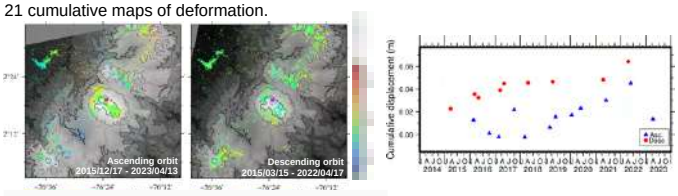

Fig 6. Cumulative maps of displacement in Puracé volcano from December 2015 to April 2023 (ascending orbit) and from March 2015 to April 2022 (descending orbit). Right side plot represents the time series of displacement of a point indicated by the magenta square on the volcano's summit, showing that the volcano is inflating.

Galeras volcano

17 sequential interferograms (9 in ascending orbit and 8 in descending).
17 cumulative maps of deformation.

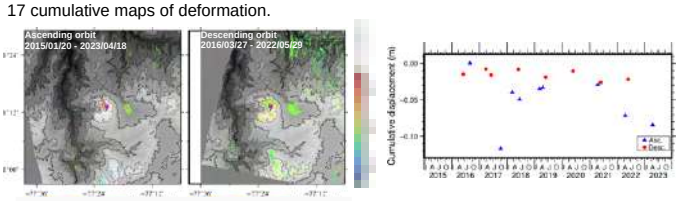

Fig 7. Cumulative maps of displacement in Galeras volcano from January 2015 to April 2023 (ascending orbit) and from March 2016 to May 2022 (descending orbit). Right side plot represents the time series of displacement of a point indicated by the magenta square on the volcano's summit. It shows slow deflation during the analyzed period.

3.2. Preliminary interpretation

Assumption: The motion is mostly vertical because ascending and descending orbits present the same sense of motion for the three volcanoes.

Volcano	Preliminary interpretation
Nevado del Ruiz	Upward trend of time series (Fig 5) could indicate volcano inflation related to magma movement to the surface. **Risk of eruption?**
Puracé	Similar as for Nevado del Ruiz volcano (Fig. 6) **Risk of eruption?**
Galeras	Downward trend of time series (Fig. 7) could indicate volcano deflation. **Risk of collapse of volcano edifice? No risk at all?**

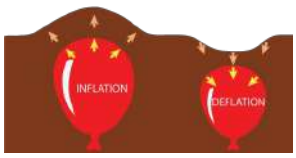

Fig 8. Cartoon representing the ground deformation due to inflation and deflation of a magma chamber beneath it → simple model. (http://www.mshslc.org/activity/volcano-deformation/)

4. FUTURE PERSPECTIVES

Future work will focus on:

- Increasing the redundancy of the time series by computing more interferograms.
- Performing further noise corrections (external data).
- Modeling the deformation signals to characterize the volcano's internal source.
- Publishing scientific papers and presenting at academic meetings.

ACKNOWLEDGMENTS

ALOS-2 images were provided by PIXEL group (PALSAR Interferometry Consortium to study our Evolving Land Surface) from the Japanese Spatial Agency – JAXA and the Earthquake Research Institute of Tokyo University – ERI. GACOS products were obtained at http://www.gacos.net/. GPS data is provided by the GeoRED project and the Volcanological Observatories of the Servicio Geológico Colombiano. I would also like to thank ISTerre researchers from UGA for their guidance in SAR data processing.

SPATIO-TEMPORAL DYNAMICS OF THE FOREST AND SAVANNAH FORMATIONS IN THE BRAZILIAN PANTANAL WETLAND

Uelison Mateus Ribeiro [1], Mauro Henrique Soares da Silva [2], Samuel Corgne [1], Damien Arvor [1]
[1] CNRS, Univ Rennes, Univ Brest, Nantes Université, LETG, UMR 6554; Universidade Federal de Mato Grosso do Sul, Campus Três Lagoas – UFMS/CPTL
uelison.ribeiro@univ-rennes2.fr

INTRODUCTION

. The Pantanal biome is a heterogeneous and dynamic ecosystem located in the heart of the South American continent.

. In the context of climate change, understanding how different plant physiognomies respond to ongoing hydroclimatic regimes is essential information for planning mitigation and adaptation strategies at the landscape level.

. Wetland functional assessment approach could improve the efficiency of environmental management [1].

. Here, we investigate the spatio-temporal variability in the dynamics of the forest and savanna formations in the Pantanal do Abobral, one of the Pantanal's sub-regions.

METHOD

1. Study area

- Pantanal do Abobral (19°18'31''S; 57°03'15''W).

- subregion of the Pantanal wetland.

2. Land cover

- Forest and Cerrado (wooded savanna) land cover classes: Brazilian Annual Land Use and Land Cover Mapping Project [2]

3. Phenology

Data: Harmonized Landat Sentinel-2 (HLS) [3]

4. Rainfall

Data: Climate Hazards Group InfraRed Precipitation with Stations (CHIRPS)[4]

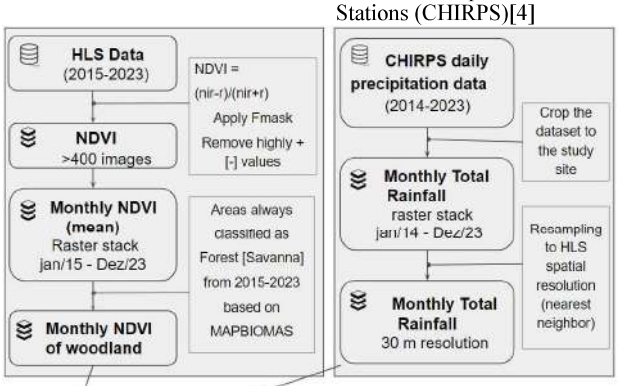

5. Pointwise Correlation

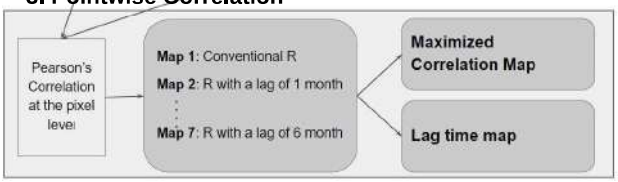

6. Functional indices

We calculated the average annual cycle from the monthly NDVI betwen 2015-2023, due to the high cloud cover. Negative values were replaced by zeros [5].

- annual NDVI integral (**NDVI-I**): sum of the NDVIs of the average annual cycle;

- Intra-annual relative range (**RREL**): subtraction between the maximum NDVI and the minimum NDVI of the average annual cycle, divided by the NDVI-I.

(R v.4.2.3 software)

RESULTS

Dynamics between phenology and rainfall

In general, tree vegetation responds to rainfall with a one to two months lag time.

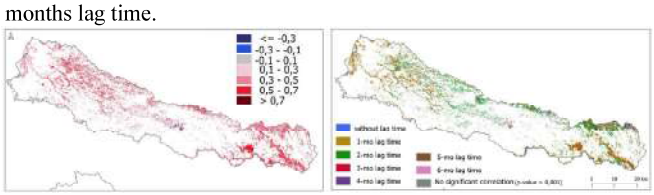

Fig. 1. Spatial distribution of the maximised Pearson correlation between monthly NDVI time series of woody vegetation and precipitation for the Pantanal do Abobral (left) and the number of months of lag needed to maximise the correlation (right).

Even within the same land cover class, different typologies respond differently to local precipitation regimes.

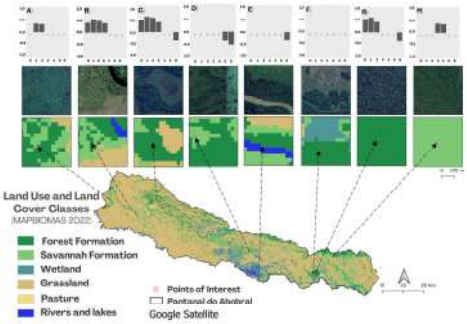

Fig. 2: Land cover in the Abobral Pantanal in 2022 (MapBiomas). Highlight points A-H with graphical representations indicating Pearson's correlations with 0 (conventional correlation) up to 6-month lag.

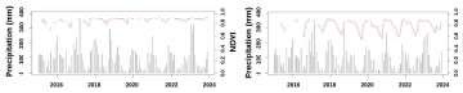

Fig. 3. Monthly NDVI and precipitation from points E (left) and G (right) shown in Fig. 2.

Spatial variations in functional indices

Riparian forests show higher NDVI-I (as a proxy for primary production) and less pronounced RREL (seasonality of carbon fluxes) than other forest typologies in the region.

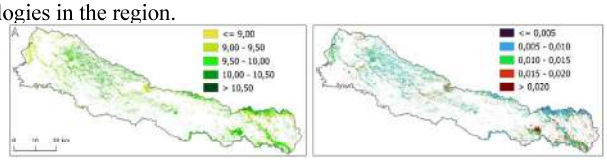

Fig. 4: NDVI-I (left) and RREL (right) of the forest and savannah formations derived from the average annual NDVI cycle (2015-2023), Pantanal do Abobral.

CONCLUSIONS

Although the change from forest to other land uses has received a great deal of monitoring effort in recent years, the habitat diversity of the remaining forests may be silently fading away. Mapping approaches that describe the functional attributes of vegetation can, therefore, contribute to landscape-level planning of mitigation and/or adaptation strategies to the effects of climate change.

REFERENCES
[1] S. Rapinel, L. Hubert-Moy, and B. Clément, 'Combined use of LiDAR data and multispectral earth observation imagery for wetland habitat mapping', *Int. J. Appl. Earth Obs. Geoinformation*, vol. 37, pp. 56–64, May 2015, doi: 10.1016/j.jag.2014.09.002.
[2] C. M. Souza *et al.*, 'Reconstructing Three Decades of Land Use and Land Cover Changes in Brazilian Biomes with Landsat Archive and Earth Engine', *Remote Sens.*, vol. 12, no. 17, p. 2735, Aug. 2020, doi: 10.3390/rs12172735.
[3] J. Masek *et al.*, 'HLS Operational Land Imager Surface Reflectance and TOA Brightness Daily Global 30m v2.0'. NASA EOSDIS Land Processes DAAC, 2021. doi: https://doi.org/10.5067/HLS/HLSL30.002.
[4] C. Funk *et al.*, 'The climate hazards infrared precipitation with stations—a new environmental record for monitoring extremes', *Sci. Data*, vol. 2, no. 1, p. 150066, Dec. 2015, doi: 10.1038/sdata.2015.66.
[5] S. Rapinel, E. Fabre, S. Dufour, D. Arvor, C. Mony, and L. Hubert-Moy, 'Mapping potential, existing and efficient wetlands using free remote sensing data', *J. Environ. Manage.*, vol. 247, pp. 829–839, Oct. 2019, doi: 10.1016/j.jenvman.2019.06.098.

Hypergolic Ignition Drop Testing of Liquid Propellants with Hydrogen Peroxide

C. Soudarin[1,2,3], M. Bellenoue[1], Y. Batonneau[2], R. Beauchet[2], B. Boust[1], L. Prévost[3]

[1]PPrime Institute, CNRS, ISAE-ENSMA, Université de Poitiers, Chasseneuil-du-Poitou, France
[2]IC2MP, Université de Poitiers, CNRS, 4 rue Michel Brunet B27, TSA 51106, 86073, Poitiers Cedex 9, France
[3]CNES, Space Transportation Directorate, 52 rue Jacques Hillairet, 75612 Paris Cedex

Context

Because of current environmental issues, space industry is looking for green and non-carcinogenic propellants to replace hydrazine. Although hydrazine and its derivatives present very conclusive propulsion performances, the European commission REACH – Registration, Evaluation, Authorization and Restriction of Chemicals – has identified hydrazine as a substance of very high concern. Under such circumstances, hydrogen peroxide, HTP, is a promising candidate to replace hydrazine in hypergolic systems which enable to avoid adding an external ignition system and allow both easy and multiple restarts.

- **Parametric study on the ignition delay time (IDT) of a reference mixture of triglyme/sodium borohydride with HTP**
- **Test and compare hypergolicity between HTP and five combinations of three fuels (hexane, heptane, THF) and three additives (TEB, TEA, TMA)**

EXPERIMENTAL SET-UP

A test-bed allowing to control atmosphere during drop test was designed:
- Volume of the chamber: 8.2 L
- Chamber wiped out of air with argon
- Fuel poured in a beaker thanks to a syringe through the top plate
- Syringe-pump to drop HTP onto the fuel
- Camera used for visualization: FASTCAM Mini UX50 type 160K-M-8G
- Acquisition frequency: 4 kHz for triglyme and sodium borohydride
  8 kHz for other additives (uncertainty on the IDT down to 0.25 ms)

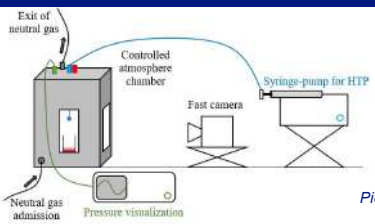

Scheme of the experimental set-up for drop tests

Picture of the inside of the controlled atmosphere chamber

CHARACTERISATION OF THE IGNITION

Triglyme and Sodium Borohydride ($NaBH_4$)

IDT = time between the first contact of the HTP droplet with the fuel (pic. 2) and the first flame/bright area (pic. 5)

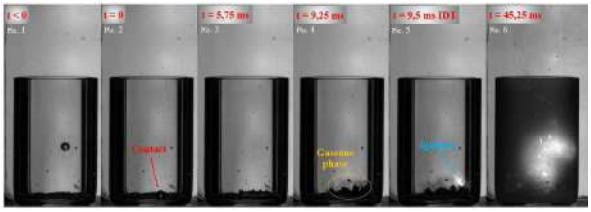

HTP 90 wt. % + triglyme/3.8 wt. % $NaBH_4$ under argon

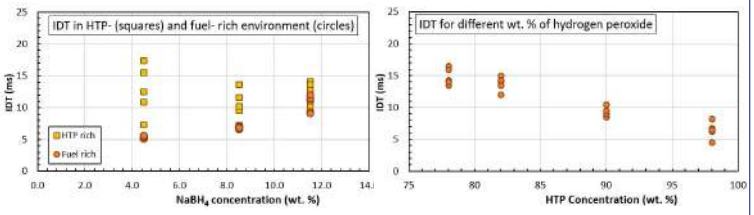

➢ IDT ↗ when HTP rich environment

➢ IDT ↘ when HTP concentration ↗

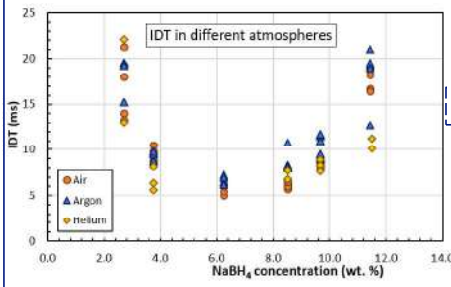

Drop tests conditions:
- HTP 98 wt. %
- Fuel rich environment
- Temperature, velocity and pressure constant [1-5]

➢ IDT min. between 4 and 8 wt. % $NaBH_4$ (viscosity ↗ with $NaBH_4$ concentration [1])
➢ No impact of the atmosphere over the IDT

Triethyl-, Trimethylaluminum and Triethylborane

TEB-tetrahydrofuran	TEB-hexane
10.2 wt. % TEB in THF	14.5 wt. % TEB in hexane

TEA-heptane	TEA-hexane	TMA-heptane
20.3 wt. % TEA in heptane	16.5 wt. % TEA in hexane	20.7 wt. % TMA in heptane

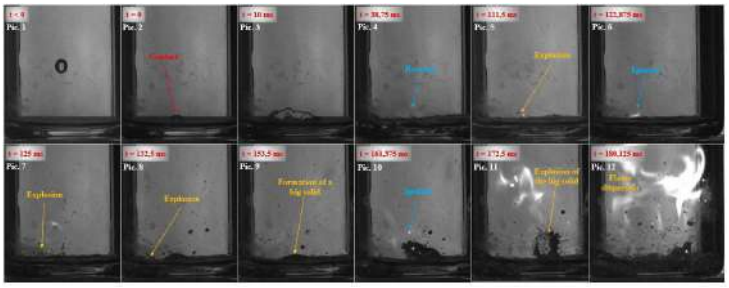

HTP 98 wt. % + heptane/15.6 wt. % TEA under argon

Contact fuel/HTP → Formation of solids → Burning of solids, sometimes followed by ignition → Solid explosions

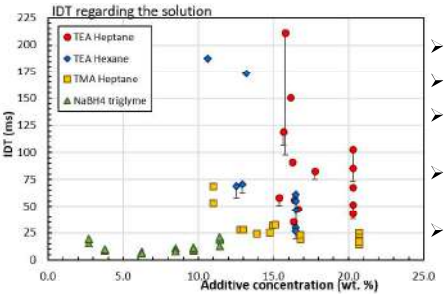

➢ **TEB:** no ignition
➢ **TEA heptane:** ignition
➢ **TEA hexane:** faster ignition (solvent properties)
➢ **TMA heptane:** faster ignition (acidic strength)
➢ **$NaBH_4$ triglyme :** fastest ignition

CONCLUSION

Optimum configuration for ignition between triglyme/$NaBH_4$ and HTP:

4-8 wt. % $NaBH_4$ — Max HTP concentration — Fuel rich environment — Velocity, pressure, temperature constant

Triglyme/$NaBH_4$ mixture presents lower IDT than TEA and TMA. However, TMA in heptane shows satisfying ignition delays. Choosing an additive more acid than TMA in a solvent with low autoignition temperature and heat capacity could decrease the IDT down to 10 ms or less.

ACKNOWLEDGEMENT
CNES and « Région Nouvelle-Aquitaine » are gratefully acknowledged for co-funding this study. The authors acknowledge financial support for some apparatus from the European Union and « Région Nouvelle-Aquitaine ». This work pertains to the French government program « Investissements d'Avenir » (EUR INTREE, reference ANR-18-EURE-0010).

CONTACT : *celia.soudarin@ensma.fr*

References

Save me!

Recueil des posters

Session 5

S05-01 | Post-doc | **BEN MAAMER Chayma** | LHCEP, Lyon | Encadrant CNES : Achraf DYANI | POSTER |
Développement de HEDMs pour la propulsion spatiale

S05-02 | Doc | **BERNABEU FRIAS Joan Miguel** | TéSA / ISAE-SUPAERO, Toulouse | Encadrant CNES : Yoan GREGOIRE | POSTER |
Precise positioning using carrier phase measurements in a swarm of satellites

S05-03 | Doc | **BOUTON Maxime** |ONERA, Palaiseau | Encadrant CNES : Marie THERON | POSTER |
Dynamique et instabilités de combustion d'une flamme Lox/CH4 en conditions d'injection transcritique dans les moteurs fusées

S05-04 | Doc | **FERNANDEZ Sébastien** | CNES, Toulouse | Encadrant CNES : Francois-Xavier ESNAULT | POSTER |
Lien optique en espace libre pour la dissémination de fréquence et la chronométrie géodésique

S05-05 | Doc | **GROUFFAL Salomé** | LAM, Marseille | Encadrant CNES : Christian MUSTIN | POSTER |
Caractérisation d'exoplanètes en transit dans la zone habitable

S05-06 | Doc | **KOUNY Karim** | Lab STICC UMR CNRS 6285, Brest | Encadrant CNES : Nicolas FIL | POSTER |
Conception, réalisation et test de solutions de filtrage innovantes pour des missions satellitaires petites plateformes

S05-07 | Post-doc | **MAILLARD Lisa** | Ifremer/LOPS, Plouzané | Encadrant CNES : Yannice FAUGERE | POSTER |
Échanges air-mer sous les cyclones tropicaux: app ort de la modélisation couplée et des observations satellite

S05-08 | Post-doc | **NAVARRETE Camila** |OCA, Nice | Encadrant CNES : Philippe LAUDET
Dissecting the Milky Way stellar components through their ages

S05-09 | Post-doc | **RAKOTOARISOA Mahefa Mamy** | ESO, Angers | Encadrant CNES : Philippe MAISONGRANDE | POSTER |
Modélisation multi-agents pour la compréhension du fonctionnement des mares de la vallée du fleuve Sénégal

S05-10 | Doc | **ROBIN Colas** |ISAE-Supaero, Toulouse | Encadrant CNES : Francis ROCARD | POSTER |
Determining the surface properties of Phobos using the MMX rover WheelCams

S05-11 | Doc | **TAHTOUH Maria** | ONERA, Toulouse | Encadrant CNES : Denis STANDAROVSKI | POSTER |
Apprentissage profond pour la prédiction et la modélisation de l'effet des éjections de masses coronales

S05-12 | Doc | **VERGERON Xavier** | UMontpellier, Montpellier | Encadrant CNES : Félix PEROSANZ | POSTER |
Utiliser les données de gravimétrie spatiale pour estimer l'état thermique et mécanique des plaques lithosphériques

Future of space propulsion: toward Polynitrogen High Energy Density Materials

Chayma Ben Maamer[1,2] (chayma.ben-maamer@univ-lyon1.fr), Pierre Cavalere[1,2] Jennifer Lesage De La Haye[2,3], François Liger[2,3], Emmanuel Lacôte[1,3], Achraf Dyani[2]
Université Claude Bernard Lyon 1, LHCEP[1], Centre National d'Etudes Spatiales[2] (CNES), Centre National de la Recherche Scientifique (CNRS)[3]

Why polynitrogen HEDMs ?

Ariane 6
propulsive system

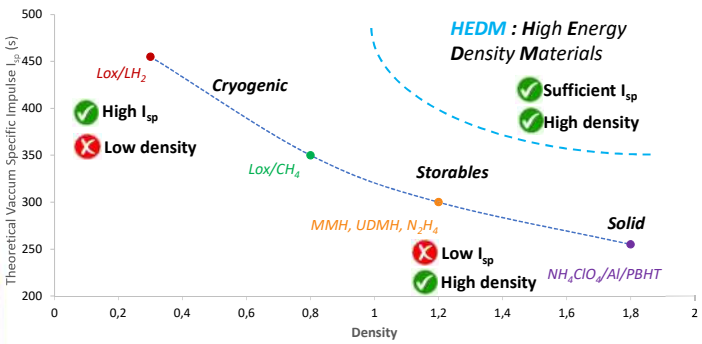

Technological breakthrough

Ariane Ultimate
propulsive system

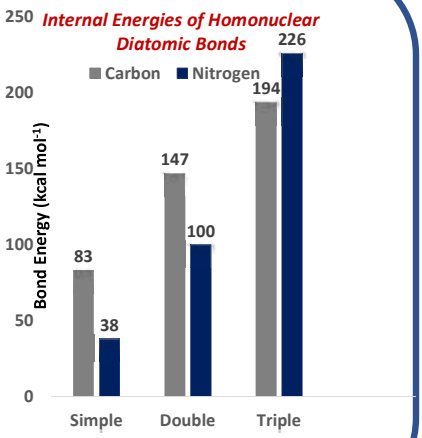

CNES Principal Innovative Vector

Fully- decarbonated cyclic poly-nitrogen *HEDM*

- Lower toxicity with N_2 and H_2 ejection gases
- Monoergol
- Cheapest and simplest reignitable rocket engine
- Small launcher by constructive Index
- High density and I_{sp} , storable
- Single Stage To Orbit
- Decomposition not combustion

Pathways to High-Energy Density Materials: Key Components

- ***Initial Insights[4]***

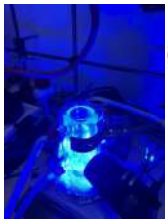

- Modulation of azide or azo compounds remains unattainable.
- Sulfonylazimines can be prepared in good yields.

- ***New Insights***

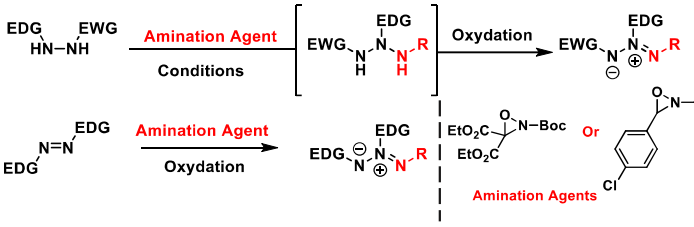

- Seamless modulation of hydrazines and amination agents
- One step reaction.

Potential Building Blocks: Nitrogen-Rich Molecules as Precursors to Polyazotic HEDMs

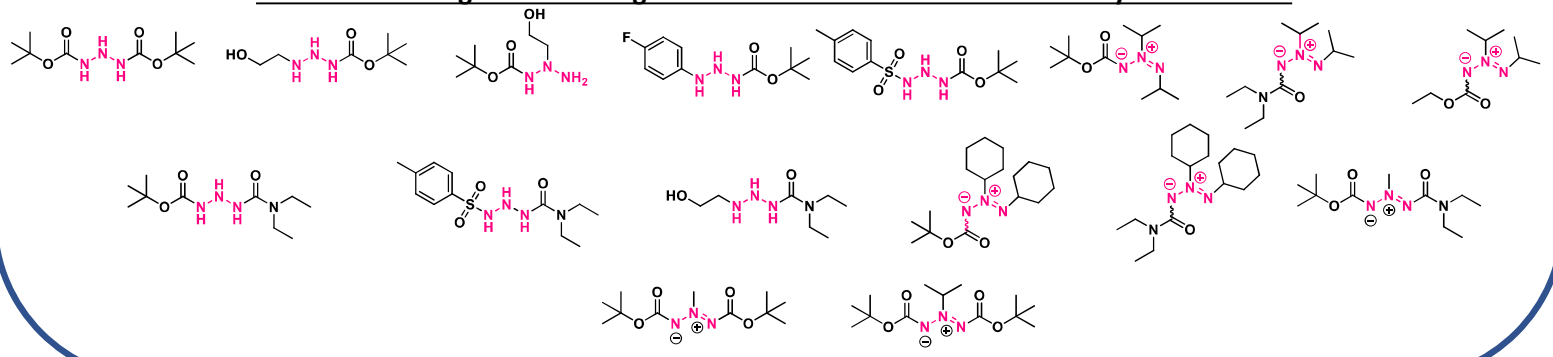

- **HEDMs** are required for greener, safer, smaller, reusable and more efficent launchers → **Technical breakthrough.**
- **HEDMs** chemistry of polynitrogen compounds is very complex and difficult → **Poor literature data for reactivity.**
  → **Lots of by-products, unstability of reactants and products.**
- **HEDMs** are key for the future of space propulsion and space exploration → **Global competitive challenge for space agencies.**

[4]E. Gamby, F. Liger, L. Joucla, E. Lacôte, *Eur. J. Org. Chem.* **2022**, e202201071.

Precise positioning using carrier-phase measurements in a swarm of satellites

Joan Bernabeu[1,2], Lorenzo Ortega[1,3], Antoine Blais[4], Yoan Grégoire[5], Eric Chaumette[1]

TéSA[1], ISAE-SUPAERO[2], IPSA[3], ENAC[4], CNES[5]

1. Context

A distributed instrument in space missions consists of multiple satellite nodes that must operate as a single entity by merging their measurements.

This demands accurate positioning of each satellite, both globally and within the group, which typically involves measuring the time delay (τ) between nodes. Finer time-delay measurements lead to more accurate positioning, which can be enhanced by considering the impact of τ on the signal's carrier phase.

This thesis aims to characterize the impact in estimating τ under such conditions through performance assessments.

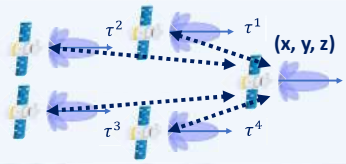

Figure 1 °

2. Signal model

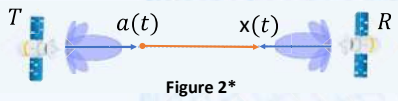

Figure 2*

$$x(t) = \left(\alpha e^{j\phi}\right) a(t;\boldsymbol{\eta}) e^{-jw_c b(t-\tau)} + n(t),$$
$$\phi = \psi - \boldsymbol{w_c\tau}, \quad \boldsymbol{\eta} = (b, \tau), \quad n(t) \sim CN(0, \sigma_n^2), \quad \alpha \in \mathbb{R}$$

- **Evidence:**
  Phase ψ and $\boldsymbol{w_c\tau}$ are mixed up together as a single entity.
- **Hypothesis:**
  If ψ is compensated, $\boldsymbol{w_c\tau}$ can be included in the signal model allowing for:
  - more representative signal model
  - more accurate estimation performance assesment of τ.
- **Methods:** Devise strategies dealing with ψ term,

3. Methods

Conduct performance assessment by deriving the CRLB [a] and MLE [b], based on assumptions on the signal model.

A. Static model [1]

Doppler b and ψ known and compensated

$$x(t) = \alpha a(t-\tau) e^{-jw_c\tau} + n(t)$$

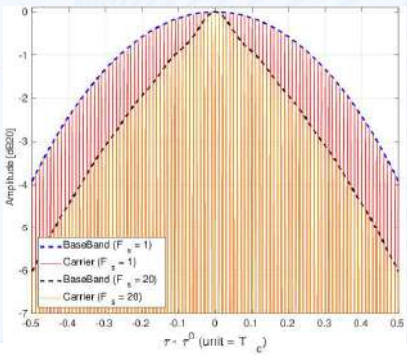

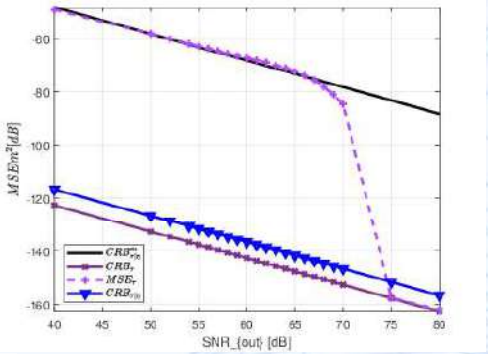

B. Dynamic model [2]

b unknown and ψ compensated

$$x(t) = \alpha a(t;\boldsymbol{\eta}) e^{j\varphi(\eta)} + n(t)$$
$$\varphi(\boldsymbol{\eta}) = w_c\,(\tau + b(t-\tau))$$

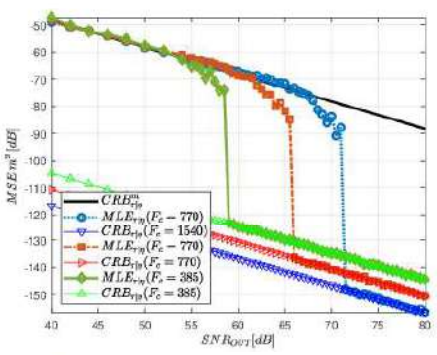

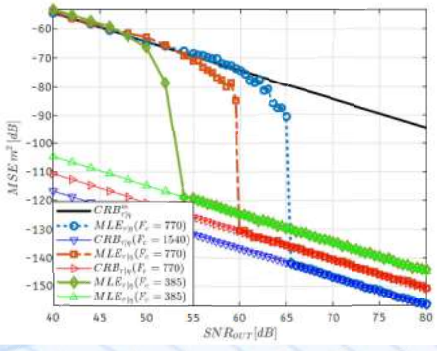

C. Dynamic model + comp.

b unknown and ψ estimated & compensated

$$x(t) = \alpha a(t;\boldsymbol{\eta}) e^{j\varphi(\eta)} \boldsymbol{e^{(\psi - \widehat{\psi})}} + n(t)$$
$$\widehat{\psi} = \psi + n_a(t), \qquad n_a(t) \sim N(0, \sigma_a^2)$$

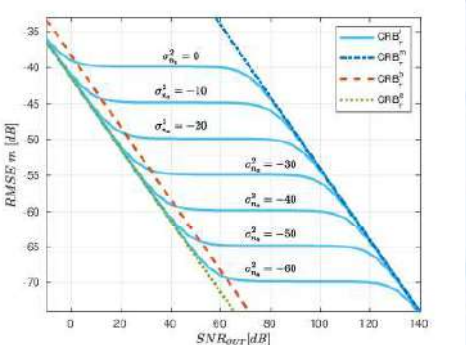

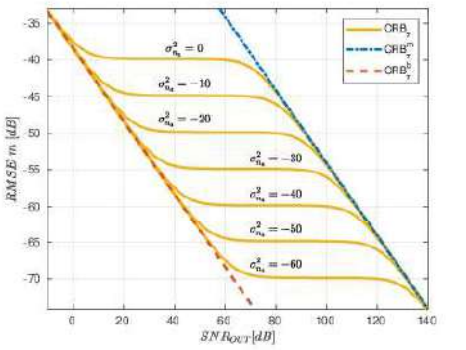

a. CRLB: Cramér-Rao Lower Bound

b. MLE: Maximum-Likelihood Estimator

°. **Figure 1:** Satellite computes its coordinates from differences in signal's time of arrival τ^k

*. **Figure 2:** Transmitter (T) sends $a(t)$ and receiver (R) receives $x(t)$

References

- [1] J. M. Bernabeu Frias, L. Ortega, A. Blais, Y. Gregoire and E. Chaumette, "Time-Delay and Doppler Estimation with a Carrier Modulated by a Band-Limited Signal," *2023 IEEE 9th International Workshop on Computational Advances in Multi-Sensor Adaptive Processing (CAMSAP)*, doi: 10.1109/CAMSAP58249.2023.10403430.
- [2] Bernabeu, J.M., Ortega, L., Blais, A. et al. On the asymptotic performance of time-delay and Doppler estimation with a carrier modulated by a band-limited signal. EURASIP J. Adv. Signal Process. 2024, 47 (2024). https://doi.org/10.1186/s13634-024-01134-2

RÉPUBLIQUE FRANÇAISE
Liberté Égalité Fraternité

cnes CENTRE NATIONAL D'ÉTUDES SPATIALES

ONERA THE FRENCH AEROSPACE LAB

Dynamique et instabilités de combustion d'une flamme swirlée LOx/CH_4 en conditions d'injection transcritiques dans les moteurs fusées

Maxime BOUTON – ONERA DMPE/MPF
Directeur de thèse : Guillaume RIBERT, CORIA
Encadrant ONERA : Aurélie NICOLE, DTIS/RFDS; Aurélien GENOT DMPE/STAT

Contexte

- Volonté de l'Europe de développer de nouveaux lanceurs réutilisables et réallumables à bas coûts
- Développement de nouvelles technologies : injecteurs swirl LOx/CH_4
- **Problème**: injecteurs susceptibles de présenter des instabilités thermo-acoustiques[1], potentiellement destructrices pour la fusée
- Collaboration CNES/ONERA pour étudier la dynamique des injecteurs swirl
- **Objectif industriel** : Disposer d'un outil permettant de simuler un injecteur swirlé et de prévoir rapidement le développement de ses instabilités thermo-acoustiques

Définitions

Instabilité thermo-acoustique:
- Interaction entre l'acoustique de la chambre et la flamme en phase [2]
- Emballement du niveau des fluctuations de pression [2] ⇨ destructeur à haute fréquence [3]
- Plusieurs mécanismes en sont à l'origine, notamment l'excitation acoustique de la vitesse d'injection des réactifs [3]

Swirl:
- Mise en rotation de la phase liquide (oxygène liquide = LOx) à l'injection [4]
- Phénomène de succion en sortie d'injecteur [4]
- Meilleur mélange des réactifs et stabilisation de la flamme [4]

Processus d'interaction flamme/acoustique

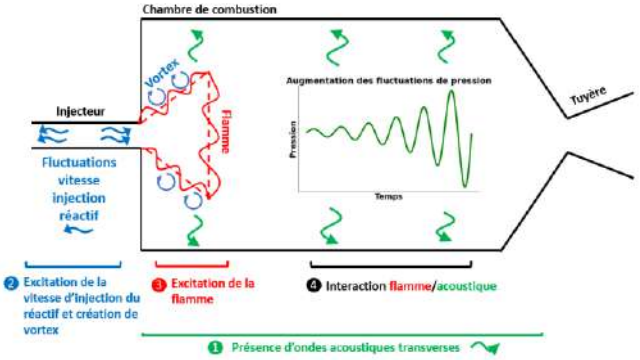

Approche expérimentale

- Post-traitement d'un tir du banc cryogénique MASCOTTE de l'ONERA
- Première compréhension de la physique de l'écoulement
- Observations vidéos de la phase liquide LOx (ombroscopie) et de la combustion (chimiluminescence OH*)

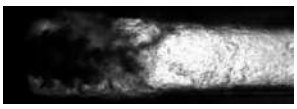

Image ombroscopie (phase liquide)

Image chimiluminescence OH* (combustion)

- Début du post-traitement et mise en évidence de modes anti-symétriques et symétriques par analyse spectrale et filtrage des vidéos

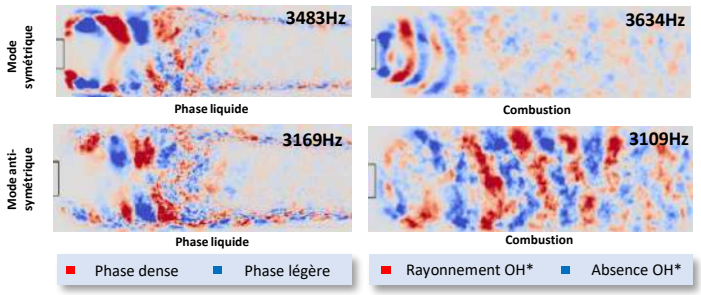

- **Données de pression en milieu de chambre et de température aux parois disponibles mais qui restent à être exploitées**
- **Objectif de l'exploitation des tirs expérimentaux : constituer une base de données détaillée pour un point de fonctionnement du banc MASCOTTE en vue de la validation des simulations numériques avant de réaliser des excitations acoustiques la flamme numérique.**

Approche numérique

- Mise en place d'une simulation à grande échelle (LES) du point de fonctionnement MASCOTTE expérimental avec le code CEDRE de l'ONERA pour une approche plus détaillée des phénomènes

Champ instantané de température, vecteurs vitesses et iso-volume de fraction massique d'oxygène liquide

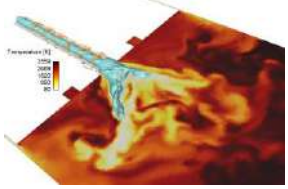

- Début de validation avec les données expérimentales : comparaison des grandeurs moyennes

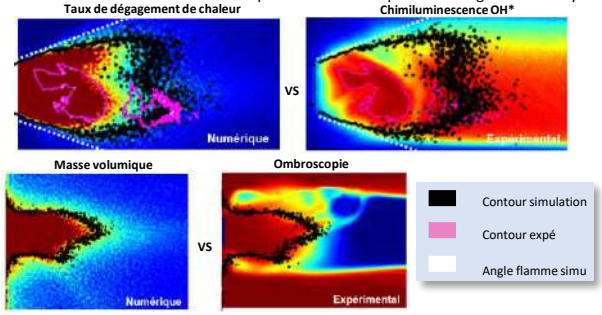

- **Objectif: confirmer, par analyse spectrale, que la flamme reproduit les comportements expérimentaux. Meilleure compréhension de l'écoulement (par visualisation 3D de multiples grandeurs physiques)**
- **Finalité: forçage acoustique de la flamme via la modulation de la vitesse d'injection des réactifs afin de valider l'approche analytique**

Méthodologie & Résultats

Approche analytique

- Mise en équation du mécanisme de déstabilisation de la flamme
- Travaux préliminaires: utilisation d'un modèle existant [5] dans des conditions de forçage fortes, impliquant une réponse de flamme non-linéaire dans le cadre d'une flamme coaxiale [6]
- **Objectif: extension du modèle à une flamme swirlée par transformation géométrique de la trajectoire d'une perturbation de vitesse autour de la flamme**
- **Finalité: modèle d'estimation rapide de la stabilité d'une flamme swirlée LOx/CH_4 pour peu de ressources numériques et matérielles**

Effet du forçage de la vitesse d'injection du CH_4 sur une flamme coaxiale

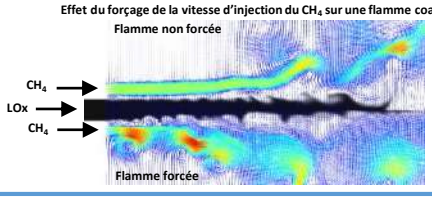

Principe d'extension par transformation géométrique du modèle initial

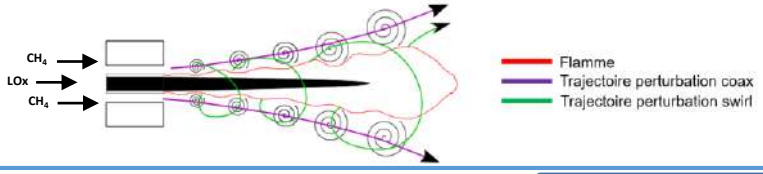

Bibliographie

[1] Guven U. (2018). Simulation haute-fidélité de la combustion pour les moteurs-fusées. PhD, Normandie Université
[2] Rayleigh, L. (1896). The Theory of Sound. *Macmillan*.
[3] Hakim, L. (2013). Dynamics of transcritical coaxial flames in high-frequency transverse acoustic fields: Application to liquid rocket engine instabilities. PhD thesis, Ecole Centrale Paris.
[4] Syred N., Beér J.M. (1974). Combustion in swirling flows: a review. *Combustion and flame*, **23**, pp143-201
[5] Nez R., Schmitt T., Gonzalez-Flesca M.S., Candel S. & Ducruix S. (2017). Response of a transcritical coaxial flame to fuel injection rate modulations: analysis and low-order modeling of the generation of unsteady heat release rate. EUCASS
[6] Bouton M., Genot A., Nicole A., Ribert G. (2024). Flame dynamics under methane injection modulations in a transcritical coaxial flow. Space Propulsion

ED 591 PSIME

Free-Space Optical link via a balloon for clock comparison

S. Fernandez*[1], F. -X. Esnault[1], T. Lévèque[1], P. Wolf[2]

1 – Centre National d'Etudes Spatiales
2 – SYRTE, Observatoire de Paris-PSL, CNRS, Sorbonne Université, LNE
*email : sebastien.fernandez@cnes.fr

Abstract

Current optical clocks reach incertitude levels as low as 10^{-18} in terms of fractionnal frequency. In the meantime, work is on the way to make them transportable.

Numerous applications will take advantages of such characteristics, such as **chronometric geodesy**, that will enable geopotential mapping over a region with centrimetric level acuracy.

Transportable, flexible and easily deployable optical link over 10 to 100km are needed to supplement the fibre metrology network.

We develop such a free space link relayed by an **optical transceiver mounted on a balloon** to avoid line-of-sight obstruction.

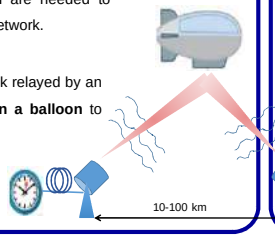

1. Introduction and State of the art

TOFU: **U**ltrastable **O**ptical free space **F**requency **T**ransfer, via the phase of a continuous 1542nm laser.

Free space optical (vs. fiber) link → high **phase and power noise levels and bandwidths** :

- **Atmospheric turbulence** ($\Delta f/f \sim 10^{-13}$ up to 500Hz)
- Balloon & payload motion (**Doppler effect** $\Delta f/f \sim 10^{-11}$)

TOFU folded link to a balloon

- Retroreflector onboard the balloon = passive payload
- Emitter & receiver co-located => easy local phase noise verification
- Reaches **8.10^{-19} uncertainty after 20s integration time [1]**

Next step: build an active flying terminal

- Onboard power coupling into a fibre
- Point-to-point architecture
- Opens the way for a 3-point operational architecture

Worldwide demonstrated free space links :

- Point-to-point vs. folded
- Ground to ground vs. ground-air
- Continuous vs. pulsed laser

Shen et al, 2022

113km point-to-point link (type I) between 2 static terminals with 89dB power loss. Time & frequency transfer. Reaches 10^{-19} frequency instability using optical frequency combs.

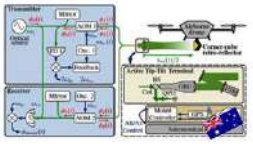

Dix-Mathews et al, 2023

1.3km folded link (type III) to a corner cube onboard a flying drone. Frequency transfer via a continuous laser's phase, reaching $2.5.10^{-18}$ fractionnal frequency stability after 3s integration time, despite drone motion up to 0.3m/s.

Caldwel et al, 2023

300km round trip folded link between two closely located (type II) optical terminals. Time and frequency transfer using frequency combs.

2. Phase-stabilized folded link to a balloon

Setup

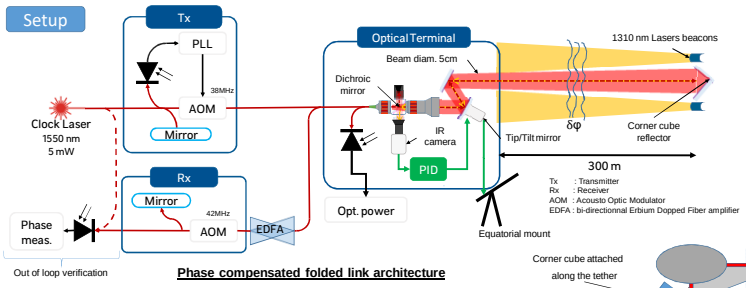

Phase compensated folded link architecture

Airborne payload

- Corner cube aligned with the tether for passive pointing at the ground terminal
- 4 laser diode beacons with λ=1330nm

Optical terminal

- Common Tx & Rx transceiver : fine optical pointing at the corner cube
- Actuators : tip-tilt mirror (+/-1mrad HF) + equatorial mount (slow motion)
- IR camera : beacons image acquisition (200fps)
- Pointing bandwidth **limited at 25Hz** due to camera USB delay

Phase stabilization unit

- Michelson unbalanced architecture
- Digital Phase Lock Loop (D-PLL) + AOM actuator : 30kHz BW
- Rx and Tx co-located => out-of-loop verification

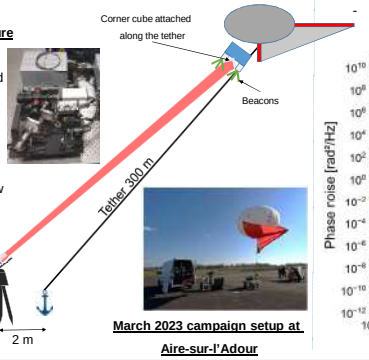

March 2023 campaign setup at Aire-sur-l'Adour

Results

Phase stabilization

Up to 20-minute long phase time series were acquired during the campaign with no power loss.

- System performance : MDEV of the out of loop beat note fractional frequency
- Reaches **8.10^{-19} after 20s** integration time, **PLL ON**
- 300m ground link for horizontal/vertical comparison
- Open loop main phase noise source :
  - GROUND : air index fluctuations (**turbulence**)
  - FLIGHT : balloon & payload motion (**Doppler effect**)

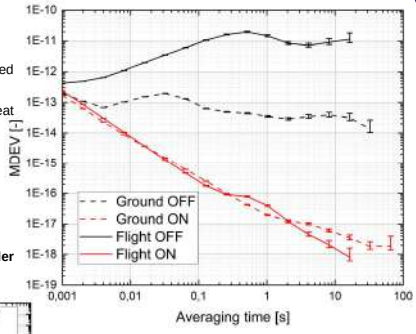

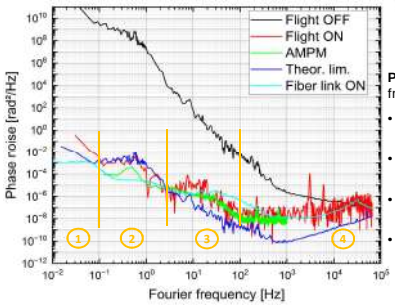

Noise characterization

Phase noise power spectral density reveals the link's frequency stability limiting factors:

- **Phase noise correction delay**: fundamental limit reached between 0.1 and 3Hz (2)
- **Thermal uncompensated effects**: below 0.1Hz (1), e.g. in the out-of-loop measurement fibre
- Amplitude to noise conversion (**AMPM**) between 3 and 100Hz (3), due to mixing in the measurement chain
- At higher frequencies (4), the PLL itself is limitating (as compared with a 300m fiber link).

3. Active airborne terminal flight tests

Next step : *active terminal* onboard the balloon

→ couple the received laser beam into a monomode fibre

→ Tests at Aire-sur-l'Adour August 2024

Terminal design

- Commercial **gimbal** : 2-axis pointing actuator
- Visible camera : ground beacons imaging
- µ-computer
- Fibre collimator + photodiode
- 1330nm laser beacons

Max. weight : 8kg (balloon limitation)

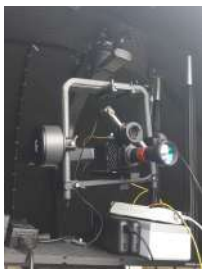

Setup

Results

Functional tests

- Software, power, wifi control
- The gimbal remains locked to ground station for hours of operation

Laser power stabilization

- Depending on weather conditions
- → Better with constant stable wind
- Gimbal max depointing +/-1mrad
- → 500µrad required
- → Frequent power extinctions

Campaign rex

- Need for a second pointing stage
- Ground terminal limitating too

Gimbal pointing error

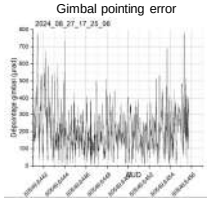

Onboard injected power

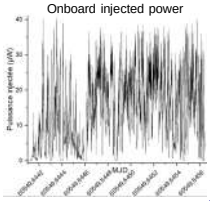

4. Coming next

Next step : **March 2025**

Goals :

1. **Onboard tip-tilt mirror** design
2. **Ground functionnal tests** : TT ability to compensate for gimbal pointing error
3. **In flight tests** at Aire-sur-l'Adour
4. Try & attach a **fibre along the tether**
5. **Point-to-point phase stabilization** (with fully deployed & folded architectures)

Both configurations offer advantages :

- I : genuine point-to-point link
- III : power budget representative of a 3-point link

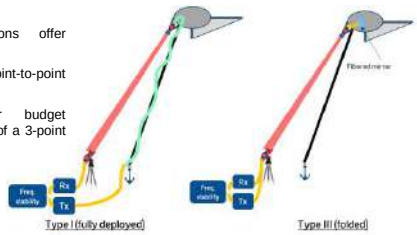

[1] Maron Nicolas, Fernandez Sébastien et al., "Free space optical link to a tethered balloon for frequency transfer and chronometric geodesy," Opt. Express **32**, 4267-4276 (2024)

Characterisation of transiting planets in the habitable zone

Salomé Grouffal Aix Marseille Univ, CNRS, CNES, LAM, Institut Origines, Marseille, France

PhD supervisor: Alexandre Santerne
CNES supervisor: Christian Mustin

The PLATO (ESA) MISSION

The PLATO mission is expected to be launched in 2026. It is the ultimate transit discovery space mission, with the objective of detecting and characterising Earth-like planets in the habitable zone of Sun-like stars. More than 5600 exoplanets have already been discovered but very few are in the habitable zone of their host stars.

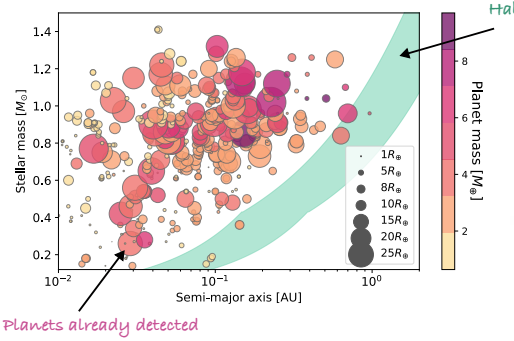

PLATO will use the method of transits to detect exoplanets: When an exoplanet passes in front of its host star, it causes a temporary dip in the star's brightness, which can be measured to determine the planet's size

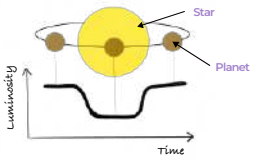

The system around HIP41378: a testbed for PLATO

HIP41378 is a fascinating planetary system hosting at least 5 transiting planets discovered by the K2 mission in 2016. HIP41378f (P = 542 days), the most well-known of the three outer planets has been observed to transit 5 times. This planet, having a size of about Saturn and a temperate climate, is classified as a 'Super-Puff' due to its unusually low density that still needs to be fully understood. The HIP41378 system will provide valuable insights and help us prepare for the upcoming PLATO mission. The study of long-period planets presents unique challenges in terms of characterization.

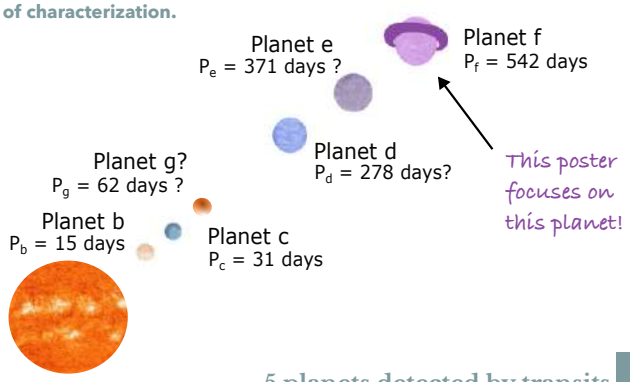

How can we better understand the nature of planet HIP41378 f and the architecture of the planetary system?

5 planets detected by transits

Two K2 campaigns, six sectors of TESS

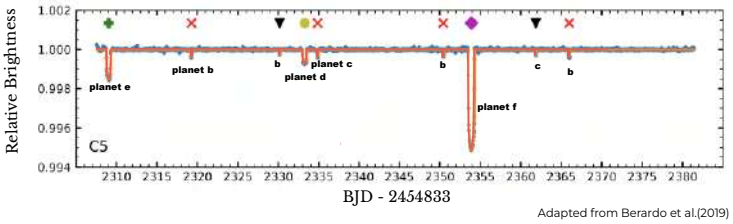

Adapted from Berardo et al.(2019)

The principle of the Rossiter-McLaughlin effect

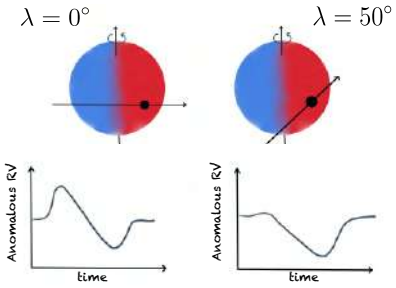

The Rossiter-McLaughlin (RM) effect is the measurement of the stellar radial velocity variation during planetary transit. With this method it is possible to measure the projected obliquity of a system.

Four transits of planet f have already been obsersed thanks to space-based instruments. In 2022 we observed the 5th transit from the ground using the Rossiter-McLaughlin effect. This enables us to follow-up the planet and understand if the planetary orbits is aligned or misaligned with the stellar rotation axis.
Problem : The transit is 19 hours long... longer than the duration of a night!

This analysis is important to plan future PLATO follow-up of long-period planets.
HIP41378f is the planet with the longest orbital period with a measured obliquity.

A Worldwide campaign of observations to detect the transit of HIP41378f

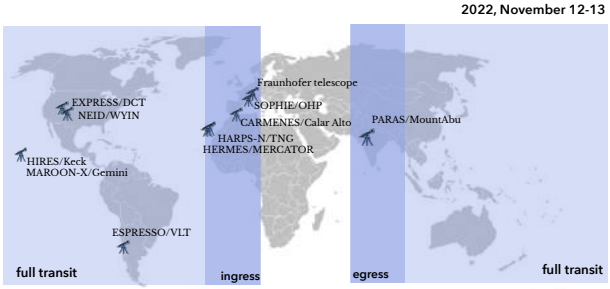

With a duration of 19 hours, the transit can only be observed in its totality by combining observations from different places on Earth. **All the instruments listed on the map had planned observations for this unique event.** Eight of them were able to observe a part of the transit.
The challenge is now to combine the observations from these different instruments with different techniques of radial velocity reduction.

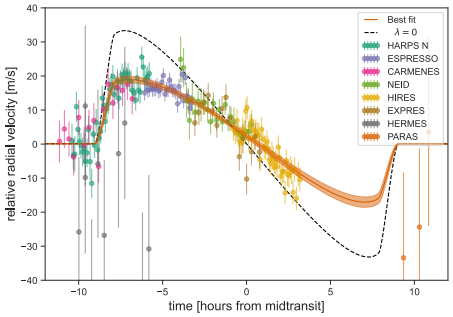

Result: From the analysis we can conclude that **the planetary orbit is misaligned with the stellar rotation axis.** This is a step forward a better understanding of planetary formation and evolution.

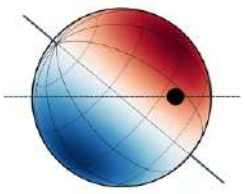

This is a view of the star and the planetary orbits with **a projected obliquity of ~ 50 degrees and a stellar inclination of ~ 70 degrees**

References: Akinsanmi et al. (2020), Alam et al. (2022), Berardo et al.(2019), Lund et al. (2019), McLaughlin (1924), Rossiter (1924), Santerne et al. (2019), Vanderburg et al. (2016)

RÉPUBLIQUE FRANÇAISE
Liberté Égalité Fraternité

cnes CENTRE NATIONAL D'ÉTUDES SPATIALES

Conception, réalisation et test de solutions de filtrage innovantes pour des missions satellitaires petites plateformes

Karim KOUNY[#], Jean – Francois FAVENNEC[#], Jessica BENEDICTO[#], Nicolas FIL[*], Eric RIUS[#]
[#]Lab-STICC UMR CNRS 6285, 29238 Brest, France
[·]Centre National d'Etudes Spatiales (CNES), 18 Avenue Edouard Belin 31400 Toulouse, France
karim.kouny@univ-brest.fr

Introduction

Contexte : Miniaturisation du volume et de la masse des équipements radiofréquences (filtres et duplexeurs) pour des missions satellitaires petites plateformes.
Solution étudiée : Filtres basés sur des résonateurs coaxiaux présentant des sauts d'impédances qui permettent d'obtenir plusieurs degrés de libertés dans les plans transversaux et longitudinaux.

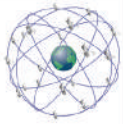

Filtre à résonateurs coaxiaux SIR $\lambda_g/2$ (CC-CC) à 4 sections

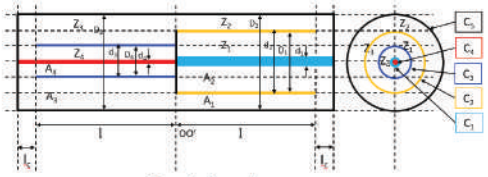

→ CC-CC,
→ 2 étages,
→ 4 sections,
→ Mode TEM,
→ $\lambda_g/2$.

Topologie retenue

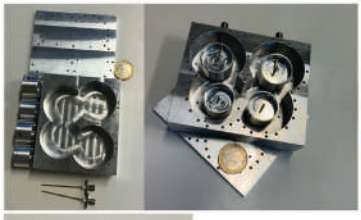

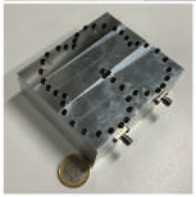

→ 44 vis de serrages
→ 22 vis de réglages
→ Usinage classique (CNC)

Filtre réalisé par usinage classique

Synthèse :

$$Z_i = \frac{1}{2\pi}\sqrt{\frac{\mu_0}{\varepsilon_0\varepsilon_{ri}}}\ln\frac{D_i}{d_i}$$

$$l = \frac{c}{2\pi f_0}\tan^{-1}\sqrt{\frac{1}{M}}$$

$$M_{ij} = \frac{Z_i}{Z_j}$$

$$M = \frac{M_{12} + M_{23} + M_{12}M_{23} + M_{12}M_{34}}{M_{12}M_{23}M_{34} + M_{23}M_{34} + M_{34} + 1}$$

$$Z_{r4_s} = jZ_4\left(\frac{\gamma tan^3\theta - \delta tan^1\theta}{\alpha tan^2\theta - \beta tan^4\theta - 1}\right)$$

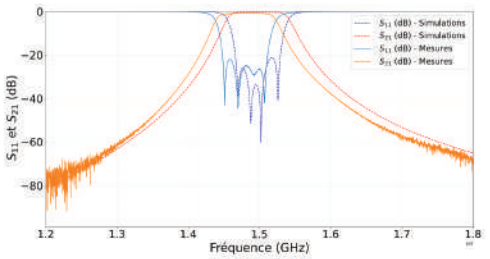

→ Bande L,
→ $f_0 = 1.5GHz$,
→ $w = 4.5\%$,
→ Volume RF = $159cm^3$,
→ Matériau utilisé : Aluminium
$\sigma_{Aluminium} = 38.10^6 S/m$
→ Version symétrique

Simulations et mesures des paramètres S (transmission et réflexion)

Champs – Mode TEM

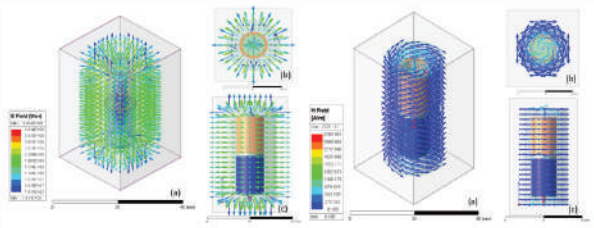

Simulation eigenMode - $\lambda_g/2$ CC-CC 4 Section : Distribution des champs électriques et magnétiques : a) vue isométrique, b) vue de dessus, et c) vue de côté.

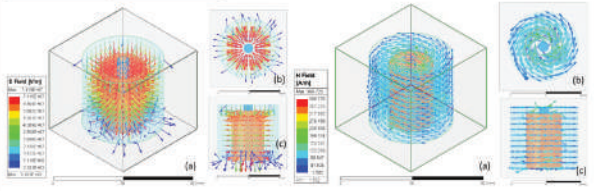

Simulation eigenMode - $\lambda_g/4$ CC-CO 2 Section : Distribution des champs électriques et magnétiques : a) vue isométrique, b) vue de dessus, et c) vue de côté.

Filtre à résonateurs coaxiaux SIR $\lambda_g/2$ et $\lambda_g/4$

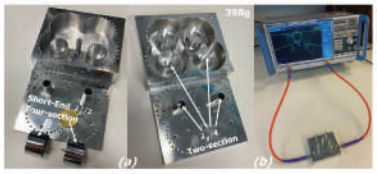

→ Bande L,
→ $f_0 = 1.5GHz$,
→ $w = 4.5\%$,
→ Volume RF = $159cm^3$,
→ Matériau utilisé : Aluminium
$\sigma_{Aluminium} = 22.10^6 S/m$
→ Version symétrique

Filtre – Mix topologique réalisé par usinage classique

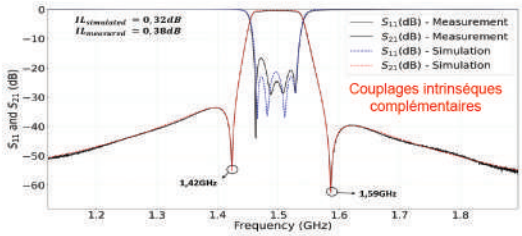

Simulations et mesures des paramètres S (Transmission et réflexion)

Conclusion

→ La topologie SIR coaxiale $\lambda_g/2$ court-circuit à quatre sections a été étudiée et présentée,
→ Filtre avec des résonateurs symétriques identiques, c'est-a-dire, $M_{12} = 1/M_{34}$ et $M_{23} = 1$, répondant aux spécifications attendues et présentant un seuil élevé de tenue en puissance pour un volume RF réduit,
→ Filtres à résonateurs coaxiaux SIR topologique $\lambda_g/2$ et $\lambda_g/4$ (association de résonateurs coaxiaux SIR différents) permettant d'obtenir des zéros de transmissions sans l'ajout d'élément physique

Lab-STICC UBO Université de Bretagne Occidentale

Région BRETAGNE

Air-sea exchanges under tropical cyclones

Lisa Maillard (lisa.maillard@ifremer.fr) [1], Swen Jullien [1]

[1] Ifremer, Univ. Brest, CNES, CNRS, IRD, Laboratoire d'océanographie physique et spatiale

1 Motivation

If the forecast of **tropical cyclone's (TC)** tracks have greatly improved in the last decades, the prediction of their intensity still fails to capture rapid intensity changes (Emanuel 2018). Among the factors likely to help improve forecasts is the in-depth understanding of air-sea interactions.

Air-sea exchanges indeed regulate exchanges of mass, heat, momentum and gas between the ocean and the atmosphere, which drives the development of TCs. **Surface waves** (the ones that surfers love) have been shown to modulate such exchanges. However, observing and modeling waves and air-sea exchanges under intense rotating and translating cyclonic winds is a real challenge. Air-sea exchanges are therefore **parameterized** in state-of-the-art forecasts and climate models, but the existing parameterizations are imperfect. Thanks to newly available **satellite observations** and **high-resolution coupled models**, we aim at evaluating and improving wave-induced effects on air-sea interactions under TCs.

2 Modeling tropical cyclones

Tropical cyclones interact with the background environment (land, basin dynamics, synoptic flow, etc.) and each tropical basin has its own specificity. To overcome these specificities and **focus on the impact of air-sea exchanges only**, a **simplified modeling framework** is constructed in which a TC is translated by a uniform zonal flow.

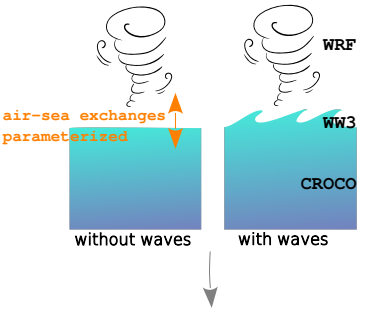

Only forced simulations for now
Coupling coming soon ...

Three high resolution models:
- **atmosphere** 9km + 3km around TC (+ 1km soon)
- **waves** 9km
- **ocean** (soon) 9km

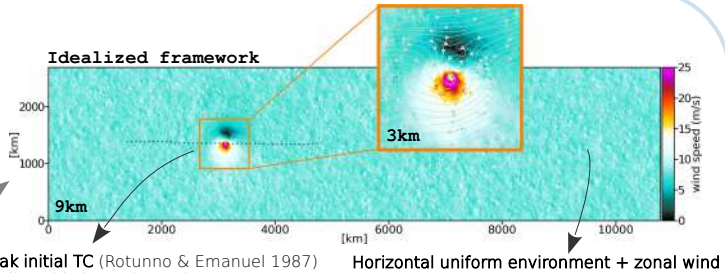

Weak initial TC (Rotunno & Emanuel 1987)
→ adjustable intensity & size

Horizontal uniform environment + zonal wind
→ adjustable coriolis, sea surface temp., wind
⚠ Not trivial! Follows Nolan et al. 2011

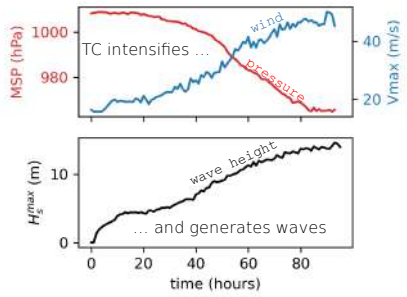

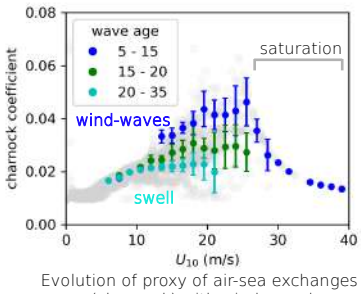

Evolution of proxy of air-sea exchanges (charnock) with wind speed

3 Observing sea state under cyclones

Our understanding of air-sea interactions in tropical cyclones is slowed down by the difficulty of observing the sea state and its spatial variability under such extremely violent conditions. Two CNES satellites have recently added new elements to the characterisation of this complex sea state:

- **CFOSAT**
  SWIM instrument
  full wave spectrum
  ✓ under TCs (Le Merle et al. 2022)
- **SWOT**
  KaRIn instrument
  wave height
  very wide swaths
- **Other data**
  altimeters
  wind (radars & radiometers)

Case study: **TC Ernesto** (Cat 2, August 2024)

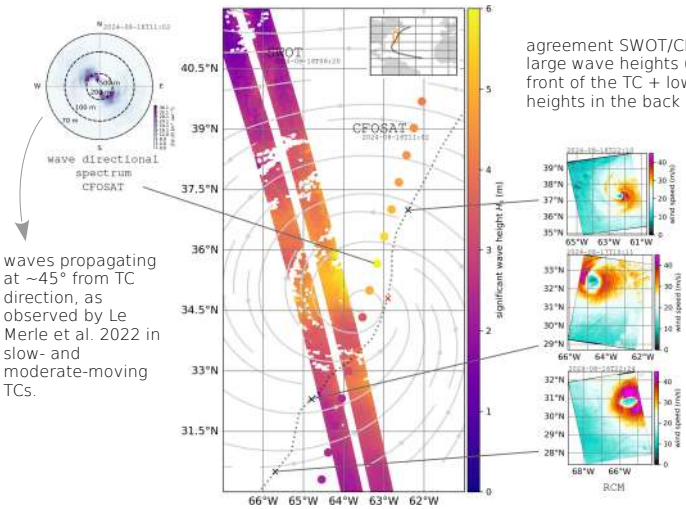

agreement SWOT/CFOSAT: large wave heights (6 m) in front of the TC + lower heights in the back

waves propagating at ~45° from TC direction, as observed by Le Merle et al. 2022 in slow- and moderate-moving TCs.

4 Toward a synergy obs. & model

Future efforts oriented toward a comparison between collected observations & simulated TCs:

- characterize the sea state in simulated & observed TCs (categories of translation speed, intensity, and size)
- evaluate the sensitivity of simulated TCs on various air-sea exchange parameterizations (based on wave age, peak period of wind waves, wave directional spreading, new source terms and coupled exchanges in WW3 ...)
- use obs. to evaluate the most realistic parameterization(s)
- compare simulations with/without waves: what physics is missing when waves are not taken into account ?

→ Results will be tested on several real-case simulations of TCs impacting French overseas territories, on which CFOSAT and/or SWOT observations are available.

5 Summary

What are most climate models missing in TC dynamics by not simulating waves ? Which parameterization should they use to be the most accurate ? How does the spatial asymetry of waves under a TC impact its dynamics and structure ? Using our idealized framework in synergy with newly acquired satellite observations of the sea state, we will try to answer these questions.

ANR AWARE
CFOSAT-LAGOON

S05-08 | Post-doc | **NAVARRETE Camila** |OCA, Nice |
Encadrant CNES : Philippe LAUDET

Dissecting the Milky Way stellar components through their ages

Absent

Un système multi-agents pour la compréhension du fonctionnement des mares de la vallée du fleuve Sénégal.

Rakotoarisoa Mahefa Mamy[1], Ba M.[2], Kebe E.A.K.[2], Taibi A. N.[1]
[1]Université d'Angers, ESO-Angers, France, UMR 6590 CNRS . [2]EDEQUE/ UCAD, Sénégal, UMI SOURCE 272 IRD.

Contexte et problématique

- Les mares du waalo (zone inondable du fleuve Sénégal):
  - un remplissage lié à la crue du fleuve et ses défluents
  - bouleversé ces dernières décennies («grande sècheresse», aménagements hydrauliques et hydro-agricoles)

Quels impacts sur la connectivité des mares avec le fleuve?

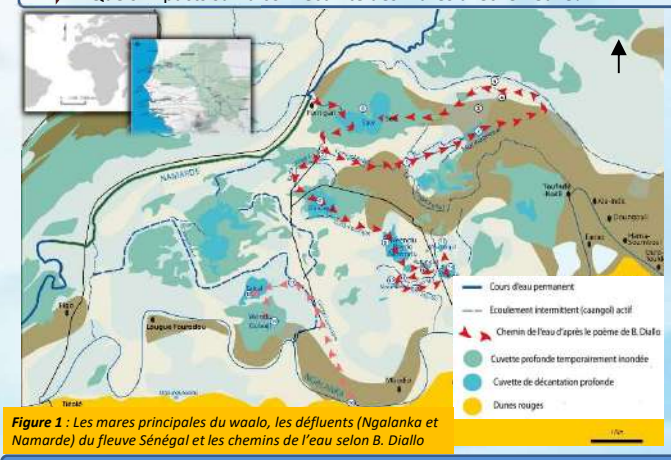

***Figure 1** : Les mares principales du waalo, les défluents (Ngalanka et Namarde) du fleuve Sénégal et les chemins de l'eau selon B. Diallo*

L'indicateur de connectivité hydrologique par SMA

- Développement d'un modèle utilisant un système multi-agents (SMA) basé sur le mouvement simple « d'agents hydrologiques »
- La simulation permet de :
  - suivre le comportement de chaque agent en interaction avec son environnement (topographie, occupation du sol, éléments du paysage)
  - reconstituer les chemins d'écoulements de l'eau
  - produire des indicateurs spatiaux à échelle fine permettant de caractériser la connectivité des entités hydrologiques

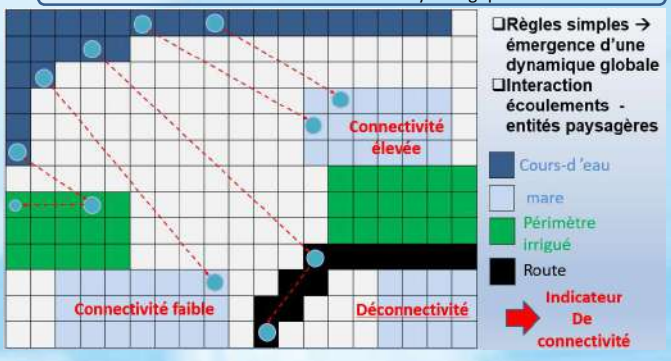

***Figure 2** : Fonctionnement du modèle multi-agents (SMA).*

Résultats : Reconstitution de l'évolution du paysage et sorties du modèle de connectivité sur le waalo

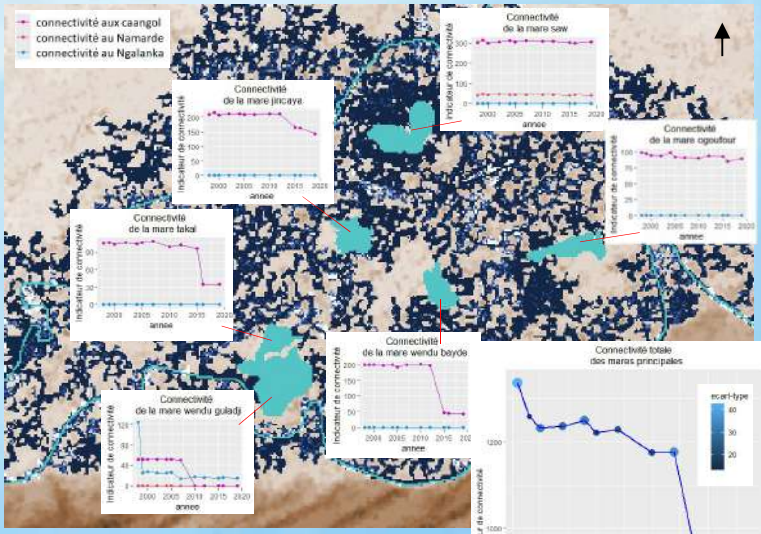

***Figure 3** : Résultats de la simulation d'une crue provenant des défluents. Extraction de l'indicateur de connectivité moyen pour les 6 mares principales du waalo de 1998 à 2020 (10 simulations pour chaque année) et des potentiels chemins d'écoulements*

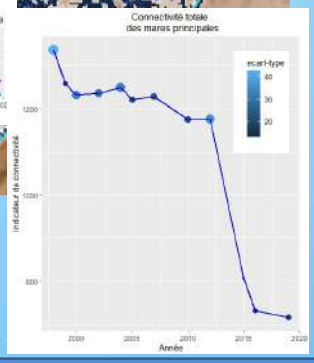

***Figure 4** : Evolution de la connectivité totale des 6 mares. Deux périodes principales de diminution rapide de la connectivité : 1999 – 2000 et 2012 – 2015*

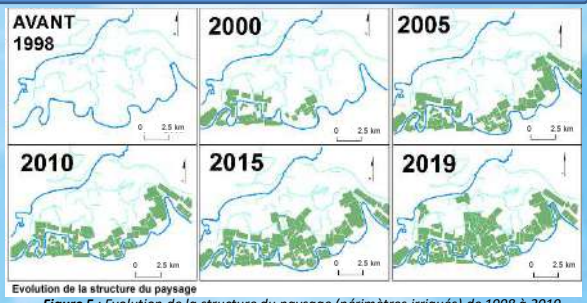

***Figure 5** : Evolution de la structure du paysage (périmètres irrigués) de 1998 à 2019 utilisée comme donnée d'entrée dans le modèle SMA.*

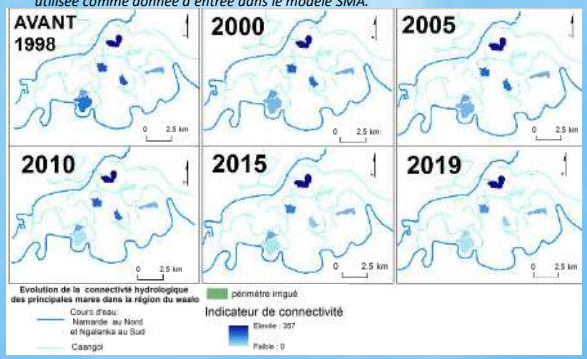

***Figure 6** : Spatialisation des connectivités issues des différentes simulations par année.*

Intérêt de l'étude de la microtopographie : vers l'analyse de l'inter-connectivité hydrologique

- Construction d'un MNT (Modèle Numérique de Terrain) à échelle fine (résolution centimétrique jusqu'à 7cm) à l'aide de relevés drones sur le complexe des mares de Koyli Goti dans le Jeeri (zone non inondable au sud du fleuve avec un remplissage des mares par les pluies)
- Utilisation des données topographiques à haute résolution pour le système multi-agents
- Identification des mares à travers un algorithme utilisant le modèle SMA
- Etude du comportement des mares entre elles, vers le développement d'un indicateur d'inter-connectivité

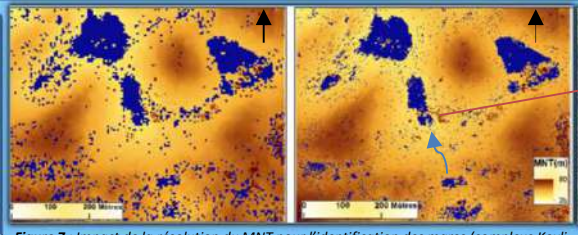

***Figure 7** : Impact de la résolution du MNT pour l'identification des mares (complexe Koyli Goti) par SMA. MNT à résolution de 5m à gauche et à résolution 50 cm à droite. Meilleure discrimination des connectivités à 50 cm.*

***Figure 8:** La mare de Koyli Goti en saison des pluies*

Discussions et perspectives

- Dans le waalo, l'indicateur de connectivité de la plupart des mares diminue au fil des années, validant ainsi l'hypothèse que la mise en place des périmètres irrigués déconnecte ces entités du fleuve. Certaines gardent une valeur constante car elles restent alimentées par les défluents.
- Les simulations à résolutions fines réalisées dans le jeeri plateau à faible dénivelée offrent un énorme potentiel pour la compréhension du comportement hydrologique à l'échelle micro topographique et pour le développement d'un autre indicateur tourné vers la notion d'inter-connectivité hydrologique

Mechanical properties of rubble pile asteroids though surface boulder morphological analysis

Colas Q. Robin [1] , Alexia Duchene [1], Naomi Murdoch [1], David Mimoun [1]

[1]Institut Supérieur de l'Aéronautique et de l'Espace (ISAE-SUPAERO), Université de Toulouse, Toulouse, France.

Context

JAXA MMX mission (launch: 2026)

- Sample return from **Phobos**
- **CNES/DLR** Rover: **IDEFIX**

Rover with scientific payload

- **WheelCams**
- Cameras observing the wheels of the rover

What are the size/shapes of the boulders/rocks at the surface of Phobos ? What are the mechanical properties of the material ?

Link with mechanical properties

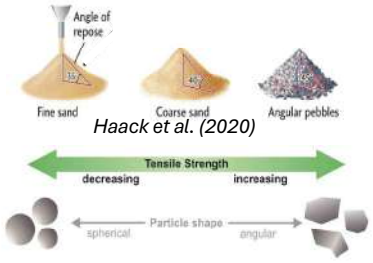

Haack et al. (2020)

The morphology of boulders provides information about mechanical properties and their history

- **Roundness** and particle size are linked to the **angle of friction**
- Lower **roundness**/larger median **particle size** = **larger friction angle** *[Bareither & al., 2008]*
- **Elongation** ratio of boulders on asteroids has also been linked with the **formation mechanism** *[Michikami & al., 2016]*

Conclusions & Perspectives

Other studies proposed that **Dimorphos** were formed by very slow **mass-shedding** of Didymos *[Pajola & al., 2024, Barnouin & al., 2024]*

Here, we propose that boulders at the surface of **Dimorphos** were formed by **catastrophic disruption** (assuming the apparent b/a is different from the real b/a)

- A further argument for the mass-shedding scenario as the formation of the binary **did not change** the shapes of the boulders
  - Assuming these boulders were on Didymos surface before
- Dimorphos surface is **40-130x older** than Didymos' *[Barnouin & al., 2024]*

Could other processes have modified the shape of the boulders ?

- **Thermal fatigue** but only **horizontal cracks** has been observed
- Dimorphos surface is **too young** for thermal cracks to reshape boulders *[Lucchetti & al., 2024]*

Demonstration of the utility of the pipeline that will be used with the WheelCams images and can be used for any other cameras observing boulders, rocks, etc. with a good enough resolution

All these results has been published in **Nature Communications**:
https://doi.org/10.1038/s41467-024-50147-w

Method

History and **physical** properties of the regolith of an asteroid may be recorded in the **shape of the boulders/pebbles** at its surface

Morphological analysis pipeline

- **Semi-automatic** boulder detection/segmentation
  - ***segmentanygrain*** python package
- 2D analysis pipeline for morphological parameters

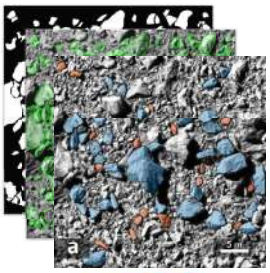

Roundness = $\frac{\Sigma_{i=1}^{N} r_i}{N.r_{max}}$

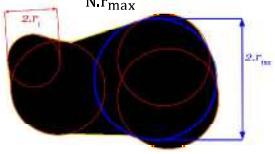

N : number of corners
r_i: radius of corner circles
r_{max}: radius of the maximum inscribed circle

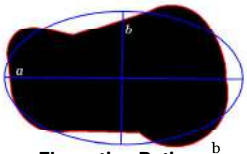

Elongation Ratio = $\frac{b}{a}$

Application of the pipeline on rubble-piles asteroids

Application of the pipeline the last image of **Dimorphos** (secondary of the binary asteroid **Didymos**) captured by the **DART** spacecraft and other rubble-pile asteroids : **Itokawa, Ryugu and Bennu**

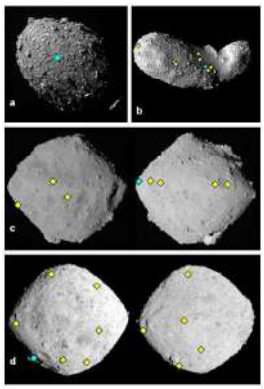

a) Dimorphos b) Itokawa
c) Ryugu d) Bennu

Angles of internal friction
(from boulders larger than 30px: minimal values):

Dimorphos : >32,7 ± 2,5°
Itokawa : >32,2 ± 2,5°
Ryugu : >31,6 ± 2,5°
Bennu : >31,1 ± 2,7°

In agreement with simulations or surface observations

Values derived from roundness values, method from *Suh & al., 2017*

$\varphi = 25,02 \times (1 - R) + 20$

Boulders formed by **catastrophic disruption**
In laboratory, disruptive impacts form fragments with b/a ~ 0,7-0,74 on average
In this study:

b/a **Dimorphos** = 0.66 ± 0.15
b/a **Itokawa** = 0.71 ± 0.15
b/a **Ryugu** = 0.71 ± 0.14
b/a **Bennu** = 0.68 ± 0.14

In agreement with other studies

References

- Bareither, C.A., Edil, T.B., Benson, C.H., Mickelson, D.M., 2008. Geological and Physical Factors Affecting the Friction Angle of Compacted Sands. Journal of Geotech. and Geoenv. Eng. 134, 1476–1489.
- Barnouin, O. et al. The geology and evolution of the Near-Earth binary asteroid system (65803)Didymos. Nat. Commun. https://doi.org/10.1038/s41467-024-50146-x (2024).
- Haack, D., Otto, K., Gundlach, B., Kreuzig, C., Bischoff, D., Kührt, E., Blum, J., 2020. Tensile strength of dust-ice mixtures and their relevance as cometary analog material. A&A 642, A218.
- Lucchetti, A., Cambioni, S., Nakano, R., Barnouin, O. S. & Pajola, M. Fast boulder fracturing by thermal fatigue detected on stony asteroids. Nat. Commun. https://doi.org/10.1038/s41467-024-50145-y (2024).
- Michikami, T., Hagermann, A., Kadokawa, T., Yoshida, A., Shimada, A., Hasegawa, S., Tsuchiyama, A., 2016. Fragment shapes in impact experiments ranging from cratering to catastrophic disruption. Icarus 264, 316–330.
- Pajola, M. et al. Evidence for multi-fragmentation andmass shedding of boulders on rubble-pile binary asteroid (65803) Didymos. Nat. Commun. https://doi.org/10.1038/s41467-024-50148-9 (2024).
- Suh, H. S., Kim, K. Y., Lee, J. & Yun, T. S. Quantification of bulk form and angularity of particle with correlation of shear strength and packing density in sands. Eng. Geol. 220, 256–265 (2017).

Deep-learning for the prediction and modelisation of the effect of CMEs on the Earth's magnetosphere

M. Tahtouh[1], G. Bernoux[1], A. Brunet[1], A. Sicard[1], D. Standarovski[2]

[1] DPHY, ONERA, Université de Toulouse, F-31000 Toulouse, France; [2] CNES, Toulouse, France

I. Context and objectives

Credits : SDO

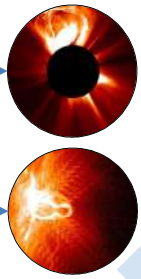

Coronal Mass Ejections (CMEs)
Credits : SOHO LASCO C2

Solar wind

Stream Interaction Region (SIR)

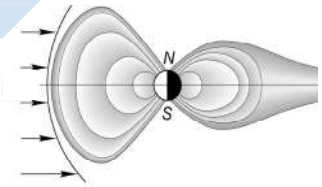

Solar flares
Credits : SDO/NASA

Geomagnetic storms

The **Solar activity** ensures an energy transfer from the Sun to the near-Earth space environment via the **solar wind** and transient structures: **CMEs** and **solar flares**. When interacting with the **Earth's magnetosphere**, these structures can strongly **deform it** and cause **geomagnetic storms** which have numerous **consequences on human activity, mainly disrupting satellite operations, communication systems and power grids.**

II. Problematic and approach

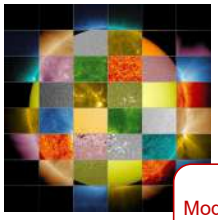

Credits: SDO

Physics-based models

ML-based models

Geomagnetic activity prediction, *directly from* ***solar imagery***, with parameters such as the **solar wind speed** and **geomagnetic indices** (Kp, Dst, etc.)

Upendran et al. 2020
Brown et al. 2022
Bernoux et al. 2022
Hu et al. 2022

Limitations
Models using **ML** show limitations in their capacity to predict storms associated to **CMEs**. This could be due to the **nature of the input data.**

Proposed solutions to enhance the predictions

- Use images at **high spectral** (512x512) and **temporal resolution** (1 image/6mins) → **SDO-ML dataset** (Galvez et al. 2019).
- Adapt a physical **feature extractor** for solar imagery.
- Use initial **CME parameters** that affect the most its **geoeffectiveness** as additional input to the model.

Initial CME parameters

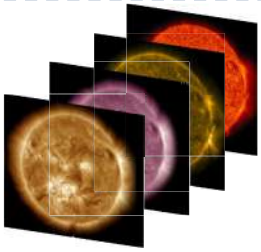

Probabilistic model to estimate the intensity and time of arrival of a storm

Development of a metamodel describing **EUHFORIA + SWING** (Collaboration with KU Leuven) for quantifying the **uncertainties** and analyzing the **sensitivity** of the **geoeffectiveness** of a CME to its **initial parameters**.

Reduced representations of the images at different wavelengths

Obtained by comparing different **dimensionality reduction methods**:
- **Pre-trained GoogLeNet**
- **Principal Component Analysis** [1]
- **AutoEncoders** [2]
- **Variational AutoEncoders**

SERENADE (Bernoux et al. 2022)

Probabilistic predictions of the daily maximum of the Kp index at t + τ days

III. Feature extraction from images and Kp index predictions using SERENADE

GoogLeNet (*Szegedy et al. 2015*, used in SERENADE)
- **ImageNet (Deng et al. 2009) pre-trained Convolutional Neural Network.**

VAE (*Pinheiro Cinelli et al. 2021*)
- Projects ***non linearly*** the data onto the *latent space (LS)* keeping the *important information.*
- **Decodes** the LS to **reconstruct** the original data.

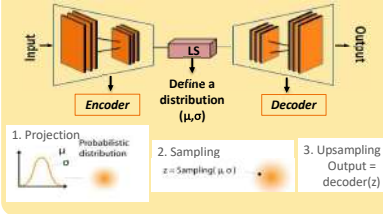

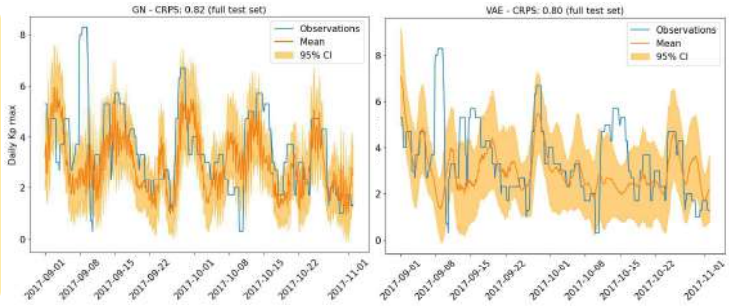

Preliminary results
- GN predictions very unstable ➔ could lead to false alerts.
- VAE predictions much more stable and smooth.
- Lower CRPS for VAE (Continuous Ranked Probability Score, equivalent to the MAE in the case of a probabilistic forecast).

Next steps
- Exhaustive test-bench.
- With further fine-tuning → better capture of CME associated storms.
- Experiment with images of different nature (magnetograms and coronographs) and initial CME parameters.

IV. Analysis of the impact of a CME's initial parameters on its geoeffectiveness

euhforia + SWING

Space weather modelisation tool (Pomoell and Poedts, 2018).

RNN → predict geomagnetic indices such as Kp and Dst (Bernoux et al. 2021).

Polynomial chaos expansion[3]: metamodel describing the 2 models

Sobol indices[4]: quantify the effect of each input parameter on the final output: max Kp.

Case study – CME July 2012

Parameter	Default value	Uncertainties
Speed (s)	$763\ km/s$	$563\ km/s - 963\ km/s$
Radius (r)	$16.8\ R_{Sun}$	$15.19\ R_{Sun} - 18.41\ R_{Sun}$
Density (d)	$10^{-18} kg/m^3$	$5 \times 10^{-18} kg/m^3 - 7.3 \times 10^{-17} kg/m^3$
Temperature (T)	$0.8 \times 10^6 K$	$0.16 \times 10^6 K - 4 \times 10^6 K$
Tilt angle (t)	$-135 deg$	$-155 deg - -115 deg$
Toroidal flux (f)	$1 \times 10^{14} Wb$	$0.5 \times 10^{14} Wb - 0.75 \times 10^{14} Wb$

Variation of the CME initial parameters given to EUHFORIA

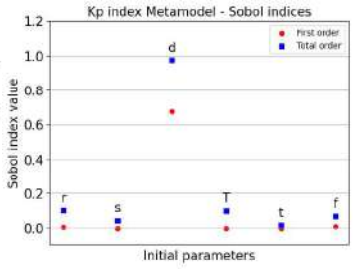

What affects the value of maximum Kp index the most?
- From the first order index → The variation of the **density** parameter.
- From the total order → the interaction between the **density** and the rest of the parameters, namely with the radius parameter.

[1] *Greenacre et al. 2022,* [2] *Bank et al. 2023,* [3] *Crestaux et al. 2009,* [4] *Owen 2013*

Gravimetric signature of slabs deep thermal structures

Xavier Vergeron[a], Cécilia Cadio[a], Fanny Garel[a]
[a]Géosciences Montpellier, univ. Montpellier, CNRS, Montpellier, France
Xavier.vergeron@umontpellier.fr

Introduction

- At subduction zones, cold lithospheric plates dive deep into the hotter Earth's mantle.
- Deep Focus Earthquakes are apparently related to their thermal structures.
- Seismic tomography provides a first-order information on slab morphology.
- Geoid and gravity gradients anomalies already evidenced over subduction zones.

Physical concept :

ΔT → Δρ → gravity anomaly

Main question :

Can gravity data from the GOCE mission be used to infer slabs' inner thermal structures ?

Focus of this study :

Estimate synthetic gravity data sensitivity to slabs inner thermal structures

Method : from deep (>200 km) slabs thermal structures to synthetic gravity signals

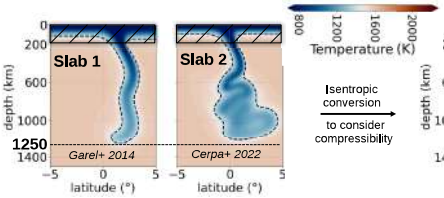

Fig.1 Thermal structure of 2 **vertical** slabs (**~ 1250 km**) from incompressible dynamic models, with the 200 first km removed.

Fig.2 **Isentropic** thermal structures of slabs 1 and 2

Thermodynamic **phase equilibria** HeFESTo, Stixrude+ 2011

Pyrolitic mantle composition

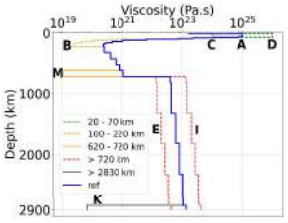

Fig4. Radial viscosity profiles considered in this study.

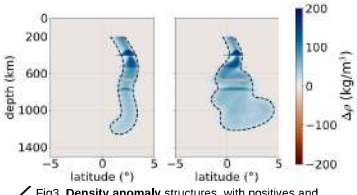

Fig3. **Density anomaly** structures, with positives and negative density anomalies due to **phase transitions** visible into the slab.

Overview of DynG³ workflow :
2D vertical grid of density anomalies in cartesian coordinates (input).
→ series of 2D **global** (horizontal) grids of surfacic mass in spherical coordinates, spaced by a vertical step of 5 km.
→ converted into spherical harmonics coefficients (SHC).
In parallel, Green's functions calculation, solving mass and momentum conservation equations system for an incompressible Newtonian viscous and spherically symmetric medium assuming a radial viscosity profile.
→ Geoid SHC by convolving Green functions and the SHC of the thin layers.
→ Geoid SHC adjusted to GOCE mean altitude (255 km)
→ Geoid, gravity and gravity gradients grids derived from Geoid adjusted SHC.

DynG³ *(freeware) Cadio+ 2011*

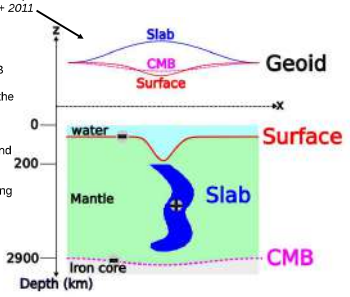

Fig.5 schema of a diving slab and mecanically induced surface and CMB deformations, and their individual contribution to the geoid total signal.
The slab (positive mass anomaly) contributes positively while surface and CMB deflections respectively contribute negatively at short and long wavelengths.

Modification of slabs inner thermal structure

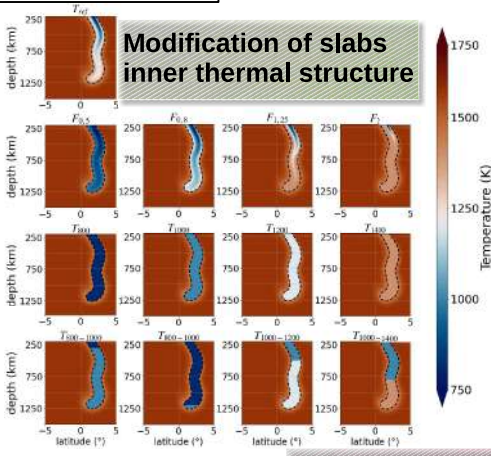

Fig.6 illustration of modifications applied on deep thermal structures.
-Top : T_{ref} , thermal structure from numerical dynamic subduction model.
-2nd line : F_i , increase or decrease of a factor i (0.5, 0.8, 1.25 or 2) of the thermal spatial gradient inside the slab.
-3rd line : T_i , constant (potential) temperature (800, 1000, 1200 or 1400 K) set to the whole slab.
-4th line : two isothermal regions T_{ic} with a shallow colder slab part (T_i of 800, 1000 or 1200 K) located above a hotter one (T_2 of 1000, 1200 or 1400 K), with a transition depth z_b varying between 300 and 1200 km. Represented bi-thermal structures are, from left to right : $T_{800-1000}$, $T_{800-1400}$, $T_{1000-1200}$ and $T_{1000-1400}$ with respectively z_b = 300, 1200, 500 and 800 km.

Take home message

-Max N leads to $\overline{T}$
-Max N combined with ΔT_{zz} leads to $\overline{T}_{200-500}$
-≠ Sensitivity of gravity signals to slab's morphology, mantle viscosity profile and SITS
-Gravimetric anomalies amplitude due to SITS modification > GOCE detection threshold

Results :synthetic gravity signals

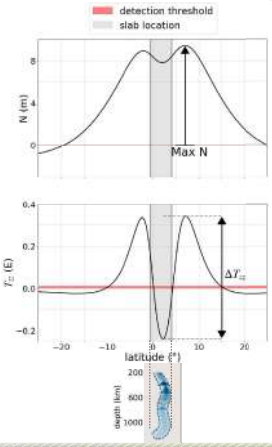

Left : Fig.7 Geoid N and vertical gravity gradient T_{zz} synthetics calculated for the slab 1 with T_{ref}. We focused on the relationship between the geoid maximum amplitude, max N, the central peak-to-peak amplitude of T_{zz}, ΔT_{zz}, and the slab inner thermal structure (SITS). The grey and red areas respectively represent the slab location and GOCE detection threshold.

Right : Fig.8 N and T_{zz} calculated for all viscosity profiles and both morphologies 1 and 2, with T_{1000} to avoid any SITS variation effect and focus on viscosity profile and slab's morphology influence on gravity signals. Black line represents the signals calculated for slab 1 with T_{ref}, in order to illustrate variation effect (compared to slab 1 with T_{1000}). Slabs 1 and 2 locations are represented by the grey areas and the dashed colored lines (resp. purple and green for slabs 1 and 2). If the slab's morphology and mantle radial viscosity profile control the signals shape at first-order, SITS variations has a significative influence on signals amplitudes.

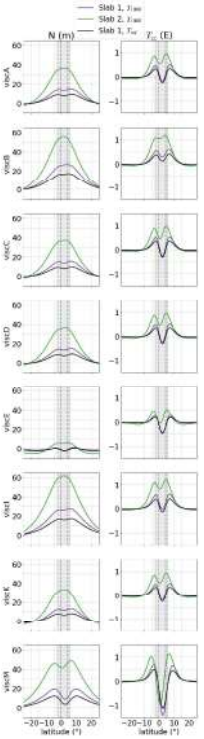

Slab's temperature vs max N and ΔT_{zz}

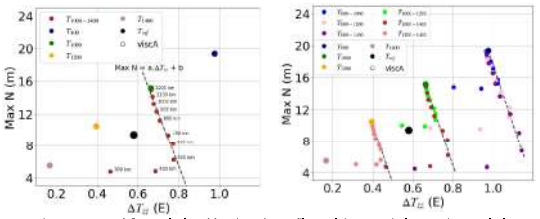

Fig.9 **Max N and ΔT_{zz}** calculated for viscosity profile A, slab 1 morphology and several SITS. Left : T_{ref}, homogeneous SITS and bi-thermal SITS with T_1 = 1000 and T_2 = 1400 K. Right : T_{ref}, homogeneous and all bi-thermal SITS. Left subplot illustrates the **linear regression** feasable on all **SITS with the same superficial temperature** (i.e $z_b \geq 500$ km). The slope, *a*, of this regression remains ~ the same for all superficial temperatures (cf. right subplot).

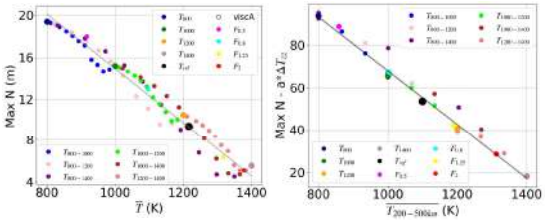

Left : Fig.10 Linear relationship between **max N** and the **whole slab's mean temperature.**

Right : Fig.11 Linear relationship between **combined information of max N and ΔT_{zz}** , and the **slab superficial's** (200-500 km) **mean temperature.**

Both figures are made for slab 1, viscosity profile A and all SITS.

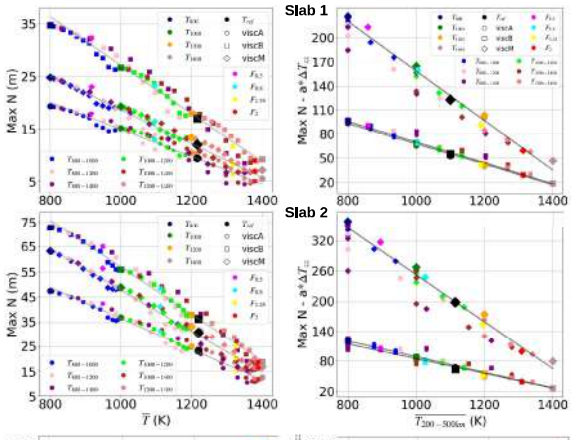

Fig.12 Left side : same as fig.10 but for viscosity profiles A, B and M, and for the slab 1 (top) and 2 (bottom).
Right side : same as fig.11 but for viscosity profiles A, B and M, and for the slab 1 (top) and 2 (bottom).

Linear regressions coefficients vary with the slab morphology and the radial viscosity profile of the mantle, but remain feasable for every tested combinaison of morphology and viscosity profile.

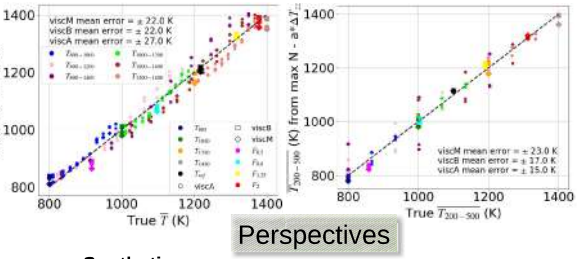

Fig.13 **Benchmark** of estimated $\overline{T}$ and $\overline{T}_{200-500}$ for viscosity profiles A, B and M and slab 1 morphology. Mean error < 30 K in each cases.

Perspectives

Synthetic case :
-Develop an inversion strategy based on *a priori* from seismic tomography
Natural case :
-Isolate the slab signal from the 200 first km in the total signal
-Apply the inversion strategy to propose a range of possible SITS

References :

Cadio, C., et al, "Pacific geoid anomalies revisited in light of thermochemical oscillating domes in the lower mantle," Earth and Planetary Science Letters 306,1-2 (2011): 123-135.

Cerpa, Nestor G., et al, "The effect of a weak asthenospheric layer on surface kinematics, subduction dynamics and slab morphology in the lower mantle," Journal of Geophysical Research: Solid Earth 127.8 (2022): e2022JB024494.

Garel, Fanny, et al. "Interaction of subducted slabs with the mantle transition-zone: A regime diagram from 2-D thermo-mechanical models with a mobile trench and an overriding plate," Geochemistry, Geophysics, Geosystems 15.5 (2014): 1739-1765.

ANR-21-CE49-0009

Recueil des posters

Session 6

S06-01 | Doc | **BIQUARD Maud** |ISAE-Supaero, Toulouse | Encadrant CNES : Florence GENIN | POSTER |
Restauration d'images satellites à l'aide d'apprentissage profond

S06-02 | Doc | **BOSHEVSKI Viktor** | LHCEP/ICBMS, Villeurbanne | Encadrant CNES : Achraf DYANI | POSTER |
Accès aux ergols spatiaux par construction catalytique de liaisons N-N

S06-03 | Doc | **BRUN Thomas** | LPC2E / SPINTEC, Grenoble | Encadrant CNES : Éric LORFEVRE
MAROT: Un magnétomètre miniature pour l'exploration spatiale

S06-04 | Doc | **FISCHER-KASZUBA Baptiste** | ONERA, Châtillon | Encadrant CNES : Nicolas VOROBYEV | POSTER |
Development of a 100 MHz quartz-MEMS resonator

S06-05 | Doc | **HASINA ANDRIAMANANTENA Heninjara Narovana** | INED, Aubervilliers | Encadrant CNES : Céline CALLEYA | POSTER | **Analyses paysagères par traitement d'image et caractéristiques de la population en milieu rural à Madagascar**

S06-06 | Post-doc | **KIEOKAEW Rungployphan** | IRAP, Toulouse | Encadrant CNES : Kader AMSIF | POSTER |
Couplage multi-échelles dans les plasmas spatiaux : une nouvelle vue sur la dynamique cinétique du plasma du vent solaire avec Solar Orbiter

S06-07 | Doc | **LALANDE Maxime** | ONERA, Toulouse | Encadrant CNES : Julien ANNALORO | POSTER |
Modélisation des phénomènes physiques fluide-structure associés à la dégradation thermochimique des matériaux en régime hypersonique continu lors de la rentrée atmosphérique des débris spatiaux

S06-08 | Post-doc | **MARTINELLI Alessandro** | Lab. Charles Coulomb, Montpellier | Encadrant CNES : Thierry BRET-DIBAT | POSTER | **Relaxations of internal and strain-induced stresses in colloidal glasses**

S06-09 | Post-doc | **MARTINOT Mélissa** | UL – CRPG, Vandœuvre-lès-Nancy | Encadrant CNES : Francis ROCARD | POSTER |
Characterization of the regions displaying featureless spectra on the Moon, using visible to near-infrared and thermal infrared remote sensing datasets: implications for the lunar crust

S06-10 | Doc | **MICHAUX Étienne** | CNRS – ICARE, Orléans | Encadrant CNES : Ulysse WELLER | POSTER |
Physique des propulseurs à arc sous vide à fort courant

S06-11 | Post-doc | **TARASENKO Anastasia** | ISOMER Nantes Université, Nantes | | Encadrant CNES : Yannice FAUGERE | POSTER | **ASAMPLE: blooms cotiere de phytoplancton en haute résolution**

S06-12 | Doc | **TERRASSE Eddy** | LMFL, Lille | Encadrant CNES : Matthieu QUEGUINEUR | POSTER |
Analyse expérimentales des instabilités de cavitation dans les inducteurs spatiaux

Régularisation par apprentissage profond pour la restauration d'images satellites

Maud Biquard [1,3] Marie Chabert [2] Florence Genin [3] Christophe Latry [3] Thomas Oberlin [1]

[1]ISAE-Supaero [2]IRIT/INP-ENSEEIHT [3]CNES

Résumé

On s'intéresse à la restauration d'images satellites (débruitage et défloutage, avec et sans super-résolution). Les méthodes de régularisation basées sur un réseau de neurones génératif offrent un cadre intéressant mais s'avèrent fortement dépendantes de la qualité du réseau utilisé. On propose ici d'utiliser un autoencodeur variationnel moins contraint, utilisé originellement pour la compression. De plus, on introduit un cadre bayésien favorable pour échantillonner la distribution a posteriori du problème, permettant la génération de plusieurs images solutions ainsi que d'estimer des incertitudes. Les simulations, sur des images naturelles ainsi que des images satellites, permettent de conclure à des performances similaires à l'état de l'art, et démontrent le potentiel de cette méthode pour la restauration d'images satellites.

Introduction

On considère le problème inverse suivant :

$$y = Ax + n \quad (1)$$

avec y la mesure, A l'opérateur de dégradation, x l'image d'origine et n le bruit.

→ $A = h*$, $n \sim \mathcal{N}(0, \sigma^2 = a^2 + b(h * x))$ pour le débruitage et défloutage d'images satellites.

Classiquement, on recherche la solution du problème (1) sous la forme:

$$\hat{x} = \arg\min_x ||y - Ax||^2 + \lambda R(x) \quad (2)$$

où R est la régularisation.

→ Apprendre R à l'aide de réseaux de neurones permet d'améliorer considérablement les performances en restauration d'images.

→ Apprendre uniquement R permet de **résoudre plusieurs problèmes inverses avec le même réseau de neurones** [3].

- Deux possibilités : implicitement à l'aide de débruiteurs [3], ou explicitement à l'aide de modèles génératifs [1].

Régularisation par réseaux génératifs

1. **Apprentissage d'un réseau génératif** G sur un dataset d'images idéales x.

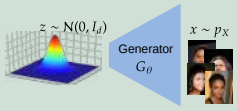

Figure 1. Principe d'un réseau génératif

2. **Restauration d'images.** On recherche la solution du problème inverse dans l'espace latent de G [2] :

$$\hat{z} = \arg\min_z ||AG(z) - y||_2^2 + \lambda||z||^2$$

avec $\hat{x} = G(\hat{z})$ (3)

+ Minimisation d'une fonction de coût explicite
+ Cadre bayésien intéressant : $\hat{z}$ peut être vu comme un estimateur MAP (Maximum A Posteriori)
- La contrainte $x = G(z)$ rend la performance de la méthode très dépendante du modèle génératif utilisé

Utilisation d'une structure d'autoencodeur compresseur

Autoencodeur choisi :

- **Grand espace** latent (= espace encodé).
- Les données sont réparties dans l'espace latent suivant une loi flexible $\mathcal{N}(\mu^z, \sigma^z)$ définie par l'hyperprior.

→ Apprentissage de **textures et formes**.

→ Applicable sur des données complexes.

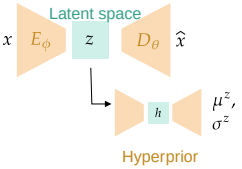

Figure 2. Structure d'autoencoder compresseur.

Estimation de la distribution a posteriori du problème

→ **Algorithme VBLE [1] : Approximation de distribution a posteriori** $p(z|y)$ **par un petit volume dans l'espace latent.**

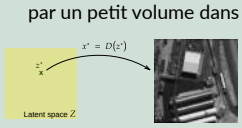

Figure 3. Algorithme déterministe

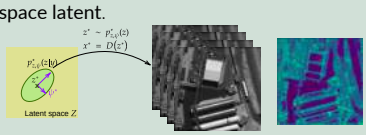

Figure 4. Notre algorithme (VBLE)

On utilise de l'inférence variationnelle:

→ Définition de la distribution paramétrique

$$E_{\bar{z},a} = \left\{ q_{\bar{z},a}(z) = \mathcal{U}(z_k; [\bar{z}_k - \frac{a_k}{2}, \bar{z}_k + \frac{a_k}{2}]) | \bar{z}, a \in \mathbb{R}^p, a > 0 \right\} \quad (4)$$

→ **Minimization** de $KL(q_{\bar{z},a}(z)||p_{Z|Y}(z|y))$ qui revient à maximiser l'ELBO

$$\arg\max_{\bar{z},a} \mathcal{L}_{\bar{z},a} = \arg\max_{z,a} \mathbb{E}_{q_{\bar{z},a}(z)} \left[\log p_{Y|Z}(y|z) + \log p_\theta(z) - \log q_{\bar{z},a}(z) \right] \quad (5)$$

with $\log q_{\bar{z},a}(z) = -\sum_k \log a_k$ and $\log p_\theta(z) = R(z)$ the hyperprior.

- Minimisation de (5) par descente de gradient

→ Estimateur MMSE: $x^*_{MMSE-x} = \frac{1}{L}\sum_{i=1}^{L} D_\theta(z_i)$ with $z_i \sim q_{\bar{z}^*,a^*}(z_i)$.

Expérimentations - images naturelles / satellites

- **Métriques :** PSNR (erreur quadratique en échelle log), SSIM (métrique perceptuelle classique), LPIPS (métrique perceptuelle deep).
- **Réseau :** Utilisation de réseaux compresseurs préentraînés, finetunés sur les datasets testés.
- **Baselines :** DPIR/PnP-ADMM (algorithmes Plug&Play avec débruiteur deep), PnP-ULA (algorithme MCMC), DiffPIR (algorithme utilisant des modèles de diffusion)

BSD	Deblur (Gaussian)			SISR ×4			SISR ×2		
Method	PSNR ↑	LPIPS ↓	SSIM ↑	PSNR ↑	LPIPS ↓	SSIM ↑	PSNR ↑	LPIPS ↓	SSIM ↑
VBLE wCAE	**29.77**	0.2002	0.8617	**25.47**	0.3459	**0.6977**	**29.65**	0.1830	0.8749
MAPz wCAE	29.28	0.2215	0.8405	25.38	0.3462	0.6966	**29.65**	0.1675	0.8757
PnP-ULA	27.71	0.2675	0.7809	24.82	0.3730	0.6894	28.42	0.1659	0.8763
DPIR	29.72	0.2127	**0.8623**	25.18	0.3652	0.6937	29.55	0.1706	**0.8784**
PnP-ADMM	28.96	0.2155	0.8456	24.77	0.4227	0.6659	29.31	0.1907	0.8678
DiffPIR	29.26	**0.1832**	0.8420	25.03	**0.3164**	0.6771	29.20	**0.1645**	0.8539

Table 1. BSD results on diverse inverse problems: Gaussian deblurring ($\sigma_{blur} = 1$, $\sigma = 7.65/255$), SISR ×4, SISR ×2. Methods in *italics* allow for posterior sampling.

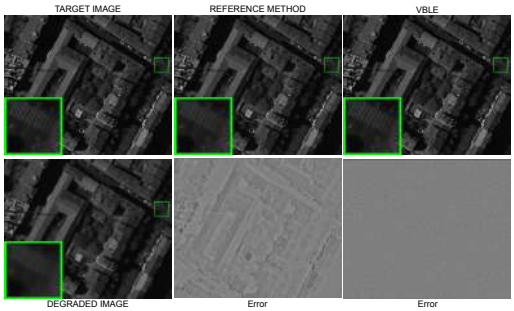

Figure 5. Exemple de restauration au point de fonctionnement Pléiades (50cm). VBLE : notre méthode. Méthode de référence : classiquement utilisée pour restaurer les images satellites (NL-Bayes + déconvolution). Milieu : images restaurées. Bas : Erreur signée $\hat{x} - x$. ©CNES 2024

Expérimentations - Images satellites réelles

- **Dataset :** Images Pélican (images aéroportées) utilisées pour simuler le point de fonctionnement Pléiades.
- **Problèmes considérés :** Débruitage + défloutage avec et sans super-résolution.

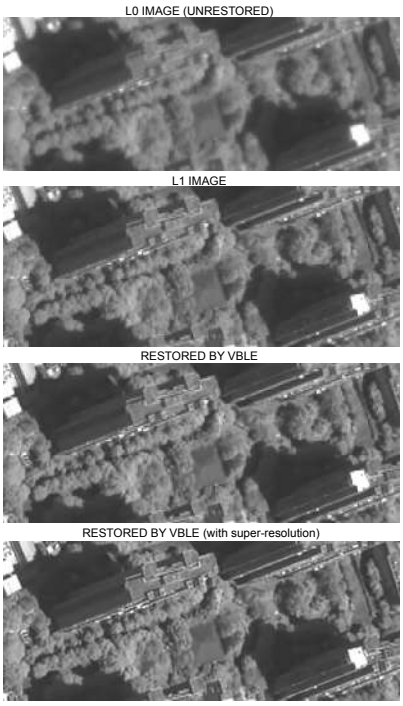

Figure 6. Exemple de restauration d'une image Pléiade réelle. Image L1: restaurée par la méthode de référence. ©CNES 2024

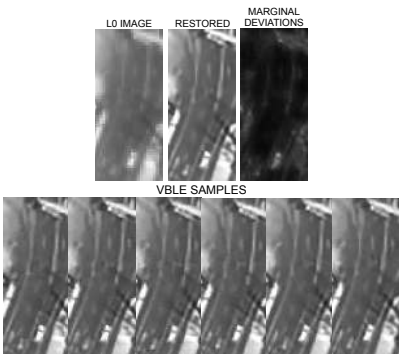

Figure 7. Restauration par VBLE d'une image Pléiade réelle, incertitude et exemple d'échantillons. ©CNES 2024

References

[1] Maud Biquard, Marie Chabert, Florence Genin, Christophe Latry, and Thomas Oberlin. Variational bayes image restoration with compressive autoencoders. *arXiv preprint arXiv:2311.17744*, 2023.

[2] Ashish Bora, Ajil Jalal, Eric Price, and Alexandros G. Dimakis. Compressed sensing using generative models. In *International Conference on Machine Learning (ICML)*, 2017.

[3] Kai Zhang, Yawei Li, Wangmeng Zuo, Lei Zhang, Luc Van Gool, and Radu Timofte. Plug-and-play image restoration with deep denoiser prior. *IEEE Transactions on Pattern Analysis and Machine Intelligence*, 44(10):6360–6376, 2021.

maud.biquard@isae-supaero.fr

Catalytic *N-N* bond formation *via* a decarbonylative *Ni*-mediated process and application to polyazanes

Viktor Boshevski[†,‡] (viktor.boshevski@univ-lyon1.fr), Gaël Tran[‡], Lionel Joucla[†], Abderrahmane Amgoune*[,‡], Emmanuel Lacôte*[,†]

Université Claude Bernard Lyon 1, LHCEP[†] (UMR 5278), ICBMS team SCORE[‡] (UMR 5246)

The Future of Space Propulsion

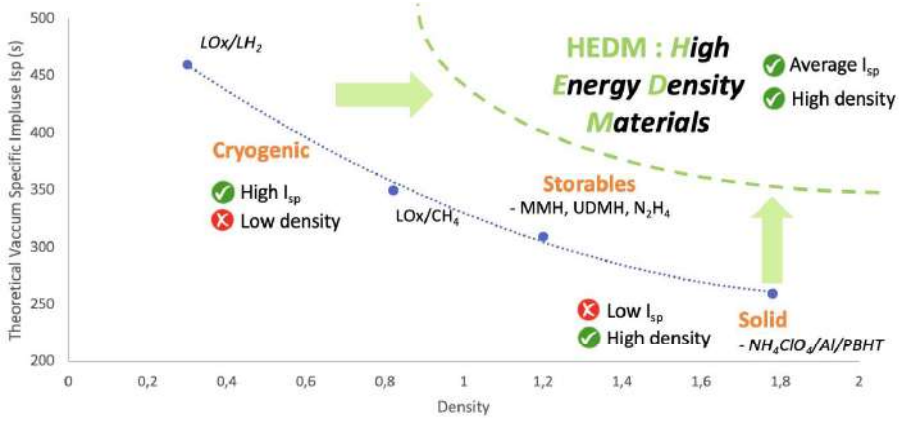

CNES Principal Innovative Vector

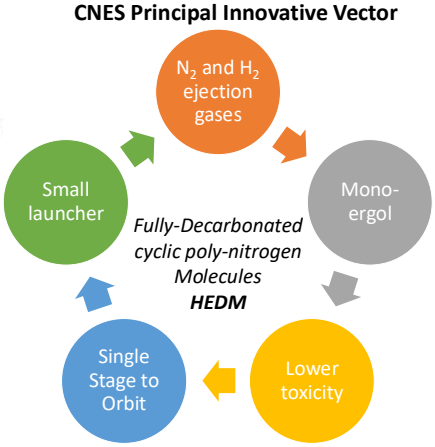

Ariane 6 propulsive system ⟷ **Technological breakthrough** ⟷ Ariane Ultimate propulsive system

Intramolecular *Ni*-catalyzed *N-N* coupling : recombination after CO extrusion[a]

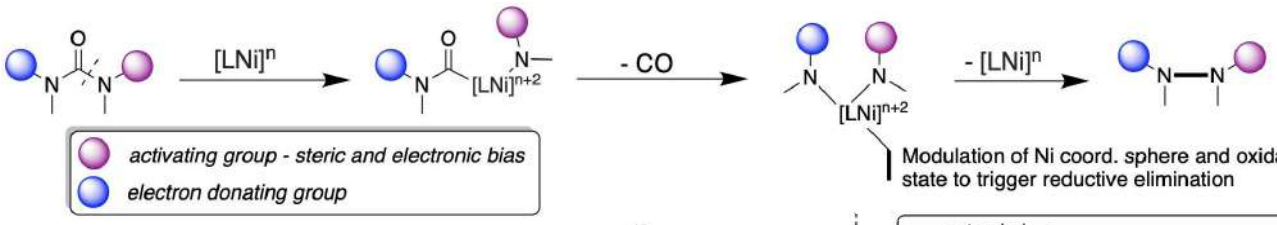

Stoichiometric study

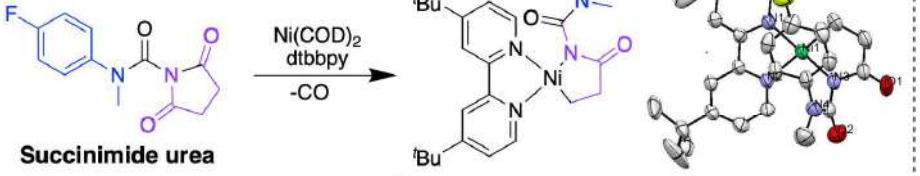

[Ni]^{II} metallacycle complex **XRD Structure**

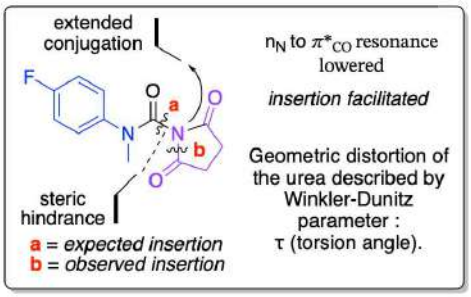

Photoinduced *N-N* Bond Formation[b,c]

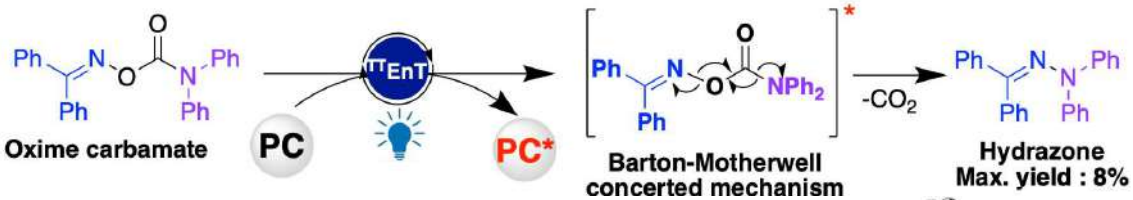

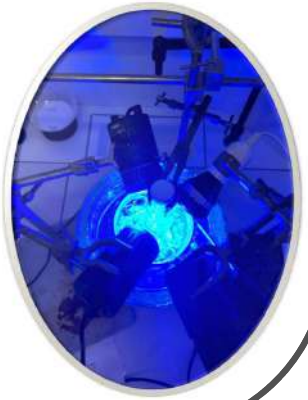

Conclusion

HEDMs are required for greener, safer, smaller, reusable and more efficent launchers → technical breakthrough
HEDMs chemistry of polynitrogen compounds is very complex and difficult → Poor literature data
HEDMs are key for the future of space propulsion → global competitive challenge for space agencies

[a] A. Amgoune, *Synlett.*, **2021**, *32*, 1531-1536; [b] G. C. Fu, *J. Am. Chem. Soc.*, **2017**, *139*, 12153−12156; [c] Y. You, *ACS Catal.*, **2019**, *9*, 10454−10463.

S06-03 | Doc | **BRUN Thomas** | LPC2E / SPINTEC, Grenoble | Encadrant CNES : Éric LORFEVRE

MAROT: Un magnétomètre miniature pour l'exploration spatiale

Absent

Development of a 100MHz Quartz-MEMS resonator

B. Fischer-Kaszuba[1], P. Lavenus[1], R. Levy[1], T. Baron[2], N.Vorobyev[3]*
1. ONERA, the French aerospace lab; 2. FEMTO-ST; 3. CNES; France

Overview[1]

What is a Quartz-MEMS resonator ?

An ideal resonator features for time & frequency domain due to :

Quartz crystal ✚ ***MEMS***

Advantages[1]:
- ***High Q-factor***
- ***High thermal stability***
- ***Naturally piezoelectric***
- ***Low power consumption***

Advantages[1]:
- ***Collective process***
- ***High production efficiency***
- ***Easy integration***
- ***Miniature size***

Application

What's the link with space?

New Space:
- **Miniaturization of satellites**
  → **Cost reduction**
- **Increase of equipment flow rates**
  → **As Telemetry, Telecommand & Inter Satellite Links**
- **Increase accuracy of navigation systems**
  → **Multi-GNSS Timing and Localization**

Design[2]

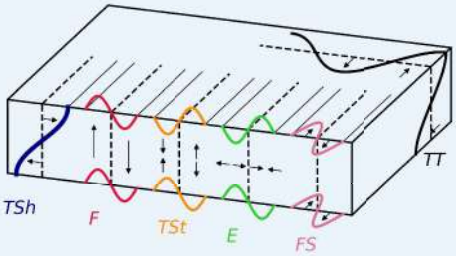

- **E: Extensional**
- **F: Flexural**
- **FS: Face-Shear**
- **TSh: Thickness-Shear**
- **TT: Thickness-Twist**
- **TSt: Thickness-Stretch**

First six vibrational mode of a quartz plate

Which one to choose to achieve 100MHz?

Thickness-shear:
- **Usually used for high frequencies**
- **High Q-factor**
- **Low motional resistance (R_m)**

How to achieve 100 MHz with thickness-shear vibration ?

$$f = \frac{n}{2h}\sqrt{\frac{C_{66}}{\rho}}$$

n : mode number (n = 1 , fundamental)
h : blade thickness (15µm)
C_{66} : stiffness matrix component (34,8GPa)
ρ : density (2648 kg / mm³)

→ ***Necessity of a thin plate of 15µm (Hair diameter ≈ 100µm)***

How to reach high performance ?

$$R_m = \frac{(\pi n)^2 h}{8k_{26}^2 \varepsilon C_{66} S}$$

S : electrode surface area (1mm²)
k_{26} : electro-mechanical coupling factor (0,77%)

→ ***Necessity of a compromise:***
- ***Thin plate***
- ***Fundamental mode***
- ***Large electrode surface area***

Fabrication

How to fabricate a Quartz-MEMS resonator ?

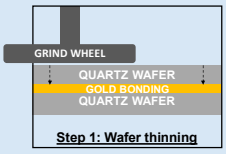

Step 1: Wafer thinning

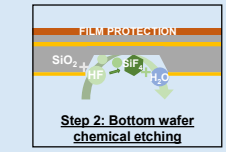

Step 2: Bottom wafer chemical etching

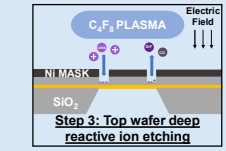

Step 3: Top wafer deep reactive ion etching

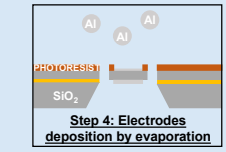

Step 4: Electrodes deposition by evaporation

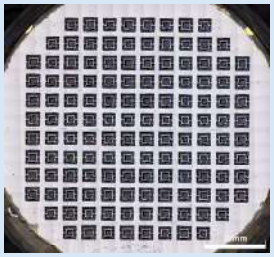
4" wafer after chemical etching in hydrofluoric acid

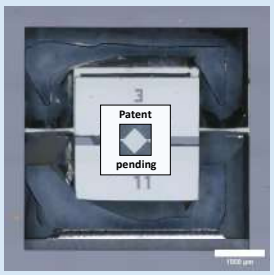

Final state of one resonator

Characterization[3]

What is the real performance?

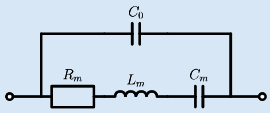

Butterworth Von Dyke equivalent circuit

	Fundamental
Frequency	114MHz
Q-factor	24 000
Motional resistance	60Ω
Q×f Product	2.5×10¹²Hz

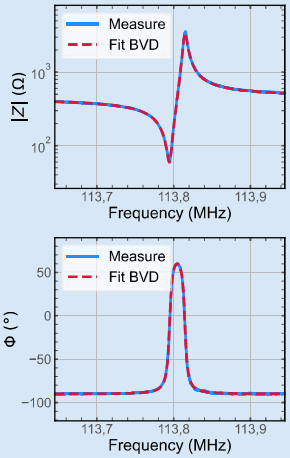

Impedance frequency response Measurement

Encouraging performance allowing a Q.f product of *2.5×10¹²Hz on the fundamental and 1.3×10¹³Hz on the 5th overtone* near the theoretical limit of quartz of 3.2×10¹³Hz in the Akhiezer regime[2] for a surface lower than *10mm²*.

Outlook

- ✓ **This work demonstrates the possibility of using a quartz-on-quartz wafer with deep reactive ion etching (DRIE) to produce a miniaturized self-suspended resonator with encouraging performance.**
- ✓ **Future work will focus on characterizing the resonator mounted as an oscillator.**

Bibliography

[1] G. Pillai and S. -S. Li, 'Piezoelectric MEMS Resonators: A Review', IEEE Sensors Journal, vol. 21, no. 11, pp. 12589–12605, 2021.

[2] R. W. Cernosek, S. J. Martin, A. R. Hillman, and H. L. Bandey, 'Comparison of lumped-element and transmission-line models for thickness-shear-mode quartz resonator sensors', IEEE Transactions on Ultrasonics, Ferroelectrics, and Frequency Control, vol. 45, no. 5, pp. 1399–1407, Sep. 1998.

[3] S. Ghaffari et al., 'Quantum Limit of Quality Factor in Silicon Micro and Nano Mechanical Resonators', Scientific Reports, vol. 3, no. 1, p. 3244, Nov. 2013.

** baptiste.fischer-kaszuba@onera.fr*

This work was partly supported by the french RENATECH network and its FEMTO-ST technological facility.

Landscape metrics for estimating population characteristics in rural areas

Narovana ANDRIAMANANTENA[1,2,4], Valérie GOLAZ[1,2], Anne-Elisabeth LAQUES[3]

1.Institut National d'Etude Démographique Paris (INED)
2.Laboratoire Population Environnement Développement (LPED)
3.Institut de Recherche pour le développement (IRD)
4.Aix-Marseille Université

Introduction and aims

- Rural landscapes change unevenly over time (fast or slow transformations depending on the local context).
- Agricultural transformations, new land management practices and deforestation or reforestation processes modify landscape structure(Lambin et al., 2003).
- Landscapes are dynamic, influenced by human and environmental factors.

Main objective of the thesis: To analyze the dynamics of land use and the evolution of structures in order to construct an indicator for assessing population density in rural areas

Aims of the poster:

- To produce land use maps using high-resolution Pleiades images.
- To calculate landscape metrics that quantify changes in rural landscape structures.

Study area

In this poster, we present the results for the Tapia Forest Landscape. Tapia forest, an endemic forest in Madagascar . It is used and managed by the local population as an economic and food resource (Kull et al., 2005).

Delimitation of landscape types on the Arivonimamo site carried out by colleagues from the LMI-Paysage Madagascar using Sentinel-2 images, with the selection of 3 study areas for each landscape type, including the sites where demographic surveys were conducted.

Methods

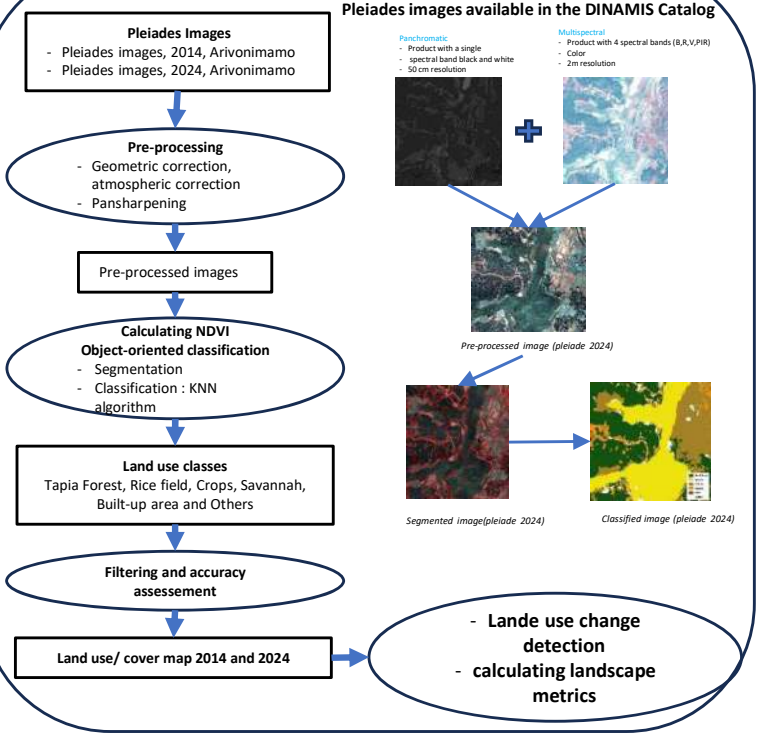

Results

Land use/cover map for 2014 and 2024 from Pleiades images

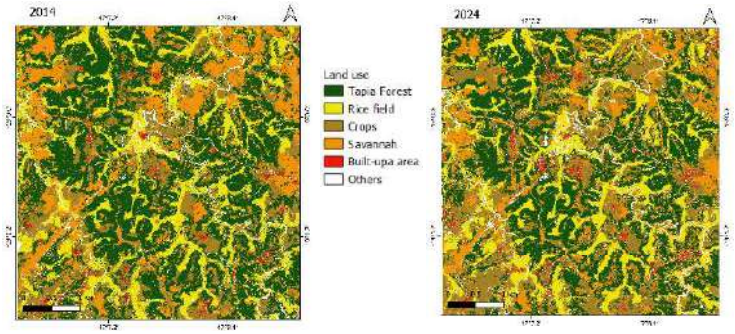

Land use map developed from Pléiades images from 2014. © CNES (2014), distribution Airbus DS.

Land use map developed from Pléiades images from 2024. © CNES (2024), distribution Airbus DS.

Detection of land use change based on land use/cover maps derived from Pléiades images for the years 2014 and 2024

Land cover	2014 (%)	2024(%)	Change (%)
Tapia Forest	41,024	35,68	-13,03
Rice field	16,992	17,11	0,69
Crops	16,729	23,59	41,01
Savannah	20,443	17,98	-12,05
Built-up area	1,085	1,39	28,11
Othres	3,728	4,25	14,00

- **increase in cultivated areas (+41%)**: agricultural expansion to meet food needs; Increased demographic pressure
- **Reduction in forests (-13%) and savannah (-12%)**: Conversion of natural land for agriculture, Deforestation due to demographic pressure

Evolution of landscape structures

Some landscape metrics

Métriques	Description
Numbers of patchs (NP)	- Indicate the degree of fragmentation of natural areas. - Creation of new fragments: Closely related to the activities of local populations and their land use practices.
Mean Patch Area (MPA) (ha)	
Area	- Enables us to quantify the extent of landscape units. - For larger agricultural areas, it is often correlated with higher population densities due to the increased need for food production.

Evolution of landscape metrics for the land use Tapia forest class and crops class

	Forêt Tapia			Culture Pluviale		
	2014	2024	Change (%)	2014	2024	Change (%)
NP	23264	33205	29,93	14130	23264	39,26
MPA (ha)	0,054	0,0324	-66,66	0,035	0,030	-16,66
Area (ha)	1237,20	1075,97	--14,98	504,51	711,36	29,07

Increase in the number and average size of cultivated plots: Increased demand for agricultural land due to population growth, indicating intensive farming practices

Creation of new forest fragments and reduction in average size of forest fragments: Demographic growth could explain the increased fragmentation of forest patches, with an increase in the number of fragments and a decrease in their average size.

Perspectives

- Spatial correlation or Spatial modeling: Use spatial modeling tools to simulate land-use scenarios based on variations in population density.

Acknowledgments:
Thank DS". to the DINAMIS platform for access to the Pleiades images and, the CNES "Pléiades © CNES 2014, © CNES 2024; Distribution Airbus

References
- Kull C.A., Ratsirarson J. & Randriamboavonjy G., 2005. Les forêts de tapia des hautes terres malgaches. *Terre Malgache*, **24**(2), 22-58.
- Lambin, E., Geist, H., Lepers, E., 2003. Dynamics of Land-use and land-cover change in tropical regions. Annu. Rev. Environ. Resour 20, 49205–41.

Cross-scale coupling of the solar-terrestrial plasmas: Novel view on kinetic plasma dynamics

Rungployphan Kieokaew (rkieokaew@irap.omp.eu). Advisors: Philippe Louarn (IRAP), Kader Amsif (CNES).
Institut de Recherche en Astrophysique et Planétologie, IRAP, Toulouse, France

Introduction

How plasmas (ionized gases) get heated and accelerated remains one of the unsolved problems in astrophysics.

The Sun-Earth environments are the most accessible laboratories where the physics at work can be probed in situ.

Understanding how these environments work also help us to mitigate effects from "**space weather**" that can damage space and ground technologies, leading to loss of several billion euros.

Solar corona ***Magnetosphere***

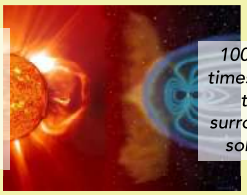

A few 100 times hotter than its surface

100 – 1000 times hotter than the surrounding solar wind

Fig 1. Solar-terrestrial plasmas

A "key" missing piece to solve this problem is the role of kinetic processes (i.e., near particle scales) as they need high-resolution observations in situ.

Plasma kinetic theory

Maxwell-Boltzmann equation is the most powerful tool for investigating plasma kinetic dynamics:

$$\frac{\partial f_s}{\partial t} + \mathbf{v}_s \cdot \nabla f_s + \frac{q_s}{m_s}(\mathbf{E} + \mathbf{v}_s \times \mathbf{B}) \cdot \frac{\partial f_s}{\partial \mathbf{v}_s} = \left(\frac{\partial f_s}{\partial t}\right)_{coll}$$

where $f_s = f_s(t, \mathbf{v}, \mathbf{r})$, the distribution of a plasma species (s) as a function of time (t), velocity (**v**), and space (**r**).

Measurements of plasma velocity distribution function (VDF) *in situ*

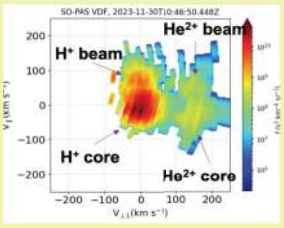

Fig 2. Example of ion VDF from PAS.

Proton-Alpha Sensor (PAS) developed at IRAP onboard SO measures VDF of major solar wind ions (H^+, He^{2+}) with unprecedented resolution[1].

High-resolution ion VDF observations show striking kinetic, non-Maxwellian features (i.e., source of free energy).

Yet, their origins and roles remain poorly understood.

References

1. P. Louarn, *et al. Astron & Astrophys*, **656**, A36 (2021).
2. P. Hellinger, *et al. Geophys. Lett.* **33**, 9 (2006).
3. P. Isenberg, *et al. J. Geophys. Res.* **106**, A12 (2001).

This research was supported by the International Space Science Institute (ISSI) in Bern, through ISSI International Team project #563 (Ion Kinetic Instabilities in the Solar Wind in Light of Parker Solar Probe and Solar Orbiter Observations).

Unsolved problem: Coronal heating and solar wind acceleration

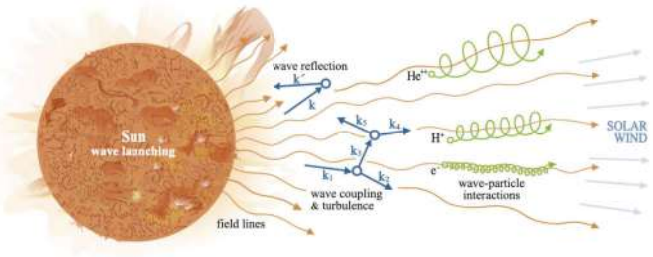

Fig 3. The Sun as an electromagnetic wave launcher.

The Sun continuously launches its matter and electromagnetic waves into space. A leading theory is that the large-scale waves launched by the Sun in Alfvénic form (~ restoring force in a rope), transport the energy outward while transferring energy to smaller-scale waves.

We still do not understand how small-scale waves (i^+,e^- gyroscales) heat and accelerate the solar wind.

Spacecraft radial alignment: unique opportunity for studying solar wind evolution

Parker Solar Probe (PSP) and Solar Orbiter (SO) are two new solar missions, launched in 2018 and 2020, respectively. PSP is the first mission that flies through the corona. SO will probe the Sun from above for the first time. PSP and SO occasionally line up in the radial direction where the solar wind propagates.

How does the solar wind evolve "kinetically" on its way to Earth?

Methodology: identifying a parcel that was intercepted by both spacecraft

On 25 – 27 February 2022, PSP and SO aligned radially (Fig. 4) with PSP being at 0.06 AU while SO being at 0.6 AU. To find an interval that was intercepted by PSP and then SO, we perform the following steps:

1. Ballistic propagation based on proton speed to find plasma origins.
2. Select interval where the He^{2+} to H^+ density ratio is similar.
3. Compare nonlinear similarity of the magnetic fields.

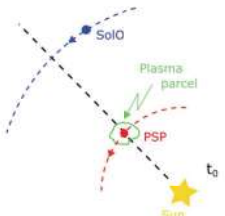

Fig 4. PSP-SO radial alignment

Outcomes: comparison of solar wind stream measured by PSP and SO

We focus on (1) magnetic turbulence, (2) proton instabilities, and (3) VDF of the protons. Magnetic power spectra (Fig. 5) shows that the magnetic field fluctuations show classic turbulent properties with the change of the turbulence cascade rate near the proton gyrofrequency (f_{ci}). The linear instability analysis[2] (Fig. 6) shows proportions of data being unstable to the proton cyclotron instability (above the black dots).

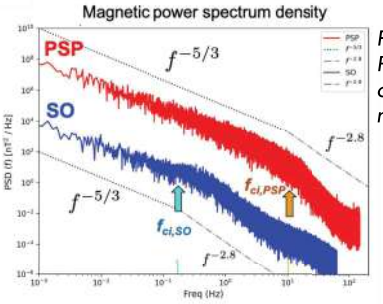

Fig 5 (left). Power spectra of magnetic measurements.

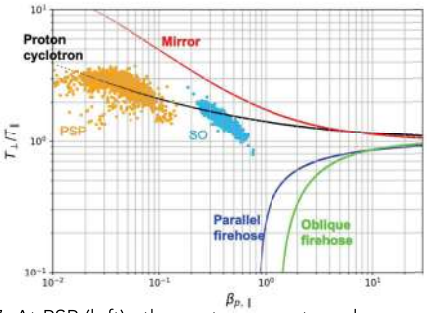

Fig 6 (right). Linear proton instability analysis.

Finally, we compare VDF evolution from PSP to SO in Fig 7. At PSP (left), the protons are strongly scattered along the $V_\perp$ direction (perpendicular to the magnetic field). At SO, the the protons are less scattered along $V_\perp$(i.e. reduced temperature anisotropy).

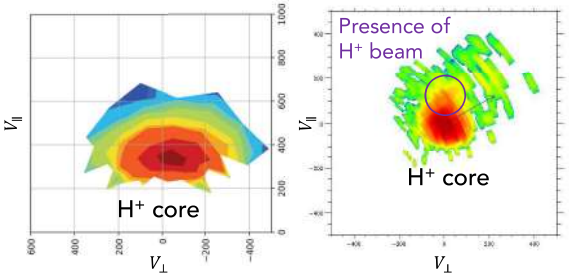

Surprisingly, we observe a presence of an accelerated population along $V_\parallel$, known as **H^+ beam**, at SO. This implies that the **accelerated H^+ beam** may be formed on its way while propagating outward from the Sun.

Fig 7. VDF measured at PSP (left) and SO (right) shown in $V_\parallel - V_\perp$ coordinates, i.e., along and perpendicular to magnetic field.

Summary and perspectives

Evolution of kinetic properties:

1. Decrease of proton $T_\perp/T_\parallel$ by half from PSP to SO.
2. Less fraction of protons being unstable to the proton cyclotron instability at SO.
3. Formation of a proton beam, 2 days later, at SO.

On the proton beam (H^+) formation:

The most-likely mechanism is the diffusion of VDF owing to wave-particle (i.e. resonance) interaction[3]. Our analysis suggests that ion cyclotron waves, driven by the instability, might play a key role.

Our work demonstrates a good showcase study for the connection between turbulence, waves, instabilities, and kinetic features, as well as the coupling from large magnetohydrodynamics to small kinetic scales. Future work includes refining the analyses and identification of wave modes.

Modélisation des phénomènes physiques fluide-structure associés à la dégradation thermochimique des matériaux en régime hypersonique continu lors de la rentrée atmosphérique des débris spatiaux

Maxime Lalande (ONERA/DMPE - Doctorant $2^{ème}$ année)
Directrices de thèse : Nathalie Bartoli (ONERA/DTIS) & Ysolde Prévereaud (ONERA/DMPE)
Encadrant : Nicolas Dellinger (ONERA/DMPE)
Référent CNES : Julien Annaloro
Co-financement ONERA/CNES

Contexte et objectifs

- Depuis 40 ans, rentrée atmosphérique de 16.000 T de débris. Menace pour la sécurité au sol.
- **Fluide :** déséquilibre thermochimique, mélange multi-espèce.
- **Interface :** échanges convecto-diffusifs, interactions physico-chimiques gaz-surface.
- **Solide :** dégradation interne de matériaux composites (pyrolyse, oxydation), dégazage.
- **Effets du dégazage :** injection gaz froid (blocage convectif), modification composition chimique.
- Codes d'analyse de survivabilité des débris spatiaux basés sur des modèles réduits à faible temps de réponse. Influence de la dégradation des matériaux composites non modélisée.

Objectifs : Développer des modèles de substitution basés sur des simulations CFD prenant en compte l'influence de la dégradation thermochimique des débris spatiaux sur le flux de chaleur convecto-diffusif.

Cadre de l'étude : Débris de type réservoir en composite carbone/époxy (*Composite Overwrapped Pressure Vessels*). Ré-entrée depuis l'orbite basse, régime hypersonique continu.

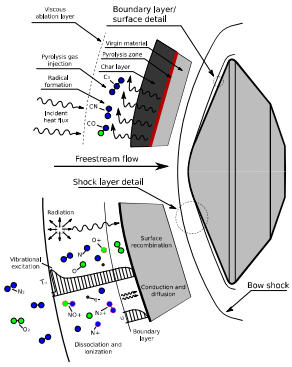

Fig. 1 – *Illustration des phénomènes d'interaction fluide-structure (Source : Potter - 2011).*

Influence du dégazage sur la modification du flux de chaleur convecto-diffusif

Déséquilibre chimique air/pyrolyse

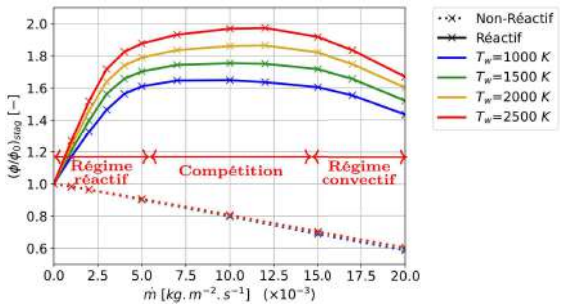

Fig. 2 – *Évolution du flux convecto-diffusif adimensionné au point d'arrêt en fonction du débit de soufflage $\dot{m}$ et de la température de paroi T_w [1].*

- **Soufflage non-réactif :** l'injection d'un gaz froid induit un blocage convectif et une réduction des réactions exothermiques proche paroi.
- **Soufflage réactif :** nouvelles réactions exothermiques air/pyrolyse. Compétition régimes réactif/convectif.

Composition des gaz de pyrolyse

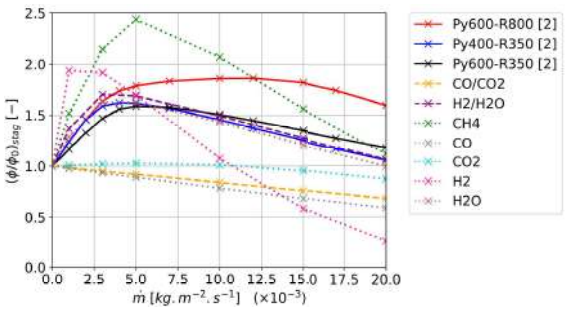

Fig. 3 – *Évolution du flux convecto-diffusif adimensionné au point d'arrêt en fonction du débit de soufflage $\dot{m}$ pour différentes compositions de gaz de pyrolyse [1, 2].*

- Composition dépendante du composite, état de dégradation, (p, T), etc. Influence majeure sur le flux de chaleur convecto-diffusif.
- Espèces composées de H : catalyseurs forts pour les réactions air/pyrolyse. Pas de régime réactif pour CO/CO_2.

Réduction de modèle par Krigeage

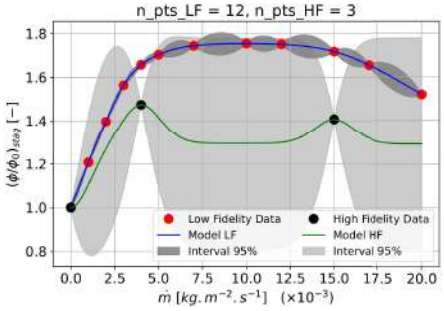

Fig. 4 – *Krigeage [3].*

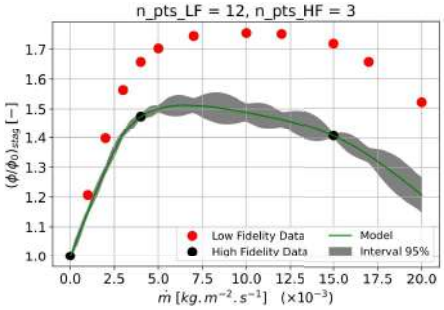

Fig. 5 – *Krigeage multi-fidélité [4, 5].*

Perspectives

- Génération d'une base d'apprentissage constituée de simulations CFD prenant en compte l'influence du soufflage des gaz de pyrolyse.
- Simulations couplées fluide/solide. Ajout de l'influence des processus physico-chimiques à la surface : recombinaison catalytique, oxydation, nitruration, sublimation.
- Intégration des modèles réduits dans un code de rentrée atmosphérique.

Références

[1] M. Lalande et al. "Assessment of Thermochemical Degradation Effects of Charring Material on the Wall Heat Flux during Atmospheric Re-Entry". In : *HiSST : 3rd International Conference on High-Speed Vehicle Science & Technology*. 2024, p. 140.
[2] F. Torres-Herrador et al. "Study of the Degradation of Epoxy Resins Used in Spacecraft Components by Thermogravimetry and Fast Pyrolysis". In : *Journal of Analytical and Applied Pyrolysis* 161 (2022), p. 105397. DOI : 10.1016/j.jaap.2021.105397.
[3] C.E. Rasmussen et al. "Gaussian Processes for Machine Learning". In : *Cambridge, MA : MIT Press* (2006).
[4] L. Le Gratiet. "Multi-Fidelity Gaussian Process Regression for Computer Experiments". Thèse de doct. Université Paris-Diderot (Paris VII), France, 2013.
[5] P. Saves et al. "SMT 2.0 : A Surrogate Modeling Toolbox with a focus on Hierarchical and Mixed Variables Gaussian Processes". In : *Advances in Engineering Sofware* 188 (2024), p. 103571. DOI : 10.1016/j.advengsoft.2023.103571.

maxime.lalande@onera.fr

S06-08 | Post-doc | **MARTINELLI Alessandro** | Lab. Charles Coulomb, Montpellier | Encadrant CNES : Thierry BRET-DIBAT

Relaxations of internal and strain-induced stresses in colloidal glasses

Ce poster n'est pas dans le recueil pour des raisons de Copyright

Characterization of the regions displaying featureless spectra on the Moon, using visible to near-infrared and thermal infrared remote sensing datasets: implications for the lunar crust

Mélissa Martinot, Jessica Flahaut

What?

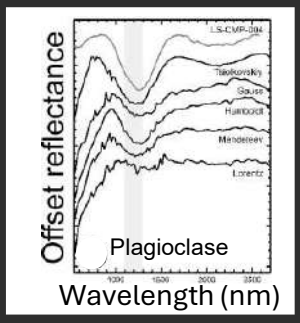

Modified after Martinot *et al.* (2020)

Relationship?

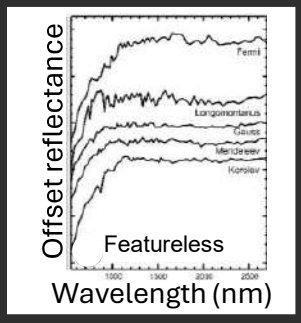

Modified after Martinot *et al.* (2020)

Shock pressures

Space weathering

Spatial mixtures

Composition (Fe content)

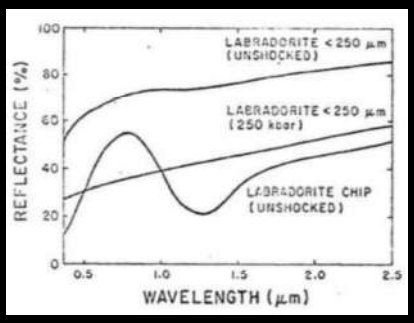

Adams, Hörz & Gibbons (1979)

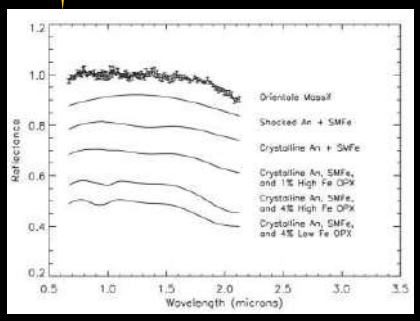

Lucey (2002)

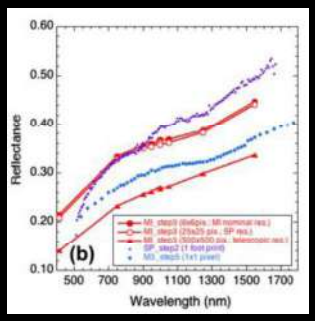

Ohtake *et al.* (2013)

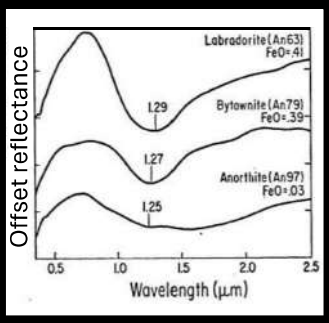

Modified after Adams & Goullaud (1978)

How?

1. M³

The Moon Mineralogy Mapper (M^3) is a VNIR hyperspectral imager that measured reflectance at the lunar surface between 0.45 and 3 μm (Pieters et al., 2009). M^3 is used to map areas that are featureless (FL), as well as areas that have a plagioclase signature.

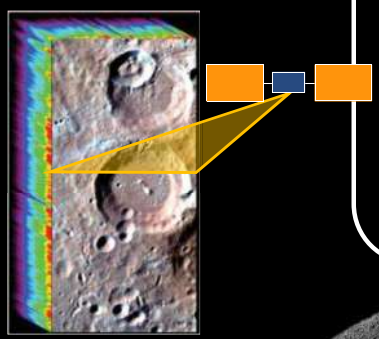

Green *et al.*, 2011

2. Diviner

FL areas are then investigated using Diviner data (0.3 to 400 μm), which channels in the 8 μm region provides key information about the composition of the lunar surface (Paige *et al.*, 2010).

3. Lab

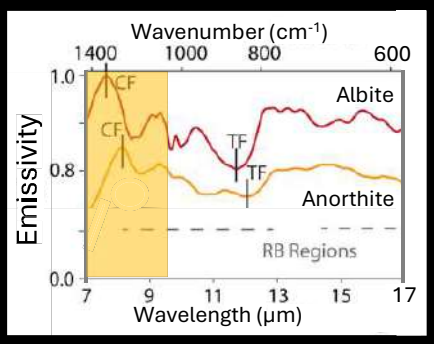

Modified after Donaldson Hanna *et al.* (2014)

Lab measurements of lunar meteorites and synthetic plagioclase will be done to investigate if composition or shock pressures cause FL spectra.

References: [1] Martinot *et al.* (2020), Icarus. [2] Adams, Hörz and Gibbons (1979), LPS X. [3] Lucey (2002), GRL. [4] Ohtake *et al.* (2013), Icarus. [5] Adams and Goullaud (1978) LPS IX. [6] Pieters *et al.* (2009), Curr. Sci. [7] Paige *et al.*, (2010), Science.

High-speed imaging of titanium cathode spots in a Vacuum Arc Thruster

Etienne Michaux, Jérémie Julien, Stéphane Mazouffre

Vacuum Arc Thruster - PJP

- Miniature space thruster
- Developed and manufactured by COMAT
- Solid propellant
- Pulsed vacuum arc discharge

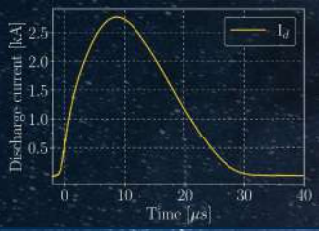

- Vaporization and ionization of metallic elements
- Plasma expansion leads to thrust generation in the opposite direction
- Plasma generation from the cathode: **cathode spots**

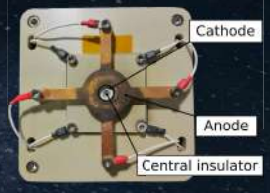

Experimental arrangement

- 130L capacity vacuum chamber
- 1 primary pump
  2 turbomolecular pumps
- 10^{-5} mbar while thruster operation

- Camera: Phantom TMX 7510
- Sampling period 2.2 µs
- Maximum resolution at 450k fps : 256 x 128
- Stochastic phenomenon: arc dynamics changes from pulse to pulse
  - Using a triggered iCCD leads to inaccuracies
  - Importance of single shot measurements

Active spot surface

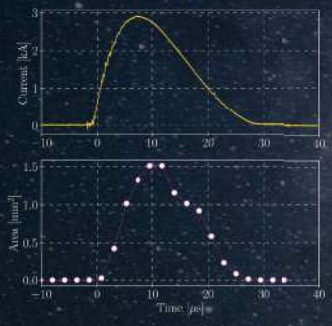

- High degree of similarity between the evolution of the surface and I_d
- Spearman rank order coefficient of 0.95 in average
- Linear augmentation of the number of active spots with the augmentation of I_d
- Rich dynamics, but repeatable values from one pulse to the other

Parameter	Averaged Value	σ
Surface [mm²]	0.345	0.078
Max surface [mm²]	1.124	0.230
I_d	0.948	0.048

Averaged values over the 150 films

Current density

- Spots tracking using a modified PTV algorithm
  - Each spot can sustain a limited j
  - Explains the linear relation between I_d and active spot surface
- Over the whole dataset: j = **4.3 ×10⁹ A/m²**
- In accordance with the "Large spot" model

Possible underestimation here

- Low camera resolution
- Dense and rapidly expanding plasma just over the spot (high brightness)
- Fractal spot model

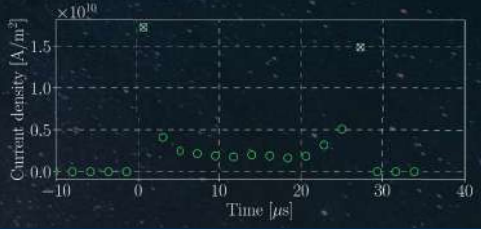

Clustering

- Detection of spots clusters with a depth-first search (DFS) algorithm
- Average cluster size: 1.83 × 10^{-2} mm²
- Maximum size reached around 5 µs: avg 0.3 mm²
- Largest clusters at the beginning of the discharge
  - Due to their inherent self avoiding walk motion

Motion tracking

First, to stress the point, the cathode spot is not moving: it only appears to move.
- Andre Anders

- Spots tracking using a modified PTV algorithm
  - Random walk behavior
  - Emergence of new spots during the discharge
- Accurate 2D tracking: spots trajectories and velocities
- Spots velocities ranging from 20 to 123 m/s
- Average velocity around 60 m/s, higher than in low current vacuum arcs
- No correlation between velocity and propagation direction

- Discharge current responsible of velocity magnitude
- External electric field is not the main driver for the acceleration

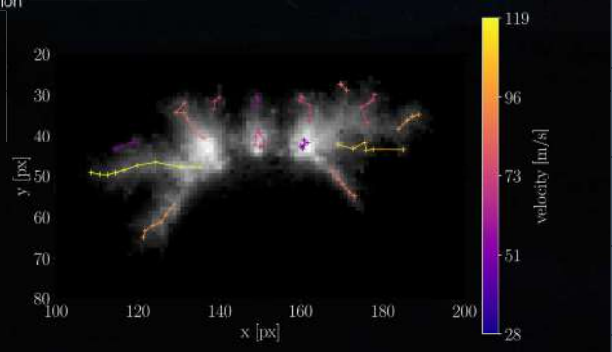

Conclusion and perspective

- New insights into cathode erosion dynamics
- Propellant use can be optimized by matching the cathode dimension and the discharge parameters
- Next experimental campaigns will be focused on seeking correlation between spot dynamics and instantaneous thrust

ASAMPLE

Analysis of submeso- and mesoscale dynamics of phytoplankton blooms in coastal waters influenced by river plumes

Dr. Anastasia Tarasenko with Dr. Pierre Gernez
Nantes Université, ISOMer laboratory

Phytoplankton blooms: why to study?

- *Phytoplankton is the base of marine food chain*
- *It plays a special role in the Earth carbon system: fixes CO2 and produces oxygen*
- *Especially important for the coastal ecosystems, but also brought into open ocean*
- *Can be toxic and create hypoxia areas*

Recent advancements in optical imagery algorithms allow the **optical bloom type** detection with *high-resolution* satellite data (as different plankton species have different pigments, thus, spectral signatures).

Some blooms, identified as "harmful algal bloom" (toxic for the environment) are also called "*red tide*". They can last from hours or months and might be difficult to predict.

Depending on the plankton species, the impact on environment will be different: toxins absorbed by mollusks, anoxia for fish and marine mammals, - they disturb coastal fishing, tourism and aquatic activities, and often need special management.

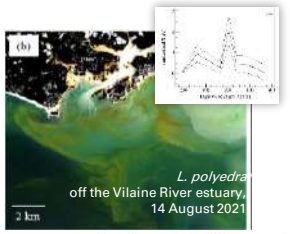

L. polyedra off the Vilaine River estuary, 14 August 2021

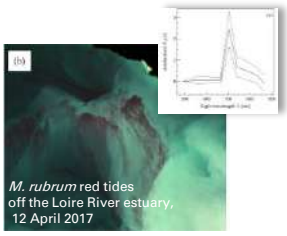

M. rubrum red tides off the Loire River estuary, 12 April 2017

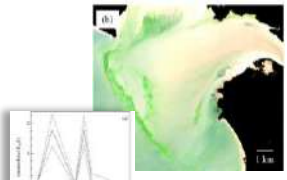

L. chlorophorum off the Loire River estuary 21 July 2019.

(from Gernez et al, 2023)

PROJECT GOALS

- observe plancton blooms at high resolution (satellite & in situ)
- describe the environmental conditions of blooms (water mass state & dynamics)
- adapt/propose algorithms for satellite data to distinguish a particular *optical bloom type* (a proxy for plankton species)
- find the descriptors to predict some phytoplankton blooms with satellite data

DATA

Satellite:
(passive) Optical, NIR, IR : Sentinel-2 (20 m), Sentinel-3 (300 m), Landsat 8&9 >> chl-a, SPM (suspended particulate matter) +SST
(active) SAR+ : Sentinel-1, SWOT (winds, surface water dynamics)
In Situ: ILICO (Infrastructure de recherche Littorale et Côtière)/REPHY data: phytoplankton, temperature, salinity
Auxiliary: Bathymetry (SHOM), currents (CMEMS Marine Copernicus), ROMAR (3D fields with physical conditions

QUESTIONS :

- What is seasonal and interannual variability of phytoplankton blooms in estuary area? Can we define the optical type of bloom ("species")?
- What are the environmental conditions: temperature, optical properties, tidal dynamics?
- Can we relate the small-scale dynamics to the phytoplankton bloom predictions?

Case study: May 31, 2022

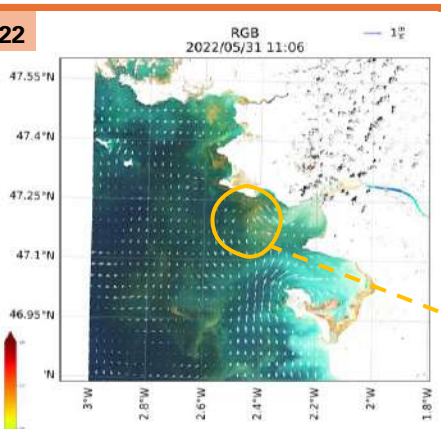

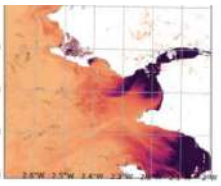

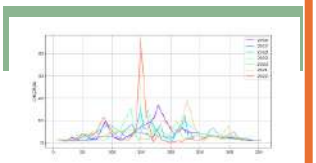

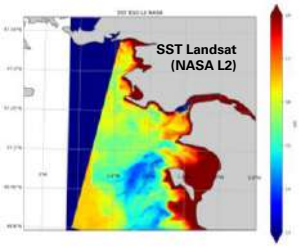

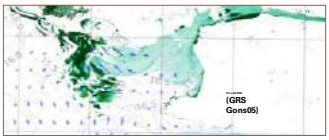

Possible explanation:

The ***Lingulodinium p.*** **bloom** area* is situated between the Loire waters (**warm, rich in SPM**) and rising tide (**colder and clearer Atlantic waters**). *Bloom has started about a week before.
Bloom is observed within resulting vertical stratification & convergence of 2 flows (Loire and Atlantic) - local vertical stirring at the shallow banc (7-15 m)

Overall, these are good conditions for the plancton development: clear waters for photosynthesis + initial stratification where plancton is situated within thermocline.

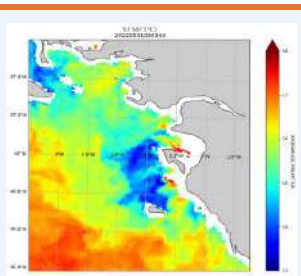

Sentinel-3 SLSTR
[L2 ESA WST,
3.74, 10.85 and 12 µm]
1000 m

Sea surface temperature
[S3 SST – LS SST] small study
(19 cases with time difference [0 – 2 hours])
Good agreement offshore, but statistically **Landsat ST > S3 SST (+0.5°C)**

(!) No coastal S3 SST data, problems within river plume area

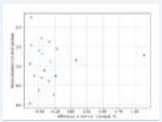

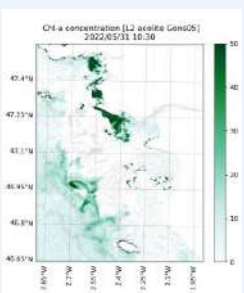

- same chl-a algorithm for S2& S3 (derived from *Gons, 2005* using 779, 705, 665 nm bands), but with different atmospheric corrections. S3 overestimate the bloom due to its spatial resolution
- Landsat lacks 705 & 779 bands, thus, OC3 algorithm is used (less precise, crucial for optical types retrieval)

(!) TRISHNA data will allow similar to L8&9 measurements and help to get longer time-series of chl-a, SPM & SST simultaneous data

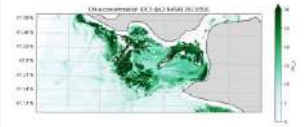

References:
Gons, Herman J., Machteld Rijkeboer, and Kevin G. Ruddick. "Effect of a waveband shift on chlorophyll retrieval from MERIS imagery of inland and coastal waters." *Journal of Plankton research* 27.1 (2005): 125-127.
Gernez, Pierre, David Doxaran, and Laurent Barillé. "Shellfish aquaculture from space: potential of Sentinel2 to monitor tide-driven changes in turbidity, chlorophyll concentration and oyster physiological response at the scale of an oyster farm." *Frontiers in Marine Science* 4 (2017): 137.
Gernez, Pierre, et al. "The many shades of red tides: Sentinel-2 optical types of highly-concentrated harmful algal blooms." *Remote Sensing of Environment* 287 (2023): 113486.

RÉPUBLIQUE FRANÇAISE
Liberté Égalité Fraternité

JC2 October 16th - 18th 2024
Cité de l'espace, Toulouse

cnes CENTRE NATIONAL D'ÉTUDES SPATIALES

Experimental analysis of cavitation instabilities on spatial inducer

Eddy TERRASSE[1,2] (eddy.terrasse@ensam.eu), Antoine DAZIN[2], Olivier ROUSSETTE[2], Matthieu QUEGUINEUR[1], Hugo STAUDT[3]
[1]CNES, [2]LMFL, [3]ArianeGroup

1 - Overview

• Cavitation

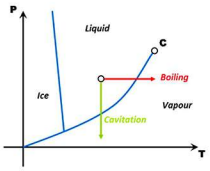

• Risks

- Performance drop
- Erosion
- Instabilities
- POGO
- Overspeed

• Inducer aims

- First overspressure
- Avoid cavitation in centrifugal
- Allow low inlet operating

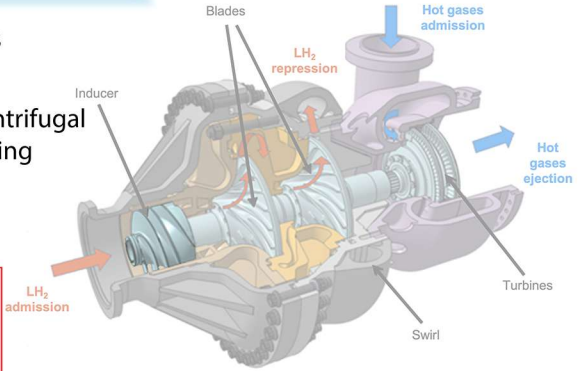

Objective:
Build some tools to identify cavitating regime dynamics and the impact on the launcher (efforts, vibrations, performance, ...)

2 - Test-rig (SESAME)

Closed loop of water driven by an electrical engine (200 kW)

- Temperature
- Acceleration
- Flow rate
- Pressure (unsteady) at the carter
- Force / moment (rotating frame)

Sampling rate: 2048Hz

Similitude laws to know the hydrogen behaviour

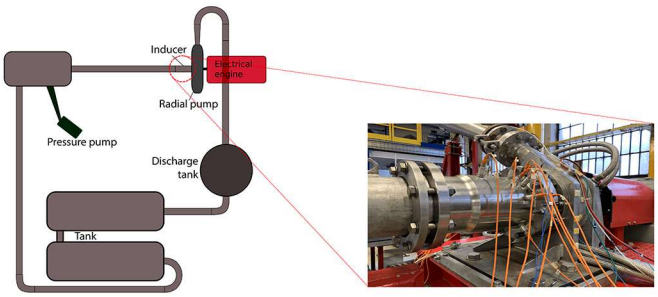

3 - Radial efforts estimation

Quantification of **radial efforts** on the shaft's turbopump

Pressure signals - P(τ)
↓
Continuous Wavelet Transform
↓
Denoising
↓
Inverse Continuous Wavelet Transform - P'(τ)

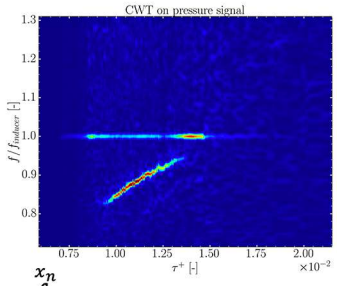

$$I_{async}, I_{sync}(\tau) = \pi R \int_{x_1}^{x_n} P'(\tau).\Delta x \, dx$$

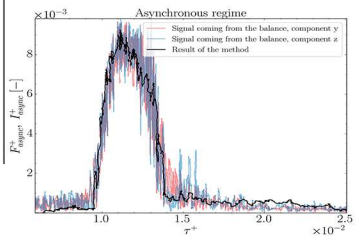

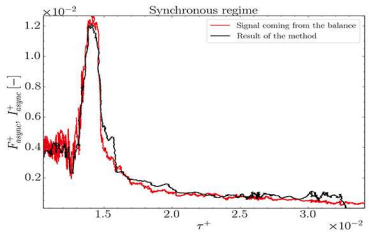

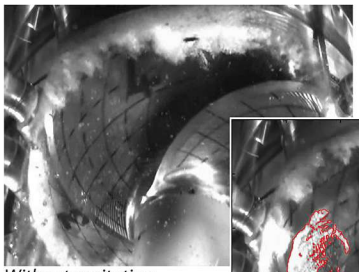
Without cavitation

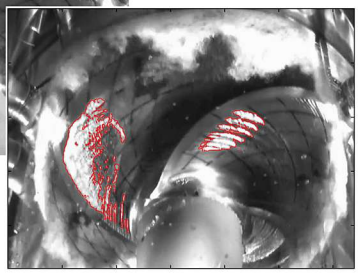
With cavitation

4 - Perspectives

Contours detection with strobostropic light and camera.

Estimation of the cavitation surface.

• Visualization test campaign with **high speed camera**

• Improvement of forces estimation method
• Understand phenomenon behavior using **Cross Wavelet Analysis**

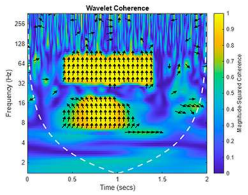

Arts et Métiers · Laboratoire de Mécanique des Fluides de Lille Kampé de Fériet · ArianeGroup

Recueil des posters

Session 7

S07-01 | Doc | **BELTRA Pierre** | Institut Pprime – ENSMA, Futuroscope Chasseneuil | Encadrant CNES : Hadrien LAMBARE | POSTER |
Étude aéro-thermo-acoustique des jets chauds diphasiques

S07-02 | Doc | **BOUM Marie-Ange** | ONERA, Palaiseau | Encadrant CNES : Pierre LASSALLE | POSTER |
Apprentissage incrémental pour le passage à l'échelle des algorithmes d'interprétation d'images de télédétection

S07-03 | Doc | **CHARPENTIER Gabin** | CNES, Toulouse | Encadrant CNES : Alexis PAILLET | POSTER |
Radioprotection pour les missions habitées vers Mars : modélisation environnementale, optimisation multicouche, prévention des risques radiatifs pour les astronautes

S07-04 | Doc | **DUCHAMP Clair** | LMD, Paris | Encadrant CNES : Adrien DESCHAMPS | POSTER |
Vortex et panaches d'aérosols (feux et volcans) dans la stratosphère

S07-05 | Doc | **FLESSELLES Benoit** | IMFT, Toulouse | Encadrant CNES : Hadrien LAMBARE | POSTER |
Étude expérimentale d'un propulseur électrohydrodynamique soumis à un écoulement forcé

S07-06 | Doc | **HOUEIBIB Ahmed** | LESIA (Obs. Paris), Meudon | Encadrant CNES : Kader AMSIF | POSTER |
Accélération de particules énergétiques dans les éjections de masse coronale

S07-07 | Doc | **KANAAN Linda** | IMT ATLANTIQUE, Lab-STICC, Brest | Encadrant CNES : Adrien GAY | POSTER |
Interference Management for robust satellite AIS receivers in dense maritime traffic areas

S07-08 | Doc | **MEDLEJ Mary-Joe** | Obs de la Cote d'Azur, Nice | Encadrant CNES : Bouchra BENAMMAR | POSTER |
Atmospheric turbulence prediction for optical links optimisation & Astronomical Observations

S07-09 | Post-doc | **VIELZEUF Pauline** | CCPM, Marseille | Encadrant CNES : Philippe LAUDET | POSTER |
Cosmic voids in Euclid

S07-10 | Post-doc | **WONGCHUIG Sly** | LEGOS – CNES, Toulouse | Encadrant CNES : Philippe MAISONGRANDE | POSTER |
Understanding the hydroclimatology of the world's largest tropical watersheds. The use of remote sensing and modeling in the Amazon and Congo basins

Étude aéro-thermo-acoustique des jets chauds diphasiques

Pierre Beltra*, Yves Gervais *, Gildas Lalizel*, Eva Dorignac, Florian Moreau et Patrick Berterretche

*Doctorant / ISAE-ENSMA
*Directeur de Thèse / Université de Poitiers
*Co-encadrant / ISAE-ENSMA

Présentation

- Lors du décollage de lanceurs, le bruit généré est suffisamment fort pour endomager le lanceur, sa charge utile ainsi que le pas de tir. Le pic d'énergie sonore est atteint lors des premières secondes du vol, lorsque les jets superoniques issus des moteurs impactent le pas de tir.
- Il est donc nécessaire de **réduire le bruit lors des premières secondes du vol**. Pour ce faire, de l'eau est injectée, en grande quantité, dans les jets supersoniques depuis le pas de tir. L'injection d'eau (ou déluge) dans les flammes des moteurs est couramment employée mais **son fonctionnement reste mal connu**. Les conditions étant complexes et transverses : écoulement supersonique, chaud, diphasique…

→L'objectif de la thèse est d'améliorer la compréhension des phénomènes physiques liés à la réduction sonore par injection d'eau. Pour ce faire:

- **Des essais acoustiques sur les effets de l'eau sont menés.**
- **Le développement d'une nouvelle méthode de mesure est entrepris pour observer l'intérieur de jets supersoniques soumis à une injection d'eau.**

Décollage du vol inaugural d'Ariane 6 à T-2s (gauche) et T+2s (droite)
Pas de tir au repos à gauche et interaction du déluge avec le laceur à droite

Etudes acoustiques

Pour étudier les effets acoustiques de l'injection d'eau, des expériences ont été réalisées sur le **banc MARTEL** (Moyen Aéroacoustique de Recherche & Technologie sur l'Environnement des Lanceurs). Elles consistent à générer un jet supersonique chaud par **combustion d'hydrogène et d'air comprimé**, dans une chambre semi-anéchoïque, et à injecter de grandes quantités d'eau (jusqu'à 2 l/s) dans ce jet.

Configuration	Mach	Température totale (K)
Jet de laboratoire	1,5	500
Jet MARTEL	3	1700
Moteur fusée	5	3500

- Pour simplifier l'étude, un jet libre, sans interaction avec le pas de tir est étudié.
- Des **microphones** sont placés sur 4 antennes à 1,5 m de la sortie du jet.
- **Différents paramètres d'injection** sont étudiés pour tenter de déterminer les meilleures conditions représentatives du phénomène pour la deuxième phase de la thèse (voir à droite) et connaitre les **paramètres les plus décisifs.**
- Par exemple, la vitesse d'injection de l'eau peut avoir un effet néfaste vers l'aval du jet, du fait de l'importance du bruit d'impact entre l'eau et le jet.

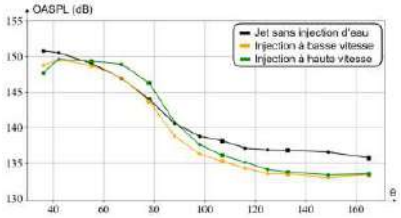

Effet de l'injection d'eau sur le bruit de jet

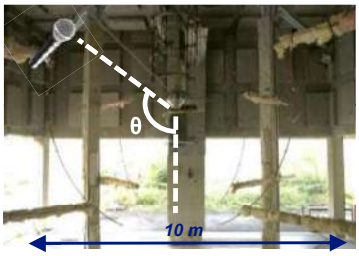

Banc MARTEL

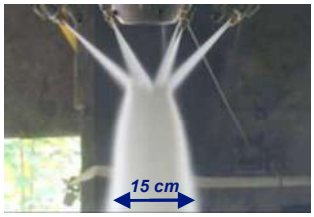

Vue rapprochée de la sortie de la tuyère de MARTEL avec une injection d'eau par 8 buses

Développement métrologie diphasique

- Pour comprendre les effets de l'injection d'eau, il est nécessaire de connaître les paramètres aérodynamiques du jet en aval de l'injection d'eau. La difficulté est de mesurer les paramètres des deux phases (gazeuse et liquide) indépendamment.
- Il est nécessaire de mettre au point une nouvelle technique de mesure pour observer l'intérieur du jet: une nouvelle métrologie diphasique est développée sur le **banc BATH** (Banc AéroTHermique): un laser double pulse à **266 nm** excite deux traceurs : de l'oxyde de zinc (**ZnO**), dans l'air, dont le rayonnement de **phosphorescence** est centré **sur 400 nm** et de la Rhodamine B (**Rh B**) dans l'eau, qui **fluoresce vers 590 nm**.
- Cette technique permet également de s'affranchir des réflexions du laser sur les gouttes d'eau susceptibles endommager les caméras.
- Des mesures de PIV peuvent alors être effectuées sur chaque phase séparément.

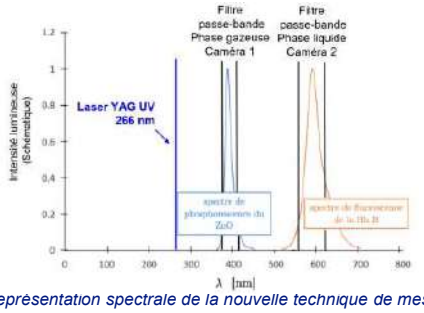

Représentation spectrale de la nouvelle technique de mesure

- Les premiers essais réalisés ont mis en lumière une mauvaise séparation des phases : les gouttes d'eau sont visibles sur l'image dédiée à la visualisation du ZnO. Il est possible que le ZnO pénètre dans les gouttes et les rende visibles à travers le filtre ZnO.

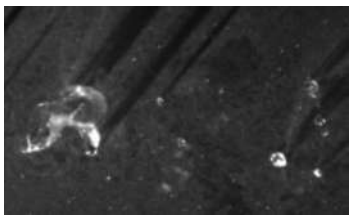

Exemple d'image de la caméra 1 - Visualisation de la phase gazeuse (ZnO) et des gouttes (non prévue)

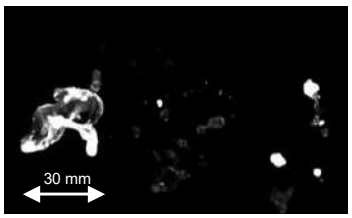

Exemple d'image de la caméra 2 - Visualisation de la phase liquide (Rh B)

CONCLUSIONS

- Les essais réalisés en première année sur MARTEL ont permis d'acquérir une meilleure compréhension de l'influence de la température, du débit d'eau, de la vitesse d'injection et de la hauteur d'injection sur l'émission acoustique issue de l'interaction d'un jet supersonique et une injection d'eau.
- Les essais sur la nouvelle méthode de diagnostic des deux phases ont mis en lumière une séparation des phases imparfaite. Il est nécessaire de développer des solutions matérielles ou logicielles (suppression des gouttes sur l'image de ZnO à l'aide des informations de l'image Rh B) avant d'appliquer cette méthode sur MARTEL pour mesurer les effets aérodynamiques d'une injection d'eau sur la dynamique d'un l'écoulement chaud et sur son émission acoustique.

CONTACT :
pierre.beltra@ensma.fr
yves.gervais@univ-poiters.fr
gildas.lalizel@ensma.fr

Cette thèse est cofinancée par la Région Aquitaine et le CNES

APPRENTISSAGE INCRÉMENTAL POUR LE PASSAGE A L'ÉCHELLE DES ALGORITHMES D'INTERPRÉTATION DES IMAGES DE TÉLÉDÉTECTION

Marie-Ange BOUM[1,2], Dawa DERKSEN[2], Pierre FOURNIER[1], Stéphane HERBIN[1]
[1]ONERA/DTIS, [2]CNES

INTRODUCTION

Les images de télédétection en **expansion** offrent de nouvelles opportunités pour la **cartographie et le suivi à grande échelle de l'utilisation des sols**.

Objectif Global

Concevoir un **système de classification à grande échelle** (ex. France), **optimisé en ressources**, et capable de s'étendre progressivement à de nouvelles zones géographiques.

Défis :

1. **Adaptation de domaines** successives.
2. Atténuation de l'**oubli catastrophique.**

FLAIR#1 (French Landcover Aerial ImageRy) [1]

- **Images aériennes THR** (0,2 m/pixel)
- Variabilité géographique plus ou moins importantes (paysages et climats).
- **Domaines spatiaux** définis par les **départements** de la Fra ce Métropolitaine.

CLASSIFICATION

Domain Incremental Probabilistic PCA [2]

Extraction de caractéristiques à l'aide d'un **modèle de fondation** :

- L'encodeur est fixe : il génère des caractéristiques invariantes.
- Le classificateur linéaire est remplacé par un **classificateur génératif** afin d'atténuer l'oubli.

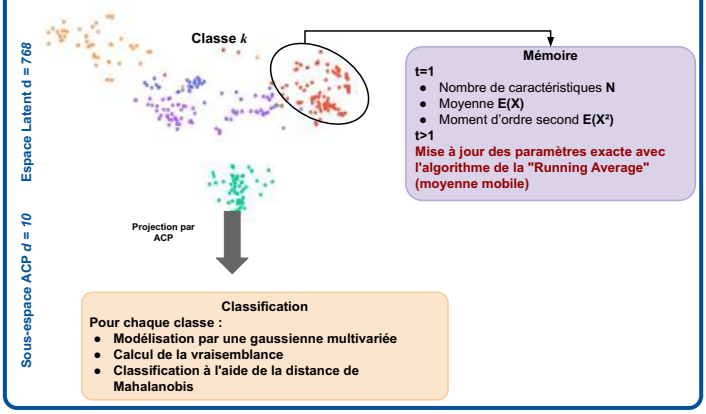

CLASSIFICATION : Expériences

Pre-training Data	SL	SSL	FT	DIPPCA ACC	DIPPCA BWT	DIPPCA DEGRAD.	ER ACC	ER BWT	ER DEGRAD.	SUP.
ImageNet21K	x			**91,7**	-2	-4,8	**90,9**	-6,9	-5,6	96,9
ImageNet1K		DINO		**91,6**	-3,2	-4,1	**91**	-6,9	-4,8	95,8
SA-1B		MAE		90	-4	-4,1	90,1	-5,6	-3,9	94
MillionAID		MAE		69,3	-24,5	-20,3	74,3	-9,5	-11,4	85,7
RSSCN7	x		x	81,3	-11,6	-7,8	81,7	-8,2	-7,4	89,1

Utilisation des modèles de fondation (FM) pour la télédétection :

- Les FM pré-entraînés sur des images naturelles sont efficaces pour extraire des caractéristiques expressives.
- L'ajout d'un classificateur génératif réduit l'oubli, à condition que les caractéristiques soient pertinentes.
- Cette méthode surpasse les baselines (ER).

Limites :

- Les caractéristiques extraites dépendent des données de pré-entraînement.
- Les RSFM sont confrontés au surajustement et à la faible diversité des datasets.

LES MODÈLES DE FONDATION

- **Pré-entraînement** sur des datasets diversifiés et vastes.
- **Généralisation** : performants sur diverses tâches en aval.
- **Accessibilité** : modèles open-source.

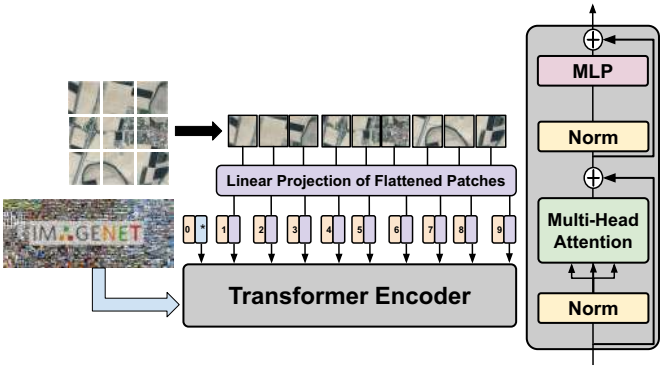

Comment exploiter efficacement les modèles de fondation pour l'apprentissage incrémental en télédétection ? [3]

SEGMENTATION

Atténuer l'oubli catastrophique par PEFT

Les **Parameter Efficient Fine Tuning (PEFT)** permettent d'ajuster efficacement un modèle pré-entraîné à de nouvelles tâches ou domaines en ne modifiant que certaines couches tout en gardant la majorité des paramètres fixes.

Choix de **PEFT** : **AdaptMLP [4]**

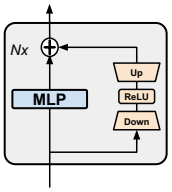

Approche proposée :

L'idée de base est d'apprendre une série de modules d'adapter, domaine par domaine, à l'aide d'un *transformer* pré-entraîné.

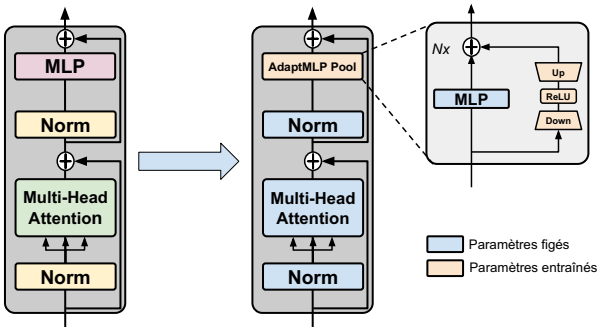

2 stratégies d'apprentissages à tester :

- **Dépendante du passé** : Les nouveaux modules AdaptMLP sont influencés par les paramètres des modules déjà appris.
- **Indépendante du passé** : Chaque nouveau module est appris de manière indépendante des modules précédemment appris.

Objectif final : Créer un modèle capable de généraliser sur l'ensemble des domaines spatiaux tout en minimisant l'oubli catastrophique.

RÉFÉRENCES

1. Garioud, Anatol, et al. "Flair# 1: semantic segmentation and domain adaptation dataset." *arXiv preprint arXiv:2211.12979* (2022).
2. Boum, Marie-Ange, et al. "Continual Learning in Remote Sensing: Leveraging Foundation Models and Generative Classifiers to Mitigate Forgetting." *IGARSS 2024-2024 IEEE International Geoscience and Remote Sensing Symposium*. IEEE, 2024.
3. Dosovitskiy, Alexey. "An image is worth 16x16 words: Transformers for image recognition at scale." *arXiv preprint arXiv:2010.11929* (2020).
4. Chen, Shoufa, et al. "Adaptformer: Adapting vision transformers for scalable visual recognition." *Advances in Neural Information Processing Systems* 35 (2022): 16664-16678.

ARAMIS : A model of Martian surface radiative environment

RÉPUBLIQUE FRANÇAISE
Liberté Égalité Fraternité

Gabin Charpentier[1,2,3,4*], Rémi Benacquista[2], Robert Ecoffet[1], Marine Ruffenach[1], Alexandre Cappe[2], Théo Pieri[1,4], Alexis Paillet[1], Julien Mekki[1], Philippe Valet[3] and Yves Gourinat[4]

CNES CENTRE NATIONAL D'ÉTUDES SPATIALES

Space Radiation Environment

Galactic Cosmic Rays (GCR) :

- Originated from outside the solar system and anti-modulated with solar cycle
- Fully charged atomic nuclei (^{1}H to ^{238}U) with 87% Protons, 12% He, ~1% Z>2
- Extremely high energy and very penetrating (difficult to shield)

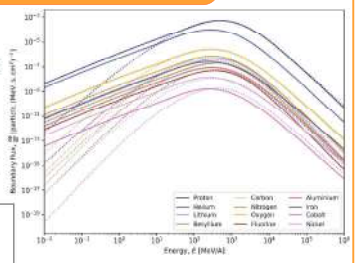

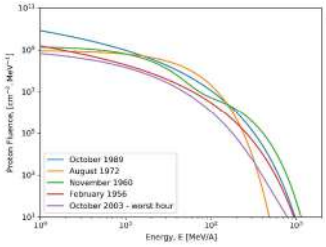

Solar Particle Events (SPEs):

- Sporadic and directional events with highest probability at solar maximum
- Mostly low energetic proton (< 1GeV)
- Alert time ~20 minutes

Martian atmosphere specificities

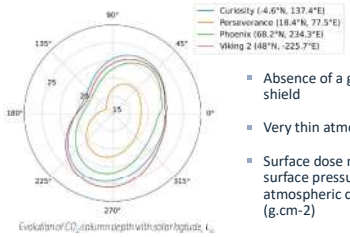

- Absence of a global magnetic shield
- Very thin atmosphere
- Surface dose modulated by surface pressure (Pa) or atmospheric column depth (g.cm-2)

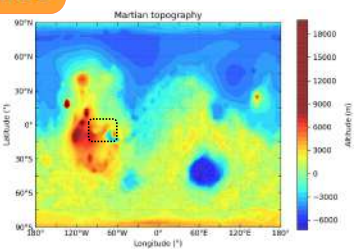

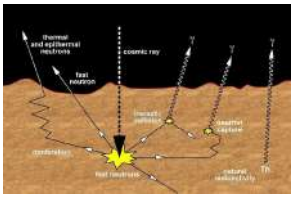

Secondary particle generation :

- All types of particle : neutrons, electrons, photons, muons, different ion isotopes, ...
- Atmospheric shower phenomenon : billions of secondary particles created by interaction with the atmosphere
- Albedo creation : nuclear interaction between the planetary surface and GCR generating mainly neutrons and photons

ARAMIS architecture and GEANT4 Geometry

ARAMIS : Atmospheric RAdiation Model for Ionizing spectra on martian Surface

Regolith (Default) composition	Ratio
SiO_2	51.2 %
$Al_2CaK_2MgNa_2O_7$	32.1 %
FeO_3	9.3 %
H_2O	7.4 %

Atmosphere elements	Ratio
CO_2	95.482 %
N_2	2.705 %
Ar	1.603 %
O_2	0.13 %

- Thermodynamic parameters of the atmosphere imported from the Mars Climate Database (MCD v6.1)
- Parametric atmosphere geometry to suit any landing site regarding altitude and position (latitude, longitude)
- Higher number of near-surface layers
- Used with every primary ion up to Z=28 and every secondary (charged or neutral particles)

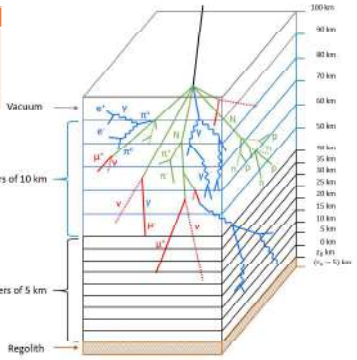

- Geant4 v11.1.0 (C++) & Python codes ran with the CNES High Performance Computing (HPC) cluster
- Physic lists : *FTFP_INCLXX_HP*
- Convolution of surface response function with primary spectra :

$$\left.\frac{d\phi_j}{dT^*}\right|_{z_0} = 2\pi \sum_i \int_T \frac{dN_{ij}}{dT^*}(T, z_0) \cdot \frac{d\phi_i}{dT} dT$$

- Relative error calculated per bin :

$$R_{k,j} = \left[\frac{\sum_{p=1}^{N} T_p^{*2}}{\left(\sum_{p=1}^{N} T_p^{*}\right)^2} - \frac{1}{N} \right]^{1/2}$$

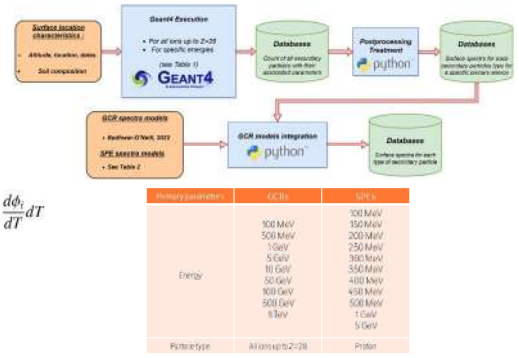

Primary parameters	GCRs	SPEs
Energy	100 MeV 500 MeV 1 GeV 5 GeV 10 GeV 50 GeV 100 GeV 500 GeV 1 TeV	100 MeV 150 MeV 200 MeV 250 MeV 300 MeV 350 MeV 400 MeV 450 MeV 500 MeV 1 GeV 5 GeV
Particle type	All ions up to Z=28	Proton

Results validation with MSL-RAD measurements

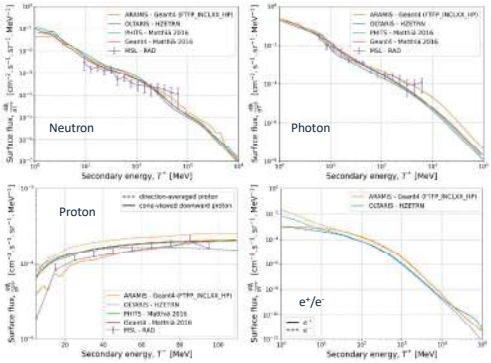

Martian surface flux of neutron, photon, proton and e+/e- on Gale Crater from 19 August 2012 to 17 February 2013, given by ARAMIS and compared to measurements and other models with FTFP_INCLXX_HP.

GCR induced spectra :

- Much wider range of energy (from 10^{-2} to 10^{9} MeV) and flux for neutron, photon, electron, proton, alpha, all isotopes up to Z=28 , ...
- ARAMIS present the best fit with the MSL Curiosity rover's measurements for protons on the all spectrum and for neutral particles at high energies (E>100 MeV) better than other existing models
- ARAMIS allows the distinction in the fluxes between Albedo particles and secondary particles created with atmospheric showers but also with particle incoming an opening angle (i.e. protons with RAD) [1]
- Photons are mostly generated by nuclear reactions between cosmic particles and regolith, while electrons are generated by nuclear reactions between cosmic particles and atmosphere and neutron's origins are equilibrated

SPE induced spectra :

- ARAMIS presents an atmospheric cut-off for protons about 160 MeV [1]
- A comparison between OLTARIS/ ARAMIS and the method from [2] defining the pivot energy as a function of surface pressure :

$$D_{surf}(p)\ [mGy] = c_\rho(p) \cdot F_{Eq(p)}$$

$$\begin{cases} E_q(p) = -0.000114 \cdot p^2 + 0.350 \cdot p + 86.9 \\ \frac{c_\rho(p)}{10^{-7}} = -0.000614 \cdot p^2 + 1.08 \cdot p + 388 \end{cases}$$

- ARAMIS and OLTARIS show good agreement with pivot method surface dose
- For combinations of events, the pivot method is therefore not the most appropriate, although it provides extremely accurate results for other spectral shapes.

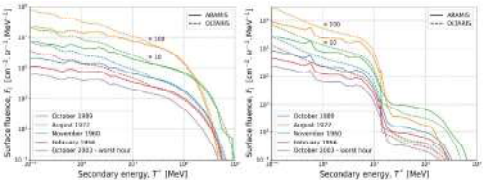

Martian surface fluence of neutrons (left) and photons (right) on Gale Crater from 19 August 2012 to 17 February 2013 for different SPE historical events

Events	Models mean absorbed dose [mGy]				Pivot method absorbed dose [mGy]	
	ARAMIS		OLTARIS		Zhang et al. (2023)	Guo et al. (2021b)
	Male	Female	Male	Female		
February 1956	3.8	3.88	3.8	3.87	4.34	5.1
November 1960	21.54	21.99	23.33	23.74	33.81	39.4
August 1972	4.87	4.94	6.72	6.84	2.28	2.75
October 1989	12.04	12.28	11.85	12.07	12.53	14.74
October 2003 worst hour	0.67	0.68	/	/	0.6	0.66

Dosimetric tools

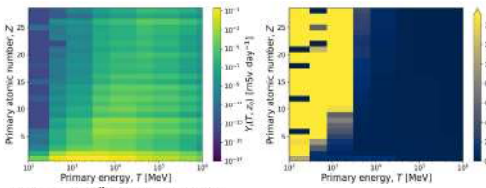

$$\begin{cases} Y_i(T, z_0) = \sum_j \int_{T^*} F_{ij}(T, T^*, z_0) C_j(T^*) dT^* \\ F_{ij}(T, T^*, z_0) = 2\pi \left[\frac{dN_{ij}}{dT^*}(T, T^*, z_0) \cdot \frac{d\phi_i}{dT} \right] \end{cases} \qquad \delta_i(T, z_0) = \frac{\left[\sum_j \left(F_{ij} R_{kj} \right)^2 C_j(T^*)^2 \right]^{1/2}}{Y_i(T, z_0)}$$

- The effective dose rate yield function, $Y_i(T, z_0)$ allows to identify the most contributing species and energies to the surface dose : GCR hydrogen and helium ions between 1 and 10 GeV represent the main contributor
- Monte Carlo uncertainty propagation in yield calculation is large (>140%) at low energies for all species where yield is minimal, which does not influence its value

Radiation cartography

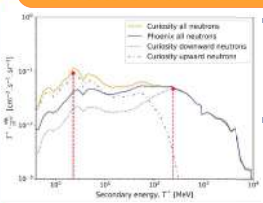

- Neutrons show two peaks in the spectrum, at 2.3 MeV and 240 MeV, corresponding to neutrons evaporating from excited nuclei and neutrons created by spallation processes between primary and atmospheric nuclei
- Downward particles shape the high-energy flow, while upward particles shape the low-energy spectrum
- Improved Shepard interpolation method, addressing screening and "bull's eye" effects (considers relative position of data points and desired slopes)
- Smooth results for neutrons in Valles Marineris for interpolation with surface pressure

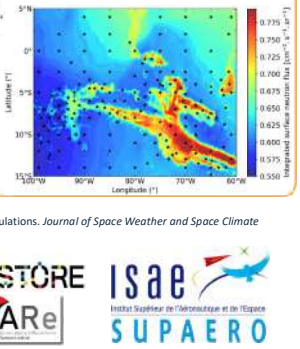

[1] Charpentier G., Ruffenach M., Benacquista R., Ecoffet R., Dossat C., et al. (2024). ARAMIS: a Martian radiative environment model built from GEANT4 simulations. *Journal of Space Weather and Space Climate*
[2] Zhang, J., J. Guo, and M. I. Dobynde, 2023. What Is the Radiation Impact of Extreme Solar Energetic Particle Events on Mars? Space Weather, 21(6)

1 : Centre National d'Etudes Spatiales (CNES)
2 : TRAD Tests & Radiations
3 : RESTORE rejuvenation research center (INSERM-CNRS)
4 : ISAE-SUPAERO
*Corresponding author : gabin.charpentier2@cnes.fr

ICA · TRAD Tests & radiations · cnrs · MEDES · IRSN INSTITUT DE RADIOPROTECTION ET DE SÛRETÉ NUCLÉAIRE · RESTORE ARe · ISAE SUPAERO

Tracking and analysis of the Hunga plume in the stratosphere

C. Duchamp[1], B. Legras[1], P. Sellitto[2,3], A. Podglajen[1], F. Wrana[4], C. von Savigny[4], E. Carboni[5], R. Siddans[5], C. Kloss[6], R. Belhadji[2], J.-U. Grooß[6], S. Khaykin[7] & F. Ploeger[6]

1 LMD-IPSL, Paris; 2 LISA-IPSL, Créteil; 3 INGV, Catania; 4 Institute of Physics, Greifswald; 5 RAL, Oxford; 6 FZJ, Jülich; 7 LATMOS-IPSL, Paris

RÉPUBLIQUE FRANÇAISE
Liberté Égalité Fraternité

CNES CENTRE NATIONAL D'ÉTUDES SPATIALES

PRESENTATION

The phreato-magmatic eruption of Hunga (20°S, 175°W) on 15 January 2022 was exceptional in several respects. Its **explosive intensity was close to that of the eruption of Pinatubo** in 1991 with a Volcanic Explosivity Index of ~6 (Poli & Shapiro, 2022).
The induced atmospheric Lamb wave circled the globe at least 4 times with an amplitude comparable to that of the 1883 Krakatau eruption (Matoza et al., 2022; Vergoz et al., 2022, Wright et al., 2022).
We report here about the impact of the eruption in the stratosphere based on the following works of the ASTuS - PyroStrat consortium :
Sellitto et al., 2022, Nat. Com., DOI: 10.1038/s43247-022-00618-z
Legras et al., 2022, ACP, DOI: 10.5194/acp-22-14957-2022
Kloss et al., 2022, GRL, DOI: 10.1029/2022GL099394
Khaykin et al., 2022, Nat. Com., DOI: 10.1038/s43247-022-00652-x
Duchamp et al., 2023, GRL, DOI: 10.1029/2023GL105076

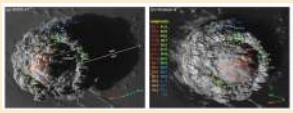

Estimation of plume altitude from stereoscopic processing of GOES 17 and Himawari 8 images
Carr et al., GRL, 2022

The **plume reached 56 km altitude** within 30 minutes following the paroxysmal explosion. The bulk of the plume was produced between 26 and 34 km.

Water vapour recorded within the plume and its vicinity displayed extremely large, never seen, values in the stratosphere with a saturated profile at least up to 33 km altitude within the plume in the hours following the eruption.
The water in excess generated precipitating ice and a rapid washout of the ashes.
The remaining water vapour in the stratosphere was estimated at **+ 140 Tg** (Millan et al., 2022), that is an instantaneous **10 % increase of the stratospheric content**.

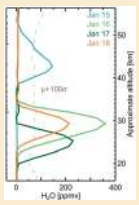

MLS H_2O profiles
Millán et al., GRL, 2022

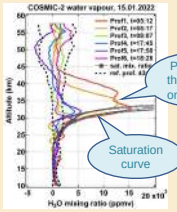

COSMIC-2 radio occultations
Khaykin et al., Nat. Com., 2022

COMPOSITION OF THE PLUME

Eumetsat RGB Ash recipe using Himawari IR channels
Brown and dark blue: ash and ice; Greenish: sulfur

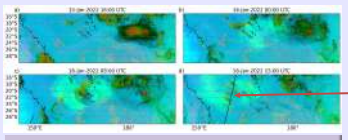

The initial ash + ice plume dissipates rapidly leaving a double plume mostly with sulfur compounds.
Fast conversion to sulfates due to the large amount of water vapour, especially in the southern and highest cloud which is also the one with largest amount of water (Sellitto et al., 2022).

LOAC measurements at La Reunion OPAR, 21°S, show **submicronic mainly non absorbing particles** (for 23 Jan)

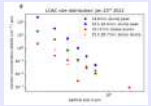

Kloss et al., GRL, 2022

On 16 Jan, **CALIOP** sees two aerosol clouds at 31 and 28 km, mostly with very large scattering ratio and **no depolarization** => liquid droplets. There are also two areas of high depolarization close to 35% which could correspond to **remaining ice crystals** (stay only for a few days).

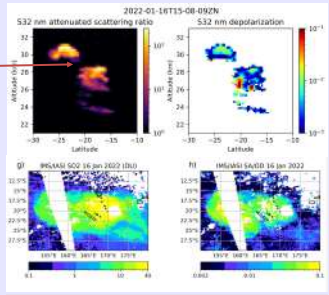

RAL IMS/IASI double retrieval of SO_2 (DU) & sulfate aerosol optical depth

Western strip: Complete conversion to sulfates (no SO_2 left)

Mainly SO_2 cloud at lower level (not seen by CALIOP and the ASH RGB and no anomalous moisture)

Eastern strip : Incomplete conversion to sulfates

RGB Ash shows sulfates, not SO_2 as usually believed!

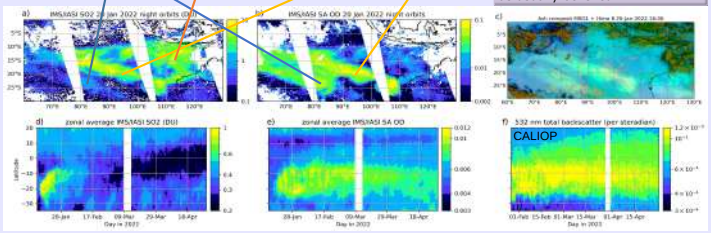

After a few days, the two clouds are turned into **elongated strips** (higher, southern and moistiest -> western strip, lower, northern -> eastern strip) which exhibit **different conversion rates** to sulfates according to their moisture and altitude.
SO_2 returns to background value by the end of January whereas sulfate aerosols persist in the stratosphere.
IMS/IASI SA optical depth and CALIOP total extinction distributions evolve in the same way.

EVOLUTION OF THE ZONAL MEAN PLUME

OMPS-LP 745 nm daily zonal average aerosol extinction ratio
CALIOP 532 nm daily zonal average attenuated aerosol scattering ratio
MLS water vapour daily zonal average mixing ratio (ppmv)

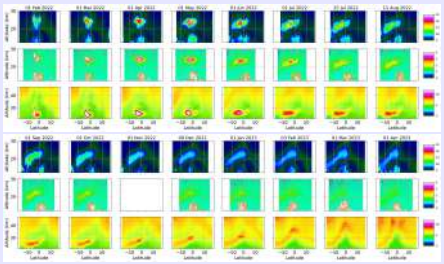

The initial fast descent of aerosols and water (>100 m/day) was attributed to **intense longwave cooling by water vapour** (Sellitto et al., 2022). Cooling is reduced but persists until June producing **temperature anomaly** (Schoeberl et al., 2022) and anomalous warming in ERA5 (here).

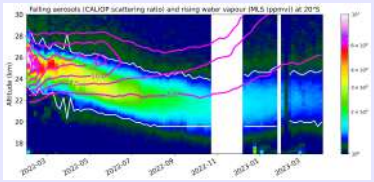

Plume's latitudinal extension stops at 20 in the NH while it extends close to the pole in the SH.
AEROSOLS : (CALIOP + OMPS-LP)
- After a period of **initial fast descent**, the plume stabilises near 24-25 km and descends slowly.
- Since 2023, **tropical ascent** linked to the Brewer Dobson circulation (BDC).
- In the same time, close to the South Pole, **fall towards the troposphere** through sedimentation.

WATER VAPOUR : (MLS)
Initially mixed with the aerosols, **water vapour separates by rising with air while aerosol sediment under gravity**, until the moist and aerosol layers are, respectively, above and below 25 km (see also Schoeberl et al., 2022). Since 2023, water vapour has behaved like aerosols, but at higher altitudes.

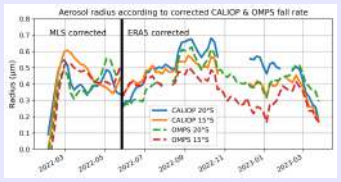

The aerosol size is estimated from fall speed using Stokes formula.
Fall speed is estimated from the apparent descent speed corrected by the MLS water vapour ascent or by the ERA5 ascent (valid when the cooling effect of water vapour has ceased).
In the long term, **aerosols radius** seems to be around **0.4 µm**.

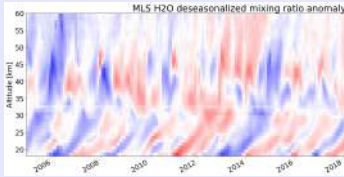

'Tape recorder' water vapour signal in the tropical stratosphere between 10°S and 10°N.
Very large water vapour disturbance which has no equivalent since at least 2006.
The **maximum perturbation is 5.36 ppmv** in March 2022 at 24.5 km altitude.

AEROSOL PLUME ANALYSIS (SAGE III)

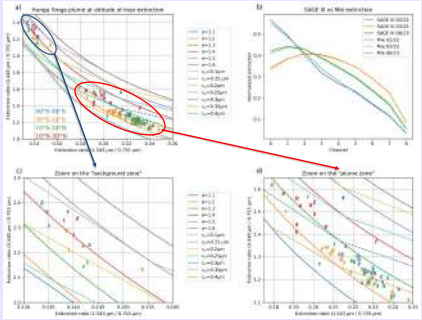

Retrieval of the **sulfate aerosols (SA) size distribution** based on the **two color ratios** 449 nm / 755 nm and 1543 nm / 755 nm for the aerosol extinction coefficients (Wrana et al., 2021).

Fig. a) : the curves for equal **mode width σ** and **median radius r_m** form a skewed grid in the domain of interest allowing the identification of the two parameters.

The good performance of the method can be appreciated from Fig. b) where modeled Mie extinctions using σ and r_m drawn from Fig. a) are compared to the SAGE III measured extinctions. The **agreement is excellent over the whole range** which is another indicator of the **absence of ash** in the plume.

Fig. c) & d) : observed extinction ratios at the level of maximum extinction in the **plume** are distributed over a domain of the diagram that clearly differs from the **background** points.

The **particle effective radius r_{eff}** can be estimated and then the **total number density N_0** using the extinction at 755 nm.

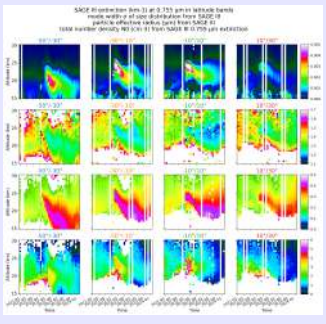

- σ : **1.2-1.3** in the plume, 1.4-1.5 for the background (Wrana et al., 2021) and 1.8-2.0 for other recent stratospheric volcanic plumes together with smaller sizes (Wrana et al., 2023).
- r_{eff} : ~ **0.4 µm** in the plume, 0.2 µm or less for the background (with Khaykin et al., 2022).
- N_0 : **3-5 cm^{-3}** in the plume, 20-30 cm^{-3} for other stratospheric volcanic plumes from recent eruptions with similar sulfur injection but much smaller particles (Wrana et al., 2023).

Recent comparison cases : Ambae in 2018, Raikoke & Ulawun in 2019 and La Soufrière in 2021.

H_2SO_4 mass in SA (H_2SO_4 weight percentage : 70%). Between March and November 2022 : **0.66 Tg ± 0.1 Tg**, remarkably **constant** in spite of a **considerable redistribution in latitude** (b).
Matches initial SO_2 injection of 0.4-0.5 Tg (Carn et al., 2022; Millan et al., 2022).

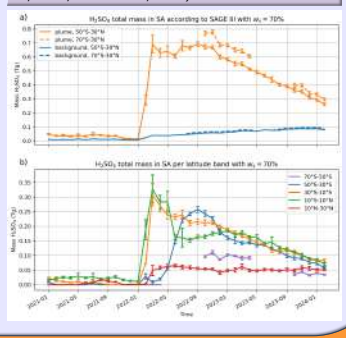

CONCLUSIONS

- Main injection of the plume by 26-34 km with a saturated water profile. No ash remains after a few days in this range of altitudes.
- Fast conversion of SO_2 to sulfates, due to the presence of water. Persistent plume for at least 2 years.
- Fast initial descent of the plume (water and aerosol) until 20 Feb due to water vapour cooling.
- Following months : unmixing and separation of water which is rising in the BDC and aerosols which are sedimenting.
- The size distribution is characterized by larger particles than recent stratospheric eruptions with an unusually small mode width.
- The unusual size distribution of aerosols is related to the fast conversion of SO_2 to sulfates (Legras et al., 2022).
- The total mass of stratospheric H_2SO_4 is estimated at 0.66 Tg (matches estimates of the stratospheric SO_2 source of ~ 0.4-0.5 Tg).
- This mass has been found to be very stable over the period March 2022 to November 2022 after which it slowly declines linearly.

OTHER PARTNERS

anr® cnrs SCIENCES SORBONNE UNIVERSITÉ IPSL LMD ENS

Ionic wind propulsion - effects of speed and confinement

Benoît Flesselles[12], Franck Plouraboué[1], Nicolas Binder[2]

[1]IMFT, [2]Isae Supaero

What is ionic wind ?

Ionic wind occurs when an electric field is applied to a gas seeded with ions of the same polarity. The ions are accelerated by the electric field, and through collisions with neutral molecules, the whole gas is accelerated. This phenomenon can easily be observed in the lab by applying a high voltage between a pair of asymmetrical electrodes, thus triggering a corona discharge on the electrode of smallest radius, called the emitter. This emits ions into the gas, which then drift to the larger electrode, called the collector.

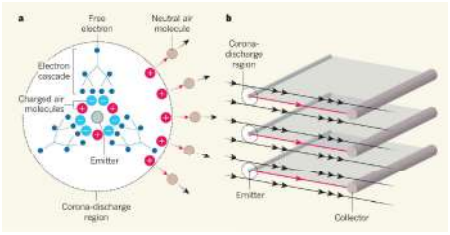

Fig. 1: Plouraboué, Nature 2018 [4] (a) : Injection de charges positives par la décharge couronne. (b) : Accélération du gaz entre l'émetteur et le collecteur.

Ionic wind for atmospheric propulsion

Fig. 2: Xu, Nature 2018 [2] Prototype of a model aeroplane powered by an ionic wind thruster.

Electrohydrodynamic (EHD) thrusters boast interesting characteristics : no moving parts, low noise, no carbon emissions, distributed propulsion. However, this technology remains challenging to implement due to its low thrust density compared to conventional propulsion technologies. Xu et al's [2] prototype shown in Figure 2 had a thrust density estimated at $3\,\mathrm{N\,m^{-2}}$, compared to around $1000\,\mathrm{N\,m^{-2}}$ for a commercial airliner. Attempts to boost this low thrust density include research on the effect of air velocity, ion sources, ion mobility, and multi-stage thrusters.

Effect of speed

Thrust F_{EHD} produced by an emitter-collector pair scales with current I :

$$F_{EHD} = \frac{ID}{\mu} \tag{1}$$

With μ the ion mobility and D the emitter-collector distance. Neglecting freestream velocity, Townsend's law gives:

$$I \propto \frac{\mu}{D^2 ln(D)} V(V - V_0) \tag{2}$$

With V the applied voltage and V_0 the corona inception voltage, which shows that increasing the emitter-collector distance for a given voltage reduces the thrust.

Taking into account the freestream velocity, the current flowing through a corona discharge has been shown by Chapman [1] to scale as :

$$I = \mu C_1 V(V - V_0) + C_2 u_\infty (V - V0) \tag{3}$$

With u_∞ the freestream velocity. This scaling was verified in an emitter-collector configuration by Grosse et al. [3].

Neglecting the electrodes' drag, thrust then scales as :

$$F_{EHD} = \frac{ID}{\mu\left(1 + \frac{u_\infty}{\mu E}\right)} \tag{4}$$

An experimental study is currently being set up at ISAE to study the influence of a high speed freestream velocity on an EHD thruster.

Effect of confinement

Studying the EHD thrusters inside a high speed wind tunnel was complicated by the electrostatic interactions between the electrodes and the dielectric walls of the test section. In order to understand these interactions, a smaller experimental apparatus was assembled to specifically study the consequences of a dielectric confinement.

This led to the unexpected observation that current and thrust do not depend monotonically on the confinement length H, equal to the emitter-dielectric distance.

The influence of confinement on current and thrust for various voltages and emitter-collector distances is shown in the following measurements, obtained at IMFT with a dropshape collector. The dotted lines are numerical simulations and the arrows show "unconfined" experiments.

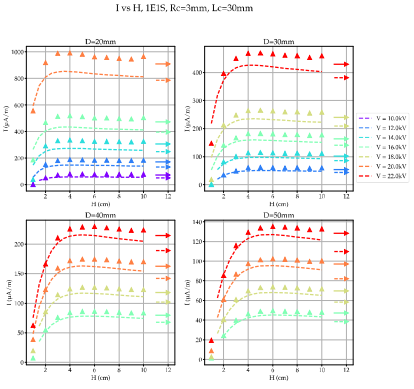

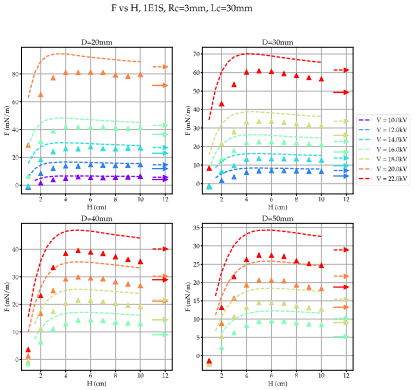

References

[1] Seville Chapman. Corona point current in wind. *Journal of Geophysical Research*, 75(12):2165–2169, April 1970.

[2] Xu et al. Flight of an aeroplane with solid-state propulsion. *Nature*, 563(7732):532–535, November 2018.

[3] Sylvain Grosse, Nicolas Benard, and Eric Moreau. Electroaerodynamic thrusters: Influence of a freestream on the current, ionic wind, and force produced by a DC corona discharge. *Journal of Electrostatics*, 130:103950, August 2024.

[4] Franck Plouraboué. Flying with ionic wind. *Nature*, 563(7732):476–477, November 2018.

Dynamics of energetic particles scattered in the solar wind

Ahmed Houeibib[1], F. Pantellini[1] & L. Griton[1]

1. LESIA, Observatoire de Paris, Université PSL, CNRS, Sorbonne Université, Université de Paris, Meudon, France.

Context

Solar Energetic Particles (SEPs) are high-energy ions and electrons emanating from the Sun, accelerated impulsivly at the sites if magnetic reconnection in the solar corona or gradually, at the shock of a Coronal Mass Ejection (CME) during its propagation through the heliosphere (Reames+ 1999). Once energized, SEPs trace path along the interplanetary magnetic field lines, drifting due to gradients and curvature of the magnetic field and the presence of an electric field (Dalla+ 2015). Due to the turbulence in the solar wind, these particles experience diffusion both in velocity space (parallel diffusion) and in real space (perpendicular diffusion).

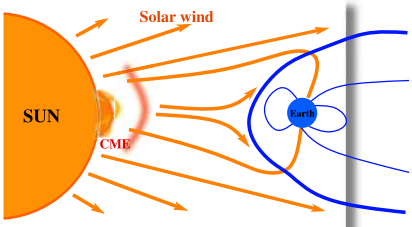

Model & numerical set-up

Solar wind 3D MHD simulation

Simulation domain :

- Sun centerd spherical grid
- Size: $144 \times 48 \times 128$ in$[r, \theta, \varphi]$
- Boundaries: $r \in [0\ 14\ \ 14]$ AU

Numerical integration of the ideal MHD equations using the MPI-AMRVAC code

(E, B, U)

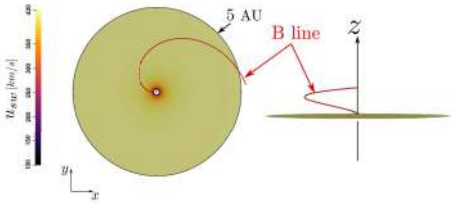

Test Particles propagation

- Integrate relativistic Guiding Center equations and use (E, B,U) from MHD simulation.

$$\frac{\mathrm{d}\mathbf{R}}{\mathrm{d}t} = v_\parallel \mathbf{b} + \mathbf{v_E} + \frac{\gamma m}{qB}\mathbf{b}\times\left[\left(\frac{\mu}{\gamma^2 m}\nabla B\right) + \frac{v_\parallel}{\gamma}E_\parallel \mathbf{v_E}\right] \quad \text{E-cross-B drift, grad-B drift}$$

$$+\left[v_\parallel^2(\mathbf{b}\cdot\nabla)\mathbf{b} + v_\parallel(\mathbf{v_E}\cdot\nabla)\mathbf{b}\right] \quad \text{curvature drift}$$

$$+\left[v_\parallel(\mathbf{b}\cdot\nabla)\mathbf{v_E} + (\mathbf{v_E}\cdot\nabla)\mathbf{v_E}\right] \quad \text{polarisation drift}$$

$$\frac{\mathrm{d}(\gamma v_\parallel)}{\mathrm{d}t} = \frac{q}{m}E_\parallel - \left[\frac{\mu}{\gamma m}\mathbf{b}\cdot\nabla B\right] + \gamma\mathbf{v_E}\cdot\left[v_\parallel(\mathbf{b}\cdot\nabla)\mathbf{b} + (\mathbf{v_E}\cdot\nabla)\mathbf{b}\right] \quad \text{mirror force}$$

where $\mathbf{b} = \frac{\mathbf{B}}{|\mathbf{B}|}$, $\mathbf{v_E} = \mathbf{E}\times\frac{\mathbf{b}}{|\mathbf{B}|}$, $\mu = \frac{m\gamma^2 v_\perp^2}{2|\mathbf{B}|}$, $\overset{(*)}{\mathbf{E}} = -\mathbf{u}\times\mathbf{B} - \frac{\nabla p}{n}$

- Parallel diffusion : probabilty of doing a collision based on a mean free path along B. If particle undergoes a collision, the pitch-angle (v,B) is randomized. When the collision is in the rest frame, the energy of the particle is conserved !

Results

Configuration

Particles crossing the inner boundary or the surface r = 5 AU are re-injected back at the same initial position with the same initial conditions.

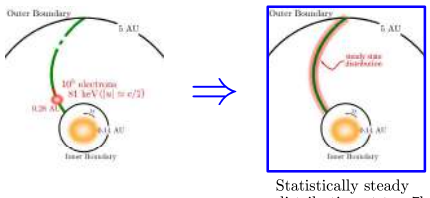

Statistically steady distribution at t = 7h

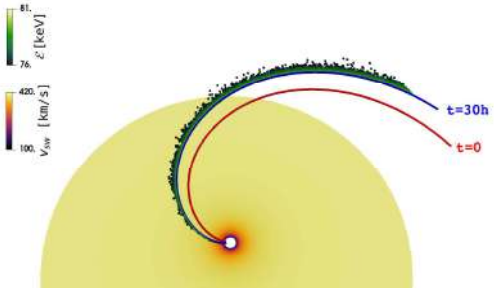

Scatter plot : particles color-coded with their enrgy

Drift velocities profiles along B-line

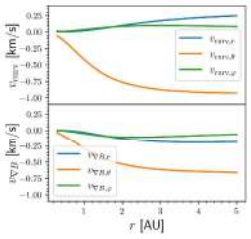

Dominant drifts : grad-B & cruvature drifts !

Both in -θ direction !

Pitch-angle distribution

Single event

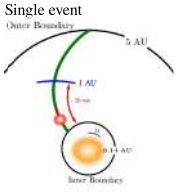

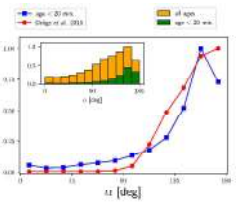

Steady state distribution

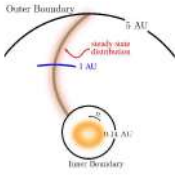

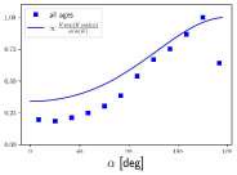

Energy evolution

Assuming time steadiness for the fields, we can then approximate (*) in terms of the time evolution a particle's kinetic energy:

$$\frac{d\mathcal{E}}{dt} \simeq m\gamma v_\parallel^2\,\mathbf{v_E}\cdot(\mathbf{b}\cdot\nabla)\mathbf{b} + m\gamma\frac{v_\perp^2}{2}\,\mathbf{v_E}\cdot\nabla\ln B$$

replacing $\mathbf{v_E}$

$$\frac{d\mathcal{E}}{dt} \simeq q\langle\mathbf{v}_{\mathrm{curv}} + \mathbf{v}_{\nabla B}\rangle\cdot\mathbf{E}$$

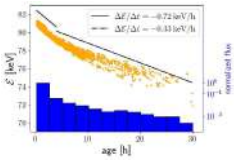

In the present configuration, $\mathbf{v_E}$ is oriented opposite to the curvature vector $(\mathbf{b}\cdot\nabla)\mathbf{b}$ and to the magnetic field gradient $\nabla\ln B$ so that the above equations describe a systematic loss of energy regardless of the direction the particle is moving towards.

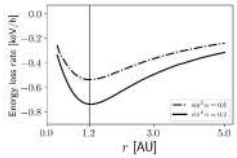

Adiabatic cooling

Energy as a function of age for electrons near r = 1 AU when scattered in the solar wind moving frame and with the absence of drifts

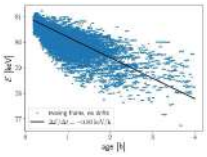

Ongoing work

The next step is to see how energetic particles are accelerated by a CME.

This PhD work is connected to current space missions as Solar Orbiter (ESA) and Parker Solar Probe (NASA).

This study has important implications for Space Weather.

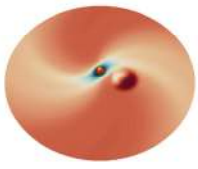

References :

- Dröge, W., Kartavykh, Y. Y., Wang, L., Telloni, D., & Bruno, R. 2018,ApJ, 869, 168
- Dalla, S., Marsh, M. S., & Laitinen, T. 2015, ApJ, 808, 62
- Mignone, A., Haudemand, H., & Puzzoni, E. 2023, CPC, 285, 108625
- Parker, E. 1965, Planetary and Space Science, 13, 9
- Ripperda, B., Porth, O., Xia, C., & Keppens, R. 2017, MNRAS, 467, 3279
- Zaslavsky, A., Kasper, J. C., Kontar, E. P., et al. 2024, ApJ, 966, 60

Interference Management for Robust Satellite AIS Receivers in Dense Maritime Traffic Areas

Linda Kanaan[1,2,4], Karine Amis[1], Frédéric Guilloud[1], Rémi Chauvat[3], Adrien Gay[4]

1- IMT Atlantique, Brest, France. 2-Tésa, Toulouse, France. 3-Kinéis, Toulouse, France.
4- CNES, Toulouse, France

I. Context

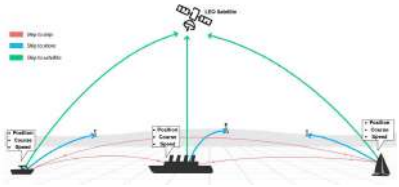

Figure 1: AIS communications

- The Automatic Identification System (AIS) [1] was mainly designed for nautical and short range communications.
- Satellite AIS emerged from the beginning of 2008's.

Problematic:

- **Characteristics of the AIS System:**

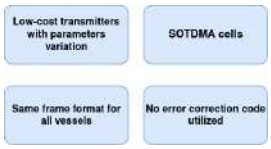

- **Difficulties of Sat-AIS receivers :**
  - *Multiple Access Interference* - Figure 2 [2]
  - *Satellite Propagation Delay* ≈ 2-10 ms
  - *Satellite Doppler Shift* ≈ ±3.8 kHz

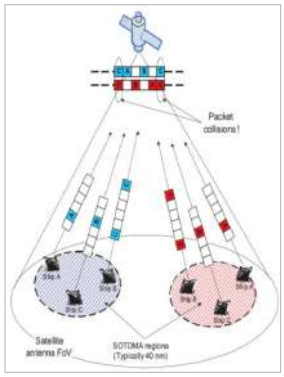

Figure 2: AIS multiple access interference [2]

Objective:

- Our main focus is to cope with the overlapping messages issue to improve the success rate of detected AIS messages.
- This could be achieved through satellite interference management.

II. Interference Management

- The multi-user received signal model during a given AIS time slot:

$$r(t) = \sum_{i=1}^{N} \alpha_i s_i(t - \tau_i, \mathbf{a}) e^{j(2\pi f_{d,i}(t)t + \phi_i)} + n(t)$$
$$f_{d,i}(t) = f_{d,i} + \eta_i t / 2$$

- Several approaches have been implemented for the purpose of interference management of AIS signals:
  - Phased Antennas Array Approach
  - Bandwidth Separation in Sub-zones Approach
  - **Interference Cancellation Approach** (PIC, SIC)

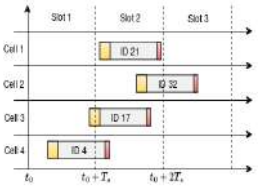

Figure 3: AIS Messages collision

- **Interference Cancellation** approach using **SIC** (Successive Interference Cancellation) is considered.

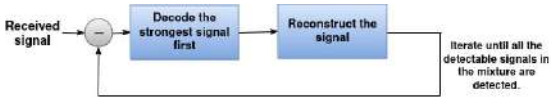

Figure 4: SIC Algorithm

- To mitigate the effect of interference and to improve the detection rate using SIC, the main goals are:
  i. Improvement of all the iterations of detection
  ii. Robust reconstruction of the modulated signal (Future work)

IV. Conclusion

- Exploiting the **a priori information** improves the probability of correct detection robustly with respect to the position of interference.
- The **optimized List Viterbi Algorithm** enhances the success rate of detection. It could be very efficient when combined with the a priori information exploitation method.
- Future Perspectives include robust reconstruction of the correctly detected signal.

III. Methodology

- For improving all the iterations of detection, two main methods are investigated:

1. Exploiting the a priori information about AIS signals in the mixture

- Utilizing the training sequence and start flag of the AIS packet in Figure 5.

Figure 5: AIS packet

2. Increasing the diversity of candidates

- List Viterbi (LV) algorithm is exploited [3].
- For each state at each time instant, store these parameters:
  1) Cost Metric
  2) Path history (previous state and path rank)

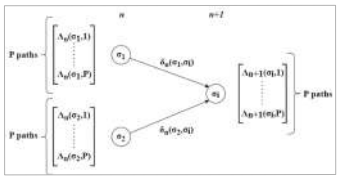

Figure 6: Cost Metric of LV algorithm

- To ensure better performance and less complexity , the parameters of LV algorithm are optimized.
- More details could be found in [4].

IV. Results

i.

- Performance of exploiting the a priori information with the CV algorithm shows remarkable gain ≈ 2 dB at PER= 10^{-3}

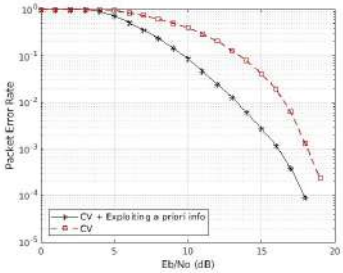

ii.

- Classical Viterbi (CV) and List Viterbi (LV) No Interference

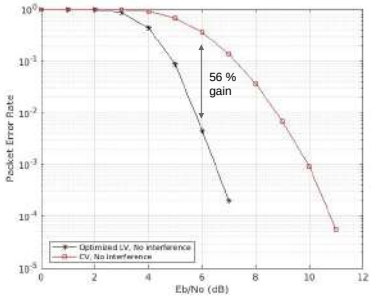

- Classical Viterbi (CV) and List Viterbi (LV) 1 Interfering signal

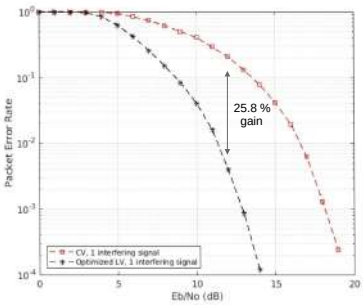

iii.

- Memory complexity of the LV algorithm with different list sizes.

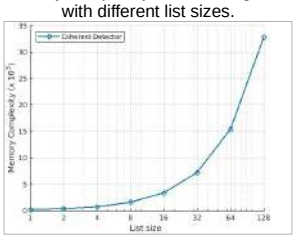

- The memory requirements increases rapidly for higher values of the list size.
- Utilizing the optimized parameters of the LV algorithm can significantly improve PER at the cost of a **limited** increase of the complexity.

IV. References

[1] ITU, Technical characteristics for an automatic identification system using time division multiple access in the VHF maritime mobile frequency band - recommendation ITU-r m.1371-5, Feb. 2014.

[2] M. A. Cervera and A. Ginesi, "On the performance analysis of a satellite-based AIS system," 2008 10th International Workshop on Signal Processing for Space Communications, Rhodes, Greece, 2008, pp. 1-8, doi: 10.1109/SPSC.2008.4686715.

[3] N. Seshadri and C.-E. Sundberg, "List viterbi decoding algorithms with applications," IEEE Transactions on Communications, vol. 42, no. 234,pp. 313–323, 1994

[4] L. Kanaan, K. Amis, F. Guilloud and R. Chauvat, "Application of List Viterbi Algorithm for Satellite-based AIS Detection"- Submitted.

Contact: Linda.Kanaan@imt-atlantique.fr

Optimizing atmospheric turbulence predictions for optical links and astronomical observations by an instrumented drone

Mary-Joe Medlej*[1], Christophe Giordano[1], Aziz Ziad[1], Alohotsy Rafalimanana[1], Eric Aristidi[1]

[1] : Laboratoire Lagrange, Bd de l'Observatoire, CS 34229, 06304 Nice cedex 4, France *Université Côte d'Azur, Observatoire de la Côte d'Azur, CNRS*

**Contact: mary-joe.medlej@oca.eu*

Why prediction ?

Anticipating atmospheric conditions in advance helps in both the astronomy and optical telecommunication communities:

Astronomical observation

Flexible scheduling:

→Prioritize observations according to optical conditions.

→Maximize scientific output quality.

→Efficient resource management.

ELT: >200k €/night

Optical telecommunication

Smart scheduling:

→Identify optimal time windows for optical laser links operation.

→Facilitates optimal selection of optical ground stations to receive information, enabling site switching in adverse conditions.

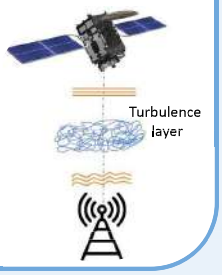

How to predict ?

We use the Weather Research and Forecasting (WRF) model, developed at NCAR (Boulder, USA), combined with an optical turbulence (OT) model.

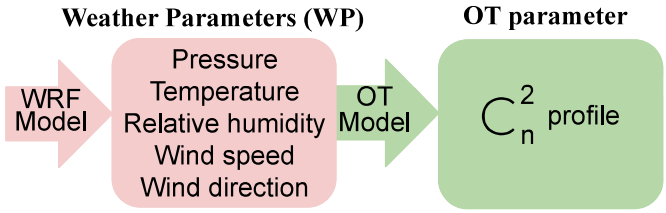

Two different turbulence models are used:

- Empirical model (radio sounding balloons)
- Tatarskii model

Prediction optimization

❖ Models alone are not enough. Optimization methods have been developed, showing improvements in free atmosphere but limited impact in the ground layer (GL):

- Statistical learning *(Ref1)*
- New Outer Scale method for Tatarskii's model *(Ref2)*
- Optimizing WRF physico-dynamics configuration *(Ref2)*

❖ GL prediction optimization by an ***instrumented drone***:

Equipement: weather probes

Scans the GL (450m), up and down above a fixed point

The collected data are injected into WRF to improve the WP predictions and then OT forecasting

Results

2023-11-22 15:40:00

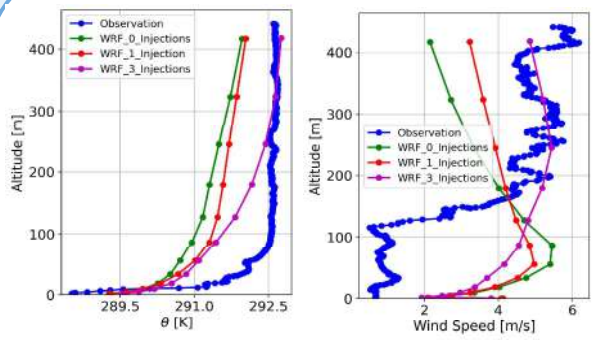

2023-11-15 10:00:00

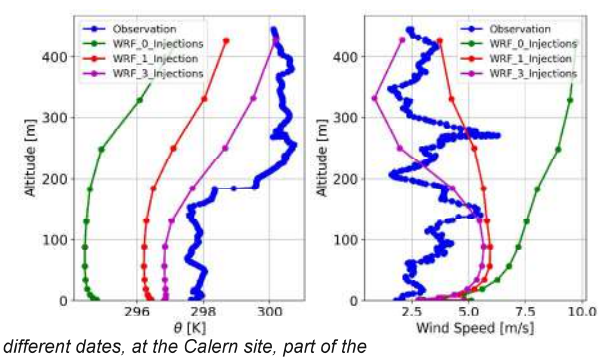

Profiles of potential temperature and wind speed for two different dates, at the Calern site, part of the observatoire de la Côte d'Azur. WRF_0_injection, WRF_1_injections, and WRF_3_injections present the predicted profiles with 0, 1, and 3 injections, respectively.

Conclusion:

→ With drone data injections, the prediction accuracy improves.

→ As the number of injections increases, the prediction becomes significantly more accurate.

Perspective:

Future improvements will focus on increasing drone injections by:

→ Implementing an automated drone station for higher daily injection frequency.

→ Incorporating better vertically resolved data in WRF for injections at more pressure levels.

References: (1) *Giordano et al. 2021, MNRAS, 10.1093/mnras/staa3709*
(2) *Rafalimanana et al. 2022, PASP, 10.1088/1538-3873/ac6536*
(3) Ziad et al. 2018, SPIE, 10.1117/12.2313386
(4) Medlej et al. 2024, SPIE, 10.1117/12.3018254

Cosmic voids with Euclid

Pauline Vielzeuf,

PostDoc CNES @Centre de Physique des Particules de Marseille, vielzeuf@cppm.in2p3.fr

Introduction and Motivations

Cosmology, the study of the universe's origin and evolution, has advanced significantly in recent decades. Observations, such as those from the cosmic microwave background radiation and distant supernovae, strongly suggest that the universe is expanding. This expansion began from a compact, warm, and dense state known as the **Big Bang**, approximately 13.8 billion years ago.

Recent evidence indicates that the universe has entered a phase of accelerated expansion, driven by an unknown force termed **dark energy**. Additionally, the presence of **dark matter**, which constitutes about 27% of the universe, plays a crucial role in the formation of cosmic structures, influencing the motion of galaxies and galaxy clusters through its gravitational effects. Together, these components challenge our understanding of gravity and the fundamental properties of the universe. As we gather more data and refine our models, cosmology continues to evolve, offering deeper insights into the cosmos and the forces that govern its dynamics.

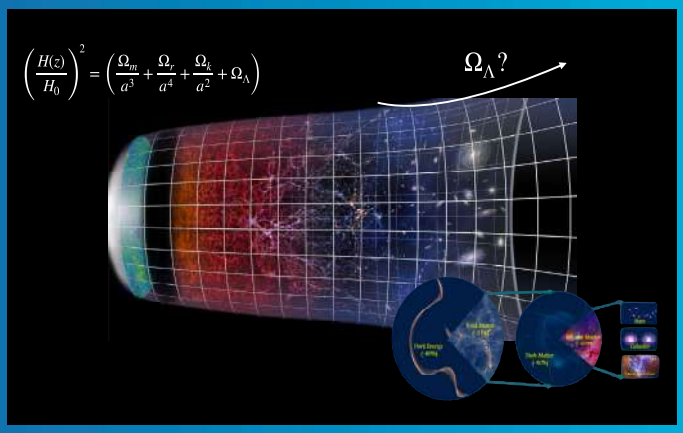

Figure 1: State of the art of the concordance model of cosmology

1) Euclid

The Euclid satellite [1] was launched in July 2023, and will observed about 1/3 of the sky after 5 years. Equipped with a visible-wavelength camera and a near-infrared spectrometer, Euclid will capture high-resolution images and spectra, allowing us to analyze the distribution and shape of billions of galaxies.

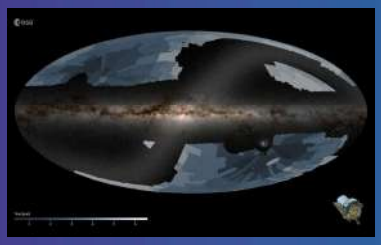

Figure 2: Area that Euclid will cover after 6 years of observations

Euclid main objective is to put cosmological constraints on Dark Energy and Dark matter, using the information contained in the position and shape of billions of galaxies.

2) Cosmic voids

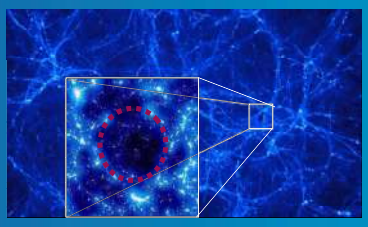

Figure 3: Exemple of a cosmic void identified in the cosmic web

Cosmic voids are large underdensities in the cosmic web, formed through gravitational interactions and the universe's expansion. As matter accumulates in denser regions, it leaves behind these relatively empty areas. While they may seem barren, cosmic voids play a crucial role in our understanding of cosmology, providing insights into dark energy, dark matter, and the overall dynamics of the universe.
Moreover, new-generation galaxy surveys, such as Euclid, will give the opportunity to cosmic voids to become a full cosmological probe and put constraints on cosmological parameters by increasing the total number of observed voids of about two degrees of magnitude, enhancing thus their statistical power.
In this project, we are using the algorithm described in [2] to identify voids in Euclid galaxy catalogues.

3) Gravitational lensing

Gravitational lensing is a powerful tool in cosmology, it occurs when the gravitational field of a massive object distorts the light from distant sources. In the context of weak lensing, the distortions manifest as slight elongations of galaxy shapes. This lensing effect allows astronomers to map the distribution of dark matter, as the amount of distortion correlates with the mass of the lensing object. By measuring the ellipticity of a large number of galaxies e_{obs}, it is possible to infer the amount of distortion of the galaxy field as:

$$e_{\rm obs} = e_{\rm int} + \gamma_t, \qquad \Delta\Sigma(r_p) \propto \gamma_t(r_p) \tag{1}$$

where $e_{\rm int}$ is the intrinsic ellipticity, that will average if the sample observed is large enough, and γ_t is the distortion of the galaxy shape due to gravitational lensing effects commonly called tangential shear. Information on the underlying matter field resides in the correlation between background galaxy for whom the shape has been distorted and foreground objects that will act as lenses, as pictured in fig.4. Since lensing is a projected effect, a common estimator of it is the Excess surface mass density $\Delta\Sigma(rp)$ defined in the right hand side of eq.1 that represent the projected mass crossed by the light as a function of the distance to the source r_p.

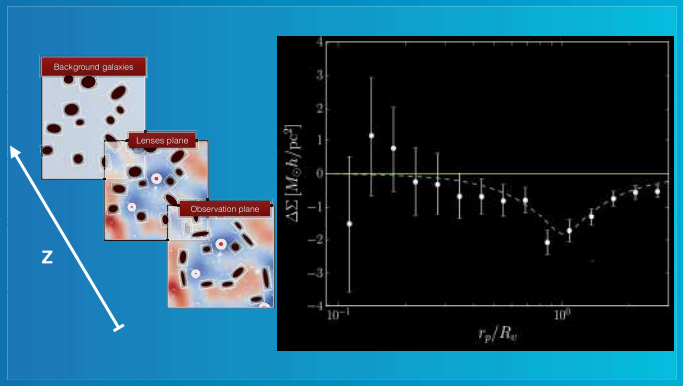

Figure 4: Left: Diagram explaining gravitational lensing caused by voids (red points), to background galaxies (brown ellipses). Right: Void lensing measurement by the Dark Energy Survey first year of observations [3]

4) Objectives

Using the lensing signal from cosmic voids, it's possible to extract cosmological information. Using cosmological simulations in a first time and Euclid first year of observation then the goal of this project is to modelize and optimised the measurement of lensing signal of cosmic voids and provide constraints on cosmological parameters from it.

References

(1) Euclid Collaboration, Y. Mellier et al., *arXiv e-prints*, 2024, arXiv:2405.13491.
(2) C. Sánchez, J. Clampitt et al., 2017, **465**, 746–759.
(3) Y. Fang, N. Hamaus et al., 2019, **490**, 3573–3587.

Understanding the hydroclimatology of the world's largest tropical watersheds: The use of remote sensing and modeling in the Amazon and Congo basins

***Sly Wongchuig[(1)], Fabrice Papa[(1,2)], Pauline Casas[(1)], Adrien Paris[(1,3)], Ayan Fleischmann[(4)], Rodrigo Paiva[(5)]**

(1) Laboratoire d'Etudes en Géophysique et Océanographie Spatiales (LEGOS), Université de Toulouse, CNES/CNRS/IRD/UT3, France; (2) Institute of Geosciences, Campus Universitario Darcy Ribeiro, Universidade de Brasília (UnB); (3) Hydro Matters, France; (4) Instituto de Desenvolvimento Sustentável Mamirauá, Tefé, AM, Brazil; (5) Institute of Hydraulic Research, Federal University of Rio Grande do Sul, Porto Alegre, Brazil

1. Introduction

- The **Amazon (ARB)** and **Congo (CRB)** river basins are the largest in terms of drainage area (~6 and ~3.7 million km^2, respectively) and flow exported to the oceans with an annual average of 206x10^3 and 41x10^3 m^3 s^{-1} (Laraque et al., 2020).
- Home of a large percentage of the **world's tropical forests**, which plays a crucial role in the local, regional, and **global climate**, hydrological and biogeochemical cycles (Nogherotto et al., 2013).
- Guarantees fundamental **ecosystem services** to the population such as food provisioning, biodiversity conservation, climate and freshwater regulation, and mitigation of natural disasters. However, these regions are now facing risk under **climate and anthropogenic changes** (Casagrande et al., 2021).

2. Objectives

1. Study the spatio-temporal variability of flow and water levels over the past 30 years (Hydrological Reanalysis).
2. Analyze the potential effects of future climate on the hydrology (e.g., discharge and water level).
3. To understand the relationships between hydroclimatic variability and local-regional or global atmospheric and oceanic processes.

3. Data and methods

3.1. The MGB model and Data assimilation

- The **hydrological-hydrodynamic MGB model** (Collischonn et al. 2007, Pontes et al., 2017) is a large-scale, distributed, process-based hydrological and hydrodynamic model.
- The sequential DA method, the **multi-observation local ensemble Kalman filter (MoLEnKF)**, is implemented and designed to effectively integrate multiple variables simultaneously (Wongchuig et al., 2024).

3.2. Study area and data

- We use information from **in-situ observations** and **remote sensing**, as well as atmospheric and oceanic **reanalysis data**.

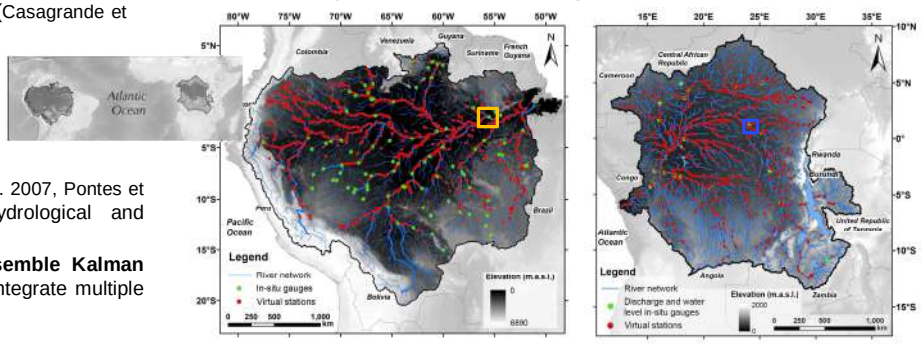

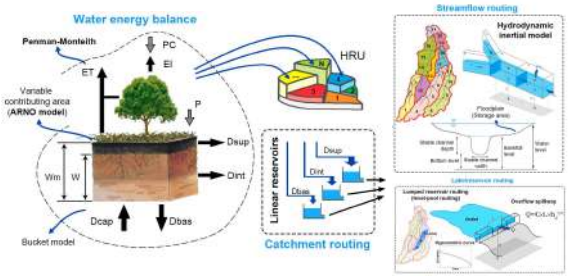

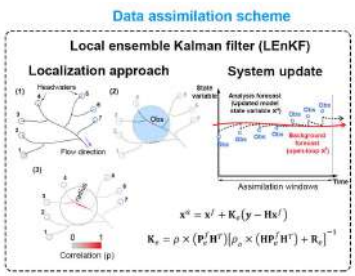

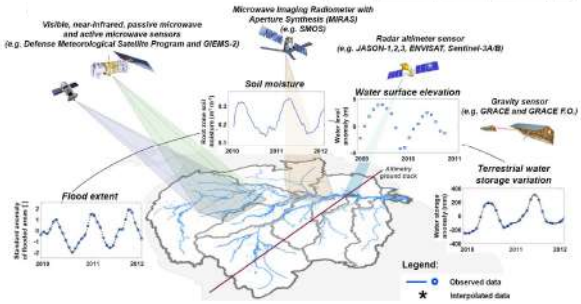

4. Ongoing results and conclusions

Amazon Hydrological Reanalysis (2000-2020)

- **MoLEnKF** was able to improve the timing and amplitude of discharge (Q), water surface elevation (WSE) (not shown) and evapotranspiration (ET) (not shown) in a **weighted manner** among each individually assimilated observation (e.g. Óbidos station).
- **MoLEnKF** provides an **intermediate condition**, being able to holistically outperform univariate experiments. Its robustness ensures **replicability worldwide**, facilitating hydrological reanalysis and improved forecasting.

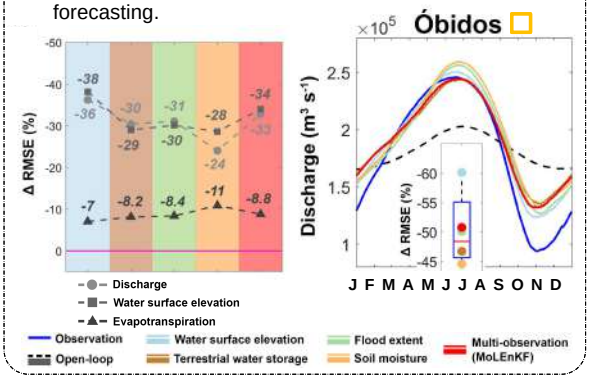

Drying of the central Congo (1981-2022)

Meteorological and hydrological level:

- The central CRB (magenta rectangle) shows a decreasing trend in **P**, with an average of **-90 mm** per decade, and an increasing in **PET** (not shown) of **30 mm** per decade.
- **River discharges** (not shown) and **water levels** are significantly decreasing over the central CRB, around **-240 m^3 s^{-1}** and **-6 cm** (**-20 cm** from radar altimetry).

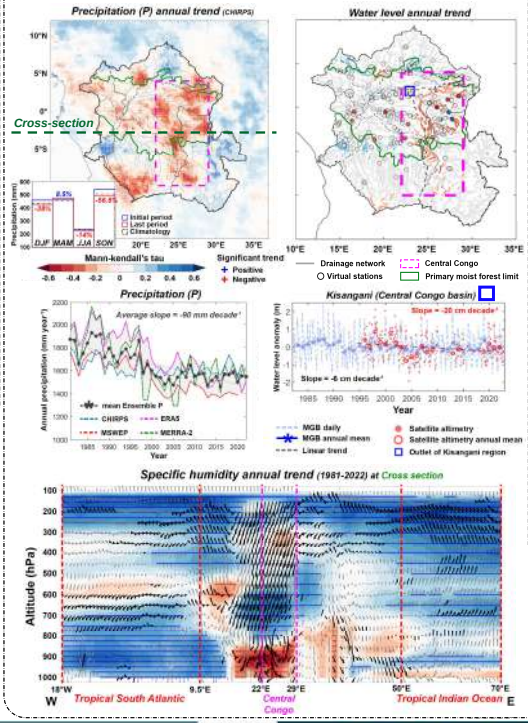

Projections of the Congo's hydrology (2070-2100)

- 14 out of 28 GCMs from **CMIP6** with the **ssp585 scenario** were chosen to force the **MGB model**, called as a multi-model ensemble (MME).
- The inter-period (2070-2100 and 1984-2014) analysis difference revealed mostly a **decrease in discharge** exceeding 25% in Sangha, Ubangui (northern regions) and Middle Congo regions by 2100.
- There is a systematic **increase of drought intensification** by about 30%.
- This pattern of decreasing discharge is mainly explained by the systematic **increase in surface temperature**, from 4°C to 5°C on average.

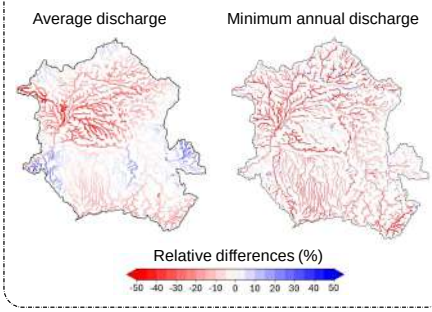

Potential drivers:

- A significant decrease in **specific humidity** at low levels, and a significant increase in **atmospheric subsidence** at different atmospheric levels over the central CRB.

References

- Collischonn, W., et al., 2007. The MGB-IPH model for large-scale rainfall—runoff modelling. Hydrological Sciences Journal, 52(5), 878–895.
- Pontes, P. R. M., et al., 2017. MGB-IPH model for hydrological and hydraulic simulation of large floodplain river systems coupled with open source GIS, Environmental Modelling & Software, 94, 1-20.
- Alain Laraque, et al., Recent Budget of Hydroclimatology and Hy- drosedimentology of the Congo River in Central Africa. Water, 12(9):2613, September 2020. ISSN 2073-4441.
- R. Nogherotto, et al., Impact of Congo Basin deforestation on the African monsoon. Atmospheric Science Letters, 14(1):45–51, January 2013. ISSN 1530-261X, 1530-261X.
- Casagrande, E., et al., 2021. Water balance partitioning for ecosystem service assessment. A case study in the Amazon. Ecological Indicators 121, 107155.
- Wongchuig, S., 2024. Multi-Satellite Data Assimilation for Large-Scale Hydrological-Hydrodynamic Prediction: Proof of Concept in the Amazon Basin. Water Resources Research 60, e2024WR037155.

Contact : *sly.wongchuig-correa@univ-tlse3.fr

Want to know more about these studies? scan this QR

Recueil des posters

Session 8

S08-01 | Doc | **ANS Simon** | LAM, Marseille | Encadrant CNES : Mathieu CASTELNAU | POSTER |
Nanostructured blazed gratings for broadband high efficiency spectrometers by topology optimization

S08-02 | Doc | **BOURCIER Germain** | LAAS-CNRS, Toulouse | Encadrant CNES : François-Xavier ESNAULT | POSTER |
Micro peignes optiques pour la synthèse de fréquence micro-onde et optique

S08-03 | Doc | **BOYER Marion** | CNES-INRIA-AIRBUS, Valbonne | Encadrant CNES : David YOUSSEFI | POSTER |
Modélisation géométrique de scènes urbaines avec le formalisme LOD2 à partir d'images satellite

S08-04 | Doc | **LEFEBVRE Thomas** | LATMOS, Guyancourt | Encadrant CNES : Laura HERMOZO | POSTER |
Mesure des propriétés dynamiques de la convection à l'aide d'un tandem de radiomètres micro- ondes

S08-05 | Doc | **PLIQUE Ronan** | ONERA, Palaiseau | Encadrant CNES : Achraf DYANI | POSTER |
Étude de l'intéraction entre une goutte mobile et une onde acoustique

S08-06 | Doc | **ROUILLÉ Erwan** | LESIA (Obs. Paris), Meudon | Encadrant CNES : Louise YU | POSTER |
Profil de mission pour un observatoire radio interférométrique en orbite lunaire constitué d'un essaim de nanosatellites

S08-07 | Doc | **SARTORI Simone** | CNRS/CPPM, Marseille | Encadrant CNES : Philippe LAUDET | POSTER |
Testing the cosmological model with cosmic voids and CMB lensing in Euclid and DESI surveys

S08-08 | Doc | **WARGNIER Antonin** | LESIA (Obs. Paris), Meudon | Encadrant CNES : Francis ROCARD | POSTER |
Caractérisation de la surface de Phobos en préparation de la mission Martian Moon eXploration

Nanostructured blazed gratings for high-performance spectrographs

Simon Ans[a,b], Guillaume Demésy[b], Frédéric Zamkotsian[a], Andrei Mursa[c], Roland Salut[c], and Nicolas Passilly[c]

[a]Aix Marseille Univ, CNRS, CNES, LAM, Marseille, France
[b]Aix Marseille Univ, CNRS, Centrale Med, Institut Fresnel, Marseille, France
[c]FEMTO-ST, CNRS, UFC, Besançon, France

Abstract : We study the light disperser of a spectrograph, which is traditionally a blazed grating with a sawtooth profile. On the one hand, preliminary manufacturing results are presented. On the other hand, in order to find the optimal opto-geometric characteristics of this keystone device, topology optimization based on the Finite Element modelling of the Maxwell's equations is used.

Context of the project

Physical problem

The classical sawtooth blazed grating in reflection is a periodic pattern that mostly reflects the incident light on a particular diffraction order (for our case the order **–**1). It is widely used in spectroscopy and the goal of the new generation of spectrographs is to be more efficient though more compact.

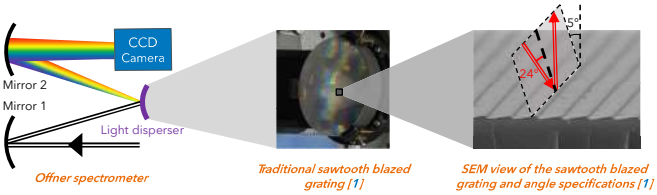

Offner spectrometer — *Traditional sawtooth blazed grating [1]* — *SEM view of the sawtooth blazed grating and angle specifications [1]*

Manufacturing metasurfaces

Optimizing the e-beam lithography

Starting from a 3D metasurface pattern developed by considering the phase shift induced by the sawtooth grating (Ans et al. OWTNM 2023), the strengths and constraints of the manufacturing of nanostructures are defined.
First samples of blazed gratings have been manufactured on an Nb_2O_5 layer of 150nm using **e-beam lithography** (RAITH Voyager lithography system) with **locally adjusted** electronic doses.

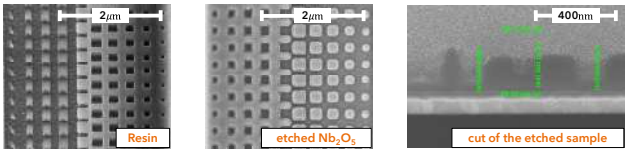

Theoretical model

Finite Element Method and topology optimization

At the nanometer scale, the grating can be seen as a **periodic** collection of diffracting objects with a pattern defined in the **design region**. The framework here is the **conical case**: the consideration of a 2D geometry where the incident plane wave parameters are let totally free [2]. Moreover the permittivity distribution within the design region is free as well.

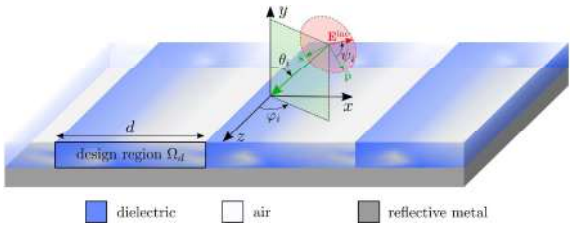

The grating considered for the mathematical model

The problem is solved numerically using the **Finite Element Method**. The triangular discretization meshing and the numerical resolution are resp. supported by the open-source softwares Gmsh [3] and GetDP [4]. It enables to access the **diffraction efficiencies** R_n.

In **topology optimization**, on each triangle the dielectric permittivity depends on a design vector $\boldsymbol{\rho}$ constant per triangle of the finite element mesh through the SIMP method :

$$\varepsilon_r^d(\boldsymbol{\rho}) = (\varepsilon_{r,\max} - \varepsilon_{r,\min})\boldsymbol{\rho} + \varepsilon_{r,\min}.$$

The optimization problem is then, for a fixed diffraction order n :

$$\begin{cases} \max\limits_{\boldsymbol{\rho}} & R_n(\boldsymbol{\rho}) \\ \text{s. t.} & \text{Maxwell's equations} \end{cases}$$

It is solved using GCMMA [5] and the **Jacobian** of R_n is computed using the **adjoint method** [6].

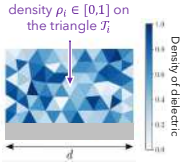

Mesh-based density distribution using SIMP

In order to obtain a readable and realistic shape after the topology optimization, both filters presented below are necessary. Their (analytic) derivative is also implemented in the calculation of the Jacobian.

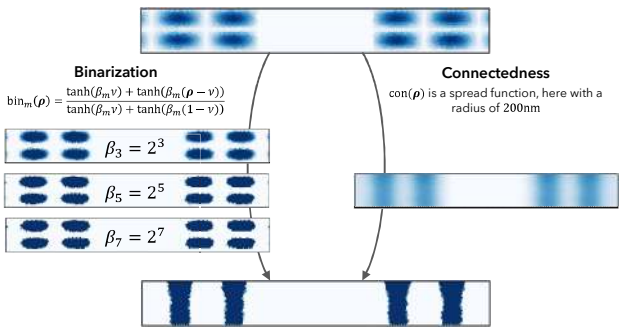

Illustration of the binarization and connectedness filters on a simple pattern

Numerical results

Optimizing blazed gratings

The optimization problem is first solved **on a single wavelength** in order to reach a diffraction efficiency close to 100%.

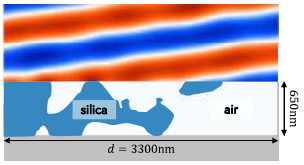

$\lambda = 700\text{nm}, \theta_i = 24{,}5°, \varphi_i = -11°, \psi_i = 90°$

Mono-wavelength optimization on a silica dielectric layer and projection of the scattered field at the targeted wavelength and angles

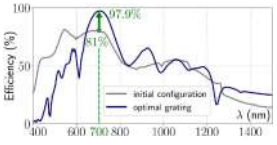

Spectral response in the -1st diffraction order as compared to the initial configuration

The **brodband optimization** outperforms the sawtooth grating on a wide range of wavelengths, so that the efficiency averaged on the interval [400,1500]nm reaches 80% instead of 52% with the traditional grating.

$\lambda \in [400,1500]\text{nm}, \theta_i = 24{,}5°, \varphi_i = -11°, \psi_i = 90°$

Broadband optimization

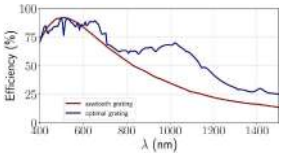

Spectral response in the -1st diffraction order as compared to the initial configuration and the sawtooth grating

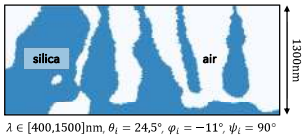

$\lambda \in [400,1500]\text{nm}, \theta_i = 24{,}5°, \varphi_i = -11°, \psi_i = 90°$

Broadband optimization for a twice higher design

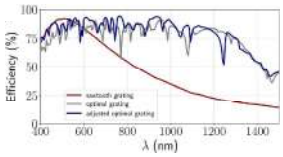

Spectral response in the -1st diffraction order

Conclusion

A totally **open-source topology optimization code** has been implemented with mathematical calculations of the tools for the gradient descent. It enables to generate designs of **blazed nanostructured gratings** made of a dielectric layer. The results show an improvement of the diffraction in the **infrared region**, which has now to be confronted to the manufacturability contraints.

Aknowledgements

The authors would like to thank CNES and Thales Alenia Space that partially fund this project with a PhD grant. Furthermore this work was supported by the French RENATECH network and its FEMTO-ST technological facility (MIMENTO). This part of the project has been partially funded by the CNRS PEPS-INSIS program through the project RESO-BATMAN.

References

[1] Zamkotsian et al. *SPIE Instru. Astro. VII.* 107025P (2018)
[2] Demésy et al. *Presses Univ. Prov.* (2014)
[3] Geuzaine et al. *Int. J. Num. Meth. Eng.* **79**, 11 (2009)
[4] Dular, Geuzaine et al. *IEEE Trans. on Magn.* **34**, 5 (1998)
[5] Svanberg. *Soc. Indus. Appl. Math.* **12**, 2 (2002)
[6] Ans et al. *JOSA A.* **41**, 8 (2024)

Micro peignes optiques pour la synthèse de fréquence micro-onde et optique

Germain BOURCIER[1,2], Stéphane BALAC[3], Julien LUMEAU[4], Antonin MOREAU[4], Olivier LLOPIS[1], Arnaud FERNANDEZ[1]

[1]LAAS-CNRS, Université de Toulouse, CNRS, UPS, Toulouse, France
[2]CNES, 18 Avenue Edouard Belin, F-31401, Toulouse, France
[3]IRMAR, Université de Rennes, CNRS, Campus de Beaulieu, 35042 Rennes, France
[4]Université Aix Marseille, CNRS, Centrale Med, Institut Fresnel, Marseille, France

Résumé

Nous explorons le résonateur Fabry-Pérot fibré (FFP), une nouvelle plateforme pour la génération de peignes de fréquences. Cette thèse permet d'étudier théoriquement et expérimentalement la génération des peignes. Les instabilités de modulation sont la première manifestation des effets non-linéaires. Une étude analytique relative à leur apparition est présentée ici et est comparée à l'expérience afin de comprendre leur déclenchement, d'améliorer les paramètres de fabrication, et ainsi de réduire la puissance nécessaire à leur génération. Pour aller plus loin, nous considérerons les pertes liées au miroir déposé. Enfin, il est possible de réaliser différent setups pour obtenir des solitons de cavité, la stabilisation par rétro-injection est présentée, celle-ci permet d'obtenir des peignes à très faible bruit de phase.

Résonateur Fabry-Pérot fibré

Le résonateur Fabry-Pérot fibré (FFP) est délimité par des miroirs diélectriques multi-couches de quelques µm d'épaisseur.

- Facilité de conception et de manipulation
- Couplage durable et reproductible
- **Q** > 10^8

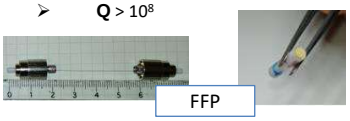

La biréfringence de la fibre crée une double cavité par la présence de deux polarisations linéaires P1 et P2 d'ISL propre.

La fibre optique est non-linéaire d'ordre 3 il est donc possible de générer du mélange à quatre ondes.

Le peigne de fréquence optique

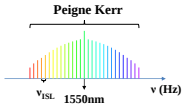

Ensemble de raies fines et équi-espacées obtenu grâce à la génération d'un étalement spectral à l'intérieur d'un résonateur optique.

Étalement spectral par mélange à quatre onde

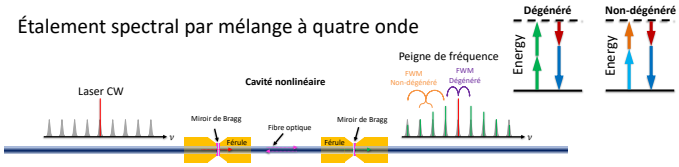

Théorie et simulation

Etude de la dynamique de formation du peigne (simulation)

Equation temporelle de Lugiato-Lefever :

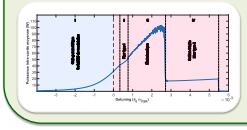

$$t_R\frac{\partial\psi}{\partial\tau} = -(1-a\rho^2)\psi - i\delta\psi + \kappa E_{in} + 2L\left[-i\frac{\beta_2}{2}\frac{\partial^2}{\partial t^2} + i\gamma|\psi|^2 + i\gamma\frac{2}{t_R}\int_{-t_R/2}^{t_R/2}|\psi|^2 dt\right]\psi$$

Pertes — Pump — Detuning — Dispersion — Non-linearité avec co-propagation et contra-propagation — Terme spécifique au FFP

Seuil d'apparition des effets non-linéaires ⇨ Instabilité de modulation

Seuil de puissance **input** : $P_{IN,th}$

$$P_{IN,th} = \frac{(1-a\rho^2)^3}{2L\gamma(1-\rho^2)}[1+(3-\Delta)^2]$$

$$R_{MI} = \frac{3a-1}{2a}$$ ⇨ Optimisation de la réflectivité ➔ 15,6% de P_{IN} en moins

Simulation des pertes par diffraction dans le miroir

- → Approximation du mode fondamental Gaussien
- → model d'optique de Fourier (fréquences spatiales)
- → Calcule des coefficients de Fresnel pour N couches minces (méthode récursive de Rouard)

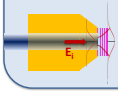

$$\eta = \iint \left(\frac{E_i}{\sqrt{P_i}}\right)^* \left(\frac{E_r}{\sqrt{P_r}}\right) dxdy$$

Intégrales de recouvrement

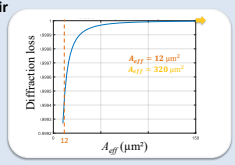

Théorie self-injection locking

Développement d'un modèle théorique : $\xi = \zeta + \frac{\alpha K}{\tau_{LC}}|T(\zeta)|\sin\psi$

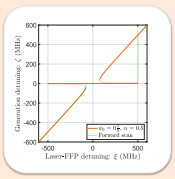

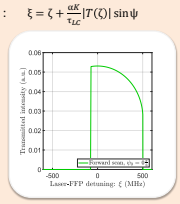

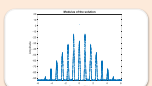
Peigne primaire


Soliton de cavité

Résultats expérimentaux

Etude de la dynamique de formation du peigne (expérimentation)

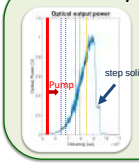

- Signal injecté :
  - P=1W
- Cavité FP:
  - $\beta_2 = -5ps^2km^{-1}$
  - $\gamma = 1{,}4W^{-1}km^{-1}$
  - $Q = 1{,}2.10^8$
- Seuil puissance intracavité :
  - P=11W

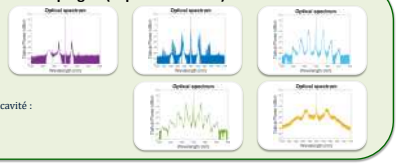

Instabilité de modulation

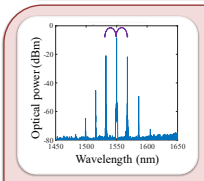

Peigne primaire

- Lobes symétriques
- Lignes supplémentaires par mélange à quatre ondes
- Espacement > 1THz ≈1000 ISL (cordon 10 cm)

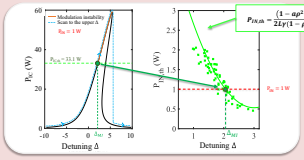

$$P_{IN,th} = \frac{(1-a\rho^2)^3}{2L\gamma(1-\rho^2)}[1+(3-\Delta)^2]$$

Validation de la théorie

Mesure des pertes par diffraction

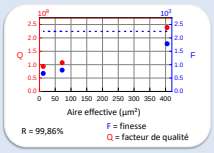

R = 99,86%
F = finesse
Q = facteur de qualité

Avec une fibre multimode = quasi sans pertes :

Q = 5.10⁹ (R = 99,96%)

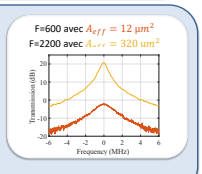

Setup self-injection locking

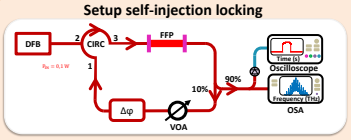

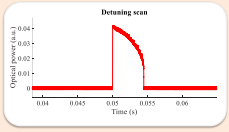


Peigne primaire


Soliton de cavité

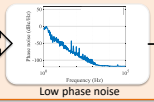
Low phase noise

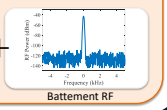
Battement RF

Conclusion

Ces travaux sur le FFP ont permis de mieux comprendre les verrous technologiques associés à sa fabrication et à son utilisation. Nous savons maintenant améliorer le seuil de déclenchement des peignes en choisissant la réflectivité optimale et en réduisant les pertes au miroir. Les outils nécessaire à la compréhension de la dynamique non-linéaire ont été développés. Différents setups ont été mis en places dont la stabilisation par rétro-injection. Cette méthode permet de générer des solitons de cavité avec des puissances de pompe inférieures à 150 mW ce qui est exceptionnel dans ce type de résonateur. De plus, la dynamique complexe de ce type de setup a été étudiée à l'aide d'un modèle théorique.

RÉPUBLIQUE FRANÇAISE
Liberté Égalité Fraternité

Modélisation géométrique de scènes urbaines avec le formalisme LOD2 à partir d'images satellite

Contexte

- Demande croissante de modèles numériques urbains
- Traditionnellement, modèles 3D via données aéroportées (Lidar, images multi-vues)
- Potentiel accru des images satellites : couverture mondiale, coût moindre, fréquence élevée
- Satellites Pléiades Neo : résolution proche des images aéroportées

Paramètres du problème

Objectif : Reconstruction 3D de zones urbaines en LOD2

Données d'entrée :

Images satellite

Résolution : 30 cm
1 bande panchromatique
6 bandes multispectrales

Informations sémantiques

Bâtiments
Végétation

Informations 3D

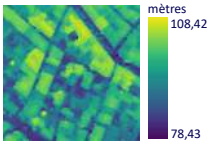

Modèle Numérique de Surface (MNS) avec cars [1]

cars [1] Chaîne de reconstruction 3D du CNES

Pipeline

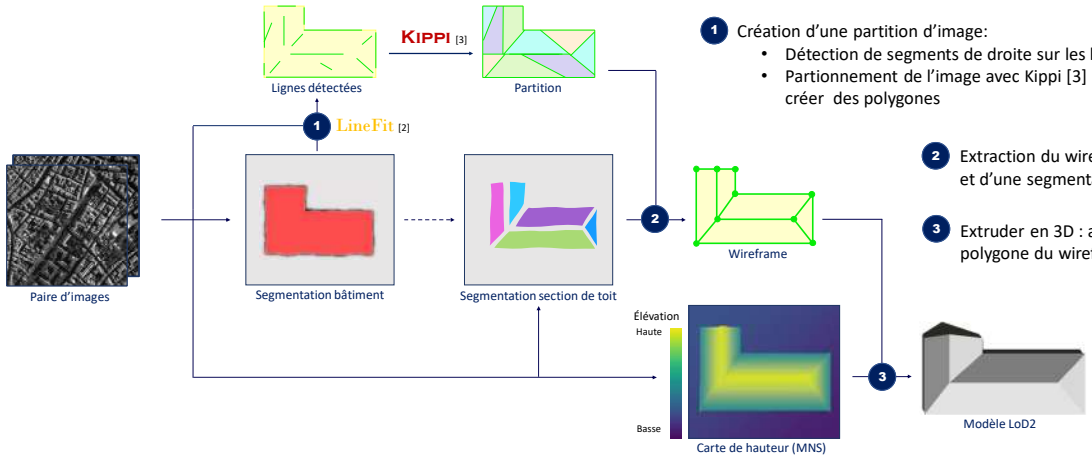

1. Création d'une partition d'image:
   - Détection de segments de droite sur les bâtiments avec LineFit [2]
   - Partitionnement de l'image avec Kippi [3] : prolongation des segments pour créer des polygones
2. Extraction du wireframe : agrégation de la partition et d'une segmentation de section de toits
3. Extruder en 3D : attribution d'un plan 3D à chaque polygone du wireframe grâce à la carte de hauteur

LineFit

Détection de segments de droites dans les images, sur les structures linéaires mais aussi sur les formes courbées.

- Utilise une carte de gradient d'image pour garder les points d'intérêt

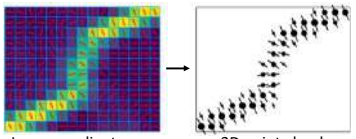

- Approximation des points par des lignes, avec une tolérance ε

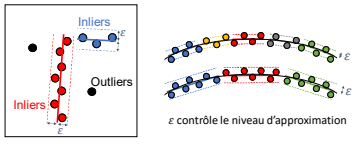

- Recherche d'une bonne configuration de ligne : qualité de la configuration $\mathbf{x} = (\mathbf{s}, \mathbf{l})$ mesurée avec l'énergie U :

$$U(\mathbf{x}) = \lambda_f U_f(\mathbf{x}) + \lambda_c U_c(\mathbf{x}) + \lambda_r U_r(\mathbf{x})$$

Fidélité
Favorise des courtes distances entre les inliers et leur lignes

Complétude
Favorise un grand nombre d'inliers

Régularité
Favorise des segments peu nombreux, et régularisés

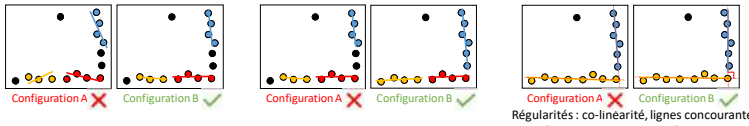

Régularités : co-linéarité, lignes concourantes, parallélisme and orthogonalité.

- Optimisation : depuis une configuration initiale, l'opérateur géométrique qui réduit le plus l'énergie est appliqué itérativement :
  - Opérateur global : toute la configuration peut être modifiée
  - Opérateur local : change une ou deux lignes

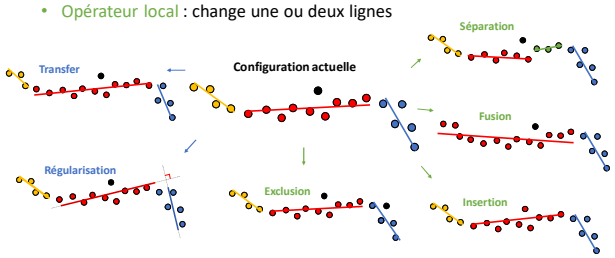

- Résultats

Images satellites — Images formes libres

Construction du wireframe

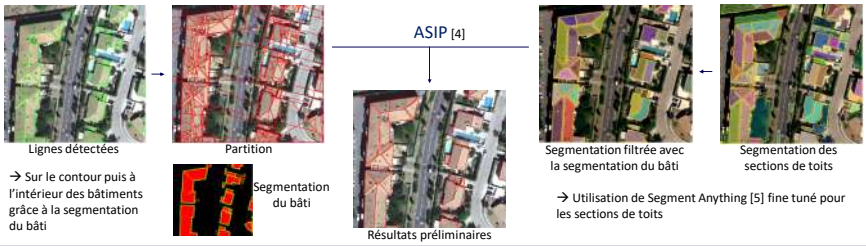

→ Sur le contour puis à l'intérieur des bâtiments grâce à la segmentation du bâti

→ Utilisation de Segment Anything [5] fine tuné pour les sections de toits

Références

[1] Youssefi, D., Michel, J., Sarrazin, E., Buffe, F., Cournet, M., Delvit, J. M., ... & Bosman, J. : Cars: A photogrammetry pipeline using dask graphs to construct a global 3d model. In IGARSS (2020)

[2] Bauchet, J. P., & Lafarge, F.: Kippi: Kinetic polygonal partitioning of images. In CVPR (2018).

[3] Bauchet, J. P., & Lafarge, F. (2018). Kippi: Kinetic polygonal partitioning of images. In CVPR (2018).

[4]] Li, M., Lafarge, F., Marlet, R.: Approximating shapes in images with low-complexity polygons. In: CVPR (2020).

[5] Kirillov, A., Mintun, E., Ravi, N., Mao, H., Rolland, C., Gustafson, L., Xiao, T., Whitehead, S., Berg, A.C., Lo, W.Y., Dollár, P., Girshick, R.: Segment anything. In: ICCV (2023)

RÉPUBLIQUE FRANÇAISE
Liberté Égalité Fraternité

Measuring dynamical properties of atmospheric convection using C²OMODO a tandem of microwave radiometers

Thomas Lefebvre[1,2,4*], Hélène Brogniez[1,3], Laura Hermozo[2] and Frédéric Chevallier[3]
1 : LATMOS/IPSL/UVSQ - 2 : CNES - 3 : LSCE/IPSL - 4: Airbus Defense and Space
Contact*: thomas.lefebvre@latmos.ipsl.fr

1 Scientific context: Deep Convection

- **Extreme cloud systems, occurs** in Intertropical zone
- air, aerosols & water updrafts up to the tropopause
- Strong impacts on : Water & Energy Cycles
- Issues around deep convection **:**
  - Lack of observations of convective updrafts
  - High spatial and temporal sampling
  - In-situ measurement difficulties over oceans.
  - Limited representation in **meteo/climate models**

2 Space mission : C²OMODO

C²OMODO (**C**onvective **C**ore **O**bservations through **M**icr**O**wave **D**erivatives in the tr**O**pics) :

- Contribution to Atmosphere Observing System (AOS) program (NASA-led with CSA, JAXA, CNES)
- Observation of **clouds and storms dynamics**
- Twin multispectral **passive microwave radiometers**
- Measurement expressed in brightness temperature (Tbs)
- Tbs related to **ice scattering attenuation**
- $\frac{dTbs}{dt}$ related to growth of convection **[1][2]**

General Description	Frequency [GHz]	IFOV [km]
Orbits Inclined ± 55° latitudes	183.31	5
Launch : [2028 – 2030]	325.15	3
Mean altitude : 427 km		
Swath : > 750 km	89	10

Table.1 : Description of C²OMODO and instrumental configuration used. IFOV at nadir.

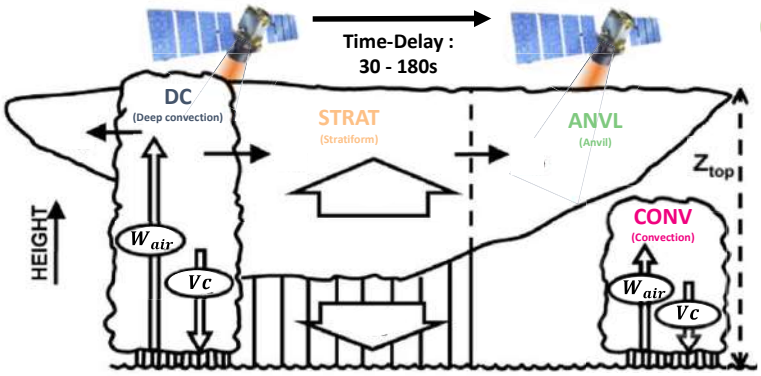

Fig.1: C²OMODO principle. Cumulonimbus (liquid and frozen water) observed with twin radiometers
W_{air} : In-cloud vertical wind velocity ; Vc : Terminal velocities ; In red : Cloud classes

3 Numerical tools

MESO-NH [5] (Cloud Resolving Model) :

- Laboratoire d'Aérologie et Météo-France
- Non-hydrostatic (Resolved convection)
- Hector simulation [6]:
  - 6h ; 256*200 km² ; up to 30km
  - Δx = 1km ; Δz = 200m ; Δt = 30s

RTTOV.13 [7] (Radiative Transfer Model) :

- Simulation of satellite measurements
- No spatial observation geometry yet
- Default particle size/shape distribution [8]
  - ➢ To be explored in another study

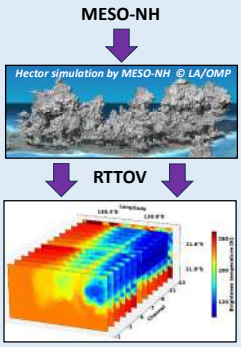

Fig.3 : Tbs samples across channels

4 Machine learning method

Method : GBDT - LightGBM [9] (Article in preparation) :

- Convective cell structure (Based on [4]) :
  - Single-radiometer : Cloud structure (Fig.4)
  - Tandem-based : Ice variation phases
- High performance retrieval of IWP and $\frac{dIWP}{dt}$

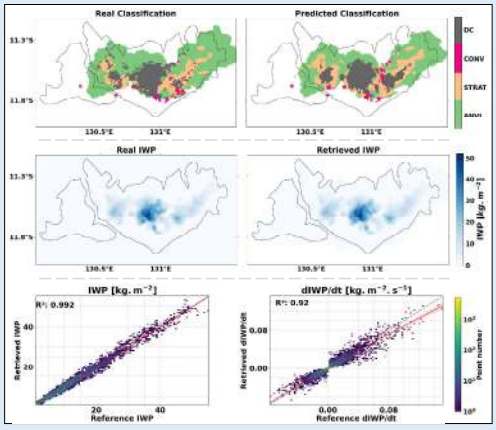

Fig.4: Results of the Machine learning methods.
Top line: map of the real and predicted classes.
Middle line: map of the real and retrieved IWP (Ice Water Path [$kg.m^{-2}$]: total atmospheric ice content).
Bottom line : Diagram of dispersion of IWP (left) and dIWP/dt (right).

5 Variational approach method (1D-VAR)

Method :

- Iterative principle - Based on Bayesian theory [5]
- Retrieval of ice water content
- Retrieval of vertical wind velocities profile, $W(z)$
  - Gaussian model based (Fig.5)
  - Advection scheme similar to MESO-NH (Fig.6)

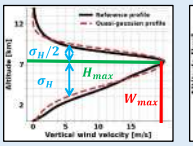

Fig.5: Wind vertical velocity profile based on gaussian model

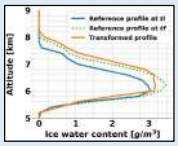

Fig.6: Advection scheme compute vertical motion between initial and final time measurement

First results :

- Fig.7: Spatial coherence of dynamical properties
- Fig.8**:** Consistent ice content and vertical velocity profile
- Fig.9: W_{max} and H_{max} well estimated

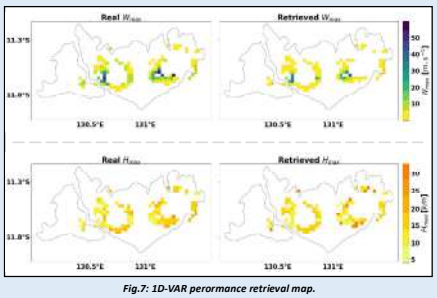

Fig.7: 1D-VAR perormance retrieval map.
Top line : map of the real and retrieved Wmax. Bottom line : map of the real end retrieved Hmax.

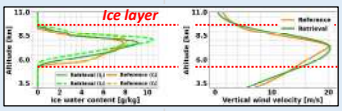

Fig.8: Real and retrieved ice profile and vertical wind velocities

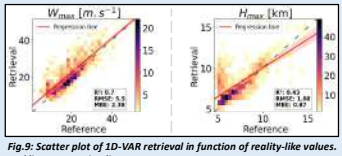

Fig.9: Scatter plot of 1D-VAR retrieval in function of reality-like values.
Red line : regression line.

- [1] : Brogniez et al, (2022), Front Remote Sens.
- [2] : Auguste F and Chaboureau J-P (2022), *Front. Remote Sens.*
- [3] : *Houze, R. A, Jr (2014), Cloud Dynamics.*
- [4] : *Marinescu et al (2016), J. Geophys. Res. Atmos.*
- [5] : *Lac et al (2018), Geosci. Model Dev.*
- [6] : Dauhut T and Chaboureau J-P (2015), Atmos. Sci. Let.
- [7] : *Saunders, R., et al (2018), Geosci. Model Dev.*
- [8] : *Geer et al (2021), Geosci. Model Dev.*
- [9] : Ke, G., et al (2017), *Neural Information Processing Systems.*
- [10] : Rodgers (2000), *World Scientific Publishing.*

5 Conclusions and perspectives

Among other possible products, **C²OMODO enable the retrieval of:**

- Using **Machine Learning** : Cells structure and Integrated geophysical variables
- Using 1D-VAR : Profile of : **Ice Water Content** & **Vertical wind velocities**

PHD perspectives : Investigation of 1D-VAR biases, Application on other cloud structure, Sensitivity analysis to tandem parameters (Tandem simulator), Publication on the 1D-VAR.

C²OMODO

AIRBUS DEFENCE & SPACE

Étude de l'interaction entre une goutte mobile et une onde acoustique

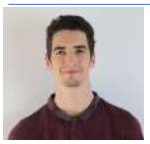

PLIQUE Ronan
Directeur de thèse : LABAUNE Julien (Onera DMPE)
Co-directeur de thèse : DUPAYS Joël (Onera DMPE)
Encadrant Onera : GRENARD Philippe (Onera DMPE)
Encadrant Cnes : DYANI Achraf

Contexte

Interaction brouillard de gouttes – onde acoustique

Moteur-fusée liquide
Tête d'injection dans la chambre de combustion

Visualisation d'un brouillard de gouttes de combustible par imagerie de fluorescence (PLIF). Onera

Moteur-fusée solide
Gouttes d'aluminium en fusion dans la chambre

Chambre de combustion détruite par les instabilités thermo-acoustiques [1]

Déluge d'eau lors des lancements

Déluge d'eau lors du décollage d'Artémis I, NASA

Simulation de l'interaction entre un brouillard de gouttes et une onde acoustique

Les modèles d'échanges de quantité de mouvement, d'énergie et de masse utilisés sont (quasi-)stationnaires et valides dans le cas d'un champ acoustique de faible amplitude. Cependant, au décollage d'un lanceur, le niveau d'intensité sonore atteint 180 dB (0,2 bar), ce qui ne rentre pas dans la plage de validité des modèles.

Le brouillard est considéré comme étant composé de gouttes indépendantes les unes des autres, il faut donc revenir à l'interaction au niveau d'une seule goutte avant d'élargir les termes d'échanges trouvés au brouillard entier. Grâce à une méthode d'intersection de maillage mobile développée à l'Onera, les maillages chevauchants conservatifs (MCC), il sera possible de simuler directement, dans un référentiel galiléen, l'interaction entre la goutte et le milieu environnant et de capturer les effets instationnaires de la goutte sur l'écoulement.

Objectif et méthode de travail

Caractériser l'interaction entre une goutte mobile et une onde acoustique en termes d'échanges de quantité de mouvement

Démarche globale incrémentale de complexité croissante :

- Validation de la méthode en écoulement stationnaire en régime de Stokes ainsi qu'en régime laminaire
- Utilisation de la méthode numérique en écoulement instationnaire à bas Reynolds :
  - Détermination de nombres caractéristiques garantissant la validité des résultats numériques
  - Mise en place d'un environnement de simulation
- Extension des simulations à haut Reynolds et adaptation des modèles analytiques

Résultats instationnaires

Bas Reynolds

Formule analytique :

$$F(t)=6\pi\mu R V(t)+\frac{2}{3}\pi R^3\rho\frac{dV(t)}{dt}+\frac{6\pi R^2\mu}{\delta\omega}\left(\frac{dU(t)}{dt}+\omega U(t)\right)$$

avec $\delta=\sqrt{\frac{2\mu}{\rho\omega}}$ profondeur de déplacement

adimensionnement

$$F'(t)=\sin(\omega t)+\frac{2}{9}R'^2\cos(\omega t)+R'(\sin(\omega t)+\cos(\omega t))$$

$$F'(t)=A(R')\sin(\omega t+\Phi(R'))$$

avec $R'=\frac{R}{\delta}$ le rayon adimensionné

Évolution de l'amplitude (A) et de la phase (Φ) en fonction du rayon adimensionné

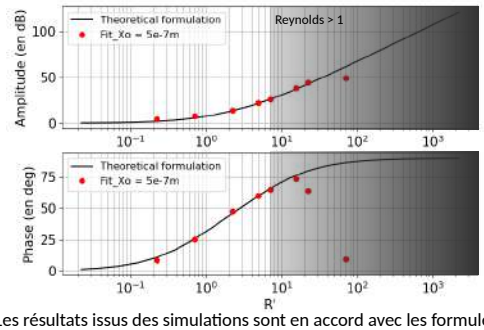

Les résultats issus des simulations sont en accord avec les formules analytiques dans le cadre de leur plage de validité. Cependant, lorsque le nombre de Reynolds ne permet plus au termes convectif d'être négligé il est nécessaire de revenir à l'étape du développement analytique afin de les prendre en compte.

Haut Reynolds

Formule analytique modifiée:

$$F(t)=C_D\frac{1}{2}\pi\rho R^2|V(t)|V(t)+C_m\frac{4}{3}\pi R^3\rho\frac{dV(t)}{dt}+\frac{C_h\pi R^2\mu}{\delta\omega}\left(\frac{dU(t)}{dt}+\omega U(t)\right)$$

Odar et Hamilton [2]

$$C_m=1{,}05-\frac{0{,}066}{Ac^2+0{,}12}$$

$$C_h=2{,}88+\frac{3{,}12}{(1+Ac)^3}$$

$Ac=\frac{U^2}{\frac{dU}{dt}D}$ Nombre d'accélération

Michaelides [3]

$$C_m=0.5$$

$$C_h=6-3{,}16\left(1-e^{\left(-0.14\,Re\,Sl^{0.82}\right)^{2.5}}\right)$$

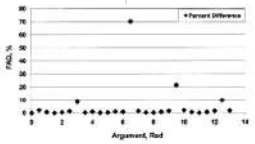

Pourcentage de différence entre les forces totales

$Sl=\frac{9\mu}{8\omega\rho R_p^2}$ Nombre de Strouhal

Évolution des coefficients en fonction du Reynolds

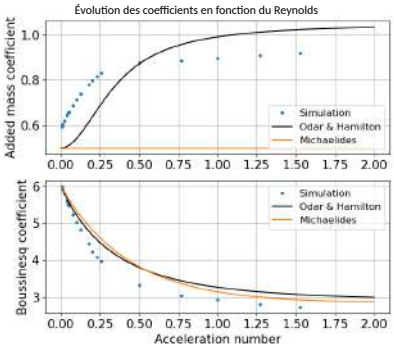

En réalisant une exploitation similaire à celle d'Odar et Hamilton il apparaît que les modèles du coefficient de Boussinesq sont cohérent avec les résultats issus des simulations. Cependant, le coefficient de masse ajoutée ne correspond pas. Il est donc possible d'y apporter des modifications.

Bibliographie

[1] S. Mariappan, *Thermoacoustics instability in a solid rocket motor : non-normally and nonlinear instabilities*, Journal of fluid mechanics, volume 653, pp 1-33, 2010
[2]F. ODAR and W. S. HAMILTON . Forces on a sphere accelerating in a viscous fluid. journal of fluid mecanics, pages 302–314, 1964.
[3] E. E. MICHAELIDES . Particles, bubbles and drops, their motion, heat and mass tranfer. World Scientific, 2006.

An Instrumental concept to monitor the sky at very low radio frequency

Erwan Rouillé[1], Baptiste Cecconi[1], Boris Segret [2]

[1] LESIA, Observatoire de Paris – PSL, [2] Census, Observatoire de Paris
Contact : erwan.rouille@obspm.fr

NOIRE project

(Nanosatellite pour un Observatoire Interférométrique Radio dans l'Espace)

NOIRE is an instrumental concept study that consists in an interferometer in space at observing at very low frequency (30kHz – 100MHz) [1]

Autonomous Scientific Observatory

~ 50 nanosat in lunar orbit in a formation of 100 km

Simulation purpose

Various specification requirements are yet to be defined.

The scientific objectives are driving their definition.

The instrumental simulation is implemented to test a given set of specification in regards to a science case.

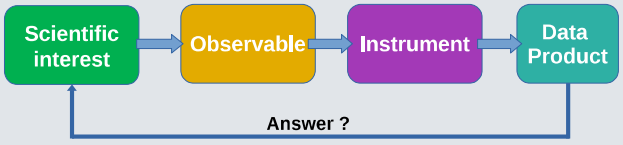

The Simulation Pipeline

- Hardware specifications
  - Clock accuracy
  - Antenna Gain
- Software specifications
  - Position accuracy
- Data Volume
- Relays
- more

- Δυ, τ
- # Satellites
- Orbits
- Strategy

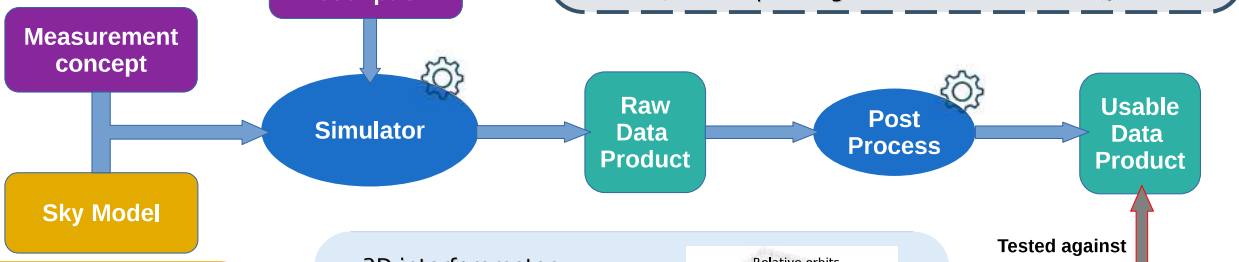

- Model of the source of interest
- Background :
  - GSM
  - USLA [2]
  - (model with absorption)

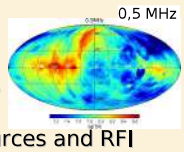

- Model of foreground sources and RFI

- 3D interferometer
- Significant relative velocities
- Full sky imaging
- SWHT [3] to simulate background visibilities
- Multiple aquisition modes

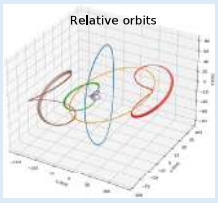

Tested against

Scientific interest

Unique Constraints

- **Topology**
  - Baselines have to be measured onboard
  - Low control → UVW coverage
  - Relative velocities → limit integration time
- **Data limitation**
  - Strong restriction on the volume produced → Telecom, Onboard computation, Power
- **Clock accuracy**
  - Regular Synchronizations, SNR degradation
- **Antenna Diagram**
  - Gain, short dipole regime

Scientific Objectives

Map the sky at extremely low frequency

The sky remains mostly unknown in this frequency range

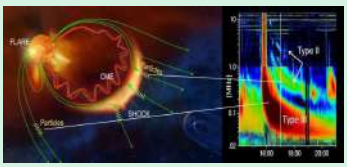

Track the propagation of Solar burst (type II and III)

As a tracer of the particle acceleration in the inner heliosphere and potential magnetic connections from the lower solar corona to the larger heliosphere.

Study planetary magnetospheres
- radiation belts
- atmospheric electricity

Opportunity to observe Uranus and Neptune (<10MHz) since Voyager

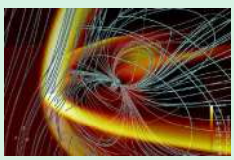

Test Different Observation strategy

Test Mission Profile vs detectability level

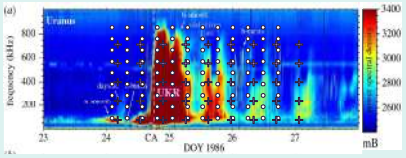

○ Observation strategy 1

✚ Observation strategy 2

Références :

[1] Cecconi *et al.* (2018), NOIRE Study : Towards a low frequency radio interferometer in space, IEEE Aerospace Conference
[2] Cong *et al.* (2021), An Ultra-long Wavelength Sky Model with Absorption Effect, *The astrophysical journal*
[3] Carozzi T. D. (2015), Imaging on a Sphere with Interferometers : the Spherical Wave Harmonic Transform, *Monthly Notices of the Royal Astronomical Society: Letters*
[4] Novaco & Brown (1978), Nonthermal galactic emission below 10MHz, *Astrophysical Journal*
[5] Lamy *et al.* (2020), Auroral emission from Uranus and Neptune. *Phil. Trans.*

Image Credit :

- Duisterwinkel et al (2018)
- dias.ie/cosmicphysics/astrophysics/astro-surround/
- Jarmak et al (2020)
- NASA/JPL-Caltech/SwRI/JunoCam

Testing the cosmological model with cosmic voids and CMB lensing in Euclid and DESI surveys

Simone Sartori [1], Stephanie Escoffier [1], Pauline Vielzeuf [1], William Gillard [1]

[1] Aix Marseille Université, CNRS/IN2P3, CPPM, Marseille, France

COSMIC VOIDS

Vaste underdense regions that dominate the Late Universe in terms of Volume.

Cosmic voids evolve through time becoming more spherical and underdense but remaining in *mildly non-linear* regime, feature that make them easier to model than their overdense counterparts.

Cosmological informations from: number counts, density profiles, shapes, geometrical and dynamical distortions, **lensing**, velocity profiles...

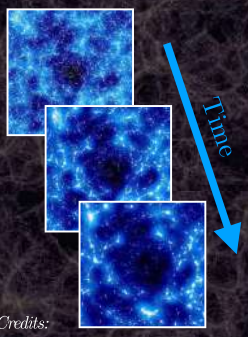

Credits: van de Waygaert & Platen (2011)

Complemental with standard cosmological probes!

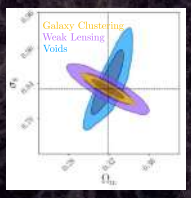

Credits: Contarini et al. (2022)

GRAVITATIONAL LENSING OF THE COSMIC MICROWAVE BACKGROUND (CMB)

Effect due to the presence of density fluctuation in the line of sight: gravitational fields change in space.

$$\phi \rightarrow \phi(x)$$

The observed CMB is modified and anisotropies are introduced.

Overdensities: $\phi(x)$ acts like a convergent lens. **Positive magnification**

Underdensities: $\phi(x)$ acts like a divergent lens. **Negative magnification**

Three main observables:

- **Convergence** κ *(magnification)*
- **Shear** γ *(distortion)*
- **Rotation** φ

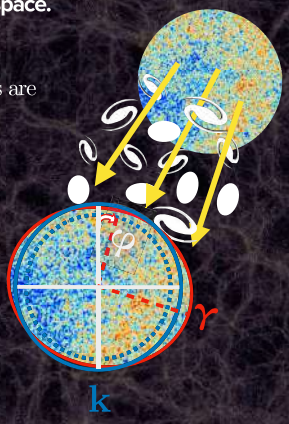

COSMIC VOIDS x CMB LESING

The cross-correlation between cosmic voids and CMB convergence maps is a powerful tool to test the cosmological model

Cosmic voids are identified in the galaxy field through specific void finding algorithms (*left panel*). Then, the CMB convergence patches behind every voids are stacked together in order to let the lensing signal arise from the instrumental noise. The radial profile of the stacked CMB patch (*central panel*) provides us our cross-correlation signal. The cosmological information is provided by the ratio between the observed cross-correlation and the simulated ΛCDM signal, in form of the *best-fitting CMB lensing amplitude parameter* $A_\kappa = \kappa_{\rm Obs}/\kappa_{\rm Sim}$ *(right panel, credits: Kovacs et al., 2022, $A_k = 1$ for ΛCDM)*

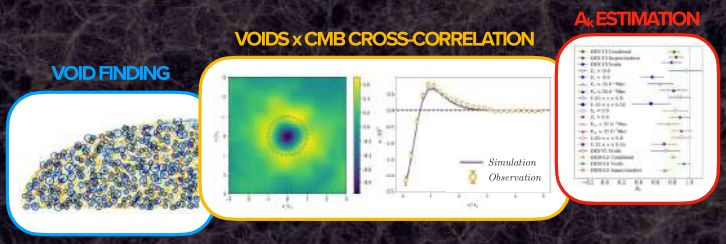

EUCLID AND DESI SURVEYS

The epoch of the large galaxy survey is started, mapping the Universe to understand its composition and to unravel the mystery of dark energy

ESA Euclid Mission

1.2m-diameter space telescope with two scientific instruments: a visible-wavelength camera (VIS) and a near-infrared camera/spectrometer (NISP). Euclid will provide observation of billion of galaxies and about 30 million spectra. Currently at the second year of operations.

The Dark Energy Spectroscopic Instrument (DESI)

Installed on the 4-diameter Mayall telescope, DESI exploits 5000 robot-fibres to measure around 40 million galaxy and quasar spectra up to a redshift z=3.5 in a time span of 5 years. Currently at the fourth year of operations.

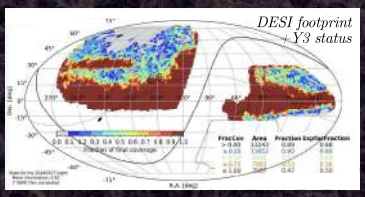

DESI LEGACY SURVEY VOIDS x PLANCK 2018 CMB CONVERGENCE MAP

A new solution to the cosmological lensing tensions

Tensions exist in previous cross-correlation analysis between cosmic voids and CMB lensing:

Different analysis leaded to different tensions with the ΛCDM simulations, depending by the void populations analysed and the identification strategies used. On average, a weaker lensing signal than the prediction is observed.

Exploitation of the DESI Legacy survey, waiting for the spectroscopic Euclid and DESI data

In order to investigate the tensions and to provide a new measurements of the signal, we exploited the photometric DESI legacy survey, that provides the targets for the DESI spectroscopic observation with more than 10 millions Luminous Red Galaxies (LRGs) over more than 13000 square degrees.

We cross correlate the voids identified in this galaxy sample with the convergence map from Planck 2018.

A new approach: mock calibration exploiting the spectroscopic data

To ensure the perfect matching between observation and mocks (Buzzard, *de Rose et al. 2019*), avoiding the arising of fake tensions due to the unaccounted systematics, we calibrate the mocks matching the sparseness and the redshift error distribution of the observations for the full redshift range, exploit the matching between 1 million spectra of the DESI Y1 observation and our photometric observations.

A tension-free set of measurements

Our cross-correlation measurement are resulting perfectly in agreement with the ΛCDM simulated predictions for all the redshift ranges and the void populations considered, with record significances for our detection up to 18σ (an improvement of around 30% compared to the best previous measurements).

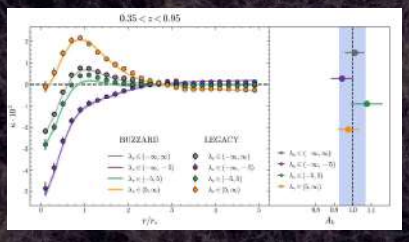

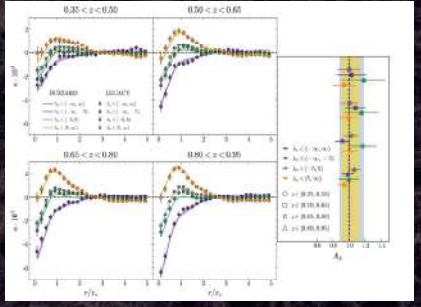

Phd thesis co-funded by CNES and CNRS

sartori@cppm.in2p3.fr

Simulations of MMX/MIRS Phobos observations

Antonin Wargnier[1,2], T. Gautier[2,1], L. Jorda[3], N. Théret[4], A. Doressoundiram[1], C. Mathé[1], E. Sawyer[4], S. Fornasier[1], and M. A. Barucci[1]

[1] LESIA, Observatoire de Paris, Université PSL, CNRS. Sorbonne Université, Université de Paris, 5 place Jules Janssen, 92195 Meudon – France
[2] LATMOS-IPSL, CNRS, UVSQ, Sorbonne Université – France
[3] Laboratoire d'Astrophysique de Marseille (LAM) – France
[4] Centre National d'Etudes Spatiales (CNES), Toulouse – France

I. Context

Phobos origins ?

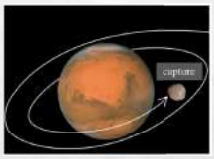

1. Asteroid capture

Small, irregular shape, low albedo, spectrum similar to D-type [1,2,3].

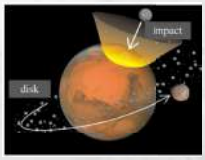

2. In situ formation

Inclination, eccentricity [4]

Objective

Prepare the observation and interpretation of the MIRS observations (near-infrared spectrometer (0.9 - 3.6 µm) onboard MMX [5]) of Phobos and Deimos

MMX mission will explore Phobos and Deimos and unravel the mystery of their origin by in situ observations and sampling of the surface.

II. Simulations

- 3 simulators (Fig. 1):

1. **AURORA** [6]: observation mission scenario
2. **OASIS** [7]: Phobos field of view, generation of geometric information + computation of bidirectional reflectance
3. **MIRAGES** [8]: instrument response

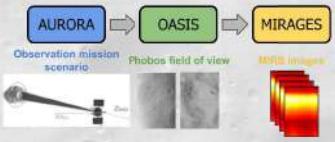

Fig. 1: Simulation chain for MIRS.

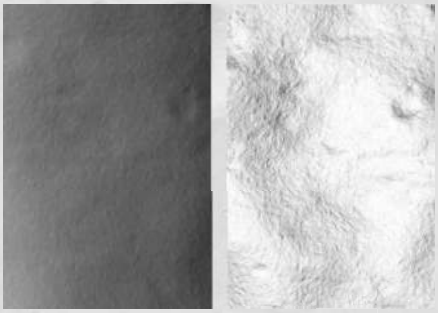

Fig. 2: Example of surface reflectance at 1 µm (left) and temperature at 3 µm (right) landscapes obtained with OASIS simulation.

Fig. 3: Example of a typical MIRS image for a QSO-H orbit, obtained after the three simulators.

- **OASIS** (Fig. 2) computes in the following order:

(1) the illuminations angles from the mission scenario defined using AURORA
(2) the bidirectional reflectance with the Hapke model
(3) the thermal component with a Standard Thermal Model

The model does not account for multiple scattering and Mars reflected light on Phobos and Deimos.

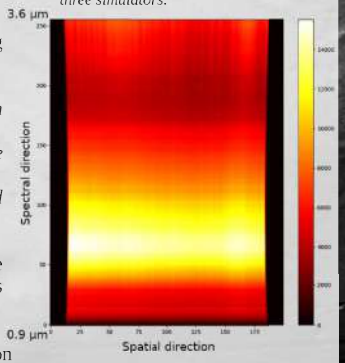

- **MIRAGES** (Fig. 3) models light propagation through the mirrors, grating, and other optical elements
- Simulated images are finally processed by part of the MIRS pipeline to obtained corrected and calibrated images
  - Distortion correction
  - ADU to I/F conversion
  - Spectral registration
- A thermal correction is applied to remove the contribution of the thermal tail

III. Detectability

- Study of the detectability of components of interest for the Phobos' surface, i.e. hydrated minerals and organics.
- We defined patches of different size from a diameter of 3.5 km to 12.9 m at the surface of Phobos (Fig. 4).
- We used laboratory spectra of Phobos simulants [9] as input for the patches spectra.
- Patches are detectable for a size of approximately 40 m → in agreement with the expected spatial resolution in QSO-H orbit (31 – 66 m/px).
- An example of a MIRS observation sequence with a hydrated mineral patches can be seen in Fig. 5.

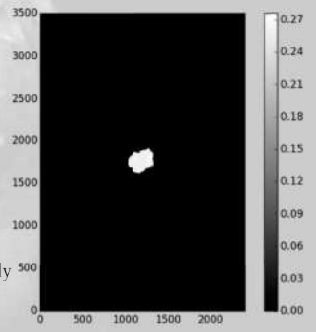

Fig. 4: Example of a patch defined at the surface of the simulated Phobos landscape.

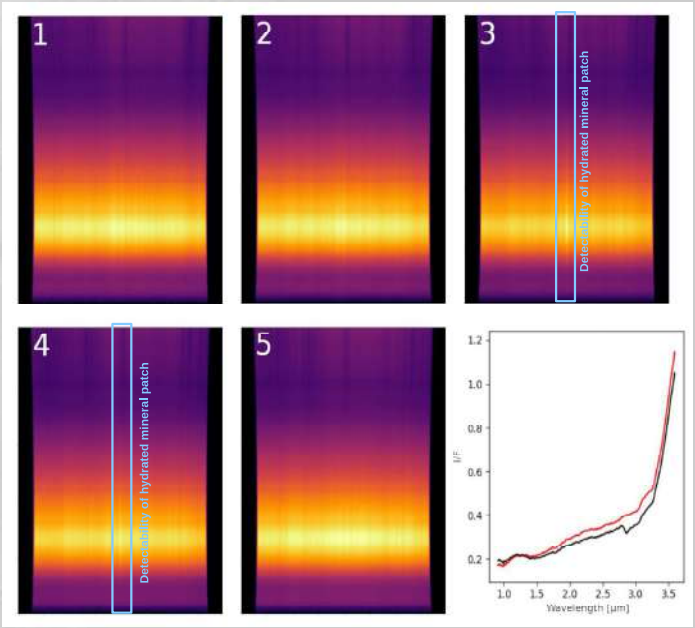

Fig. 5: Example of 5 images of a MIRS observation sequence on a landscape obtained by OASIS. The passage on the hydrated mineral patch can be visually seen as a bright line through the spectral direction in the center of the images 3 and 4. Bottom left corner: Example of two 1D spectra extracted for a MIRS image (panel 3), before thermal tail removal. The black solid line corresponds to the phyllosilicate patch MIRS rendered spectrum, and the red solid line correspond to the 'classic' Phobos surface MIRS spectrum. The 2.7 µm band due to OH in hydrated mineral is clearly visible in the black spectrum.

IV. Conclusions

- We demonstrate the possibility of simulated MIRS observations to prepare the future interpretation of the data.
- The expected MIRS spatial resolution is achieved in our simulations for a typical QSO-H orbit.

V. Further investigations

- Simulation of the Deimos flyby scheduled in September 2027
- Implementation of the Martian contribution

References

[1] Murchie *et al*, 1999. JGR. [2] Rivkin *et al*, 2002. Icarus. [3] Fraeman *et al*, 2012. JGR. [4] Craddock, 2011. Icarus. [5] Barucci *et al.*, 2021. EPS. [6] Sawyer *et al.*, 2023. Acta Astr. [7] Jorda *et al.*, 2010. SPIE. [8] Théret *et al.*, 2023. LPSC abstract. [9] Wargnier *et al.*, 2024. Icarus.

Acknowledgments

This work was carried out in support for the MIRS instrument onboard the future MMX mission, and financed by the Centre National d'Etudes Spatiales (CNES).